Chemical Approaches for 'Undruggable' Targets:
The Discovery of Ligands for Small Heat Shock Proteins

by
Leah Nicole Makley

A dissertation submitted in partial fulfillment
Of the requirements for the degree of
Doctor of Philosophy
(Medicinal Chemistry)
In The University of Michigan
2014

Doctoral Committee:

Adjunct Professor Jason E. Gestwicki, Co-Chair
Professor Heather A. Carlson, Co-Chair
Assistant Professor Tomasz Cierpicki
Assistant Professor Brandon T. Ruotolo
Research Professor Hollis D. Showalter

2014

Acknowledgements

I am grateful to Jason Gestwicki, a fantastic mentor and teacher and brilliant scientist. Jason has taught me a lot about science, but a few lessons stand out that I will take away from my graduate education. The first is the importance of paying attention: Jason taught me the value of self-education through simply paying attention and incorporating that knowledge into my own approaches. The second lesson is that we have an obligation to keep our research translationally focused; if we can do something good for the world, we should, and this should give us urgency and define the goals of our work. The third lesson, less tangibly, is that people rise to meet expectations. Jason has a confident, fearless approach to science, and also appears to have more confidence in his students than we have in ourselves. This attitude, more than anything, makes the lab a great place to work; it conveys the spirit that our capacity for learning and for doing is limited only by our own energy and enthusiasm. Jason, thanks for working so hard to keep the lab supplied with the resources we need to do really cool experiments. Thanks for your patience, your kindness, your generosity with your time, and your constant positivity and enthusiasm.

I am very grateful to my committee for providing advice, collaborative support, personal mentorship, feedback and encouragement. I feel that I lucked out with my committee members. I hope you realize that while it cost you little, words of encouragement from you kept e fueled for weeks. I enjoyed learning from you and I appreciate that you were so engaged in each of my committee meetings and had creative and insightful suggestions for experiments.

Thanks to my first teachers in the lab – Chris Evans, Andrea Thompson, Srikanth Patury, Lyra Chang, Ashley Reinke, and Matt Smith. I had so much fun learning new techniques from each of you; thanks for being generous with your time and experimental knowledge. I am also grateful to Tomoko Komiyama, who was an inspiring presence in my life and one of the strongest women I've ever had the honor of knowing. I think of her often and she is dearly missed. Thanks to all of the other wonderful members of the Gestwicki lab for being super lab mates and all-

around awesome people. You were fantastic sounding boards for experimental design and interpreting results, and you always lifted my spirits whenever my experiments didn't go as well as I'd hoped.

I want to express my appreciation to the professors who taught me in the first two years of my Ph.D, notably John Montgomery, John Wolfe, Erik Zuiderweg, and Adam Matzger. Your lectures in synthetic chemistry, reaction mechanisms, and nuclear magnetic resonance were some of the most challenging and rewarding experiences I had in graduate school; thanks for opening the door to those subjects for me, and for sharing your passion and expertise.

I am thankful for constant support and encouragement from Owen Cadwalader over the past year. Thanks for your presence in my life; everything seems easier with you by my side.

Lastly, I am grateful for the unconditional love and support of my parents, Karen and Terry Makley and my sisters, Libby, Amy, and Meghan Makley.

Preface

This thesis is the compilation of published and unpublished work on the discovery and development of ligands for a class of non-enzymatic molecular chaperones called small heat shock proteins. Small heat shock proteins (sHsps) are important though poorly understood components of the proteostasis network, and this work represents initial attempts to develop chemical probes for sHsps to enable the study of their structures and functions. In Chapter 1, we introduce biophysical strategies for ligand discovery that are amenable to non-canonical targets and introduce sHsps as an example of such targets. A part of this chapter is published as Makley L.N. and Gestwicki J.E., "Expanding the number of 'druggable' targets: non-enzymes and protein-protein interactions," (2013) *Chem Biol Drug Des*. 81(1):22-32. Chapter 2 discusses mutations in sHsps that cause protein aggregation, in some cases leading to gain of toxic function phenotypes, including cataract. This sets the stage for the development of pharmacological chaperones that stabilize the native folds of sHsps to prevent their aggregation. In Chapter 3, a ligand discovery effort utilizing differential scanning fluorimetry to achieve this end is described in detail. One scaffold discovered in this screening effort is being developed as a potential therapeutic for the treatment of cataract, and data supporting its proposed mechanism of action is discussed here. A portion of this chapter is under revision and will be published as McMenimen KA*, Makley LN*, DeVree BT, Rajagopal P, McQuade TJ, Thompson AD, Sunahara R, Klevit RE, Andley UP, and Gestwicki JE., "Pharmacological rescue of an aggregation-prone small heat shock protein in a cataract model." Chapter 4 describes an orthogonal discovery effort that resulted in the identification of ligands for Hsp27 despite its absence of enzymatic activity or known small molecule binding sites, work carried out in collaboration with the Cierpicki and Carlson laboratories. Three *de novo* identified ligand binding sites and the chemical matter that interacts with those sites are described, and the discovery that one site can accommodate pharmacological chaperones that prevent this protein from aggregating is described. Chapter 5 is a discussion of future work required to continue the development and application of the chemical probes described herein, as well as broader future directions in strategies for ligand discovery for noncanonical targets. The appendix provides a discussion of early efforts in the

biophysical characterization and high-throughput screening against the transcription factor HSF1, a canonically ‘undruggable’ target that presents many of the same challenges as the sHsp family.

Table of Contents

List of Figures

List of Tables

List of Abbreviations

1,8-ANS	8-(phenylamino)-1-napthalenesulfonic acid
ACD	α-crystallin domain
AD	Alzheimer's disease
AD	Autosomal dominant
AD	Acidic transactivation domain (of HSF-1)
ALS	Amyotrophic lateral sclerosis
APII	Antiparallel II strand register
AR	Autosomal recessive
AS-MS	Affinity-selection mass spectrometry
ATP	Adenosine triphosphate
AxD	Alexander's disease
BCA	Bicinchoninic acid assay
BLI	Biolayer interferometry
CFTR	Cystic fibrosis transmembrane conductance regulator
CJD	Creutzfeldt-Jakob disease
CMT	Charcot-Marie-Tooth disease
cryAB	αB-crystallin
CT	C-terminus
DBD	DNA-binding domain
DCM	Dilated cardiomyopathy
DMF	Dimethylformamide
DHMN	Distal hereditary motor neuropathy
DRM	Desmin-related myopathy
DELS	DNA-encoded libraries
DMSO	Dimethylsulfoxide
DOS	Diversity-oriented synthesis

DSF	Differential scanning fluorimetry
DTT	Dithiothreitol
EGCG	Epigallocatechin gallate
ER	Endoplasmic reticulum
EtOAc	Ethyl acetate
FP	Fluorescence polarization
GFAP	Glial fibrillar acidic protein
GWAS	Genome-wide association study
HDX	Hydrogen-deuterium exchange
HL	Human lenses
HPLC	High pressure liquid chromatography
HSE	Heat shock element
HSF1	Heat shock transcription factor 1
Hsp22	Heat shock protein (22 kilodaltons)
Hsp27	Heat shock protein (27 kilodaltons)
Hsp27c	Core domain of Hsp27
HSQC	Heteronuclear single quantum coherence
HTS	High-throughput screen
iPrOH	Isopropanol
LC	Liquid chromatography
LZ	Leucine zipper
MALS	Multi-angle light scattering
MeOH	Methanol
MFM	Myofibrillary myopathy
MixMD	Mixed solvent molecular dynamics
MS	Mass spectrometry
MSCS	Mixed solvent crystal structures
mRNA	Messenger ribonucleic acid
NMR	Nuclear magnetic resonance
NT	N-terminus
PBS	Phosphate buffered saline
PC	Pharmacological chaperone

PD	Parkinson's disease
PN	Peripheral neuropathy
PPI	Protein-protein interaction
RD	Regulatory domain (of HSF1)
RT	Room temperature
RU	Response units
SAR	Structure-activity relationships
SD	Standard deviation
SEC	Size-exclusion chromatography
SEM	Standard error margin
sHsp	Small heat shock protein
SOD1	Superoxide dismutase
SPR	Surface plasmon resonance
TCEP	Tris(2-carboxyethyl)phosphine
THF	Tetrahydrofuran
T_m	Melting temperature

ABSTRACT

Chemical Approaches for 'Undruggable' Targets: The Discovery of Ligands for Small Heat Shock Proteins

by

Leah Makley

Co-Chairs: Jason E. Gestwicki and Heather C. Carlson

Small heat shock proteins (sHSPs) are molecular chaperones that protect against protein aggregation in response to stress. These chaperones have been linked to a number of protein misfolding diseases, including neurodegenerative disorders and cataracts. However, sHSPs are considered "undruggable" because they lack enzymatic activity or obvious ligand-binding sites. Thus, sHSPs are emblematic of potential drug targets emerging from large-scale genetic efforts. They are clearly linked to disease, yet it is not clear how to develop drug-small molecules to act on this knowledge. In this thesis work, I employed a number of high throughput biophysical approaches to discover cryptic binding sites on two sHSPs: Hsp27 and alphaB-crystallin (cryAB). Using a multifaceted approach involving computational approaches, differential scanning fluorimetry, fragment-based NMR screening and rational design, three unanticipated binding sites were discovered. Medicinal chemistry and structural efforts yielded four classes of small molecules, with representatives that bind each of the three cryptic pockets. One of these chemical series was developed as a potential new therapeutic for the topical treatment of cataract. These molecules bind the native dimer of cryAB and promote its chaperone functions, reversing cataracts in mouse and human lens models. Another series binds to a region of Hsp27

that is important for its interactions with the Hsp70 class of chaperones, showing promise as a chemical probe for understanding how chaperones regulate protein homeostasis. This thesis work has significantly advanced our knowledge of sHSP 'druggability' and revealed at least three binding sites for further development. Moreover, these efforts represent a detailed, head-to-head comparison of modern HTS methods to discover ligands for cryptic binding sites. The strengths and weaknesses of these approaches are important in designing screening campaigns for other 'undruggable' targets emerging from genetic studies.

Chapter 1

Small Heat Shock Proteins as "Undruggable" Targets

1.1. Abstract

With the emergence of genomic and proteomic information, the preferred methods for identification of new drug targets have changed dramatically. Modern tactics such as genome-wide association studies (GWAS) and deep sequencing are fundamentally different from the pharmacology-guided approaches used previously, in which knowledge of small molecule ligands acting at their cellular targets was the primary discovery engine. A consequence of the "target-first, pharmacology-second" strategy is that many predicted drug targets are non-enzymes, such as scaffolding, regulatory or structural proteins, and their activities are often dependent on protein-protein interactions (PPIs). These types of targets create unique challenges to drug discovery efforts because enzymatic turnover cannot be used as a convenient surrogate for compound potency. Moreover, it is often challenging to predict how ligand binding to non-enzymes might affect changes in protein function and/or pathobiology. Thus, in the post-genomic era, targets might be strongly implicated by molecular biology-based methods, yet they often later earn the designation of "undruggable." Can the scope of available targets be widened to include these promising, but challenging, non-enzymes? In this chapter, we introduce a class of molecular chaperones called small heat shock proteins as examples of genetically identified therapeutic targets, with a focus on the aspects of small heat shock protein structure and function that present challenges to drug discovery efforts. We then discuss advances in high throughput screening technology and chemical library design that are emerging to deal with these challenges.

1.2. Challenges associated with non-enzyme targets

The majority of current drug targets are G-protein coupled receptors, nuclear receptors, ion channels or enzymes (*e.g.* kinases, proteases, deacetylases, *etc.*) (1, 2). Many of these targets were historically identified based on their pharmacology: agonists or antagonists were used to probe the biology of the target, followed by progression to therapeutic candidates. As a consequence, many of these proteins, by definition, contain deep grooves that are amenable to binding by low molecular weight, "drug-like" small molecules. For enzymes, the substrate or transition state can often be used to develop potent inhibitors. In contrast, the modern shift towards molecular biology- and genomics-based target identification has often implicated other types of targets, including **non-enzymes** (Figure 1.1). Non-enzymes make up a majority of the human proteome and they include proteins involved in organizing signaling pathways, maintaining structural integrity, assembly/disassembly of protein complexes, chaperoning, subcellular transport, transcription, translation and other critical functions. Rather than using enzymatic turnover to carry out their biology, most non-enzymes use protein-protein interactions (PPIs), either transient or stable contacts that form the backbone of all major cellular pathways (3). In turn, the challenges of targeting PPIs have been well documented (4-6).

Modern drug discovery approaches, such as high-throughput screening (HTS), typically rely on the measurement of enzymatic turnover to drive discovery of potential clinical leads; thus, non-enzymes pose a particular challenge. Rather, known "inhibitors" of non-enzymes typically bind to the target and either block binding to other proteins or otherwise alter structure-function (*e.g.* change oligomerization, alter protein stability, *etc.*). It is often difficult to predict what will happen to biological pathways in response to these changes and it is more difficult to envision HTS platforms that will rapidly identify potential ligands. To make matters worse, non-enzymes often lack **natural ligands** or even **ligand binding sites**, posing a further hurdle to drug discovery campaigns. Finally, many non-enzymes are either **structurally uncharacterized** or intractable for structural biology (*i.e.* they contain regions of intrinsic disorder), which often precludes the use of most structure-guided design methods.

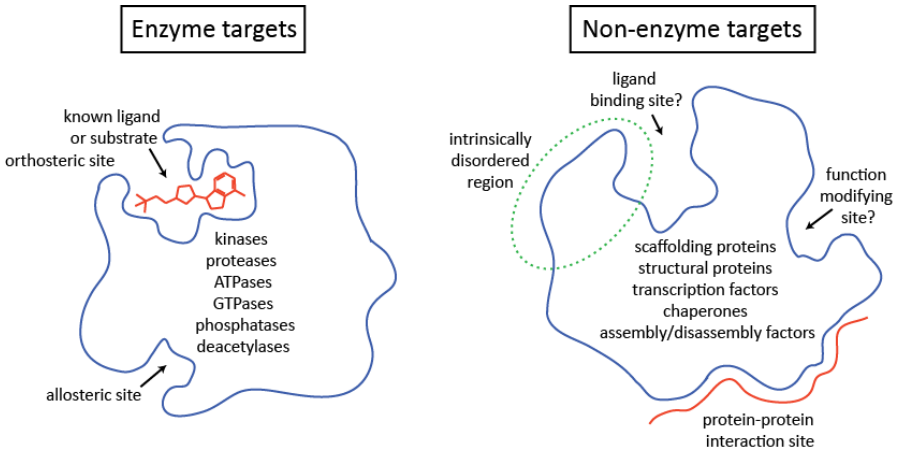

Figure 1.1. Non-enzyme targets present unique challenges to drug discovery. Classic enzyme targets have well-defined active sites and many have clear allosteric sites, which make attractive binding regions for orthosteric and allosteric inhibitors. In contrast, most non-enzymes lack obvious binding pockets or they are involved in protein-protein interactions that involve larger, more diffuse contact areas.

Despite these significant challenges, the prominent role of non-enzymes in biology and pathobiology is certain, so what can be done to expand the number of "druggable" targets to include these proteins? What HTS methods can be adapted for use against non-enzymes? What strategies are amenable to hit identification in the absence of structural information? Is it possible to identify a ligand binding site *de novo*? If so, how can one predict whether or not such a site is "druggable"? In this chapter, we introduce small heat shock proteins as examples of compelling but non-canonical drug targets and discuss some of the structural features that complicate discovery efforts targeting this class. We provide a survey of the methods being used to identify molecules that bind to non-canonical targets and categorize them into affinity-, computational- and stability-based techniques. Lastly, we discuss how chemical library design is evolving to meet the specific challenges of post-genomic drug discovery.

1.3. Small heat shock proteins are examples of non-canonical targets

An intricate network of molecular chaperones is responsible for the maintenance of protein homeostasis in the cell. Heat shock proteins, so named because of their characteristic upregulation under elevated temperature stress conditions, can be classified as ATP-hydrolyzing 'foldases' or non-enzymatic 'holdases'. The well-known heat shock protein 90 (Hsp90) and Hsp70 chaperone families are examples of foldases, which utilize ATP in nucleotide-dependent cycles of client binding and release to favor native client conformations and prevent off-pathway aggregation (7). In contrast, small heat shock proteins (sHsps) are non-enzymatic holdases (8, 9).

sHsps can bind and sequester misfolded client proteins, effectively preventing client protein aggregation in an ATP-independent manner (9, 10). These non-enzymatic chaperones act as proteostasis buffers and maintain their substrates in a folding-competent state for the ATP-hydrolyzing chaperone foldases to then refold or otherwise triage (11-15).

There are eleven human sHsps that range in monomeric size from 16 to 28 kDa and vary in tissue distribution and stress-inducibility, as summarized in the table below (16-18).

Small Heat Shock Protein	Alternative name	Molecular mass (kDa)	Tissue Distribution	HSF1 inducible
HspB1	Hsp27	22.3	Ubiquitous	yes
HspB2	MKBP	20.2	Heart, muscle	no
HspB3	HspL27	17.0	Heart, muscle	no
HspB4	αA-crystallin	19.9	Eye lens	no
HspB5	αB-crystallin	20.2	Ubiquitous	yes
HspB6	Hsp20	17.1	Ubiquitous	no
HspB7	cvHsp	18.6	Heart, muscle	no
HspB8	Hsp22	21.6	Ubiquitous	yes
HspB9	CT51	17.5	Testis	no
HspB10	ODF1	28.4	Testis	no
HspB11	HSP16.2	16.3	Placenta	no

Table 1.1. Human small heat shock proteins vary in tissue distribution and stress-inducibility.

Hsp27, αB-crystallin, Hsp20, and Hsp22 are ubiquitously expressed, while the other sHsps exhibit tissue-specific expression (16). Hsp27, αB-crystallin, and Hsp22 are stress-inducible under the control of the transcription factor heat shock factor 1 (HSF1) (18). These sHsps are upregulated in a variety of stress conditions, which in many cases are proteotoxic; these include protein misfolding, translation inhibitors, cytoskeletal stress, or transport issues. Heat stress, hypoxia, oxidative stress, pH fluctuations, exposure to arsenite or heavy metals, and viral infection are all examples of stress conditions that upregulate sHsp expression (19).

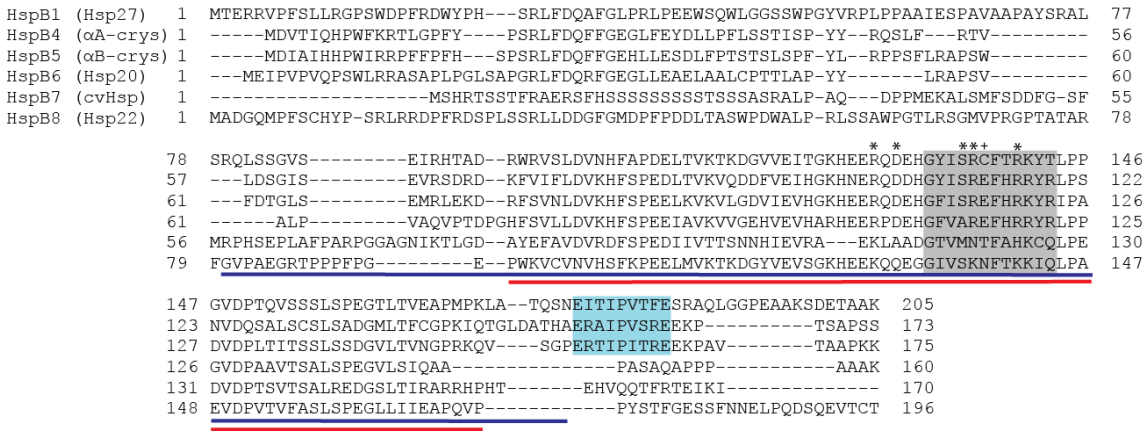

Figure 1.2. Alignment of primary sequences of six human small heat shock proteins, aligned using NCBI Cobalt multiple sequence alignment tool. The red line indicates the α-crystallin domain according to (20), and the blue line indicates the Hsp27 solution NMR construct. The light teal box demarcates the conserved palindromic IXI-containing motif important for oligomerization. The grey box highlights the dimer interface. Asterisks indicate the sites of mutation discussed in Chapter 2, and the plus sign indicates the location of the single endogenous cysteine in Hsp27.

Structurally, sHsps share a characteristic, conserved α-crystallin domain (or 'core domain') of about one hundred amino acid residues (Figure 1.2). This domain has a β-sandwich immunoglobulin-like fold and mediates dimerization of protomers. Stable α-crystallin domain dimers have been structurally characterized at high resolution for Hsp27, αB-crystallin, and Hsp20 (Figure 1.3) (21, 22).

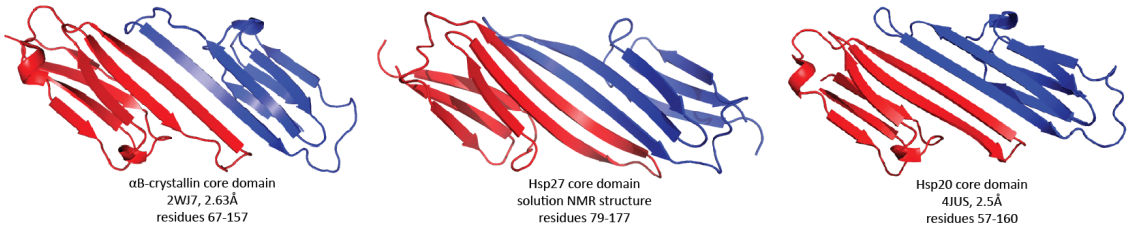

Figure 1.3. Atomic resolution structures of core domain dimers of αB-crystallin, Hsp27, and Hsp22. In each structure, one protomer is shown in red and the other in blue.

Flanking the α-crystallin domain are less-conserved N- and C-terminal extensions (Figure 1.2). The intrinsically disordered N-terminus is between 60 and 90 residues long and contains a short WDPF motif that contacts the core domain to mediate higher-ordered oligomerization (23, 24). The C-terminal extension, which comprises 10 to 30 residues, contains an important palindromic sequence of about 8 amino acids called the IXI motif (highlighted in blue rectangle in Figure 1.2). This palindromic sequence binds to a groove within the core domain of a different protomer to mediate oligomerization (24, 25). The C-terminus also contains a high proportion of charged residues thought to be important in maintaining the solubility of sHsps (9). Full-length sHsps

exhibit quaternary structure polydispersity as large oligomers of between 20 and 40 subunits per oligomer. The exceptions include Hsp20 and Hsp22, which lack the C-terminal IXI motif and consequently only form smaller oligomers (21, 26).

The N-terminus also contains serine residues that are phosphorylated in response to stress conditions in the cell (27-29). Upon phosphorylation, oligomers dissociate to smaller species, and this dynamic regulation of oligomeric size appears to be coupled to chaperone function (27-29). Both the N-terminus and the core domain are involved in chaperone function and client-binding ability (9). Client binding sites have yet to be fully characterized, and the field has not yet reached a consensus on what types of conformations of sHsps are capable of binding misfolded or unfolded protein clients (30). For at least some clients, large oligomers appear to be competent client-binding conformations. Because phosphorylation and dephosphorylation are required for optimal function (31), it has been proposed that chaperone activity requires dynamic changes in oligomerization state, and flux through an ensemble of quaternary structures is necessary for chaperone activity. One possible model for sHsp activation and client binding is shown in Figure 1.4 (9, 30).

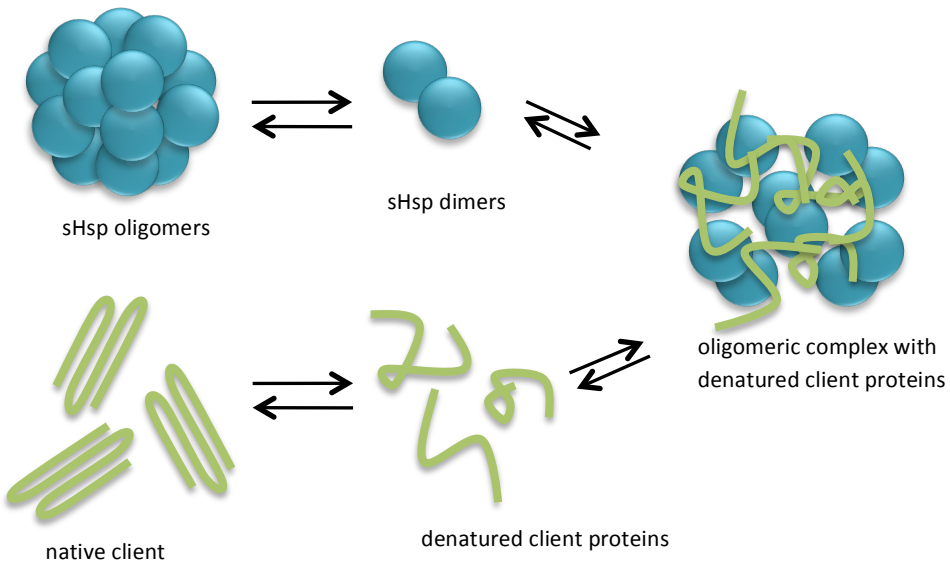

Figure 1.4. Model for sHsp client protection. Cellular stress induces phosphorylation of N-terminal residues in sHsps, which cause dissociation of large oligomers and are associated with 'activation' of sHsp chaperone activity. sHsps may be activated by the same cellular stresses that cause proteins to denature (*i.e.* heat shock), thus acting as the 'first line of defense' in the proteostasis network.

Small heat shock proteins are of interest in a number of disease states. Mutations in the coding sequences of the sHsps cause hereditary cataracts, myopathies, and neuropathies (32-36).

These mutations and known aspects of the associated pathobiologies will be described in Chapter 2. Aside from mutations in sHsp genes, the expression of wild type sHsps has also been linked to neurodegenerative diseases, cancer, acute ischemic shock and neuroinflammation. The involvement of sHsps is thought to be generally protective, except in the case of cancer, as high levels of sHsps confer a survival advantage. The majority of our understanding of this protein family comes from studies of Hsp27 (HspB1) and αB-crystallin (HspB5), so the role of these sHsps in disease will be discussed in more detail.

1.4. sHsps are genetically validated therapeutic targets in neurodegenerative diseases

Impaired proteostasis is a prominent feature of neurodegenerative diseases (37). The intrinsic chaperone activity of small heat shock proteins is protective in such neuropathologies, including amyotrophic lateral sclerosis, Alexander's disease, Alzheimer's disease, Parkinson's disease, and prion diseases. Each of these pathologies is accompanied by upregulation of sHsps, often with colocalization of sHsp in inclusion bodies containing the pathological protein or proteins.

1.4.1. Amyotrophic lateral sclerosis

Amyotrophic lateral sclerosis (ALS) is a multifactorial neurodegenerative disease involving the progressive death of motor neurons. A small fraction of ALS patients express mutations in the enzyme superoxide dismutase 1 (SOD1). In mouse models of familial ALS mutations (G37R, G93A or L126Z mutations in SOD1) αB-crystallin and Hsp27 are upregulated in the affected neurons and reactive glial cells (38). In cultured mouse embryonic fibroblasts, αB-crystallin co-immunoprecipitates with aggregation-prone G93A SOD1 but not wild type SOD1 (39). Double transgenic mice expressing human Hsp27 and G93A SOD1 have delayed motor neuron degeneration compared to SOD1 single transgenic mice during the early stages of the disease (40). Mechanistically, these results suggest that sHsps are molecular chaperones for destabilized Sod1; consistent with this idea, both αB-crystallin and Hsp27 suppress the aggregation of G93A SOD1 via the formation of a stable complex that is isolable by size-exclusion chromatography (41). However, the SOD1 transgenic mice do not have extended lifespans when Hsp27 is overexpressed (40), and in the later stages of the progressive disease Hsp27 levels decrease though mRNA levels are unchanged (40-42). In two other mouse models of ALS expressing G37R or L126Z SOD1, knockouts of αB-crystallin have shorter lifespans than the mice with endogenous levels of αB-crystallin (43). Together, these data point to a protective effect of sHsps but

possible saturation of sHsp chaperone capacity in later stages of mutant SOD1 associated disease. Consequently, it has been proposed that sHsp activation has therapeutic utility, but that it may have the most impact in the early stages of ALS.

1.4.2. Alexander's disease

Alexander's disease (AxD) is a rare, progressive, and usually fatal childhood leukodystrophy. Alexander's disease is caused by mutations in glial fibrillary acidic protein (GFAP) that causes abnormal myelin sheath development and the accumulation of fibrous proteinacious deposits called Rosenthal fibers in astrocytes. Hsp27 and αB-crystallin are both upregulated in astrocytes of children with AxD (44). The protective, disease-modifying role of αB-crystallin in AxD has been studied using mouse models that conditionally express the chaperone (44). Transgenic mice expressing the human GFAP protein recapitulate the symptoms of AxD and typically exhibit <10% mortality at 30 days of age. αB-crystallin knockouts in the GFAP transgenic mouse exhibit significantly increased mortality in a gene-dosage dependent manner, with one-third of αB-crystallin$^{+/-}$ and two-thirds of αB-crystallin$^{-/-}$ mice dying at 32 days. In the GFAP transgenic mice lacking αB-crystallin, cell-specific expression of αB-crystallin in astrocytes under the control of the GFAP promoter recover the phenotype, and the majority of the mice live to three months (44). The role of αB-crystallin has also been studied in a second mouse model expressing a mutant form of GFAP (R236H), which causes a more severe disease phenotype with complete lethality observed by 40 days. Powerfully, 100% of R236H transgenic mice with astrocyte specific overexpression of αB-crystallin survive to 180 days. The phenotypic recovery is accompanied by fewer hippocampal Rosenthal fibers and a reduction in insoluble GFAP (44), indicating that in this context αB-crystallin may act as a chaperone for GFAP, stabilizing nonfibrillar and nontoxic species. Together, this body of work argues for the utility of αB-crystallin-based therapeutics in a fatal orphan indication in which no treatments currently exist.

1.4.3. Alzheimer's disease

Alzheimer's disease (AD), the most common form of age-related dementia, is a progressive neurodegenerative disease that involves the aggregation of amyloid-β and the microtubule stabilizing protein tau (45). Accumulation of protein aggregates in the brain leads to subsequent neuronal death and dementia. Amyloid-β accumulates and forms senile plaques, while tau is hyperphosphorylated, released from microtubules, and aggregates to form neurofibrillary

tangles. AD is accompanied by upregulation of Hsp27 and αB-crystallin, and Hsp27 is perhaps best studied in the context of this neurodegenerative disease (46). In particular, Hsp27 expression levels correlate with disease severity and levels of phosphorylated tau (47, 48), and the chaperone activity of Hsp27 appears to be protective in the context of AD. In cellular assays using rat neuroblastoma neurons, Hsp27 overexpression or adenoviral delivery results in decreased levels of hyperphosphorylated and total tau and correspondingly lessened toxicity (31, 48, 49). Moreover, in a transgenic mouse model of tauopathy expressing the P301L mutant of tau (rTg4510), adenoviral transfection of Hsp27 rescues tau-associated deficits in long-term potentiation (31). Powerfully, transgenic overexpression of human Hsp27 corrected hippocampal deficits in long-term potentiation in a double-transgenic mouse model of Alzheimer's disease that expresses the Swedish mutation of amyloid precursor protein and presenilin 1 deleted in exon 9 (APPswe/PS1dE9). In behavioral assays of learning and memory, the transgenic mice overexpressing Hsp27 actually resembled normal wild type animals, recovering the severe behavioral phenotypes seen in the vector control animals (50). Mechanistically, little is known about how Hsp27 exerts this protective effect, though Hsp27 can chaperone tau *in vitro* and prevents the elongation of tau fibrils (31). Moreover, Hsp27 preferentially interacts with phosphorylated versus unphosphorylated tau in immunoprecipitation assays with recombinant protein, suggesting that the chaperone may be able to distinguish between the pathological and normal conformations of the polypeptide (48).

In addition to its roles in tau homeostasis, Hsp27 also plays a protective role in amyloid-β aggregation and toxicity, a second major component of AD pathology (51, 52). In mouse neuroblastoma neurons, Hsp27 is upregulated 6- to 7-fold when the neurons are exposed to toxic amyloid-β oligomers. When the amyloid-β oligomers were pre-treated with substoichiometric amounts of Hsp27, Hsp27 completely abrogated neurotoxicity, an effect that was specific to Hsp27 and dependent upon the order of addition (that is, the effect of Hsp27 was from its interaction with oligomers of amyloid-β and not directly with cells). Electron and atomic force microscopy suggests that Hsp27 remodels neurotoxic amyloid-β oligomers into larger, non-toxic aggregates (52). A separate study demonstrated a direct binding interaction between Hsp27 as well as three other sHsps with monomeric amyloid-$\beta_{1\text{-}40}$ and $_{1\text{-}42}$, and found that the apparent affinity of each interaction correlated with the degree of sHsp inhibition of amyloid-β cytotoxicity and the degree of sHsp inhibition of amyloid-β fibril formation (53).

Together, this suggests that Hsp27's chaperone activity is responsible for mitigating toxicity of amyloid-β.

The sHsp αB-crystallin is also overexpressed in AD patients, most highly in neurons that are adjacent to extracellular neurofibrillary tangles or senile plaques (54). αB-crystallin is known to efficiently suppress the aggregation of amyloid-β at substoichiometric concentrations. A number of studies have characterized direct binding interactions between the proteins using orthogonal techniques, suggesting multiple modes of interaction. Solution NMR studies found that the αB-crystallin weakly and transiently interacts with the hydrophobic core residues of monomeric amyloid-$\beta_{1\text{-}40,}$ the same residues that form monomer-monomer contacts in its aggregation (55), suggesting that αB-crystallin is a competitive inhibitor of amyloid-$\beta_{1\text{-}40}$ aggregation. In addition, a surface plasmon resonance study confirmed binding of αB-crystallin to immobilized amyloid-$\beta_{1\text{-}40}$ or $_{1\text{-}42}$ and measured relatively tight (mid-nanomolar) apparent affinities, which may reflect multivalency (53). Third, several *in vitro* studies have shown that αB-crystallin binds to elongating fibrils of amyloid-$\beta_{1\text{-}40}$ or $_{1\text{-}42}$ along the lengths of fibrils to suppress fibrillization, possibly by suppressing fragmentation and secondary nucleation (56-58). This series of studies indicates that αB-crystallin may interact with multiple conformations of amyloid-β (i.e. monomers, oligomers, fibrils) to prevent aggregation. Reports conflict as to whether αB-crystallin favors species that are toxic or nontoxic to cells (56-58), and more work is required to understand the therapeutic utility of αB-crystallin in models of AD.

1.4.4. Parkinson's disease

Parkinson's disease (PD) is a progressive neurodegenerative disease characterized by the aggregation and deposition of α-synuclein in inclusions called Lewy bodies and the loss of dopaminergic neurons. Though most cases of PD are idiopathic, a few cases involve mutations in α-synuclein that cause the protein to aggregate more rapidly. Both Hsp27 and αB-crystallin are upregulated in the brains of Parkinson's disease patients and show similarly elevated expression in the transgenic A53T α-synuclein mouse. αB-crystallin inhibits A53T α-synuclein fibrillization and is thought to interact both with partially folded monomers as well as elongating fibrils (59, 60). Similarly, Hsp27 interacts weakly and transiently with α-synuclein protomers to suppress fibrillization (61). Viral delivery of Hsp27 to human neuroglioma cells expressing α-synuclein confers protection from apoptosis (62). In separate studies, knockdown of Hsp27 increases the

susceptibility of dopaminergic neurons to A53T α-synuclein-associated toxicity. Neurons with increased expression of Hsp27 contain fewer Lewy-body-like aggregates and are protected from A53T α-synuclein-associated toxicity (63). Consequently, Hsp27 and αB-crystallin may represent interesting targets for the development of therapeutics for PD, though no proof-of-concept experiments have been carried out in animal models of the disease to date.

1.4.5. Prion diseases

Prion diseases are infectious neurodegenerative diseases that are transmitted by misfolded proteins. In Creutzfeldt-Jakob disease (CJD), a rapidly progressing and invariably fatal encephalopathy, αB-crystallin is highly upregulated in glia and neurons (64, 65). In hamsters infected with the scrapie prion, αB-crystallin expression levels in reactive astrocytes increased as the disease progressed from the time of inoculation. It is not clear if αB-crystallin is playing a protective role as a molecular chaperone in prion diseases; however, because of the similarities between prion diseases and tauopathies, sHsps may be protective in each case and warrant further study (66).

1.5. sHsps are potential therapeutic targets in ischemic stroke

Neurodegenerative diseases are chronic diseases where the burden on the molecular chaperone network to restore proteostasis is clear. However, sHsps are also upregulated in acute neurological conditions where protein misfolding is not a central component of the disease etiology; these include epileptic seizures and ischemic stroke (66). Little is known about the involvement of sHsps in epilepsy, though many studies have observed upregulation of sHsps in areas of the brain where epileptic seizures occur (67-69), and one study observed over 50% reduction in kainate-induced seizure severity and associated mortality in a transgenic mouse expressing Hsp27 (69). The protective effect of sHsps in ischemic stroke is better understood. Ischemic strokes are caused when blood and oxygen supply to the brain is restricted, resulting in the death of neurons within minutes. Both Hsp27 and αB-crystallin are upregulated in neurons and plasma following strokes. Overexpression of Hsp27 is neuroprotective in transgenic mouse models of cerebral ischemia; infarct size was reduced by about a third in mice expressing Hsp27 after permanent artery occlusion (70, 71). In a study by a different group, viral delivery of Hsp27 to neurons of living mice three days before induction of ischemic stroke reduced the volume of resulting lesions by 44% compared to controls (72). In a third model of ischemia-reperfusion

injury, human Hsp27 purified from human lymphocytes was injected intravenously one hour after the ischemic event. The protein crossed the blood brain barrier and was taken up by neurons surrounding the area of ischemic injury. Treatment was accompanied by attenuation of neuronal death; lesions were one-third of the size of those in untreated controls (73). In similar studies, mice lacking αB-crystallin exhibited lesions nearly twice the size of those in wild-type animals and scored significantly worse in neurobehavioral tests following ischemic injury than animals with endogenous levels of the chaperone (74). In wild type mice, intraperitoneal injection of recombinant, purified αB-crystallin up to 12 hours following experimental stroke reduced lesion volume by approximately half (74). It is not clear whether the protective effect of sHsps in ischemic stroke is due to sHsp chaperone activity, or if it is, what relevant protein clients are involved. However, if the protective effect could be translated to human patients, it would represent a significant improvement over the standard of care for stroke victims, both in terms of therapeutic impact and treatment modality.

1.6. sHsps are potential therapeutic targets in cancers

Upregulation of sHsps is advantageous to cancer cells, contributing to tumor formation, growth, and metastasis and resulting in resistance to chemotherapies (75). High levels of sHsps are especially common in carcinomas, including ovarian, breast, head, and neck carcinomas, and high levels of sHsps in tumors are associated with poor clinical prognoses (75). In a proof-of-concept xenograft study in mice, peptide aptamers targeting Hsp27 strongly reduced tumor growth. The same aptamers inhibited Hsp27's anti-apoptotic activity in HeLa cells (76). The anti-apoptotic function of sHsps may represent a general effect of their chaperone activity towards any number of client proteins involved in apoptotic cascades, or it may represent the result of a protein-protein interaction with a specific effector of apoptosis. A few studies have examined direct interactions of sHsps with apoptotic inducers, for example cytochrome C (77). Cytochrome C is released from the mitochondria in response to apoptotic signals, and then forms a complex with several other pro-apoptotic effectors including procaspase-9 and Apaf-1 (19, 77), initiating caspase cleavage and the beginning of apoptosis. Hsp27 interacts with cytochrome C and prevents it from forming a complex with these effectors, thus preventing apoptosis. Truncations and point mutations in Hsp27 tuned its ability to bind to cytochrome C and the extent of binding predicted caspase cleavage activity and apoptosis, confirming that the effect of Hsp27 was via its direct or indirect interaction with cytochrome C (19, 77). Hsp27 also

plays a role in maintaining cytoskeletal integrity by interacting with and perhaps chaperoning many proteins that make up the cytoskeleton, as reviewed in (78). Solid tumor metastasis requires an epithelial-to-mesenchymal transition, invasion of cancer cells into other tissues, then reversion back to epithelial cells and subsequent adhesion and growth. Both transitional processes involve dramatic cytoskeletal remodeling, so it has been hypothesized that the requirement of Hsp27 for tumor metastasis involves its chaperoning of cytoskeletal elements (19, 78). Though more work remains to be done to understand the mechanism of sHsp tumorigenic functions, inhibition of Hsp27's interaction with cytochrome C or cytoskeletal elements appear promising to be promising targets.

1.7. sHsps are non-canonical drug targets

While many studies suggest that sHsps may represent promising drug targets, the structure of these chaperones precludes standard methods for the discovery of small molecule modulators. Small heat shock proteins have no intrinsic enzymatic activity, and as such are not amenable to the high-throughput screening assays that rely on enzymatic turnover as a reporter. Additionally, sHsps do not have endogenous cofactors or tight binding natural ligands, and correspondingly there are no known ligand binding sites. While sHsps are known to engage in a number of protein-protein interactions (recently reviewed in (78)), these are largely transient and weak interactions that are poorly suited for the design of a high-throughput screening platform. To make matters worse, oligomeric sHsps are very large (>500 kDa) and polydisperse, and are consequently very difficult problems for structure-based design. As discussed earlier in this chapter, genetic proof-of-concept studies suggest that sHsps may represent attractive therapeutic targets in a number of indications. However, to date these studies have all examined the phenotypic effects of modulating total levels of protein, rather than tuning the function of sHsps at endogenous levels. An sHsp modulator might act at the level of transcription to change total levels of sHsp, for example by modulating HSF1 activation. With this goal in mind, pilot studies involving targeting HSF1 with small molecules were carried out and are described in the Appendix of this thesis. Conversely, a small molecule may act by directly engaging an sHsp or sHsp-client complex and tuning chaperone function at the protein level. The discovery of such ligands is the long-term goal of this body of work, and this thesis represents important first steps towards achieving this aim.

It is not obvious how a small molecule may be designed to modulate the chaperone activity of sHsps, given the incomplete mechanistic understanding of structure-function relationships in this class of proteins. A useful sHsp-based therapeutic for neurodegeneration would agonize the protein's chaperone activities, which are protective in these disease states. An sHsp **agonist** could stabilize sHsp-client interactions or favor active conformations of sHsps that are competent to bind clients. Conversely, an sHsp **antagonist** would be useful in cancers, where inhibition of sHsp chaperone function is desirable. A molecule that inhibits sHsp-client protein-protein interactions or contacts between sHsp protomers is hypothesized to antagonize chaperone activity. Our incomplete mechanistic understanding of sHsp structure and function is at once the greatest challenge of targeting sHsps and the underlying motivation for discovering useful chemical probes that perturb or stabilize sHsp structure and protein-protein interactions in useful and predictable ways. The discovery of chemical probes for sHsps is expected to contribute greatly to our mechanistic of this class of molecular chaperones.

1.8. Strategies for ligand discovery for non-canonical targets

sHsps have been genetically validated as promising therapeutic targets. However, this class of proteins has been labeled 'undruggable' because of a number of aspects of sHsp structure and function that preclude application of many of the common strategies for drug discovery to this family of molecular chaperones. Thus, this class of proteins may be considered as genetically validated but chemically unvalidated therapeutic targets. In the remainder of this chapter, we discuss biophysical and *in silico* strategies for identifying ligands for noncanonical targets such as sHsps, and consider expansions in chemical library design that support this process.

1.8.1. Affinity-based techniques for ligand discovery

A major problem in many potential drug discovery campaigns involving non-enzymes is that it is difficult to identify molecules that bind the target. In the absence of an enzymatic function, there is no convenient surrogate for ligand binding, so the interaction must be directly measured. **Nuclear magnetic resonance (NMR)-based screening** has proven to be particularly amenable to the label-free, affinity-based selection of ligands that bind a target of interest, including non-enzymes (79). The most information-rich platform for NMR-based screening uses a two-dimensional experiment (HSQC or TROSY) and observes ^{15}N or ^{13}C isotopically labeled protein. In these experiments, mixtures of library compounds, generally low molecular weight

fragments, are added to a solution of the protein. Hits result in binding-induced perturbations of the chemical shifts associated with N-H or C-H bonds (Figure 1.5A) and, if the NMR spectrum is assigned to the protein's primary sequence, then the ligand binding site may be directly determined from this experiment. The binding site is often used to prioritize hits and the screen may be carried out in the presence of a competitive orthosteric ligand to favor the identification of second-site binders. False positive rates are typically low, and nonspecific binding is often readily recognizable. However, protein-observed NMR screening requires that the protein be highly soluble, stable, and homogenous at high concentrations (50 to 500 μM (80)), able to be recombinantly expressed in isotopically enriched media, and relatively small (less than ~80 kDa, though this limit depends on the type of labeling and experiment used (81)). Thus, to complement the protein-observed experiments, a number of one-dimensional, ligand-observed experiments may also be used, including saturation transfer (82, 83) and diffusion based experiments (84, 85). These approaches are selection-based, meaning that only the ligands interacting with the target protein are identified from mixtures. Ligand-observed experiments require relatively low concentrations of protein (typically 1 to 10 μM), and the protein need not be isotopically labeled. In addition, they have higher throughput and lower experimental cost than protein-observed experiments. However, ligand-observed methods do not distinguish between specific and nonspecific interactions, they offer no information on the binding site, and they suffer from higher false positive rates (though the combination of several ligand-observed experiments may increase reliability (86)). For both ligand- and protein-observed NMR experiments, relatively weak interactions (K_D values between 0.1 μM to 10 mM) can be measured, but stronger interactions can give false negatives (81).

In addition to its utility as a screening strategy, NMR can be extremely valuable for *de novo* binding site identification in targets for which no orthosteric site is known or for which an allosteric site is desired (87-91). These methods might even reveal sites that are not obvious from available crystal structures because NMR is solution-based. Because of the reliability of NMR in identifying binding sites for small molecules, hit rates from fragment-based NMR screens are often used to categorize a protein target for its potential "druggability" (92). The theory in this approach is that higher hit rates are suggestive of more and deeper binding sites. For example, Hajduk and colleagues observed a correlation between high experimental NMR hit rates (>0.2%) and the success of medicinal chemistry campaigns to develop molecules with high

affinity (<300 nM) among a set of 23 protein targets (92). This approach might be particularly useful in targeting PPIs, because of the notoriously shallow contact surfaces involved and the advantages of using allostery to disrupt these interfaces (93, 94). My attempts to identify ligands for Hsp27 using NMR-based screening will be discussed in Chapter 4.

To illustrate the potential of NMR-based screening campaigns, it is useful to consider the specific example of survivin. Survivin is a cell cycle regulator and inhibitor of apoptosis that is upregulated in most tumor cell types but absent in most other adult tissues (95). High levels of survivin have been associated with poor prognosis in patients (96) and antisense oligonucleotides and siRNA against survivin decrease proliferation in a number of cancer cell lines (97, 98). Survivin has no enzymatic activity or known endogenous small molecule regulators, and, accordingly, no robust biochemical assay of survivin function has been established. Wendt and colleagues at Abbott Laboratories chose to employ two complementary affinity-based screening methods, **NMR-based screening** and **affinity selection mass spectrometry (AS-MS)** to pursue lead generation of molecules that bind survivin (79). AS-MS experiments start with the incubation of a mixture of ligands with the protein target of interest, followed by a separation step to remove unbound molecules and mass spectrometry-based identification of eluted compound(s) (99). These methods are highly sensitive and allow for the evaluation of large chemical libraries (up to 10^8 to date, (100)) without the need to add labels (99, 101). However, because it is prone to false positives, this method is complemented by protein-based NMR screening. Thus, the Abbott group used these two methods in combination to discover a novel small molecule-binding site on the dimer interface of survivin. They also used the relative hit rates from the screening campaign to evaluate the relative druggability of this new site, concluding that the dimer interface may be particularly promising (0.35% relative to 0.01% for a known peptide-binding interface). One lead series was developed into a class of compounds with nanomolar affinity for survivin (79). Although it is not yet clear how interactions with this binding site impact survivin biology, the lead compounds from this campaign are expected to be powerful probes for target validation.

Surface plasmon resonance (SPR) is a label-free platform for the detection of direct binding interactions. Briefly, the target protein is typically immobilized to a gold chip, and potential ligands are introduced to this surface. Real-time association and dissociation rates of the

interaction are measured, giving useful information about binding kinetics. The well-known nutlin class of MDM2-p53 protein-protein inhibitors originated from a competition SPR screen, in which the ability of molecules to disrupt this PPI was monitored (102). The throughput of SPR experiments is lower than that of other affinity-based techniques, but these rates are increasing with newer generations of the technology; the latest instrument from GE Healthcare, the Biacore 4000, handles up to 4,800 samples per day (103). However, this technique is still more widely applied to the evaluation of small, focused libraries during lead optimization. Some improvement in throughput can be obtained using **biolayer interferometry (BLI)**. In commercialized BLI platforms, pins with immobilized ligand are dipped into wells of 96- or 384-well microtiter plates containing solutions of analytes, and the association and dissociation rates are measured in real-time. Using this approach, the OctetRed384 (ForteBio) can process up to 7000 samples per day (104). Both SPR and BLI are flexible platforms that are well suited to the study of non-canonical targets because no structural information is required, no ligand binding site needs to be identified and no enzymatic activity is necessary.

Microarray techniques facilitate the discovery of new ligands via binding of a target to arrays of immobilized compounds. In this approach, small molecules or peptides are covalently attached to modified glass microscope slides, followed by incubation with the protein target of interest that is either directly labeled with a fluorophore or detected using a fluorescent antibody (Figure 1.5A). This approach has been used to discover new ligands for non-enzymes, including the yeast transcription factor Hap3p (105) and the extracellular signaling protein Sonic hedgehog (106). In the Hap3p campaign, a collection of 12,400 immobilized compounds was screened, leading to the discovery of haptamide B. Haptamide B binds Hap3p and inhibits its transcriptional activity (105), likely by blocking PPIs in the transcription complex. In a similar strategy, Stanton and colleagues screened 10,000 immobilized compounds and identified robotnikinin, which binds the N-terminus of Sonic hedgehog and inhibits signaling (106, 107). In another recent adaptation of this technology, Landry and colleagues combined microarrays with ellipsometry to obtain affinity values for binding to 10^4 immobilized small molecules (108, 109). The oblique-incidence reflectivity difference microscope that was constructed for this use is not yet commercialized (110), but it has the potential to accelerate affinity-based lead discovery by microarrays by facilitating rank-ordering of potential ligands.

Tethering is a technique that uses disulfide exchange to identify small molecule ligands for a given site on a protein (111). This technique enables discovery targeting orthosteric or allosteric sites. Such sites may be apparent from prior structural knowledge of the target and its mechanism of action, or may be identified *de novo* using computational methods (see section 1.10). Tethering may also be applied to the inhibition of protein-protein interactions, which often involve large, diffuse surfaces of the binding partners (5). In these instances, alanine scanning may be useful in identifying 'hot spots' on a protein surface that account for most of the binding energy (112), which may then be targeted for inhibitor binding. In disulfide tethering, a cysteine residue is introduced within or adjacent to the site of interest, and any endogenous reactive cysteines are mutated to alanines. The target protein is then exposed to a library of small molecules (generally fragments) containing reactive thiols, in the presence of competing amounts of a thiol reducing agent such as β-mercaptoethanol. A molecule that has favorable physicochemical interactions with residues in the site will outcompete β-mercaptoethanol and form a mixed disulfide adduct with the protein target. The resulting 'tethered' protein-ligand adduct can then be identified by mass spectrometry (111). Hits from a tethering screen may be elaborated and optimized, using structure guided design and competition with β-mercaptoethanol as a proxy for affinity. The thiol in the ligand can then be removed or replaced and the ligand will retain affinity for the wild-type target protein. In some cases, tethering can be used to target endogenous cysteines; the thiol in the ligand may be converted to a stronger electrophile (e.g. acrylamides or vinyl sulfonamides) to generate an irreversibly covalent ligand (113). Efforts to apply tethering to the endogenous cysteine in Hsp27 are underway in the Gestwicki lab and will be briefly discussed in the context of Chapter 4.

1.8.2. Stability-based methods for ligand discovery

Monitoring ligand-induced changes in protein stability is another way to discover potential ligands for non-enzymes. Historically, the drug discovery applications of ligand-induced stability were pioneered in attempts to develop "pharmacological chaperones", or molecules that stabilize the folded form of a mutated or damaged protein. Pharmacological chaperones have been successfully used to correct disease phenotypes in a number of disorders caused by a loss of protein stability (114), including phenylketonuria (115, 116), Gaucher disease (117, 118), Tay-Sachs disease (119), cystic fibrosis (120, 121), and transthyretin amyloidosis (122, 123). One molecule, tafamidis, has been approved in Europe for the treatment of a form of transthyretin

amyloidosis, familial amyloid polyneuropathy (124). Tafamidis kinetically stabilizes the tetrameric conformation of transthyretin, increasing the activation barrier of dissociation of the tetramer to an unstable monomer (122). Similarly, a recently discovered peptide inhibitor of caspase-6 acts by stabilizing an inactive, tetrameric conformation of the protein (125). Recent work suggests that even some classic ligands might, in fact, use a pharmacological chaperone mechanism; for example, nicotine appears to exert its effects by thermodynamically stabilizing a specific conformation of the acetylcholine receptor (126, 127). There are a number of methods available for discovering ligands that bind and stabilize targets and, because these methods do not rely on enzymatic turnover, they are particularly versatile tools for discovery in a post-genomic era.

Differential scanning fluorimetry (DSF) is one technique for measuring the ligand-induced changes in the thermal stability of a protein (128). In these experiments, a protein solution is heated, leading to thermal denaturation. This unfolding is monitored using an environmentally sensitive fluorophore, such as 8-(phenylamino)-1-naphthalenesulfonic acid (1,8-ANS) (Figure 1.5B) and ligands are identified by their ability to shift the apparent melting transition (ΔT_m). DSF experiments can be miniaturized for use in 384-well microtiter plates (129-132), permitting the screening of chemical libraries.

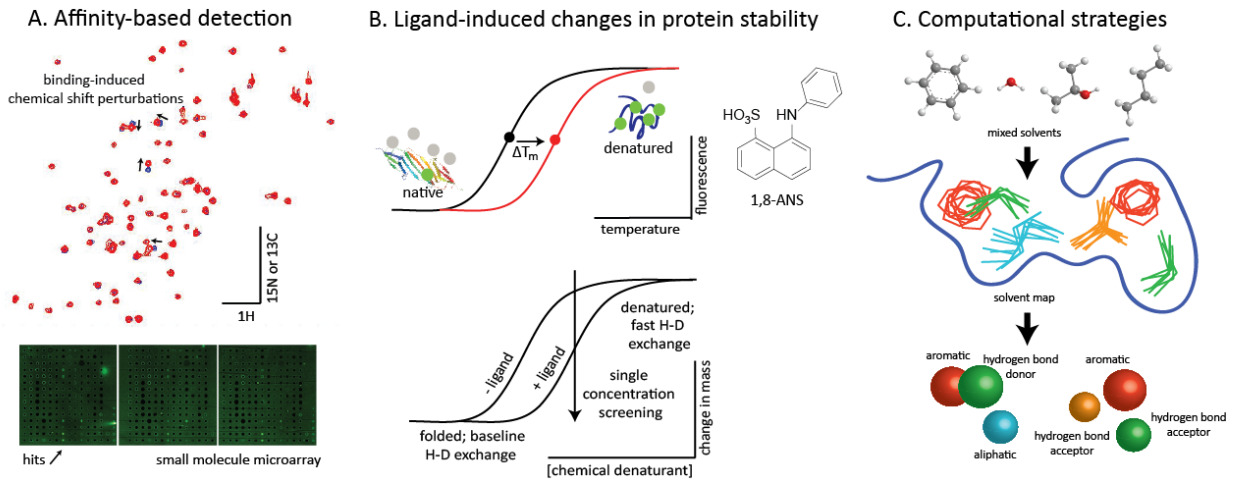

Figure 1.5. Selected biophysical methods for ligand discovery. A: Ligand-induced changes in chemical shifts of a ^{1}H, ^{15}N HSQC spectrum of a protein target suitable for NMR-based screening indicate binding. Fluorescent spots on a small molecule microarray indicate the presence of a fluorescently labeled protein bound to the immobilized ligands. B: Differential scanning fluorimetry measures changes in the melting temperature (T_m) of a protein target induced by ligand binding. Similarly, hydrogen-deuterium exchange can measure changes in stability to chemical denaturation

due to small molecule binding. C: The mixed-solvent molecular dynamics method may be used for both binding site identification and the construction of a pharmacophore.

One illustrative example of a DSF campaign was reported for the transcription factor p53, which is a tumor suppressor that normally functions to regulate cell cycle arrest and apoptosis. Knockout mice ($p53^{-/-}$) have high rates of spontaneous tumors, and p53 null or mutant tumors are associated with poor prognosis and resistance to chemotherapy in a number of human cancers (133). The suppressor oncogenes MDM2 and HDM2 engage in PPIs that activate p53, leading to cell cycle arrest and apoptosis. These observations suggested that inhibitors of the p53-MDM2/HDM2 interactions might be promising anti-tumor agents, yet the drug target was clearly a non-enzyme, PPI interface. A team at Johnson & Johnson used DSF to screen a focused collection of 22,000 1,4-benzodiazepine-2,5-diones for affinity to HDM2 (134, 135). The screening hits were then evaluated for inhibition of the p53-HDM2 PPI by a competitive fluorescence polarization (FP) assay, resulting in the development of inhibitors with nanomolar potency in cancer cell lines (133). In this example, the candidate molecules, discovered by DSF, appear to bind HDM2 and stabilize a conformation that prevents the p53 interaction. DSF has more recently been applied to an HTS campaign against the F508Δ mutant of the cystic fibrosis transmembrane conductance regulator (CFTR) (136). This point mutant is responsible for most cases of cystic fibrosis and it is known to destabilize the protein, causing F508Δ CFTR to be aberrantly retained in the ER and degraded rather than trafficked to the plasma membrane, where it normally functions as a chloride channel. DSF was used to prioritize hits from a cell-based primary screen and it was found that the most promising molecules bind to the first nucleotide-binding domain of the CFTR, helping to restore the folding free energy (ΔG) lost by the mutant. These efforts resulted in the identification of a phenylhydrazone, RDR1, which acts as a pharmacological chaperone for the misfolded F508Δ CFTR mutant (136). My attempts to adopt this approach to study Hsp27 and αB-crystallin will be discussed in Chapter 3. Finally, several variations of DSF experiments have been reported. For example, intrinsic fluorophores, such as tryptophan or a cofactor, can be used in place of an extrinsic dye (137); cysteine residues can be used in combination with thiol-specific fluorochromes in the same manner (138).

Hydrogen-deuterium exchange (HDX) coupled with NMR or mass spectrometry can be a powerful method for the detection of ligand-induced changes in protein stability. When a folded

protein is placed in buffer containing deuterated water, exchangeable protons on amide nitrogens and side chain heteroatoms are replaced with deuterons at a rate that is proportional to their relative solvent accessibility. Upon unfolding of the protein, internal protons become exchangeable (139), thus ligands can be detected by their ability to delay or prevent deuteration (Figure 1.5B) (140). This technique has been developed for HTS by the Fitzgerald laboratory using the prolyl isomerase cyclophilin A as a model system (141-143). In this example, a library of 10^4 compounds was screened at a single timepoint and a single denaturant concentration, with a throughput of ~100,000 compounds per day.

1.8.3. *In silico* methods for ligand discovery

Another tool in the discovery of ligands for non-enzyme targets is ***de novo* binding site identification**, which uses geometrical, energy-based, evolutionary, or probe mapping techniques to scan for sites that may be deep enough to accommodate small molecules with good binding affinity (144, 145). This approach is often used as a prelude to the development of pharmacophores that might bind the new site, which enriches subsequent HTS campaigns with predicted inhibitors. Most of the available *de novo* site prediction methods search for potential sites by identifying concave 'pockets' on the surface of a rigid protein structure (144). Alternatives include energy-based approaches, which use a 3D potential grid to identify contiguous regions of predicted low energy interactions (146) and evolutionary (or genomic) methods, which consider the degree of conservation of amino acids on a protein's surface (145, 147). Lastly, probe mapping techniques coat the surface of the protein with small organic molecules and calculate the interaction energies between the probes and the surface to predict likely sites (144). These four strategies may be used alone or in combination (144).

One significant limitation of the current *de novo* methods is that they are generally used with a rigid protein structure, which makes them fast but inaccurate for flexible binding sites (145). However, one recent advance is based on the multiple-solvent crystal structure (MSCS) approach (148). In the MSCS experiment, a target protein is crystallized and placed in solutions containing organic solvent. The organic probes displace water and they tend to accumulate at sites where favorable interactions may be possible. When multiple solvents are used, the contributions of aromatic, aliphatic, and hydrogen bonding interactions are identified (Figure 1.5C). The computational equivalent of the MSCS approach is **mixed-solvent molecular**

dynamics (149), which employs an ensemble of protein structures from multiple crystal or NMR experiments in a virtual box of mixed aqueous and organic solvent molecules (e.g. benzene + propane + water). This system is minimized in a molecular dynamics (MD) simulation to build pharmacophore models of potential binding sites (149). While the incorporation of explicit solvents and protein flexibility represent an improvement, the predictive power of any *de novo* method remains to be demonstrated for any non-enzyme. Together with the Carlson group, we have applied these methods to the study of sHsps (Chapter 4).

Another possible contribution of *in silico* methods is that, once binding sites are identified, they may be **computationally assessed for potential druggability**. Though this subfield is in its early stages, a number of interesting studies have been reported (150-153). Briefly, these methods use a combination of physical and physicochemical parameters, including the shape, size, hydrophobicity, and hydrogen bonding capability of the pocket, and they compare these values to training sets of known ligand-protein pairs. Cheng *et al.* developed one such method for predicting maximal affinity using a scoring system based on the hydrophobicity of the solvent accessible surface area (SASA) and the shape (curvature) of the ligand binding sites (150). This method was able to confirm approximately 60 known protein-ligand maximal affinities. More importantly, they also carried out pilot screens of 11,000 compounds against two target enzymes, one of which was predicted to be "druggable" (*i.e.* good maximal affinities) by their computational method and the other "difficult" (*i.e.* weak maximal affinities). These screens gave hit rates of 1.8% and 0.15%, respectively, consistent with the prediction. Moreover, additional optimization at Pfizer produced eleven sub-micromolar potency leads from the "druggable" target project, but none for the "difficult" one. Further development of these methods may yield an important tool for non-enzymes.

1.9. What Is the appropriate chemical space for libraries that target non-enzymes?

One theory to describe the apparent "un-druggability" of a non-enzyme target is that the types of molecules being used in most HTS campaigns do not sample the appropriate chemical space (156, 157). For example, commercial chemical libraries appear to be ill suited for the discovery of inhibitors that bind PPIs (157, 158). Inhibitors of PPIs tend to have higher molecular mass and more complex topology (*e.g.* macrocycles, high number of chiral centers) than inhibitors of traditional, enzyme targets (recently reviewed in (159)). Thus, the success of HTS for non-

canonical targets may be critically dependent on the selection of the appropriate chemical library and seemingly failed screens for non-enzymes may, in fact, have arisen from poor sampling of chemical space. Consequently, creative construction of new chemical libraries is a vibrant and important area of research that is likely to expand our definition of "druggable" targets.

Diversity-oriented synthesis (DOS) is one approach to expand the chemical space sampled by synthetic chemical libraries. Many current HTS libraries consist of molecules representing a relatively small number of chemical scaffolds, with physicochemical properties resembling existing drugs (156). DOS approaches rely on divergent synthetic steps, in which the product of one complexity-generating transformation is a substrate in a second, and so on (160-162) (Figure 1.6A). Thus, in contrast to target-oriented synthesis or medicinal chemistry, DOS methods tend to access structures with increased scaffold complexity and variety in a limited number of synthetic steps.

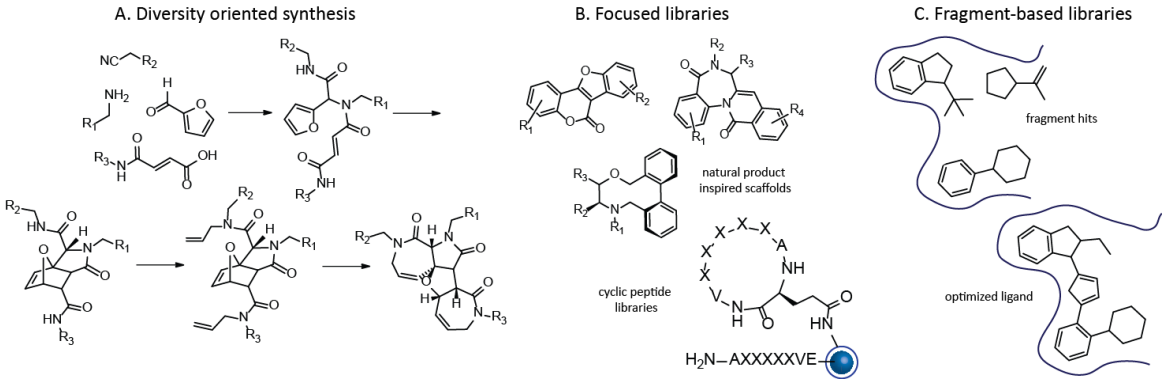

Figure 1.6. A: Diversity-oriented synthesis uses sequences of modular, complexity-generating reactions to build compound libraries of diverse scaffolds (figure adapted from (162)). B: Focused libraries of natural product-inspired scaffolds and cyclic peptides may be useful for lead generation against non-enzymes and protein-protein interactions. C: Fragment-based screening enables the evolution of low-affinity, high-efficiency binders into high affinity leads.

Natural products provided some of the original inspiration for DOS libraries (163, 164), because these natural compounds tend to be more structurally complex, with more chiral centers, a higher proportion of carbon, hydrogen, and oxygen atoms and fewer nitrogen atoms than synthetic compounds (reviewed in (165)). They also tend to be larger (> 500 Da) and frequently more water-soluble (166). These compounds have evolved to be bioactive; thus, they tend to have relatively favorable pharmacokinetic properties and high affinity and specificity (166). Unsurprisingly, a large proportion (>60%) of FDA-approved drugs are natural products or natural

product derivatives (167-169). Inspired by these favorable properties, libraries assembled based on **privileged core natural products** have been constructed around a number of scaffolds, including carbohydrates, steroids and sterols, fatty acid derivatives, polyketides, linear and cyclic peptides, terpenoids, flavonoids, alkaloids, macrolactones and macrolactams, and many others (165) (Figure 1.6B). In a related concept, Hopkins and Groom presented the idea that the majority of drugs compete against endogenous small molecule regulators for binding sites on proteins (170). This concept has led to the use of metabolomic profiling as a way to identify druggable binding sites, and to the development of **metabolite and cofactor mimetic** libraries (171).

Another interesting property of natural products is that they can sometimes inhibit otherwise intractable classes of drug targets, such as PPIs (172). For example, we recently screened a small library of plant-derived natural products and successfully identified inhibitors of the challenging PPI between the anti-bacterial targets DnaK and DnaJ (173, 174). The difficulty of targeting PPIs using commercial libraries is thought to result, in part, from incompatible physicochemical properties (94, 158). For example, a 2010 analysis compared 66 PPI inhibitors with a diverse set of 557 typical drugs, using 1,666 molecular descriptors (158). The study concluded that PPI inhibitors are larger, more lipophilic, and have more aromatic rings and fused ring systems (158). Thus, natural products may be especially suitable for targeting PPIs, as many natural products overlap with this region of chemical space (156, 175).

Ribosomal and non-ribosomal **peptides** are natural products that exhibit a wide range of biological activities. Synthetic peptides are often assembled by solid phase synthesis, using functionalized polystyrene resin beads as solid support. Natural and unnatural amino acids may be modularly incorporated to rapidly assemble a large amount of diversity using split-and-pool methods. In one-bead-one-compound combinatorial libraries, each solid-support resin bead is coated with a homogenous population of a unique peptide or peptoid (176-178). Such libraries can then be incubated with a fluorescently labeled target of interest to find binding partners. Like other affinity-based selection techniques, such as phage display (179), this platform can be applied to any type of target molecule, even non-enzymes (177). Linear peptides generally have poor pharmacokinetic properties (poor absorption and susceptibility to rapid degradation by proteases), but this can be circumvented using a number of well-established strategies (180).

For example, **synthetic biological** agents such as stapled peptides with covalently constrained secondary structure may be cell-permeable and resistant to cellular proteases (181, 182). Moreover, the conformational restriction imposed by the covalent stabilization of secondary structure can efficiently mimic the binding surface of a protein (most notably α-helices), resulting in tight and productive binding. Stapled peptides have been successfully developed to modulate a number of noncanonical targets such as transcription factors as well as PPIs (183-185). **Cyclic peptides** are another class of natural products suitable for use in targeting non-enzymes. The reduced conformational flexibility of cyclized peptides is advantageous for target binding, membrane permeability, and stabilization against digestion by endoproteases (186). Until recently, the one-bead-one-compound technique was limited to the screening of linear peptide or peptoid libraries, because Edman degradation sequencing requires a free amino terminus. However, Liu et al. developed a clever strategy to circumvent this obstacle (186), including both linear and cyclic versions of peptides embedded on either the inner or outer layers of a polymeric resin support (Figure 1.6B) (186). In a proof-of-principle study, a library of 10^7 cyclic peptides was generated and screened against the human prolactin receptor, resulting in molecules with low micromolar affinity for an allosteric site on the receptor (186). Similarly, a screen of a focused library of over 10^6 cyclic peptides designed to competitively inhibit the calcineurin-NFAT PPI resulted in the discovery of several ligands with low micromolar potency (187).

DNA-encoded libraries (DELs) are another way to select for small molecules with affinity for a target of interest (101, 188, 189). Analogous to phage-display, DELs link small molecule selection with unique, covalently attached DNA "bar codes" (189). Molecules with affinity for the target are identified by PCR amplification and sequencing of the DNA tag. DELs may be synthesized using split-and-pool combinatorial assembly or DNA-templated synthetic methods (188). For example, Wrenn *et al.* synthesized and screened 10^8 DNA-encoded 8-mer peptoids for binding to the N-terminal SH3 domain of the proto-oncogene Crk (p38) (100), which successfully resulted in the identification of several peptoids with low- to mid-micromolar affinity for Crk. One drawback of this approach is that synthetic transformations used in library construction must be DNA-compatible, but a relatively wide range of orthogonal reactions have been reported (190). Compound discovery by DELs may be applied to any type of target class, and is relatively inexpensive after the initial investment of library construction.

Fragment-based screening utilizes chemical libraries consisting of low-molecular weight, low complexity compounds ("fragments"), which are tested for binding to a target protein by NMR, x-ray crystallography, or SPR. Low-affinity hits (generally with K_D values between 0.1 and 10 mM (85)) are then evolved into higher-affinity binders though structure-based design and medicinal chemistry (Figure 1.6C). Fragment-based screening has gained widespread application over the past decade (191), and provides several strategic advantages. First, fragment-based screening libraries exhibit *high sampling efficiency*; they offer greater coverage of chemical space with a smaller number of library members (192). In fact, a library of 10^3 fragments represents the same chemical space as 10^{13} drug-like molecules (192). Second, fragment based screening produces *weak but high-quality binders*. Absolute binding affinities range from micromolar to millimolar, but ligand efficiency (or binding energy per non-hydrogen atom (193)), is comparable or stronger than HTS hits (194). The reason for this observation is that molecules binding to their target must overcome the entropic cost of the interaction, estimated for a rigid body to be ~15-20 kJ/mol (193). As a result, a fragment that binds with 100 μM affinity actually contributes over half of the binding energy to an optimized, nanomolar K_D molecule (193), as long as the incorporated fragment still takes advantage of the same binding interactions. Lastly, fragment hits have *favorable physicochemical properties* as starting points for pharmaceutical design. As compared to typical HTS hits, fragment hits are much lower in molecular weight, less lipophilic, and more soluble (195).

It may be the case that "failure of a [well-designed] screen to identify a chemical starting point can be simplified to one of two factors: the target itself is un-druggable (unable to be modulated appropriately by a small molecule), or the screen did not test the correct compounds (yet)" (196). The expansion of screening collections may therefore increase the number of targets that are considered "druggable."

1.10. Application of biophysical strategies for ligand discovery to small heat shock proteins

To illustrate these concepts, my thesis is focused on using a full suite of modern methods to develop molecules that bind sHsps. Because of their complex structures, these proteins are challenging and non-canonical targets. However, using multiple methods, I show that they are amenable to drug discovery. In **Chapter 2**, I characterize disease-related mutations in sHsps that

result in aggregation. In **Chapter 3**, I discuss the application of differential scanning fluorimetry to one such aggregation-prone mutant of αB-crystallin and characterization of the resulting lead molecule *in vitro* and in animal models of disease. This work was carried out in close collaboration with the Andley laboratory. **Chapter 4** describes orthogonal discovery efforts that resulted in the identification of ligands for Hsp27 despite its absence of enzymatic activity or known small molecule binding sites; this work was carried out in collaboration with the Klevit, Carlson, and Cierpicki laboratories. **Chapter 5** is a discussion of future work required to continue the development and application of the chemical probes described herein, as well as broader future directions. The appendix describes my contribution to early efforts in ligand identification for the transcription factor HSF1, a canonically 'undruggable' target that presents many of the same challenges as the sHsp family. This work was undertaken in collaboration with the Thiele laboratory and is ongoing.

1.11. Notes

A portion of this chapter has been published as L. N. Makley, J. E. Gestwicki, *Expanding the Number of 'Druggable' Targets: Non-Enzymes and Protein-Protein Interactions.* Chemical Biology & Drug Design 81, 22-32 (2013).

1.12. References

1. Overington JP, Al-Lazikani B, Hopkins AL. Opinion - How many drug targets are there? Nature Reviews Drug Discovery. 2006;5(12):993-6.
2. Imming P, Sinning C, Meyer A. Opinion - Drugs, their targets and the nature and number of drug targets. Nature Reviews Drug Discovery. 2006;5(10):821-34.
3. Rual JF, Venkatesan K, Hao T, Hirozane-Kishikawa T, Dricot A, Li N, et al. Towards a proteome-scale map of the human protein-protein interaction network. Nature. 2005;437(7062):1173-8.
4. Arkin MR, Whitty A. The road less traveled: modulating signal transduction enzymes by inhibiting their protein-protein interactions. Curr Opin Chem Biol. 2009;13(3):284-90.
5. Smith MC, Gestwicki JE. Features of protein-protein interactions that translate into potent inhibitors: topology, surface area and affinity. Expert reviews in molecular medicine. 2012;14:e16.
6. Thompson AD, Dugan A, Gestwicki JE, Mapp AK. Fine-tuning multiprotein complexes using small molecules. ACS Chemical Biology. 2012;7(8):1311-20.
7. Hartl FU, Bracher A, Hayer-Hartl M. Molecular chaperones in protein folding and proteostasis. Nature. 2011;475(7356):324-32.
8. Sun Y, MacRae TH. Small heat shock proteins: molecular structure and chaperone function. Cell Mol Life Sci. 2005;62(21):2460-76.

9. Haslbeck M, Franzmann T, Weinfurtner D, Buchner J. Some like it hot: the structure and function of small heat-shock proteins. Nature structural & molecular biology. 2005;12(10):842-6.
10. Jakob U, Buchner J. Assisting spontaneity: the role of Hsp90 and small Hsps as molecular chaperones. Trends in biochemical sciences. 1994;19(5):205-11.
11. Narberhaus F. Alpha-crystallin-type heat shock proteins: socializing minichaperones in the context of a multichaperone network. Microbiol Mol Biol Rev. 2002;66(1):64-93; table of contents.
12. Lee GJ, Roseman AM, Saibil HR, Vierling E. A small heat shock protein stably binds heat-denatured model substrates and can maintain a substrate in a folding-competent state. EMBO J. 1997;16(3):659-71.
13. Ehrnsperger M, Graber S, Gaestel M, Buchner J. Binding of non-native protein to Hsp25 during heat shock creates a reservoir of folding intermediates for reactivation. EMBO J. 1997;16(2):221-9.
14. Eyles SJ, Gierasch LM. Nature's molecular sponges: small heat shock proteins grow into their chaperone roles. Proc Natl Acad Sci U S A. 2010;107(7):2727-8.
15. Cashikar AG, Duennwald M, Lindquist SL. A chaperone pathway in protein disaggregation. Hsp26 alters the nature of protein aggregates to facilitate reactivation by Hsp104. The Journal of biological chemistry. 2005;280(25):23869-75.
16. Kampinga HH, Hageman J, Vos MJ, Kubota H, Tanguay RM, Bruford EA, et al. Guidelines for the nomenclature of the human heat shock proteins. Cell stress & chaperones. 2009;14(1):105-11.
17. Arrigo AP, Gibert B. Protein interactomes of three stress inducible small heat shock proteins: HspB1, HspB5 and HspB8. International journal of hyperthermia : the official journal of European Society for Hyperthermic Oncology, North American Hyperthermia Group. 2013;29(5):409-22.
18. Garrido C, Paul C, Seigneuric R, Kampinga HH. The small heat shock proteins family: the long forgotten chaperones. The international journal of biochemistry & cell biology. 2012;44(10):1588-92.
19. Kampinga HH, Garrido C. HSPBs: small proteins with big implications in human disease. The international journal of biochemistry & cell biology. 2012;44(10):1706-10.
20. Baranova EV, Weeks SD, Beelen S, Bukach OV, Gusev NB, Strelkov SV. Three-dimensional structure of alpha-crystallin domain dimers of human small heat shock proteins HSPB1 and HSPB6. Journal of molecular biology. 2011;411(1):110-22.
21. Bagneris C, Bateman OA, Naylor CE, Cronin N, Boelens WC, Keep NH, et al. Crystal structures of alpha-crystallin domain dimers of alphaB-crystallin and Hsp20. Journal of molecular biology. 2009;392(5):1242-52.
22. Weeks SD, Baranova EV, Heirbaut M, Beelen S, Shkumatov AV, Gusev NB, et al. Molecular structure and dynamics of the dimeric human small heat shock protein HSPB6. Journal of structural biology. 2014;185(3):342-54.
23. Lelj-Garolla B, Mauk AG. Roles of the N- and C-terminal sequences in Hsp27 self-association and chaperone activity. Protein science : a publication of the Protein Society. 2012;21(1):122-33.
24. Jehle S, Vollmar BS, Bardiaux B, Dove KK, Rajagopal P, Gonen T, et al. N-terminal domain of alphaB-crystallin provides a conformational switch for multimerization and structural heterogeneity. Proceedings of the National Academy of Sciences of the United States of America. 2011;108(16):6409-14.
25. Delbecq SP, Jehle S, Klevit R. Binding determinants of the small heat shock protein, alphaB-crystallin: recognition of the 'IxI' motif. The EMBO journal. 2012;31(24):4587-94.

26. Fuchs M, Poirier DJ, Seguin SJ, Lambert H, Carra S, Charette SJ, et al. Identification of the key structural motifs involved in HspB8/HspB6-Bag3 interaction. The Biochemical journal. 2010;425(1):245-55.
27. Ahmad MF, Raman B, Ramakrishna T, Rao Ch M. Effect of phosphorylation on alpha B-crystallin: differences in stability, subunit exchange and chaperone activity of homo and mixed oligomers of alpha B-crystallin and its phosphorylation-mimicking mutant. Journal of molecular biology. 2008;375(4):1040-51.
28. Ecroyd H, Meehan S, Horwitz J, Aquilina JA, Benesch JL, Robinson CV, et al. Mimicking phosphorylation of alphaB-crystallin affects its chaperone activity. The Biochemical journal. 2007;401(1):129-41.
29. Peschek J, Braun N, Rohrberg J, Back KC, Kriehuber T, Kastenmuller A, et al. Regulated structural transitions unleash the chaperone activity of alphaB-crystallin. Proceedings of the National Academy of Sciences of the United States of America. 2013;110(40):E3780-9.
30. Basha E, O'Neill H, Vierling E. Small heat shock proteins and alpha-crystallins: dynamic proteins with flexible functions. Trends in biochemical sciences. 2012;37(3):106-17.
31. Abisambra JF, Blair LJ, Hill SE, Jones JR, Kraft C, Rogers J, et al. Phosphorylation dynamics regulate Hsp27-mediated rescue of neuronal plasticity deficits in tau transgenic mice. The Journal of neuroscience : the official journal of the Society for Neuroscience. 2010;30(46):15374-82.
32. Almeida-Souza L, Goethals S, de Winter V, Dierick I, Gallardo R, Van Durme J, et al. Increased monomerization of mutant HSPB1 leads to protein hyperactivity in Charcot-Marie-Tooth neuropathy. J Biol Chem. 2010;285(17):12778-86.
33. Andley UP, Hamilton PD, Ravi N, Weihl CC. A knock-in mouse model for the R120G mutation of alphaB-crystallin recapitulates human hereditary myopathy and cataracts. PloS one. 2011;6(3):e17671.
34. Clark JI, Muchowski PJ. Small heat-shock proteins and their potential role in human disease. Curr Opin Struct Biol. 2000;10(1):52-9.
35. Arrigo AP, Simon S, Gibert B, Kretz-Remy C, Nivon M, Czekalla A, et al. Hsp27 (HspB1) and alphaB-crystallin (HspB5) as therapeutic targets. FEBS letters. 2007;581(19):3665-74.
36. Dierick I, Irobi J, De Jonghe P, Timmerman V. Small heat shock proteins in inherited peripheral neuropathies. Ann Med. 2005;37(6):413-22.
37. Powers ET, Morimoto RI, Dillin A, Kelly JW, Balch WE. Biological and chemical approaches to diseases of proteostasis deficiency. Annual review of biochemistry. 2009;78:959-91.
38. Vleminckx V, Van Damme P, Goffin K, Delye H, Van Den Bosch L, Robberecht W. Upregulation of HSP27 in a transgenic model of ALS. Journal of neuropathology and experimental neurology. 2002;61(11):968-74.
39. Shinder GA, Lacourse MC, Minotti S, Durham HD. Mutant Cu/Zn-superoxide dismutase proteins have altered solubility and interact with heat shock/stress proteins in models of amyotrophic lateral sclerosis. The Journal of biological chemistry. 2001;276(16):12791-6.
40. Sharp PS, Akbar MT, Bouri S, Senda A, Joshi K, Chen HJ, et al. Protective effects of heat shock protein 27 in a model of ALS occur in the early stages of disease progression. Neurobiology of disease. 2008;30(1):42-55.
41. Yerbury JJ, Gower D, Vanags L, Roberts K, Lee JA, Ecroyd H. The small heat shock proteins alphaB-crystallin and Hsp27 suppress SOD1 aggregation in vitro. Cell stress & chaperones. 2013;18(2):251-7.

42. Maatkamp A, Vlug A, Haasdijk E, Troost D, French PJ, Jaarsma D. Decrease of Hsp25 protein expression precedes degeneration of motoneurons in ALS-SOD1 mice. The European journal of neuroscience. 2004;20(1):14-28.
43. Karch CM, Borchelt DR. An examination of alpha B-crystallin as a modifier of SOD1 aggregate pathology and toxicity in models of familial amyotrophic lateral sclerosis. Journal of neurochemistry. 2010;113(5):1092-100.
44. Hagemann TL, Boelens WC, Wawrousek EF, Messing A. Suppression of GFAP toxicity by alphaB-crystallin in mouse models of Alexander disease. Human molecular genetics. 2009;18(7):1190-9.
45. Selkoe DJ. Alzheimer's disease. Cold Spring Harbor perspectives in biology. 2011;3(7).
46. Wilhelmus MM, Otte-Holler I, Wesseling P, de Waal RM, Boelens WC, Verbeek MM. Specific association of small heat shock proteins with the pathological hallmarks of Alzheimer's disease brains. Neuropathology and applied neurobiology. 2006;32(2):119-30.
47. Renkawek K, Bosman GJ, de Jong WW. Expression of small heat-shock protein hsp 27 in reactive gliosis in Alzheimer disease and other types of dementia. Acta neuropathologica. 1994;87(5):511-9.
48. Shimura H, Miura-Shimura Y, Kosik KS. Binding of tau to heat shock protein 27 leads to decreased concentration of hyperphosphorylated tau and enhanced cell survival. The Journal of biological chemistry. 2004;279(17):17957-62.
49. Bjorkdahl C, Sjogren MJ, Zhou X, Concha H, Avila J, Winblad B, et al. Small heat shock proteins Hsp27 or alphaB-crystallin and the protein components of neurofibrillary tangles: tau and neurofilaments. Journal of neuroscience research. 2008;86(6):1343-52.
50. Toth ME, Szegedi V, Varga E, Juhasz G, Horvath J, Borbely E, et al. Overexpression of Hsp27 ameliorates symptoms of Alzheimer's disease in APP/PS1 mice. Cell stress & chaperones. 2013;18(6):759-71.
51. King M, Nafar F, Clarke J, Mearow K. The small heat shock protein Hsp27 protects cortical neurons against the toxic effects of beta-amyloid peptide. Journal of neuroscience research. 2009;87(14):3161-75.
52. Ojha J, Masilamoni G, Dunlap D, Udoff RA, Cashikar AG. Sequestration of toxic oligomers by HspB1 as a cytoprotective mechanism. Molecular and cellular biology. 2011;31(15):3146-57.
53. Wilhelmus MM, Boelens WC, Otte-Holler I, Kamps B, de Waal RM, Verbeek MM. Small heat shock proteins inhibit amyloid-beta protein aggregation and cerebrovascular amyloid-beta protein toxicity. Brain research. 2006;1089(1):67-78.
54. Renkawek K, Voorter CE, Bosman GJ, van Workum FP, de Jong WW. Expression of alpha B-crystallin in Alzheimer's disease. Acta neuropathologica. 1994;87(2):155-60.
55. Narayanan S, Kamps B, Boelens WC, Reif B. alphaB-crystallin competes with Alzheimer's disease beta-amyloid peptide for peptide-peptide interactions and induces oxidation of Abeta-Met35. FEBS letters. 2006;580(25):5941-6.
56. Shammas SL, Waudby CA, Wang S, Buell AK, Knowles TP, Ecroyd H, et al. Binding of the molecular chaperone alphaB-crystallin to Abeta amyloid fibrils inhibits fibril elongation. Biophysical journal. 2011;101(7):1681-9.
57. Stege GJ, Renkawek K, Overkamp PS, Verschuure P, van Rijk AF, Reijnen-Aalbers A, et al. The molecular chaperone alphaB-crystallin enhances amyloid beta neurotoxicity. Biochemical and biophysical research communications. 1999;262(1):152-6.
58. Dehle FC, Ecroyd H, Musgrave IF, Carver JA. alphaB-Crystallin inhibits the cell toxicity associated with amyloid fibril formation by kappa-casein and the amyloid-beta peptide. Cell stress & chaperones. 2010;15(6):1013-26.

59. Waudby CA, Knowles TP, Devlin GL, Skepper JN, Ecroyd H, Carver JA, et al. The interaction of alphaB-crystallin with mature alpha-synuclein amyloid fibrils inhibits their elongation. Biophysical journal. 2010;98(5):843-51.
60. Rekas A, Jankova L, Thorn DC, Cappai R, Carver JA. Monitoring the prevention of amyloid fibril formation by alpha-crystallin. Temperature dependence and the nature of the aggregating species. The FEBS journal. 2007;274(24):6290-304.
61. Bruinsma IB, Bruggink KA, Kinast K, Versleijen AA, Segers-Nolten IM, Subramaniam V, et al. Inhibition of alpha-synuclein aggregation by small heat shock proteins. Proteins. 2011;79(10):2956-67.
62. Zourlidou A, Payne Smith MD, Latchman DS. HSP27 but not HSP70 has a potent protective effect against alpha-synuclein-induced cell death in mammalian neuronal cells. Journal of neurochemistry. 2004;88(6):1439-48.
63. Outeiro TF, Klucken J, Strathearn KE, Liu F, Nguyen P, Rochet JC, et al. Small heat shock proteins protect against alpha-synuclein-induced toxicity and aggregation. Biochemical and biophysical research communications. 2006;351(3):631-8.
64. Kato S, Hirano A, Umahara T, Kato M, Herz F, Ohama E. Comparative immunohistochemical study on the expression of alpha B crystallin, ubiquitin and stress-response protein 27 in ballooned neurons in various disorders. Neuropathology and applied neurobiology. 1992;18(4):335-40.
65. Renkawek K, de Jong WW, Merck KB, Frenken CW, van Workum FP, Bosman GJ. alpha B-crystallin is present in reactive glia in Creutzfeldt-Jakob disease. Acta neuropathologica. 1992;83(3):324-7.
66. Brownell SE, Becker RA, Steinman L. The protective and therapeutic function of small heat shock proteins in neurological diseases. Frontiers in immunology. 2012;3:74.
67. Kato K, Katoh-Semba R, Takeuchi IK, Ito H, Kamei K. Responses of heat shock proteins hsp27, alphaB-crystallin, and hsp70 in rat brain after kainic acid-induced seizure activity. Journal of neurochemistry. 1999;73(1):229-36.
68. Bidmon HJ, Gorg B, Palomero-Gallagher N, Behne F, Lahl R, Pannek HW, et al. Heat shock protein-27 is upregulated in the temporal cortex of patients with epilepsy. Epilepsia. 2004;45(12):1549-59.
69. Akbar MT, Lundberg AM, Liu K, Vidyadaran S, Wells KE, Dolatshad H, et al. The neuroprotective effects of heat shock protein 27 overexpression in transgenic animals against kainate-induced seizures and hippocampal cell death. The Journal of biological chemistry. 2003;278(22):19956-65.
70. van der Weerd L, Tariq Akbar M, Aron Badin R, Valentim LM, Thomas DL, Wells DJ, et al. Overexpression of heat shock protein 27 reduces cortical damage after cerebral ischemia. Journal of cerebral blood flow and metabolism : official journal of the International Society of Cerebral Blood Flow and Metabolism. 2010;30(4):849-56.
71. Stetler RA, Cao G, Gao Y, Zhang F, Wang S, Weng Z, et al. Hsp27 protects against ischemic brain injury via attenuation of a novel stress-response cascade upstream of mitochondrial cell death signaling. The Journal of neuroscience : the official journal of the Society for Neuroscience. 2008;28(49):13038-55.
72. Badin RA, Lythgoe MF, van der Weerd L, Thomas DL, Gadian DG, Latchman DS. Neuroprotective effects of virally delivered HSPs in experimental stroke. Journal of cerebral blood flow and metabolism : official journal of the International Society of Cerebral Blood Flow and Metabolism. 2006;26(3):371-81.

73. Teramoto S, Shimura H, Tanaka R, Shimada Y, Miyamoto N, Arai H, et al. Human-derived physiological heat shock protein 27 complex protects brain after focal cerebral ischemia in mice. PloS one. 2013;8(6):e66001.
74. Arac A, Brownell SE, Rothbard JB, Chen C, Ko RM, Pereira MP, et al. Systemic augmentation of alphaB-crystallin provides therapeutic benefit twelve hours post-stroke onset via immune modulation. Proceedings of the National Academy of Sciences of the United States of America. 2011;108(32):13287-92.
75. Gibert B, Eckel B, Gonin V, Goldschneider D, Fombonne J, Deux B, et al. Targeting heat shock protein 27 (HspB1) interferes with bone metastasis and tumour formation in vivo. British journal of cancer. 2012;107(1):63-70.
76. Gibert B, Hadchity E, Czekalla A, Aloy MT, Colas P, Rodriguez-Lafrasse C, et al. Inhibition of heat shock protein 27 (HspB1) tumorigenic functions by peptide aptamers. Oncogene. 2011;30(34):3672-81.
77. Bruey JM, Ducasse C, Bonniaud P, Ravagnan L, Susin SA, Diaz-Latoud C, et al. Hsp27 negatively regulates cell death by interacting with cytochrome c. Nature cell biology. 2000;2(9):645-52.
78. Arrigo AP. Human small heat shock proteins: protein interactomes of homo- and hetero-oligomeric complexes: an update. FEBS letters. 2013;587(13):1959-69.
79. Wendt MD, Sun C, Kunzer A, Sauer D, Sarris K, Hoff E, et al. Discovery of a novel small molecule binding site of human survivin. Bioorg Med Chem Lett. 2007;17(11):3122-9.
80. Renaud JP, Delsuc MA. Biophysical techniques for ligand screening and drug design. Curr Opin Pharmacol. 2009;9(5):622-8.
81. Holdgate GA, Anderson M, Edfeldt F, Geschwindner S. Affinity-based, biophysical methods to detect and analyze ligand binding to recombinant proteins: matching high information content with high throughput. J Struct Biol. 2010;172(1):142-57.
82. Dalvit C, Fogliatto G, Stewart A, Veronesi M, Stockman B. WaterLOGSY as a method for primary NMR screening: practical aspects and range of applicability. J Biomol NMR. 2001;21(4):349-59.
83. Mayer M, Meyer B. Characterization of ligand binding by saturation transfer difference NMR spectroscopy. Angewandte Chemie-International Edition. 1999;38(12):1784-8.
84. Hajduk PJ, Olejniczak ET, Fesik SW. One-dimensional relaxation- and diffusion-edited NMR methods for screening compounds that bind to macromolecules. Journal of the American Chemical Society. 1997;119(50):12257-61.
85. Scott DE, Coyne AG, Hudson SA, Abell C. Fragment-Based Approaches in Drug Discovery and Chemical Biology. Biochemistry. 2012.
86. Brough PA, Barril X, Borgognoni J, Chene P, Davies NG, Davis B, et al. Combining hit identification strategies: fragment-based and in silico approaches to orally active 2-aminothieno[2,3-d]pyrimidine inhibitors of the Hsp90 molecular chaperone. J Med Chem. 2009;52(15):4794-809.
87. Stockman BJ, Kothe M, Kohls D, Weibley L, Connolly BJ, Sheils AL, et al. Identification of allosteric PIF-pocket ligands for PDK1 using NMR-based fragment screening and 1H-15N TROSY experiments. Chem Biol Drug Des. 2009;73(2):179-88.
88. Jahnke W, Blommers MJ, Fernandez C, Zwingelstein C, Amstutz R. Strategies for the NMR-based identification and optimization of allosteric protein kinase inhibitors. Chembiochem. 2005;6(9):1607-10.
89. Kristiansen M, Andersen B, Iversen LF, Westergaard N. Identification, synthesis, and characterization of new glycogen phosphorylase inhibitors binding to the allosteric AMP site. J Med Chem. 2004;47(14):3537-45.

90. Krimm I, Lancelin JM, Praly JP. Binding evaluation of fragment-based scaffolds for probing allosteric enzymes. J Med Chem. 2012;55(3):1287-95.
91. Jahnke W, Rondeau JM, Cotesta S, Marzinzik A, Pelle X, Geiser M, et al. Allosteric non-bisphosphonate FPPS inhibitors identified by fragment-based discovery. Nat Chem Biol. 2010;6(9):660-6.
92. Hajduk PJ, Huth JR, Fesik SW. Druggability indices for protein targets derived from NMR-based screening data. J Med Chem. 2005;48(7):2518-25.
93. Arkin MR, Wells JA. Small-molecule inhibitors of protein-protein interactions: progressing towards the dream. Nat Rev Drug Discov. 2004;3(4):301-17.
94. Pagliaro L, Felding J, Audouze K, Nielsen SJ, Terry RB, Krog-Jensen C, et al. Emerging classes of protein-protein interaction inhibitors and new tools for their development. Curr Opin Chem Biol. 2004;8(4):442-9.
95. Altieri DC. Survivin, cancer networks and pathway-directed drug discovery. Nat Rev Cancer. 2008;8(1):61-70.
96. Altieri DC. Targeting survivin in cancer. Cancer Lett. 2012;http://dx.doi.org/10.1016/j.canlet.2012.03.005.
97. Zaffaroni N, Pennati M, Daidone MG. Survivin as a target for new anticancer interventions. J Cell Mol Med. 2005;9(2):360-72.
98. Carrasco RA, Stamm NB, Marcusson E, Sandusky G, Iversen P, Patel BK. Antisense inhibition of survivin expression as a cancer therapeutic. Mol Cancer Ther. 2011;10(2):221-32.
99. Jonker N, Kool J, Irth H, Niessen WM. Recent developments in protein-ligand affinity mass spectrometry. Anal Bioanal Chem. 2011;399(8):2669-81.
100. Wrenn SJ, Weisinger RM, Halpin DR, Harbury PB. Synthetic ligands discovered by in vitro selection. J Am Chem Soc. 2007;129(43):13137-43.
101. Clark MA. Selecting chemicals: the emerging utility of DNA-encoded libraries. Curr Opin Chem Biol. 2010;14(3):396-403.
102. Vassilev LT, Vu BT, Graves B, Carvajal D, Podlaski F, Filipovic Z, et al. In vivo activation of the p53 pathway by small-molecule antagonists of MDM2. Science. 2004;303(5659):844-8.
103. GE Healthcare Biacore 4000 Systems Overview, http://www.biacore.com/lifesciences/products/systems_overview/Biacore_4000/System-Information/index.html.
104. ForteBio OctetRed384 System Specifications, http://www.fortebio.com/octet_384_specs.html.
105. Koehler AN, Shamji AF, Schreiber SL. Discovery of an inhibitor of a transcription factor using small molecule microarrays and diversity-oriented synthesis. J Am Chem Soc. 2003;125(28):8420-1.
106. Stanton BZ, Peng LF, Maloof N, Nakai K, Wang X, Duffner JL, et al. A small molecule that binds Hedgehog and blocks its signaling in human cells. Nat Chem Biol. 2009;5(3):154-6.
107. Peng LF, Stanton BZ, Maloof N, Wang X, Schreiber SL. Syntheses of aminoalcohol-derived macrocycles leading to a small-molecule binder to and inhibitor of Sonic Hedgehog. Bioorg Med Chem Lett. 2009;19(22):6319-25.
108. Landry JP, Fei Y, Zhu XD. High Throughput, Label-free Screening Small Molecule Compound Libraries for Protein-Ligands using Combination of Small Molecule Microarrays and a Special Ellipsometry-based Optical Scanner. Int Drug Discov. 2011:8-13.
109. Landry JP, Fei Y, Zhu X. Simultaneous Measurement of 10,000 Protein-Ligand Affinity Constants Using Microarray-Based Kinetic Constant Assays. Assay Drug Dev Technol. 2012;10(3):250-9.

110. Fei YY, Landry JP, Sun YS, Zhu XD, Luo JT, Wang XB, et al. A novel high-throughput scanning microscope for label-free detection of protein and small-molecule chemical microarrays. Rev Sci Instrum. 2008;79(1):013708.
111. Erlanson DA, Wells JA, Braisted AC. Tethering: fragment-based drug discovery. Annual review of biophysics and biomolecular structure. 2004;33:199-223.
112. Bogan AA, Thorn KS. Anatomy of hot spots in protein interfaces. Journal of molecular biology. 1998;280(1):1-9.
113. Ostrem JM, Peters U, Sos ML, Wells JA, Shokat KM. K-Ras(G12C) inhibitors allosterically control GTP affinity and effector interactions. Nature. 2013;503(7477):548-51.
114. Ulloa-Aguirre A, Janovick JA, Brothers SP, Conn PM. Pharmacologic rescue of conformationally-defective proteins: implications for the treatment of human disease. Traffic. 2004;5(11):821-37.
115. Kozarich JW. The biochemistry of disease: desperately seeking syzygy. Annu Rev Biochem. 2009;78:55-63.
116. Pey AL, Ying M, Cremades N, Velazquez-Campoy A, Scherer T, Thony B, et al. Identification of pharmacological chaperones as potential therapeutic agents to treat phenylketonuria. J Clin Invest. 2008;118(8):2858-67.
117. Sawkar AR, D'Haeze W, Kelly JW. Therapeutic strategies to ameliorate lysosomal storage disorders--a focus on Gaucher disease. Cell Mol Life Sci. 2006;63(10):1179-92.
118. Yu Z, Sawkar AR, Kelly JW. Pharmacologic chaperoning as a strategy to treat Gaucher disease. FEBS J. 2007;274(19):4944-50.
119. Tropak MB, Blanchard JE, Withers SG, Brown ED, Mahuran D. High-throughput screening for human lysosomal beta-N-Acetyl hexosaminidase inhibitors acting as pharmacological chaperones. Chem Biol. 2007;14(2):153-64.
120. Wang Y, Loo TW, Bartlett MC, Clarke DM. Additive effect of multiple pharmacological chaperones on maturation of CFTR processing mutants. Biochem J. 2007;406(2):257-63.
121. Wang Y, Loo TW, Bartlett MC, Clarke DM. Modulating the folding of P-glycoprotein and cystic fibrosis transmembrane conductance regulator truncation mutants with pharmacological chaperones. Mol Pharmacol. 2007;71(3):751-8.
122. Hammarstrom P, Wiseman RL, Powers ET, Kelly JW. Prevention of transthyretin amyloid disease by changing protein misfolding energetics. Science. 2003;299(5607):713-6.
123. Johnson SM, Wiseman RL, Sekijima Y, Green NS, Adamski-Werner SL, Kelly JW. Native state kinetic stabilization as a strategy to ameliorate protein misfolding diseases: a focus on the transthyretin amyloidoses. Acc Chem Res. 2005;38(12):911-21.
124. Johnson SM, Connelly S, Fearns C, Powers ET, Kelly JW. The Transthyretin Amyloidoses: From Delineating the Molecular Mechanism of Aggregation Linked to Pathology to a Regulatory-Agency-Approved Drug. J Mol Biol. 2012;421(2-3):185-203.
125. Stanger K, Steffek M, Zhou L, Pozniak CD, Quan C, Franke Y, et al. Allosteric peptides bind a caspase zymogen and mediate caspase tetramerization. Nat Chem Biol. 2012;8(7):655-60.
126. Kuryatov A, Luo J, Cooper J, Lindstrom J. Nicotine acts as a pharmacological chaperone to up-regulate human alpha4beta2 acetylcholine receptors. Mol Pharmacol. 2005;68(6):1839-51.
127. Lester HA, Xiao C, Srinivasan R, Son CD, Miwa J, Pantoja R, et al. Nicotine is a selective pharmacological chaperone of acetylcholine receptor number and stoichiometry. Implications for drug discovery. AAPS J. 2009;11(1):167-77.
128. Holdgate GA, Ward WH. Measurements of binding thermodynamics in drug discovery. Drug Discov Today. 2005;10(22):1543-50.

129. Cummings MD, Farnum MA, Nelen MI. Universal screening methods and applications of ThermoFluor. J Biomol Screen. 2006;11(7):854-63.
130. Niesen FH, Berglund H, Vedadi M. The use of differential scanning fluorimetry to detect ligand interactions that promote protein stability. Nat Protoc. 2007;2(9):2212-21.
131. Lo MC, Aulabaugh A, Jin G, Cowling R, Bard J, Malamas M, et al. Evaluation of fluorescence-based thermal shift assays for hit identification in drug discovery. Anal Biochem. 2004;332(1):153-9.
132. DeSantis K, Reed A, Rahhal R, Reinking J. Use of differential scanning fluorimetry as a high-throughput assay to identify nuclear receptor ligands. Nucl Recept Signal. 2012;10:e002.
133. Koblish HK, Zhao S, Franks CF, Donatelli RR, Tominovich RM, LaFrance LV, et al. Benzodiazepinedione inhibitors of the Hdm2:p53 complex suppress human tumor cell proliferation in vitro and sensitize tumors to doxorubicin in vivo. Mol Cancer Ther. 2006;5(1):160-9.
134. Grasberger BL, Lu T, Schubert C, Parks DJ, Carver TE, Koblish HK, et al. Discovery and cocrystal structure of benzodiazepinedione HDM2 antagonists that activate p53 in cells. J Med Chem. 2005;48(4):909-12.
135. Parks DJ, Lafrance LV, Calvo RR, Milkiewicz KL, Gupta V, Lattanze J, et al. 1,4-Benzodiazepine-2,5-diones as small molecule antagonists of the HDM2-p53 interaction: discovery and SAR. Bioorg Med Chem Lett. 2005;15(3):765-70.
136. Sampson HM, Robert R, Liao J, Matthes E, Carlile GW, Hanrahan JW, et al. Identification of a NBD1-binding pharmacological chaperone that corrects the trafficking defect of F508del-CFTR. Chem Biol. 2011;18(2):231-42.
137. Forneris F, Orru R, Bonivento D, Chiarelli LR, Mattevi A. ThermoFAD, a Thermofluor-adapted flavin ad hoc detection system for protein folding and ligand binding. FEBS J. 2009;276(10):2833-40.
138. Isom DG, Marguet PR, Oas TG, Hellinga HW. A miniaturized technique for assessing protein thermodynamics and function using fast determination of quantitative cysteine reactivity. Proteins. 2010;79(4):1034-47.
139. Ghaemmaghami S, Fitzgerald MC, Oas TG. A quantitative, high-throughput screen for protein stability. Proc Natl Acad Sci U S A. 2000;97(15):8296-301.
140. Tang L, Hopper ED, Tong Y, Sadowsky JD, Peterson KJ, Gellman SH, et al. H/D exchange- and mass spectrometry-based strategy for the thermodynamic analysis of protein-ligand binding. Anal Chem. 2007;79(15):5869-77.
141. Powell KD, Fitzgerald MC. High-throughput screening assay for the tunable selection of protein ligands. J Comb Chem. 2004;6(2):262-9.
142. Hopper ED, Roulhac PL, Campa MJ, Patz EF, Jr., Fitzgerald MC. Throughput and efficiency of a mass spectrometry-based screening assay for protein-ligand binding detection. J Am Soc Mass Spectrom. 2008;19(9):1303-11.
143. Dearmond PD, West GM, Anbalagan V, Campa MJ, Patz EF, Jr., Fitzgerald MC. Discovery of novel cyclophilin A ligands using an H/D exchange- and mass spectrometry-based strategy. J Biomol Screen. 2010;15(9):1051-62.
144. Perot S, Sperandio O, Miteva MA, Camproux AC, Villoutreix BO. Druggable pockets and binding site centric chemical space: a paradigm shift in drug discovery. Drug Discov Today. 2010;15(15-16):656-67.
145. Henrich S, Salo-Ahen OM, Huang B, Rippmann FF, Cruciani G, Wade RC. Computational approaches to identifying and characterizing protein binding sites for ligand design. J Mol Recognit. 2010;23(2):209-19.

146. An JH, Totrov M, Abagyan R. Pocketome via comprehensive identification and classification of ligand binding envelopes. Molecular & Cellular Proteomics. 2005;4(6):752-61.
147. Kozakov D, Hall DR, Chuang GY, Cencic R, Brenke R, Grove LE, et al. Structural conservation of druggable hot spots in protein-protein interfaces. Proc Natl Acad Sci U S A. 2011;108(33):13528-33.
148. Mattos C, Ringe D. Locating and characterizing binding sites on proteins. Nat Biotechnol. 1996;14(5):595-9.
149. Lexa KW, Carlson HA. Full Protein Flexibility Is Essential for Proper Hot-Spot Mapping. J Am Chem Soc. 2010;133(2):200-2.
150. Cheng AC, Coleman RG, Smyth KT, Cao Q, Soulard P, Caffrey DR, et al. Structure-based maximal affinity model predicts small-molecule druggability. Nat Biotechnol. 2007;25(1):71-5.
151. Halgren TA. Identifying and characterizing binding sites and assessing druggability. J Chem Inf Model. 2009;49(2):377-89.
152. Zhong S, MacKerell AD, Jr. Binding response: a descriptor for selecting ligand binding site on protein surfaces. J Chem Inf Model. 2007;47(6):2303-15.
153. Nayal M, Honig B. On the nature of cavities on protein surfaces: application to the identification of drug-binding sites. Proteins. 2006;63(4):892-906.
154. Dar AC, Shokat KM. The evolution of protein kinase inhibitors from antagonists to agonists of cellular signaling. Annu Rev Biochem. 2011;80:769-95.
155. Chang L, Miyata Y, Ung PM, Bertelsen EB, McQuade TJ, Carlson HA, et al. Chemical screens against a reconstituted multiprotein complex: myricetin blocks DnaJ regulation of DnaK through an allosteric mechanism. Chemical Biology. 2011;18(2):210-21.
156. Bauer RA, Wurst JM, Tan DS. Expanding the range of 'druggable' targets with natural product-based libraries: an academic perspective. Current opinion in chemical biology. 2010;14(3):308-14.
157. Dandapani S, Marcaurelle LA. Grand challenge commentary: Accessing new chemical space for 'undruggable' targets. Nat Chem Biol. 2010;6(12):861-3.
158. Sperandio O, Reynes CH, Camproux AC, Villoutreix BO. Rationalizing the chemical space of protein-protein interaction inhibitors. Drug Discov Today. 2010;15(5-6):220-9.
159. Smith MC, Gestwicki JE. Features of protein-protein interactions that translate into potent inhibitors: topology, surface area and affinity. . Expert Reviews in Molecular Medicine. 2012;http://dx.doi.org/10.1017/erm.2012.10.
160. Schreiber SL. Organic chemistry: Molecular diversity by design. Nature. 2009;457(7226):153-4.
161. Galloway WR, Isidro-Llobet A, Spring DR. Diversity-oriented synthesis as a tool for the discovery of novel biologically active small molecules. Nat Commun. 2010;1:80.
162. Burke MD, Schreiber SL. A planning strategy for diversity-oriented synthesis. Angew Chem Int Ed Engl. 2004;43(1):46-58.
163. Isidro-Llobet A, Murillo T, Bello P, Cilibrizzi A, Hodgkinson JT, Galloway WR, et al. Diversity-oriented synthesis of macrocyclic peptidomimetics. Proc Natl Acad Sci U S A. 2011;108(17):6793-8.
164. Renner S, Popov M, Schuffenhauer A, Roth HJ, Breitenstein W, Marzinzik A, et al. Recent trends and observations in the design of high-quality screening collections. Future Med Chem. 2011;3(6):751-66.
165. Boldi AM. Libraries from natural product-like scaffolds. Curr Opin Chem Biol. 2004;8(3):281-6.
166. Clardy J, Walsh C. Lessons from natural molecules. Nature. 2004;432(7019):829-37.

167. Harvey AL. Natural products as a screening resource. Curr Opin Chem Biol. 2007;11(5):480-4.
168. Harvey AL. Natural products in drug discovery. Drug Discov Today. 2008;13(19-20):894-901.
169. Bottcher T, Pitscheider M, Sieber SA. Natural products and their biological targets: proteomic and metabolomic labeling strategies. Angew Chem Int Ed Engl. 2010;49(15):2680-98.
170. Hopkins AL, Groom CR. The druggable genome. Nat Rev Drug Discov. 2002;1(9):727-30.
171. Zhang L, Yan K, Zhang Y, Huang R, Bian J, Zheng C, et al. High-throughput synergy screening identifies microbial metabolites as combination agents for the treatment of fungal infections. Proc Natl Acad Sci U S A. 2007;104(11):4606-11.
172. Hegde NS, Sanders DA, Rodriguez R, Balasubramanian S. The transcription factor FOXM1 is a cellular target of the natural product thiostrepton. Nat Chem. 2011;3(9):725-31.
173. Chang L, Miyata Y, Ung PM, Bertelsen EB, McQuade TJ, Carlson HA, et al. Chemical screens against a reconstituted multiprotein complex: myricetin blocks DnaJ regulation of DnaK through an allosteric mechanism. Chem Biol. 2011;18(2):210-21.
174. Evans CG, Chang L, Gestwicki JE. Heat shock protein 70 (hsp70) as an emerging drug target. J Med Chem. 2010;53(12):4585-602.
175. Koehn FE, Carter GT. The evolving role of natural products in drug discovery. Nat Rev Drug Discov. 2005;4(3):206-20.
176. Lam KS, Lebl M, Krchnak V. The "One-Bead-One-Compound" Combinatorial Library Method. Chem Rev. 1997;97(2):411-48.
177. Chen X, Wu J, Luo Y, Liang X, Supnet C, Kim MW, et al. Expanded polyglutamine-binding peptoid as a novel therapeutic agent for treatment of Huntington's disease. Chem Biol. 2011;18(9):1113-25.
178. Zuckermann RN, Kodadek T. Peptoids as potential therapeutics. Current Opinion in Molecular Therapeutics. 2009;11(3):299-307.
179. Pande J, Szewczyk MM, Grover AK. Phage display: concept, innovations, applications and future. Biotechnol Adv. 2010;28(6):849-58.
180. Audie J, Boyd C. The synergistic use of computation, chemistry and biology to discover novel peptide-based drugs: the time is right. Curr Pharm Des. 2010;16(5):567-82.
181. Harrison RS, Shepherd NE, Hoang HN, Ruiz-Gomez G, Hill TA, Driver RW, et al. Downsizing human, bacterial, and viral proteins to short water-stable alpha helices that maintain biological potency. Proc Natl Acad Sci U S A. 2010;107(26):11686-91.
182. Verdine GL, Hilinski GJ. All-hydrocarbon stapled peptides as Synthetic Cell-Accessible Mini-Proteins. Drug Discov Today. 2012;9(1):e41-e7.
183. Kawamoto SA, Coleska A, Ran X, Yi H, Yang CY, Wang S. Design of triazole-stapled BCL9 alpha-helical peptides to target the beta-catenin/B-cell CLL/lymphoma 9 (BCL9) protein-protein interaction. J Med Chem. 2012;55(3):1137-46.
184. Madden MM, Muppidi A, Li Z, Li X, Chen J, Lin Q. Synthesis of cell-permeable stapled peptide dual inhibitors of the p53-Mdm2/Mdmx interactions via photoinduced cycloaddition. Bioorg Med Chem Lett. 2011;21(5):1472-5.
185. Moellering RE, Cornejo M, Davis TN, Del Bianco C, Aster JC, Blacklow SC, et al. Direct inhibition of the NOTCH transcription factor complex. Nature. 2009;462(7270):182-8.
186. Liu T, Joo SH, Voorhees JL, Brooks CL, Pei D. Synthesis and screening of a cyclic peptide library: discovery of small-molecule ligands against human prolactin receptor. Bioorg Med Chem. 2009;17(3):1026-33.

187. Liu T, Qian Z, Xiao Q, Pei D. High-throughput screening of one-bead-one-compound libraries: identification of cyclic peptidyl inhibitors against calcineurin/NFAT interaction. ACS Comb Sci. 2011;13(5):537-46.
188. Kleiner RE, Dumelin CE, Liu DR. Small-molecule discovery from DNA-encoded chemical libraries. Chem Soc Rev. 2011;40(12):5707-17.
189. Mannocci L, Leimbacher M, Wichert M, Scheuermann J, Neri D. 20 years of DNA-encoded chemical libraries. Chem Commun (Camb). 2011;47(48):12747-53.
190. Gartner ZJ, Kanan MW, Liu DR. Expanding the reaction scope of DNA-templated synthesis. Angew Chem Int Ed Engl. 2002;41(10):1796-800.
191. Leach AR, Hann MM. Molecular complexity and fragment-based drug discovery: ten years on. Curr Opin Chem Biol. 2011;15(4):489-96.
192. Edfeldt FN, Folmer RH, Breeze AL. Fragment screening to predict druggability (ligandability) and lead discovery success. Drug Discov Today. 2011;16(7-8):284-7.
193. Murray CW, Rees DC. The rise of fragment-based drug discovery. Nat Chem. 2009;1(3):187-92.
194. Carr RA, Congreve M, Murray CW, Rees DC. Fragment-based lead discovery: leads by design. Drug Discov Today. 2005;10(14):987-92.
195. Keseru GM, Makara GM. The influence of lead discovery strategies on the properties of drug candidates. Nat Rev Drug Discov. 2009;8(3):203-12.
196. Drewry DH, Macarron R. Enhancements of screening collections to address areas of unmet medical need: an industry perspective. Curr Opin Chem Biol. 2010;14(3):289-98.

Chapter 2

Mutations in sHsps Destabilize the Native Fold and Favor Formation of Amyloids

2.1. Abstract

In Chapter 1, we introduced small heat proteins (sHsps) as undruggable targets. Mutations in the coding sequences of this family of proteins cause hereditary cataracts, myopathies, and neuropathies (1-5). An unresolved question in the field of sHsp biology is how each of these mutations causes disease. While most early studies focused on studying whether the mutations caused loss-of-function, recent evidence suggests that some of these mutations might destabilize sHsp structure, leading to aggregation and potential gain-of-function toxicity. For example, aggregates formed from misfolded R120G αB-crystallin are associated with cataracts. However, the aggregation propensity of the analogous mutations in Hsp27 or other sHsps has not been similarly analyzed. In this Chapter, we explore the biochemistry of disease-associated sHsp mutants. Our goals were two-fold: (a) to understand whether these mutations might destabilize the sHsp dimers to favor amyloid formation and (b) to establish a framework in which to develop potential disease-modifying molecules targeting the sHsps. Using light scattering assays and electron microscopy, we show that four disease-causing mutations, including R120G αB-crystallin and R140G Hsp27, are prone to amyloid formation. Based on the conserved location of other disease-associated mutations at the dimer interface, we propose that many (if not all) of the sHsp mutations lead to protein instability and aggregation. Importantly, these studies provide a model in which ligands of sHsps would be expected to stabilize the native fold and potentially restore normal function, a concept that will be tested in Chapters 3 and 4.

2.2. Introduction

Small heat shock proteins are molecular chaperones that act as the first line of defense in the proteostasis network. These proteins bind to destabilized client proteins and prevent off-pathway aggregation, maintaining a folding-competent state for enzymatic components of the chaperone network to refold or triage (6, 7). Structurally, sHsps have a conserved core α-crystallin domain that mediates dimerization via an antiparallel β-strand interface (8, 9). This core domain is flanked by less conserved N- and C-terminal extensions that permit sHsp dimers to further oligomerize into polydisperse ensembles of between 20 and 40 protomers (10, 11). Mutations in sHsps have been associated with disease.

2.3. Mutations in sHsps are associated with disease

In 1998, an arginine to glycine point mutation in αB-crystallin (R120G) was identified in a French family with cataracts and desmin-related myopathy (12). Mutations in the corresponding residue in three other sHsps (R140 in Hsp27, R116 in 120 in αA-crystallin, and K141 in Hsp22) are also associated with disease (13). The R140G mutation in Hsp27 was discovered in families with Charcot-Marie-Tooth (CMT) type 2 disease or distal hereditary motor neuropathy (1), progressive neurodegenerative disorders that affect the peripheral nervous system (14, 15). Two other 'hot spot' sHsp mutations affect the residue R116 in αA-crystallin and K141 in Hsp22. R116C αA-crystallin is associated with congenital cataract (16), and the mutations K141E and K141N in Hsp22 cause peripheral neuropathies (13).

2.4. Hot spot mutation destabilizes the dimeric substructure of αB-crystallin and leads to its aggregation

The R120 residue is located within the β6+7 strand that forms the antiparallel dimer interface of the α-crystallin domain. The arginine at this position forms a salt bridge with an aspartic acid residue on the opposite protomer (D109); the mutation therefore disrupts two salt bridges that normally help define the dimer interface (see Figure 3.1). Interestingly, R120G αB-crystallin readily forms amyloid fibrils both *in vitro* and *in vivo*, a characteristic which is thought to contribute to the mutant pathology in both cataracts and myopathy (17-21). These observations suggested to us that the R120G mutation might destabilize the αB-crystallin dimer and lead to the release of unstable monomers that re-arrange into beta-sheet rich amyloid fibrils. Consistent with this hypothesis, mutation of the ion-pairing aspartic acid residue results in a similar syndrome that is also associated with protein aggregation (22).

2.5. Amyloids are ordered protein aggregates that overwhelm the proteostasis network

Amyloids are ordered, insoluble protein aggregates that are formed when unstable protein monomers adopt a 'cross-β' rich structure and stack together in higher-order filaments stabilized by hydrogen bonds between backbone atoms. Amyloid fibrils have an elongated, rope-like appearance by electron microscopy and they bind to the dyes thioflavin T and Congo red. Amyloid formation is kinetically disfavored under normal conditions, but amyloid fibrils are typically more thermodynamically stable than the native protein fold (23). Some of this stability is granted by secondary interactions involving steric intercalation of side chain residues in so-called 'steric zippers' that exclude water (23, 24). Amyloid deposits are classically associated with Alzheimer's disease, in which they were first discovered, but an increasing number of human diseases in other organs have been linked to amyloid deposition as well (23). In these diseases, protein misfolding is thought to cause toxicity by overwhelming the capacity of the chaperone and degradation machineries to maintain proper protein homeostasis. This results in more extensive protein misfolding and aggregation, resulting in a self-propagating cycle that eventually causes cell death (25).

2.6. Pathological point mutations are clustered in the dimer interface

We reviewed the locations of the known disease-associated mutations in sHsps and were struck by the fact that many of the pathological mutations can be found within the β6+7 strand that forms the dimer interface. For example, eight of the eighteen mutations (44%) in Hsp27 fall within the β6+7 strand or the residues that make up the adjacent loops, though this represents only 12% of the primary sequence of the protein (Table 2.1 and Figure 2.1). Overall, among the four sHsps listed in the table, sixteen of the forty-two reported mutations (38%) fall within this region. This highlights the importance of the stability of the dimer interface to sHsp biology.

Protein	Mutation	Region	Disease	Known effects
Hsp27 (HSPB1)	G34R	NT	DHMN	Uncharacterized
	P39L	NT	CMT2 and DHMN (AD)	Uncharacterized
	E41K	NT	DHMN (AD)	Uncharacterized
	G84R	NT	CMT2 and DHMN (AD)	Promotes phosphorylation-dependent dissociation of oligomers (26); may affect phosphorylation by MAPKAP2 at nearby Ser78 and Ser82

	L99M	ACD	CMT2 and DHMN (AR)	Promotes phosphorylation-dependent dissociation of oligomers (26)
	R127W	ACD	DHMN (AD)	Increases monomerization; increases binding to tubulin (1, 27)
	S135F	ACD	CMT2 and DHMN (AD)	Increases monomerization; increases binding to tubulin; colocalizes with intermediate filament aggregates; impairs axonal transport (1, 27)
	S135M	ACD	CMT2 and DHMN (AD)	Uncharacterized
	R136W	ACD	CMT2 (AD)	Increases binding to tubulin
	R136L	ACD	CMT2 (AD)	Uncharacterized
	R140G	ACD	CMT2 and DHMN (AD)	Hot spot residue; mutation decreases melting temperature (28)
	K141N	ACD	PN (AD)	Uncharacterized
	K141Q	ACD	PN (AD)	Mutation decreases melting temperature (28)
	T151I	ACD	DHMN (AD)	Uncharacterized; does not increase monomerization or binding to tubulin (1, 27)
	T164A	ACD	CMT2 (AD)	Uncharacterized
	T180I	IXI motif	CMT2 and DHMN (AD)	Uncharacterized
	P182L	IXI motif	DHMN (AD)	Aggregates; impairs axonal transport by interfering with dynein/dynactin
	P182S	IXI motif	DHMN (AD)	Uncharacterized
	R188W	CT	CMT2	Uncharacterized
αA-crystallin (HSPB4)	R12C	NT	Cataract (AD)	Increases oligomeric size and alters secondary structure (29); aggregates in cells (22)
	R21L	NT	Cataract (AD)	Alters secondary structure (29); aggregates in cells (22)
	R21W	NT	Cataract (AD)	Alters secondary structure (29); aggregates in cells (22)
	R49C	NT	Cataract (AD)	Alters secondary structure (29); aggregates *in vitro* (30), in cells (22), and in knock in mice (31); causes co-aggregation of αB-crystallin in knock in mice (31)
	R54C	NT	Cataract (AD, AR)(32)	Increases oligomeric size and alters secondary structure (29); aggregates in cells (22)
	F71L	ACD	Senile cataract	Decreases thermal stability and diminishes chaperone activity towards αB-crystallin (33, 34)
	G98R	ACD	Pre-senile cataract (AD)	Less stable (35); forms detergent-insoluble aggregates in lens epithelial cells (36); more sensitive to copper induced aggregation *in vitro* (37)
	D105H	ACD	Cataract (AD)	Uncharacterized; expected to have similar effects as R116C and R116H (ion-paired partner, see text)

	R116C	ACD	Cataract (AD)	Hot spot residue; alters secondary structure (29); aggregates (22, 29, 30); interacts more tightly with Hsp27 and αB-crystallin (38); binds less tightly to actin (39)
	R116H	ACD	Cataract (AD)	Hot spot residue; alters secondary structure (29); aggregates (22, 29); exhibits decreased stability (30)
αB-crystallin (HSPB5)	R11H	NT	Cataract (AD)	Alters secondary structure, decreases surface hydrophobicity, induces apoptosis (40)
	P20S	NT	Cataract (AD)	May affect phosphorylation (located next to Ser19)
	R56W	NT	Cataract (AR)	Uncharacterized
	R69C	NT	Cataract (AD)	Uncharacterized
	D109H	ACD	Cataract, MFM, DM, respiratory insufficiency, dysphonia, dysphagia (AD)	Uncharacterized *in vitro*; aggregates in cells (22)
	R120G	ACD	Cataract, DRM (AD)	Hot spot residue; alters secondary, tertiary, and quaternary structure, dramatically increases propensity to aggregate *in vitro* and in cells (12, 22, 30); forms amyloids (17); increases affinity for desmin filaments (41)
	D140N	ACD	Congenital lamellar cataract (AD)	Alters tertiary and quaternary structure, increases surface hydrophobicity, decreases temperature stability (42); aggregates in cells (22)
	G154S	IXI motif	Distal myopathy, cardiomyopathy	Aggregates in cells (43)
	R157H	IXI motif	DCM (AD)	Increases interaction with titin, aggregates in cells (22)
	A171T	CT	Cataract (AD)	Uncharacterized
Hsp22 (HSPB6)	**K141E**	ACD	DHMN	Hot spot residue; loss of stability (44); impaired chaperone activity towards polyglutamine and P182L Hsp27 in cells (30); impaired binding to Bag3 and impaired autophagy (30); aggregates (13)
	K141N	ACD	DHMN	Hot spot residue; impaired chaperone activity towards polyglutamine and P182L Hsp27 in cells (30); impaired binding to Bag3 and impaired autophagy (30); aggregates (13)

Table 2.1: Disease-causing point mutations in sHsps reported to date. Abbreviations: NT, N-terminus; ACD, α-crystallin domain; CT, C-terminus; DHMN, distal hereditary motor neuropathy; CMT, Charcot-Marie-Tooth disease; PN, peripheral neuropathy; MFM, myofibrillary myopathy; DRM, desmin-related myopathy; DCM, dilated cardiomyopathy; AD, autosomal dominant; AR, autosomal recessive. Table compiled from (32), (45) and the sources listed.

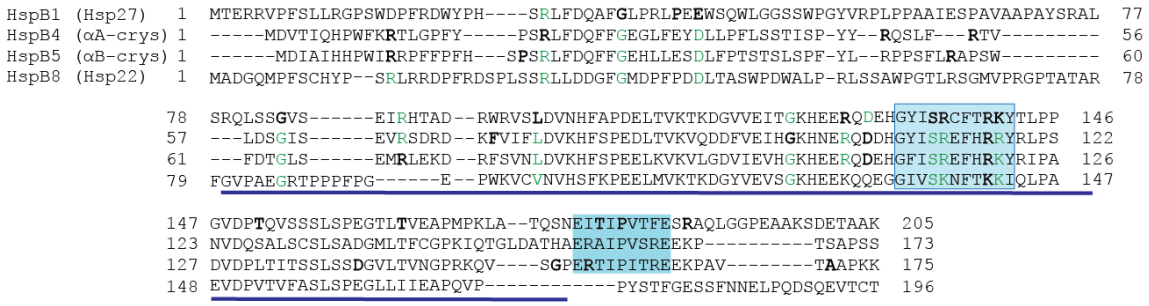

Figure 2.1. Disease-associated mutations in sHsps cluster to the dimer interface. Sequences were aligned using the NCBI Cobalt multiple sequence alignment tool. Mutations are shown in bold, and conserved residues at the mutation positions are shown in green. The highly conserved α-crystallin core domain is indicated by the blue line. The β6+7 strand that forms the antiparallel dimer interface is shown in a pale blue rectangle, as is the IXI palindromic motif in the C-terminus.

We wondered if other pathological mutations in sHsps might also destabilize the native dimer. By analogy to R120G αB-crystallin, disrupting the stability of the dimer interface would be expected to result in protein aggregation and potentially amyloid formation. We wanted to test this hypothesis by examining the aggregation and amyloid-forming propensity of disease related mutant sHsps.

2.7. Small heat shock proteins are predicted to form amyloids

We used the ZipperDB steric zipper prediction algorithm (24) to identify regions of sHsps that are particularly prone to amyloid formation. Each sHsp analyzed (Hsp27, αA-crystallin, αB-crystallin, and Hsp22) meets the criteria for high fibrillization propensity (Figure 2.2). Inclusion of the R120G or R140G mutations does not change the predicted amyloidogenic regions.

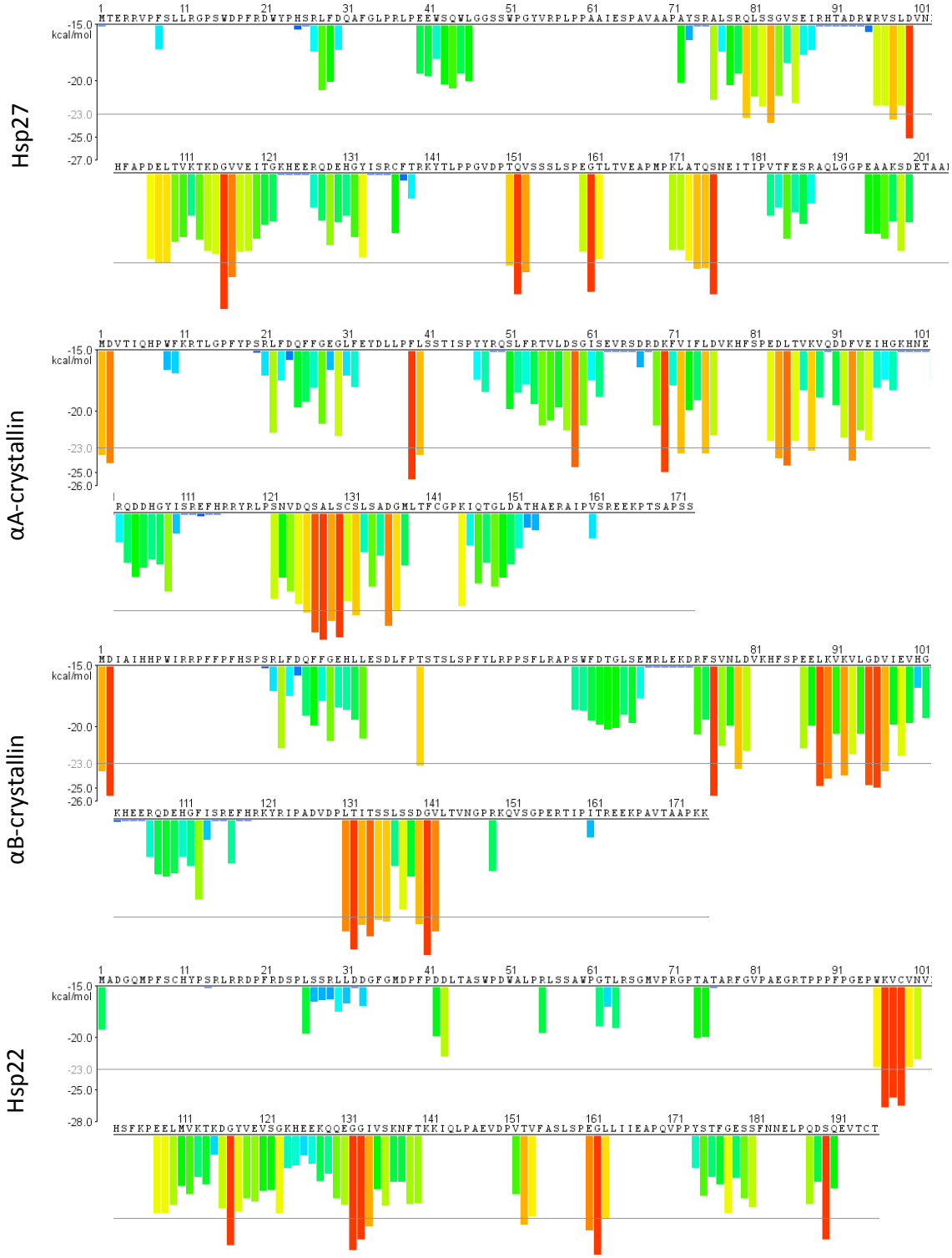

Figure 2.2: αB-crystallin and Hsp27 contain regions predicted to form amyloids. Using Zipper DB, regions predicted to form stable amyloids were detected. Regions of strong propensity are shown in red in the ”heat map”, as pioneered by the Eisenberg group (24).

2.8. Aggregates formed from αB-crystallin are amyloids and this conversion is accelerated by the pathological mutation R120G

We first wanted to characterize the mutation R120G αB-crystallin to confirm the results of literature studies that suggest this protein forms amyloids *in vitro*. We used light scattering to compare the aggregation kinetics of R120G and wild type αB-crystallin under a variety of conditions. We found that R120G αB-crystallin rapidly aggregated on mild heating under near physiological buffer conditions (Figure 2.3).

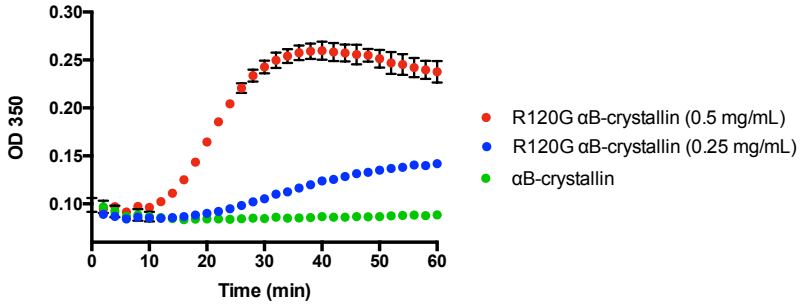

Figure 2.3. R120G αB-crystallin aggregates rapidly under mild conditions and at relatively low concentrations. Light scattering curves are shown for R120G at 0.5 mg/mL and 0.25 mg/mL, in phosphate buffer at physiological pH at 46 °C with shaking. Conversely, the wild-type protein (0.5 mg/mL) does not aggregate under these conditions.

Even at room temperature, R120G is prone to form aggregates within 30 minutes. We observed the formation of white insoluble protein aggregates upon incubating 1 mg/mL solutions of R120G αB-crystallin at room temperature (~23 °C), while the wild type protein solutions remained clear. The samples were visualized by transmission electron microscopy, and the R120G sample contained dense amyloid-like aggregates uniformly distributed across the majority of the fields of the grids, while the grids prepared with wild type protein were mostly empty with a few small aggregates (Figure 2.4).

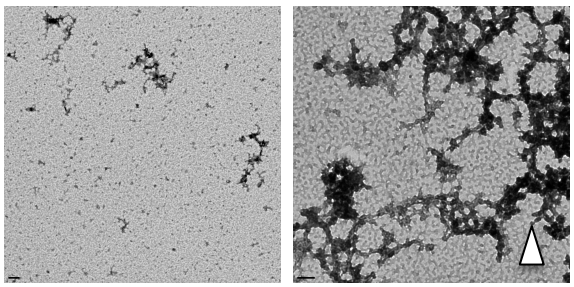

Figure 2.4. Dense aggregates (indicated by arrow) are observed within 30 minutes of incubation at room temperature for R120G αB-crystallin (right), while the wild type αB-crystallin grids were mostly clear with a few small aggregates (left). Results are representative of experiments performed four times. Magnification is 11kx and scale bar is 1 µm.

We wondered if this difference between the aggregation propensity of wild type and the mutant proteins might reflect a difference in thermal stability. Using differential scanning fluorimetry, a technique that was introduced in Chapter 1 and that will be applied in Chapters 3 and 4 for ligand discovery, we measured the apparent melting temperatures of full-length wild type and R120G αB-crystallin. The wild type protein melted at 60 ± 0.19°C (Figure 2.5). Rather than decreasing the apparent melting temperature as expected, the R120G mutation resulted in an increased melting temperature (here, 63.9 ± 0.35°C). There was some variability observed in the melting temperature of R120G αB-crystallin among preparations of protein, but it consistently melted between ~3 °C and 9 °C higher than the wild type protein. We hypothesized that amyloids of R120G αB-crystallin might be forming in the course of the differential scanning fluorimetry experiment. In this model, the thermally stable amyloid fibrils might explain the apparent increase in the observed melting temperature. To test this conjecture, we removed samples at various times throughout the DSF experiment and visualized the protein by negative stain transmission electron microscopy (Figure 2.6).

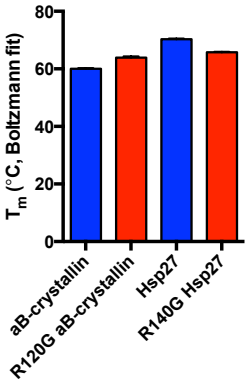

Protein	T_m (°C)	SEM	n
αB-crystallin	60.0	0.19	6
R120G αB-crystallin	63.9	0.35	6
Hsp27	70.3	0.23	6
R140G Hsp27	65.8	0.10	6

Figure 2.5. Thermal stability measurements. The melting temperature of each sHsp solution was measured using DSF (see the Methods section). Each value is the average of six measurements and error bars represent standard error of the mean (SEM). Melting temperatures were calculated using a Boltzmann equation fit of the fluorescence curves.

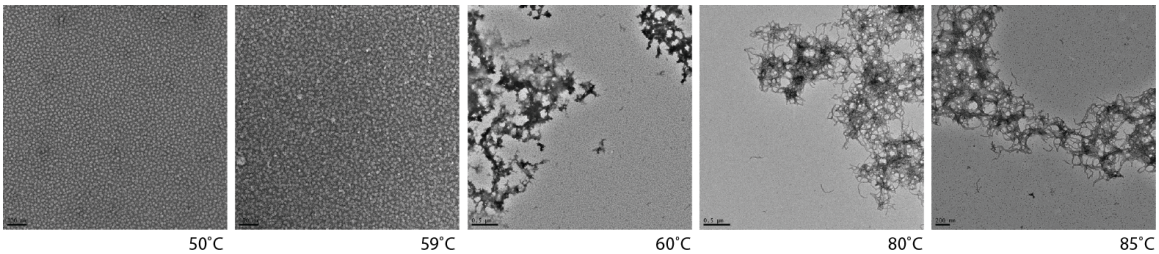

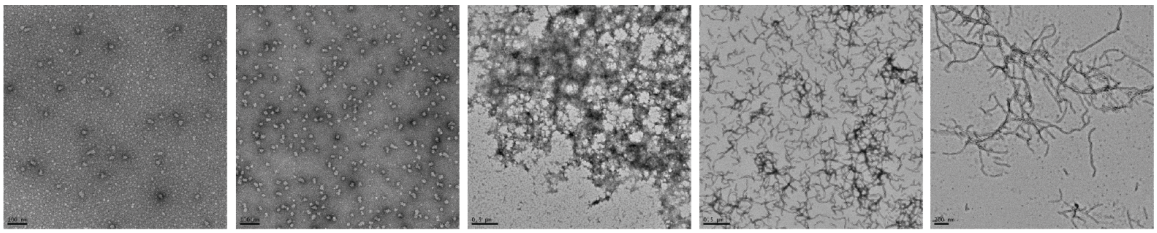

Figure 2.6. Mutant αB-crystallin is prone to forming amyloids during the DSF experiment. Samples of wild type αB-crystallin (top) or R120G αB-crystallin (bottom) were taken from the DSF studies and imaged by electron microscopy.

In this DSF experiment, a protein solution was heated to a given temperature, incubated for 130 seconds, then cooled to room temperature before the fluorescence of the environmentally-sensitive dye was measured. To prepare samples for electron microscopy, a protein solution (without the fluorophore) was treated in this way and samples collected for EM. Before heating, both wild type and mutant αB-crystallin are visible as small, globular oligomers, consistent with previous observations. Upon heating/cooling in the DSF platform, these structures grow larger and more irregular. Then, both proteins transition through a somewhat irregular aggregate pattern. The R120G αB-crystallin eventually formed classical, elongated amyloid fibrils upon heating to 80 °C and re-cooling. The wild type protein, in contrast, was visible as branched fibrils that tended to clump in regions of the grids, while the mutant assumed mostly unbranched, linear amyloids that were evenly dispersed across the grid. The morphology of the R120G amyloid formed under these conditions closely resembles the fibrils reported by Meehan et al (17) to be formed upon partial denaturation with 1 M guanidine hydrochloride and heating to 60 °C for two hours.

From these studies, it is clear that both the wild type and R120G αB-crystallin form amyloids during the DSF experiment, which by definition completely denatures the proteins. However, the room temperature electron microscopy (Figure 2.4) and the light scattering result (Figure 2.3) support the conclusion that the R120G mutant destabilizes the protein to increase its aggregation propensity. Furthermore, the difference in the measured thermal stabilities of the two proteins from DSF may be due to differences in the extent of amyloid fibrillization at given temperatures. This was an interesting result for two reasons: 1) the morphology of the aggregates formed under the conditions of the experiment are very clearly classic amyloid fibrils (versus amorphous aggregates) and 2) this assay suggests a potential screening platform for the discovery of ligands that stabilize R120G αB-crystallin against aggregation; this application of the DSF platform will be discussed in Chapter 3.

2.9. Hsp27 forms amyloids accelerated by the pathological mutation R140G

Next, we wanted to explore the biochemistry of the R140G mutation in Hsp27. *In vitro*, R140G Hsp27 has been reported to be slightly destabilized relative to the wild type protein; it is slightly more susceptible to proteolysis and melts at a lower temperature (64.0 ± 0.2 versus 69.8 ± 0.2 °C (28)). However, its aggregation propensity has not been reported. We wanted to investigate the amyloid-forming propensity of R140G Hsp27 to see if it behaves analogously to R120G αB-crystallin. We expressed and purified Hsp27 containing the R140G mutation and measured its thermal stability by DSF. In good agreement with the literature, R140G Hsp27 appeared to be slightly less stable than the wild type protein, melting with an apparent T_m of 65.9 ± 0.10 °C versus 70.3 ± 0.23 °C (Figure 2.5). Using light scattering, we found that R140G aggregated under relatively mild conditions at physiological pH with mild heating, though the lag time for aggregation was much longer than that observed for R120G αB-crystallin and it required higher concentrations of protein (Figure 2.7).

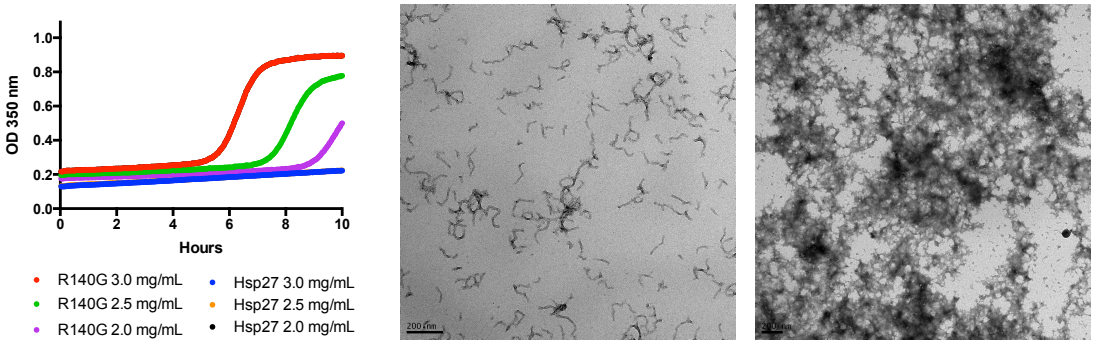

Figure 2.7. Aggregation of R140G and wild type Hsp27 as measured by light scattering and electron microscopy. Light scattering results are the average of triplicate wells and are representative of results obtained in three independent experiments. The micrographs show wild type Hsp27 (left) and R140G Hsp27 (right) samples after 10 to 12 hr incubation in the light scattering assay. Microscopy is representative of at least 12 fields imaged per grid.

Unexpectedly, even though wild type Hsp27 did not give rise to a light scattering signal, both the wild type and R140G Hsp27 samples contained amyloid fibrils under these conditions. The electron micrographs in Figure 2.7 show the morphology of the aggregated wild type Hsp27 (left) and R140G Hsp27 (right). The wild type protein formed short protofibrils with little branching, while the R140G Hsp27 formed much more extensive clumps of short, branched amyloid.

R140G Hsp27 also formed amyloids by electron microscopy when a 3 mg/mL solution was heated to 70 °C for ten minutes and then cooled to room temperature for 30 minutes before gridding for electron microscopy (Figure 2.8, top right). Conversely, the wild type protein did not exhibit amyloid formation when treated identically, and native-like oligomers could still be seen by electron microscopy (Figure 2.8, top left and inset). However, when solutions of the protein were fully denatured by incubating at 95 °C for ten minutes and then cooled to room temperature for 30 minutes before gridding, short amyloid fibrils were evident in both the R140G and wild type samples (Figure 2.8, bottom panels). Interestingly, though, the wild type protein still contains small oligomers that resemble the native protein (bottom inset), while R140G is depleted of native oligomers. This suggests that, while both proteins form amyloids under these conditions, unfolded wild-type protein can refold into native-like structures while the unfolded R140G protein preferentially forms amyloids and is entirely sequestered in fibrils.

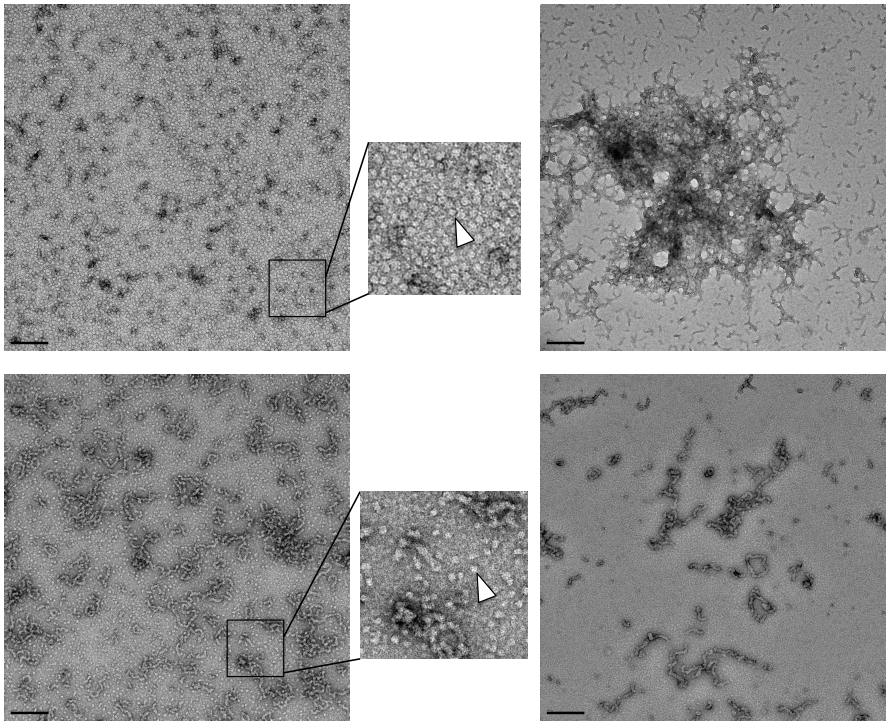

Figure 2.8: Hsp27 forms amyloids accelerated by the pathological mutation R140G by electron microscopy. Top left, wild type Hsp27 incubated at 70 °C; top right, R140G Hsp27 incubated at 70 °C; bottom left, wild type Hsp27 heated to 95 °C; bottom right, R140G Hsp27 heated to 95 °C. Images are representative of at least 12 fields visualized per grid. All images are taken at 26,000x magnification and scale bars are 200 nm.

We also observed fibrils formed by Hsp27 in the course of repeated cycles of heating and cooling in the DSF experiment (Figure 2.9). These fibrils resemble classic amyloids, but have different morphologies depending on the composition of the buffer used in the experiment.

Lithium chloride is routinely included to our DSF experiments because it was empirically determined to improve signal-to-noise and improve variability. In standard phosphate buffer, Hsp27 forms short protofibrils similar to those that formed under the light scattering assay conditions. However, when 50 mM lithium chloride was added, the observed amyloid fibrils were much more extensive and appeared to be more branched.

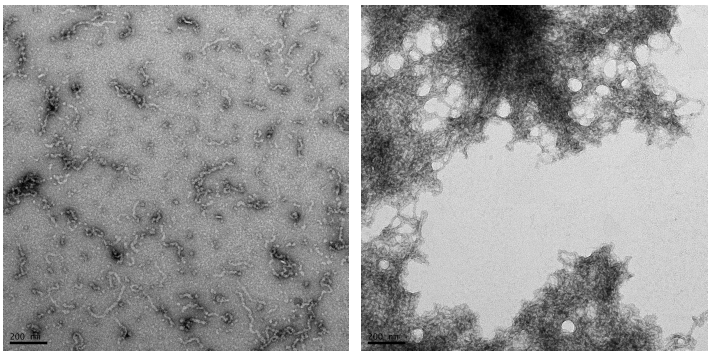

Figure 2.9. Buffer conditions impact Hsp27 fibril morphology. Left, species observed from heating and cooling in sodium phosphate buffer; right, species observed upon the same heating and cooling profile when 50 mM LiCl was added.

These experiments demonstrated that both R140G and wild type Hsp27 form amyloids *in vitro* and the mutant appeared to be more prone to extensive aggregation than the wild type protein. This is an interesting result, as the observation that Hsp27 forms amyloids has not been previously reported. Next, we wondered if the R140G mutation disrupted the native fold of the protein. We chose to study the α-crystallin domain of Hsp27, which consists of the central 98 amino acids (residues 79-176) and forms a stable dimer in solution. R140G disrupts two inter-protomer salt bridges that normally stabilize the dimer interface. We introduced the R140G mutation into this core domain construct of Hsp27, measured the thermal stability by DSF, and recorded a ^{15}N-HSQC spectrum of the protein. Interestingly, while full-length R140G exhibited a decreased melting temperature, the mutation did not have a large effect on thermal stability in the context of the core domain; the wild type protein melts at 53 ± 0.038 °C and the mutant slightly higher at 54 ± 0.49 °C. This is consistent with the similar thermal stabilities observed for the wild type and R120G αB-crystallin core domains, which melt at 65 ± 0.13 °C and 64 ± 0.13 °C, respectively, despite the dramatic change in stability in the context of the full length protein.

We obtained the HSQC spectra of the uniformly ^{15}N-labelled core domains, as shown in Figure 2.10, and observed no gross structural deficiencies in folding. The R140G spectrum is as disperse

and contains most of the peaks that are present in the wild type spectrum, indicating that both proteins are initially folded and native-like under these conditions. Consequently, the destabilizing effect of the loss of the inter-protomer salt bridges may be due to changes in the kinetics of protomer interactions or due to the mutation's effects on the structure of the full-length, oligomeric protein.

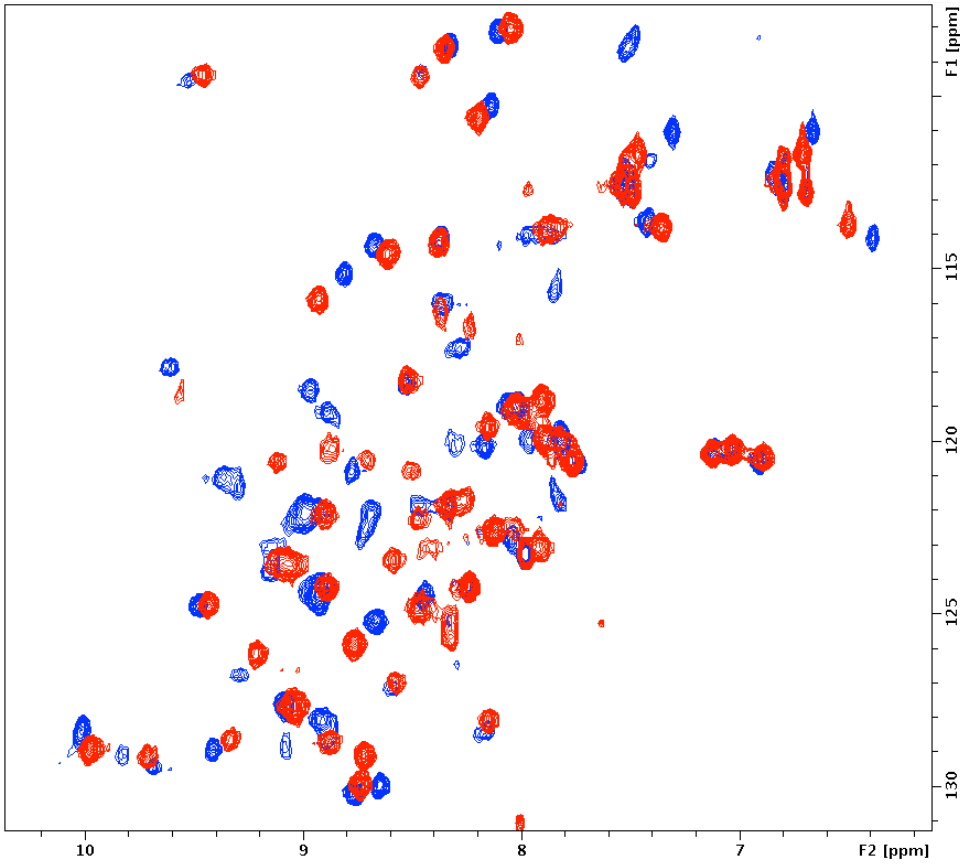

Figure 2.10. $^{1}H,^{15}N$-HSQC spectrum of wild type Hsp27 core domain (residues 79-176) in blue and the overlaid R140G Hsp27 core domain in red. The R140G mutation caused significant chemical shift perturbations, but the spectrum is disperse and most peaks are still present, suggesting that the protein is well-behaved under these conditions and closely resembles the native fold.

2.10. R127W and S135F mutations in Hsp27 are associated with Charcot-Marie-Tooth disease

In 2004, Evgrafov et al. reported the identification of a mutation S135F in Hsp27 in a Russian family with Charcot-Marie-Tooth disease (14). A cohort of 301 individuals with Charcot-Marie-Tooth disease and 115 individuals with distal hereditary neuropathy were subsequently screened for mutations in the same gene, and four additional missense mutations were identified (R127W, R136W, T151I, and P182L; see Table 2.1). The five mutations segregated

perfectly with disease phenotypes and were absent in 200 healthy controls (14). Some evidence was reported that suggests the R127W and S135F mutations in Hsp27 may destabilize its dimeric β-sandwich substructure, leading to its aggregation and gain of toxic function phenotypes. In SH-SY5Y and HEK293 cells, the transfected Hsp27 mutants R127W or S135F appeared to reduce the ability of the protein to form disulfide-crosslinked dimers (1). Because of this, we wanted to examine the effect of these mutations on the structure and stability of the core domain; specifically, we hypothesized that if the dimer stability were compromised by these mutations (outside of the conserved hot-spot residue) then these mutants may be more aggregation prone as well.

2.11. The R127W mutation destabilizes the core domain dimer and results in aggregation

The R127 residue is located on the loop between the β5 and β6+7 strands, and ion pairs with H102 from the same protomer, located on the adjacent loop formed from the β3 and β4 strands. In the core domain structures, the R127 residue is solvent exposed, but the environment of the R127 residue in the context of the full-length protein is not known; replacement of the arginine with a tryptophan could have steric effects in the context of the full-length oligomer in addition to the effect of the loss of a salt bridge on the stability of the core domain.

We used site-directed mutagenesis to introduce the R127W mutation into the core domain construct of Hsp27. By differential scanning fluorimetry, its stability was very similar to that of the wild type core domain (53.8 ± 0.04 °C versus 53.4 ± 0.038 °C, respectively). However, by HSQC it appeared that the native fold of the protein was compromised. In contrast to the R140G Hsp27 core domain spectrum, the R127W spectrum is missing about half of its cross-peaks, suggesting that its native fold may be very different than that of the wild type protein (Figure 2.11). Indeed, when a solution of 1 mg/mL R127W Hsp27 core domain in sodium phosphate buffer at physiological pH was gently heated for one hour at 46 °C, extensive aggregation was observed by electron microscopy (Figure 2.12). Conversely, grids of wild type protein did not show appreciable aggregation. Given the rapid aggregation behavior observed for R127W core domain, it is possible that the loss of cross-peaks in the HSQC spectrum was due to protein aggregation during the course of the 45-minute experiment at 30 °C, though no aggregation was observed by eye in the sample tube.

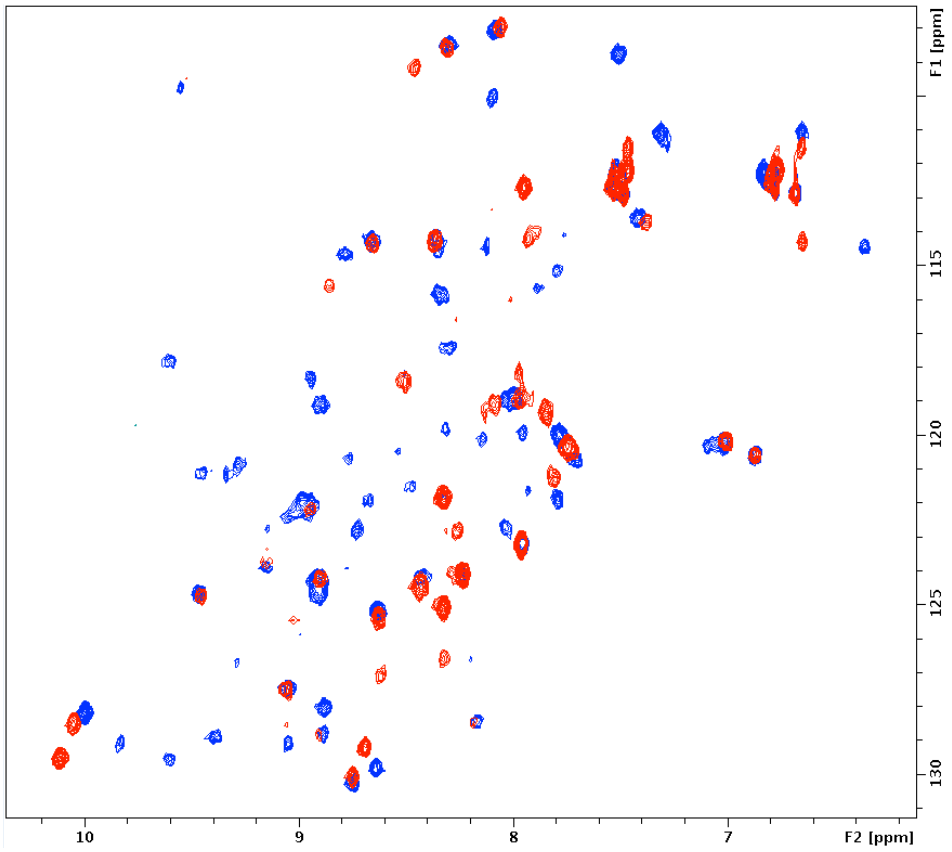

Figure 2.11. $^{1}H,^{15}N$-HSQC spectrum of wild type Hsp27 core domain (residues 79-176) in blue and the overlaid R127W mutant Hsp27 core domain in red. The mutant had fewer identifiable peaks, suggesting disruption of the core structure.

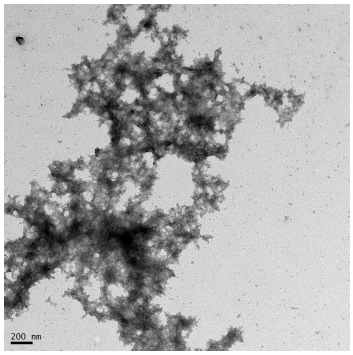

Figure 2.12. Aggregates formed from R127W core domain after one hour of incubation at 46 °C. Grids of wild type Hsp27 core domain did not show aggregates under these conditions (data not shown).

2.12. The S135F mutation destabilizes the core domain dimer and results in aggregation

The mutant S135F, which is also associated with Charcot-Marie-Tooth disease and distal hereditary peripheral neuropathy, was also reported to reduce the ability of the protein to form disulfide-crosslinked dimers in SH-SY5Y and HEK293 cells (1). The S135 residue is located within

the β6+7 strand that forms the antiparallel dimer interface of Hsp27. Its side chain forms a hydrogen bond with a backbone carbonyl group across the dimer interface, presumably contributing to the stability of the dimer. Mutation of this serine to a phenylalanine would be expected to disrupt this hydrogen bond interaction and also to contribute steric bulk to the dimer interface, which could account for increased monomerization of this mutant.

Unlike R127W, introduction of the S135F mutation did result in a decreased thermal stability of 48.8 ± 0.56 °C relative to 53.4 ± 0.038 °C for the wild type core domain. This mutation was accompanied by even more dramatic changes to the HSQC spectrum of the protein (Figure 2.13), with loss of >50% of the cross-peaks and reduced dispersion of the amide resonances, suggesting a dramatic alteration to the native fold of the protein.

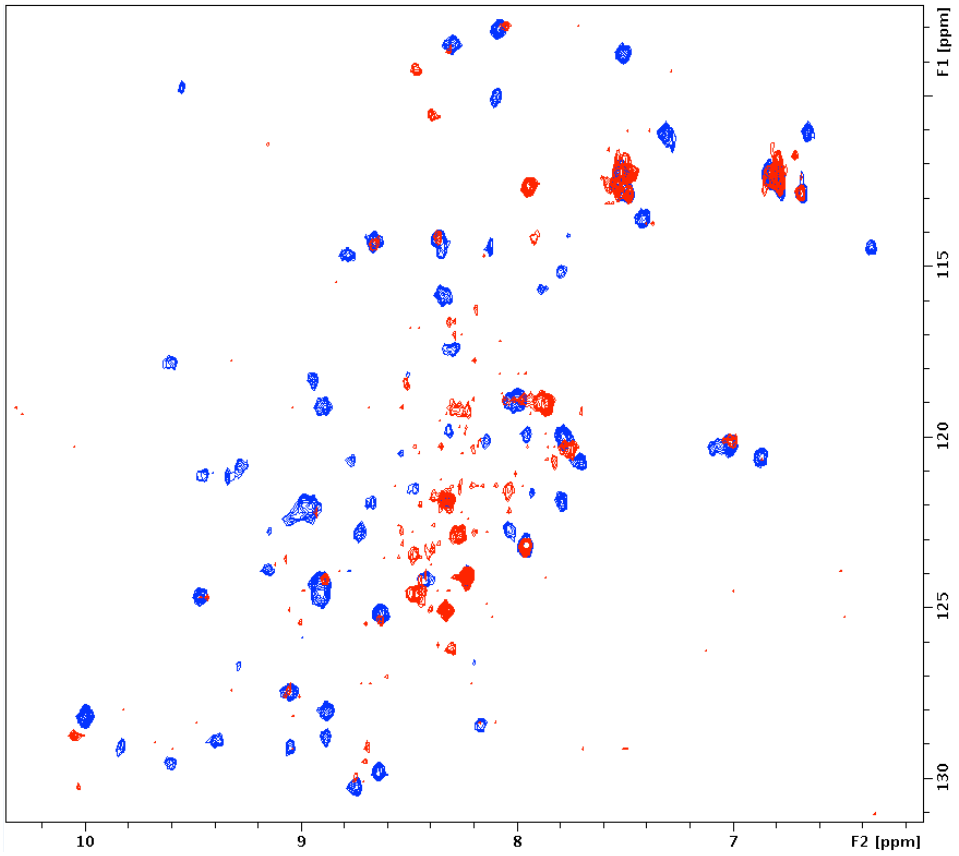

Figure 2.13. $^{1}H,^{15}N$-HSQC spectrum of wild type Hsp27 core domain (residues 79-176) in blue and the overlaid S135F mutant Hsp27 core domain in red. The mutation causes dramatic disruption of the core structure.

Interestingly, S135F also increases the aggregation propensity of the core α-crystallin domain, decreasing lag time. Samples of each protein were incubated at 46 °C and light scattering was

monitored at 350 nm (Figure 2.14). The core domain containing the mutation R140G is included for comparison; both aggregate more quickly than the wild type protein.

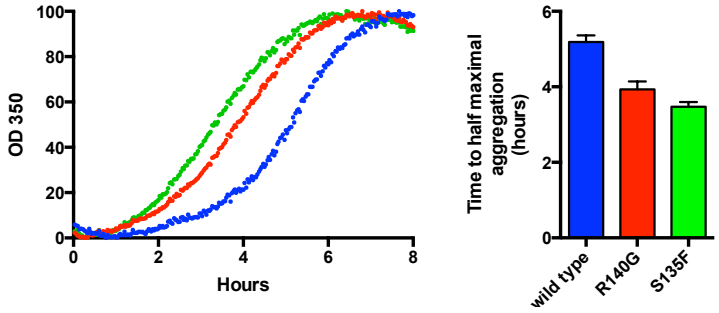

Figure 2.14. The S135F Hsp27 core domain aggregates more quickly than the wild type protein and slightly faster than R140G mutant. Results are the average of triplicate wells and represent two independent experiments, and error shown is standard error.

This suggests that the R127W and S135F mutations destabilize the core domain of Hsp27, resulting in protein aggregation. These mutations may also cause protein aggregation in diseased neurons, contributing to gain-of-toxic function pathology in Charcot-Marie-Tooth disease and distal hereditary peripheral neuropathy. Together, this leads to a model in which mutation of key residues along the dimer interface of sHsps, including the hot spot residues, contribute to gain-of-toxic function protein aggregation diseases.

2.13. Conclusions and future work

2.13.1. Model for sHsp aggregation and amyloid formation

We have shown that the hot spot mutations R120G in αB-crystallin and R140G in Hsp27 increase the aggregation propensity of small heat shock proteins. Additionally, the peripheral neuropathy associated mutations R127W and S135F alter the native tertiary structure of the protein and result in accelerated protein aggregation. Each of these mutations appear to compromise the stability of the dimer interface, leading to a model in which sHsp monomers may misfold and form ordered, β-sheet rich amyloid fibrils. For the hot spot residues, the loss of two inter-protomer salt bridges destabilizes the dimer; for S135F, it is the loss of two inter-protomer hydrogen bonds. A molecular rationalization for the effect of the R127W mutation is less obvious, but it is clearly destabilizing in the context of the dimer and favors aggregation. Together, these results suggest that mutations in sHsps cause amyloid formation and gain-of-function toxicity; these results are supported by observations from cell culture and patient samples in the literature.

2.13.2. Additional evidence that mutant sHsps cause gain-of-function aggregation diseases

We presented evidence that R120G αB-crystallin forms amyloids *in vitro.* Studies from the literature suggest that it also aggregates in cells, and that this is a key component of the disease pathology in both cataracts and desmin-related myopathy (17-21). Most compellingly, an R120G mouse model exhibits Congo red positive staining patterns in cardiomyocytes, evidence of amyloid deposition (18, 46), and recovers fully when expression of the mutant protein is halted (2, 18). While R140G Hsp27 has not been studied in cells or *in vivo,* the other 'hot spot' mutations in αA-crystallin and Hsp22 have been shown to aggregate in physiological contexts. In knock-in mice expressing human, mutant R116C αA-crystallin, immunohistochemical staining indicated that the protein was distributed in a granular, punctate pattern in the lens (47, 48). R116C αA-crystallin partitioned into the insoluble fraction of lysate from human lens epithelial cells and eluted in the void volume of a size exclusion chromatography column (48, 49). All of these studies suggest that R116C αA-crystallin is prone to aggregation, which may account for its role in hereditary cataracts. Moreover, R116C αA-crystallin interacts more tightly than the wild type protein with Hsp27 and with αB-crystallin, suggesting that aggregates of R116C might sequester Hsp27 and αB-crystallin, exacerbating the phenotype (38). Lastly, the K141E and K141N mutant proteins also appear to aggregate in peripheral neuropathy (13). Cells expressing these mutations exhibited a greater tendency to form inclusion bodies containing Hsp22 (13, 50), and patient derived fibroblasts from individuals carrying these mutations also contained increased numbers of aggresomes or inclusion bodies (51). In addition to the studies presented here, this body of evidence suggests that in these diseases sHsp mutations cause gain-of-toxic function protein aggregation.

It is important to also discuss evidence linking some sHsps mutations to loss-of-function. First, though most sHsp mutations are autosomal dominant, there are a few examples of autosomal recessive disease (L99M in Hsp27, R54C in αA-crystallin) (15, 32). Phenotypes associated with loss-of-function diseases are typically recessive, suggesting that a few of the sHSP mutations may be loss-of-function disorders. However, the majority of diseases linked to sHsp mutations are dominantly inherited. Although this observation could support a gain-of-function phenotype, it is also consistent with haploinsufficiency (32). In the absence of a molecular understanding of disease etiology, haploinsufficiency is indistinguishable from a dominant

negative phenotype. But, in at least some cases, the mutant small heat shock proteins recruit and co-aggregate with wild-type protein (e.g. R12C, R21L, R21W, R49C, R54C, R116C, and R116H αA-crystallin (22), R120G αB-crystallin (52), and P182L Hsp27 (53)), supporting that these mutations are dominant negative in character. Together, these studies and our own suggest that some sHsp mutations cause gain-of-function pathology. A few research groups in the field are beginning to recognize this possibility (32). Still, the possibility that these proteins form ordered amyloids is still underappreciated.

2.13.3. The potential use of pharmacological chaperones to recover mutant pathologies

Point mutations in sHsps appear to destabilize the native fold of the proteins and result in gain-of-toxic function aggregation. Thus, potential treatments for these sHsp-associated diseases might recover the stability of the native fold, preventing or reversing the aggregation process. Molecules that act in this matter are known as pharmacological chaperones, because they work in protein folding analogous to help maintain normal folding and proteostasis analogously to molecular chaperones. In order to test this concept, we wanted to identify ligands that bind to native sHsps and evaluate their utility as pharmacological chaperones. Chapters 3 and 4 describe our efforts to do so for αB-crystallin and Hsp27, respectively.

2.14. Experimental Procedures

2.14.1. QuikChange mutagenesis.

Mutants were introduced using an adapted site-directed mutagenesis protocol (Stratagene, La Jolla, CA) and PfuUltra DNA polymerase (Agilent). Briefly, primers were designed containing five to seven bases of the wild type sequence, followed by the mutated codon, and eight to ten bases of the wild type sequence. Separate reactions were initiated with the forward and reverse primers for six cycles of PCR amplification, and then the reactions were combined and the remaining ten cycles were completed. Products were confirmed by sequencing.

2.14.2. Purification of Hsp27c or αB-crystallin core domain

This purification method was adapted from protocols kindly provided by the Klevit laboratory. Terrific broth was inoculated with fresh overnight cultures of BL21 (DE3) cells containing the plasmids. Cultures were grown at 37 °C with shaking at 150 rpm for 4-5 hours, to an OD_{600} of ~1. After cooling to room temperature for about one hour, cultures were induced with 1 mL of 1 M

IPTG (a final concentration of 1 mM). Lower concentrations of IPTG resulted in poor expression levels. Cultures were allowed to induce overnight at room temperature for about 18 hours, cells were harvested by centrifugation 4000 rpm for 10 min and pellets were stored at -80 °C until ready to purify. To lyse the cells, pellets were first suspended in 30 mL of lysis buffer per liter of cells using vortexing and pipetting. Lysis buffer contained 20 mM Tris, 100 mM NaCl, 10 mM EDTA, pH 8.0, and Roche Complete protease inhibitor (one mini tablet per 100 mL of buffer). The cells were lysed by two passes of microfluidization or 5 x 30 sec of sonication. The lysate was clarified by centrifugation at 15,000 rpm for 30 min, the supernatant was decanted, and PMSF was added to a final concentration of 300 µM. The protein was then subjected to a two-step ammonium sulfate precipitation as follows: Ammonium sulfate was slowly added to a final concentration of 16.9 (w/v)%. The salt was allowed to dissolve completely and the mixture was allowed to stir for an additional ten minutes at room temperature. The resulting mixture was centrifuged at 15,000 rpm for 30 minutes, the supernatant was decanted, and an additional 16.9 (w/v)% ammonium sulfate was added to the supernatant. After stirring for ten minutes at room temperature, the resulting mixture was again centrifuged at 15,000 rpm for 30 minutes, resulting in precipitation of the sHsp protein in the pellet. Pellets were resuspended into MonoQ buffer A (20 mM Tris, pH 8.0) and dialyzed into 4 L of buffer A overnight. Protein was purified by MonoQ anion exchange chromatography with a gradient of 0 to 1 M NaCl over 20 column volumes. The wild-type proteins eluted at around 150 mM NaCl. Fractions containing protein were pooled and concentrated, then subjected to size exclusion chromatography using a SuperDex75 column in 50 mM NaPi, pH 7.5, 100 mM NaCl.

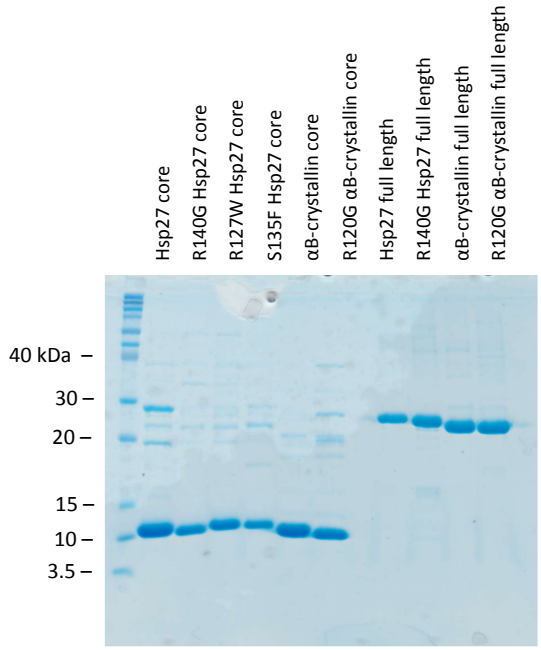

Figure 2.15: Purified core domain and full length constructs.

2.14.3. Purification of full length Hsp27 and R140G Hsp27

Hsp27 lacking an affinity tag was used for these experiments. Cells were expressed in terrific broth as described above, except cultures were induced with 500 µL of 1 M IPTG (final 500 µM) and cultures were induced at 18°C instead of room temperature. Lysis buffer contained 50 mM Tris HCl pH 8.0, 10 mM $MgCl_2$, 1 mM NaCl, and 1 mM EDTA. Size exclusion chromatography was performed on a SuperDex 200 column in 25 mM NaPi pH 7.5, 160 mM NaCl, and 0.5 mM EDTA.

2.14.4. Purification of His-tagged αB-crystallin and R120G αB-crystallin

Hexahistidine-tagged αB-crystallin and R120G αB-crystallin were expressed in lysogeny broth or terrific broth as described above. The cells were lysed in 20 mM Tris pH 8.0, 100 mM NaCl, 6 M urea, 5 mM β-mercaptoethanol, and 15 mM imidazole. After centrifugation, the supernatant was loaded onto Ni-NTA resin (10 mL per liter of culture) and washed with ten column volumes of buffer containing 20 mM Tris pH 8.0, 100 mM NaCl, 6 M urea, 5 mM β-mercaptoethanol, and 30 mM imidazole. Proteins were eluted with buffer containing 20 mM Tris pH 8.0, 100 mM NaCl, 6 M urea, 5 mM β-mercaptoethanol and 150 mM imidazole. EDTA was then added to 5 mM, and the concentrated protein was refolded portion-wise by size exclusion chromatography on a SuperDex 200 10/30 column in 20 mM sodium phosphate pH 7.2, 100 mM NaCl.

2.14.5. Electron microscopy

Proteins were applied to glow-discharged Formvar/carbon 300-mesh copper grids (Electron Microscopy Sciences) and stained with 2% uranyl formate. Grids were visualized on a Phillips CM-100 transmission electron microscope at an accelerating voltage of 80 kV with magnification settings ranging from 10,500–92,000x (University of Michigan), or a Fei Technai T20 transmission electron microscope at an accelerating voltage of 200 kV with magnification from 11,000-21,000x (UCSF). Shown are representative images and at least 12 random fields were imaged per treatment condition. Typically, at least two grids were prepared for each condition.

2.14.6. Light scattering assay of protein aggregation

Light scattering assays were carried out in 384-well clear bottom plates in a SpectraMax 3000 plate reader. Protein concentration was determined by BCA and proteins were centrifuged at 13,200x rpm for 10 minutes prior to initiation of the assay. Each well contained 100 µL final well volume containing 0.5-3 mg/mL protein in buffer containing 20 mM sodium phosphate pH 7.2, 100 mM NaCl, and 5 mM DTT. Plates were centrifuged to remove air bubbles and read every two minutes with shaking between each read for 5 sec.

2.14.7. Thermal stability measurements

DSF experiments were performed in a BioRad CFX384 RT-PCR thermocycler. A temperature gradient of 25 – 85 °C ramping at 1°C/1 min was used for melting curves. For all proteins described here, solutions were heated to each given temperature for 130 sec, cooled to 25°C for 15 sec, and the fluorescence was read before heating the solution to the next incremental temperature ("up/down mode"). Fluorescence readings were taken using the FRET channel. Protein solutions contained 0.2-0.4 mg/mL protein (calculated for monomer) in 20 mM NaPi pH 7.5, 100 mM NaCl, 5 mM DTT, and 5x SYPRO Orange Dye (Invitrogen). Curves were fit using a Boltzmann equation (GraphPad Prism version 6).

2.14.8. HSQC NMR

HSQC spectra were acquired at 30 °C on a Bruker DRX500 with a QCI Z-axis gradient Cryoprobe, running Topspin version 1.3. Spectra were acquired on samples containing 150-200 µM Hsp27 core domain in 50 mM NaPi, pH 7.5, 100 mM NaCl at 30°C. 256 scans were acquired per t_1 value

and spectral widths of 1500 Hz and 9615 Hz were used in the ^{1}H and ^{15}N dimensions, respectively. Processing and spectral visualization was performed using rNMR (54) and Sparky (55).

2.15. Notes

The Klevit laboratory kindly provided the constructs and purification protocols for the full length Hsp27, Hsp27 core domain, αB-crystallin core domain, and R120G αB-crystallin core domain. The construct for Hsp22 was a kind gift from Jean-Marc Fontaine.

2.16. References

1. Almeida-Souza L, Goethals S, de Winter V, Dierick I, Gallardo R, Van Durme J, et al. Increased monomerization of mutant HSPB1 leads to protein hyperactivity in Charcot-Marie-Tooth neuropathy. The Journal of biological chemistry. 2010;285(17):12778-86.
2. Andley UP, Hamilton PD, Ravi N, Weihl CC. A knock-in mouse model for the R120G mutation of alphaB-crystallin recapitulates human hereditary myopathy and cataracts. PloS one. 2011;6(3):e17671.
3. Clark JI, Muchowski PJ. Small heat-shock proteins and their potential role in human disease. Curr Opin Struct Biol. 2000;10(1):52-9.
4. Arrigo AP, Simon S, Gibert B, Kretz-Remy C, Nivon M, Czekalla A, et al. Hsp27 (HspB1) and alphaB-crystallin (HspB5) as therapeutic targets. FEBS letters. 2007;581(19):3665-74.
5. Dierick I, Irobi J, De Jonghe P, Timmerman V. Small heat shock proteins in inherited peripheral neuropathies. Ann Med. 2005;37(6):413-22.
6. Sun Y, MacRae TH. Small heat shock proteins: molecular structure and chaperone function. Cell Mol Life Sci. 2005;62(21):2460-76.
7. Haslbeck M, Franzmann T, Weinfurtner D, Buchner J. Some like it hot: the structure and function of small heat-shock proteins. Nature structural & molecular biology. 2005;12(10):842-6.
8. Bagneris C, Bateman OA, Naylor CE, Cronin N, Boelens WC, Keep NH, et al. Crystal structures of alpha-crystallin domain dimers of alphaB-crystallin and Hsp20. Journal of molecular biology. 2009;392(5):1242-52.
9. Weeks SD, Baranova EV, Heirbaut M, Beelen S, Shkumatov AV, Gusev NB, et al. Molecular structure and dynamics of the dimeric human small heat shock protein HSPB6. Journal of structural biology. 2014;185(3):342-54.
10. Lelj-Garolla B, Mauk AG. Roles of the N- and C-terminal sequences in Hsp27 self-association and chaperone activity. Protein science : a publication of the Protein Society. 2012;21(1):122-33.
11. Jehle S, Vollmar BS, Bardiaux B, Dove KK, Rajagopal P, Gonen T, et al. N-terminal domain of alphaB-crystallin provides a conformational switch for multimerization and structural heterogeneity. Proceedings of the National Academy of Sciences of the United States of America. 2011;108(16):6409-14.
12. Vicart P, Caron A, Guicheney P, Li Z, Prevost MC, Faure A, et al. A missense mutation in the alphaB-crystallin chaperone gene causes a desmin-related myopathy. Nature genetics. 1998;20(1):92-5.

13. Irobi J, Van Impe K, Seeman P, Jordanova A, Dierick I, Verpoorten N, et al. Hot-spot residue in small heat-shock protein 22 causes distal motor neuropathy. Nature genetics. 2004;36(6):597-601.
14. Evgrafov OV, Mersiyanova I, Irobi J, Van Den Bosch L, Dierick I, Leung CL, et al. Mutant small heat-shock protein 27 causes axonal Charcot-Marie-Tooth disease and distal hereditary motor neuropathy. Nature genetics. 2004;36(6):602-6.
15. Houlden H, Laura M, Wavrant-De Vrieze F, Blake J, Wood N, Reilly MM. Mutations in the HSP27 (HSPB1) gene cause dominant, recessive, and sporadic distal HMN/CMT type 2. Neurology. 2008;71(21):1660-8.
16. Litt M, Kramer P, LaMorticella DM, Murphey W, Lovrien EW, Weleber RG. Autosomal dominant congenital cataract associated with a missense mutation in the human alpha crystallin gene CRYAA. Human molecular genetics. 1998;7(3):471-4.
17. Meehan S, Knowles TP, Baldwin AJ, Smith JF, Squires AM, Clements P, et al. Characterisation of amyloid fibril formation by small heat-shock chaperone proteins human alphaA-, alphaB- and R120G alphaB-crystallins. Journal of molecular biology. 2007;372(2):470-84.
18. Sanbe A, Osinska H, Villa C, Gulick J, Klevitsky R, Glabe CG, et al. Reversal of amyloid-induced heart disease in desmin-related cardiomyopathy. Proceedings of the National Academy of Sciences of the United States of America. 2005;102(38):13592-7.
19. Ecroyd H, Carver JA. Crystallin proteins and amyloid fibrils. Cell Mol Life Sci. 2009;66(1):62-81.
20. Sanbe A, Yamauchi J, Miyamoto Y, Fujiwara Y, Murabe M, Tanoue A. Interruption of CryAB-amyloid oligomer formation by HSP22. J Biol Chem. 2007;282(1):555-63.
21. Meehan S, Berry Y, Luisi B, Dobson CM, Carver JA, MacPhee CE. Amyloid fibril formation by lens crystallin proteins and its implications for cataract formation. The Journal of biological chemistry. 2004;279(5):3413-9.
22. Raju I, Abraham EC. Mutants of human alphaB-crystallin cause enhanced protein aggregation and apoptosis in mammalian cells: influence of co-expression of HspB1. Biochemical and biophysical research communications. 2013;430(1):107-12.
23. Knowles TP, Vendruscolo M, Dobson CM. The amyloid state and its association with protein misfolding diseases. Nature reviews Molecular cell biology. 2014;15(6):384-96.
24. Goldschmidt L, Teng PK, Riek R, Eisenberg D. Identifying the amylome, proteins capable of forming amyloid-like fibrils. Proceedings of the National Academy of Sciences of the United States of America. 2010;107(8):3487-92.
25. Hipp MS, Park SH, Hartl FU. Proteostasis impairment in protein-misfolding and -aggregation diseases. Trends in cell biology. 2014.
26. Nefedova VV, Sudnitsyna MV, Strelkov SV, Gusev NB. Structure and properties of G84R and L99M mutants of human small heat shock protein HspB1 correlating with motor neuropathy. Archives of biochemistry and biophysics. 2013;538(1):16-24.
27. Almeida-Souza L, Asselbergh B, d'Ydewalle C, Moonens K, Goethals S, de Winter V, et al. Small heat-shock protein HSPB1 mutants stabilize microtubules in Charcot-Marie-Tooth neuropathy. The Journal of neuroscience : the official journal of the Society for Neuroscience. 2011;31(43):15320-8.
28. Nefedova VV, Datskevich PN, Sudnitsyna MV, Strelkov SV, Gusev NB. Physico-chemical properties of R140G and K141Q mutants of human small heat shock protein HspB1 associated with hereditary peripheral neuropathies. Biochimie. 2013;95(8):1582-92.

29. Kore R, Hedges RA, Oonthonpan L, Santhoshkumar P, Sharma KK, Abraham EC. Quaternary structural parameters of the congenital cataract causing mutants of alphaA-crystallin. Molecular and cellular biochemistry. 2012;362(1-2):93-102.
30. Carra S, Boncoraglio A, Kanon B, Brunsting JF, Minoia M, Rana A, et al. Identification of the Drosophila ortholog of HSPB8: implication of HSPB8 loss of function in protein folding diseases. The Journal of biological chemistry. 2010;285(48):37811-22.
31. Xi JH, Bai F, Gross J, Townsend RR, Menko AS, Andley UP. Mechanism of small heat shock protein function in vivo: a knock-in mouse model demonstrates that the R49C mutation in alpha A-crystallin enhances protein insolubility and cell death. The Journal of biological chemistry. 2008;283(9):5801-14.
32. Boncoraglio A, Minoia M, Carra S. The family of mammalian small heat shock proteins (HSPBs): implications in protein deposit diseases and motor neuropathies. The international journal of biochemistry & cell biology. 2012;44(10):1657-69.
33. Validandi V, Reddy VS, Srinivas PN, Mueller NH, Bhagyalaxmi SG, Padma T, et al. Temperature-dependent structural and functional properties of a mutant (F71L) alphaA-crystallin: molecular basis for early onset of age-related cataract. FEBS letters. 2011;585(24):3884-9.
34. Santhoshkumar P, Sharma KK. Phe71 is essential for chaperone-like function in alpha A-crystallin. The Journal of biological chemistry. 2001;276(50):47094-9.
35. Singh D, Raman B, Ramakrishna T, Rao Ch M. Mixed oligomer formation between human alphaA-crystallin and its cataract-causing G98R mutant: structural, stability and functional differences. Journal of molecular biology. 2007;373(5):1293-304.
36. Gong B, Zhang LY, Pang CP, Lam DS, Yam GH. Trimethylamine N-oxide alleviates the severe aggregation and ER stress caused by G98R alphaA-crystallin. Molecular vision. 2009;15:2829-40.
37. Singh D, Tangirala R, Bakthisaran R, Chintalagiri MR. Synergistic effects of metal ion and the pre-senile cataract-causing G98R alphaA-crystallin: self-aggregation propensities and chaperone activity. Molecular vision. 2009;15:2050-60.
38. Fu L, Liang JJ. Detection of protein-protein interactions among lens crystallins in a mammalian two-hybrid system assay. The Journal of biological chemistry. 2002;277(6):4255-60.
39. Brown Z, Ponce A, Lampi K, Hancock L, Takemoto L. Differential binding of mutant (R116C) and wildtype alphaA crystallin to actin. Current eye research. 2007;32(12):1051-4.
40. Chen Q, Yan M, Xiang F, Zhou X, Liu Y, Zheng F. Characterization of a mutant R11H alphaB-crystallin associated with human inherited cataract. Biological chemistry. 2010;391(12):1391-400.
41. Perng MD, Muchowski PJ, van Den IP, Wu GJ, Hutcheson AM, Clark JI, et al. The cardiomyopathy and lens cataract mutation in alphaB-crystallin alters its protein structure, chaperone activity, and interaction with intermediate filaments in vitro. The Journal of biological chemistry. 1999;274(47):33235-43.
42. Liu Y, Zhang X, Luo L, Wu M, Zeng R, Cheng G, et al. A novel alphaB-crystallin mutation associated with autosomal dominant congenital lamellar cataract. Investigative ophthalmology & visual science. 2006;47(3):1069-75.
43. Reilich P, Schoser B, Schramm N, Krause S, Schessl J, Kress W, et al. The p.G154S mutation of the alpha-B crystallin gene (CRYAB) causes late-onset distal myopathy. Neuromuscular disorders : NMD. 2010;20(4):255-9.
44. Kim MV, Kasakov AS, Seit-Nebi AS, Marston SB, Gusev NB. Structure and properties of K141E mutant of small heat shock protein HSP22 (HspB8, H11) that is expressed in human neuromuscular disorders. Archives of biochemistry and biophysics. 2006;454(1):32-41.

45. Datskevich PN, Nefedova VV, Sudnitsyna MV, Gusev NB. Mutations of small heat shock proteins and human congenital diseases. Biochemistry Biokhimiia. 2012;77(13):1500-14.
46. Sanbe A, Osinska H, Saffitz JE, Glabe CG, Kayed R, Maloyan A, et al. Desmin-related cardiomyopathy in transgenic mice: a cardiac amyloidosis. Proceedings of the National Academy of Sciences of the United States of America. 2004;101(27):10132-6.
47. Cobb BA, Petrash JM. Structural and functional changes in the alpha A-crystallin R116C mutant in hereditary cataracts. Biochemistry. 2000;39(51):15791-8.
48. Hsu CD, Kymes S, Petrash JM. Characterization of lens defects in transgenic mice expressing a human R116C {alpha}A–crystallin mutant Investigative ophthalmology & visual science. 2004;2004(45):3965.
49. Andley UP, Patel HC, Xi JH. The R116C mutation in alpha A-crystallin diminishes its protective ability against stress-induced lens epithelial cell apoptosis. The Journal of biological chemistry. 2002;277(12):10178-86.
50. Fontaine JM, Sun X, Hoppe AD, Simon S, Vicart P, Welsh MJ, et al. Abnormal small heat shock protein interactions involving neuropathy-associated HSP22 (HSPB8) mutants. FASEB journal : official publication of the Federation of American Societies for Experimental Biology. 2006;20(12):2168-70.
51. Irobi-Devolder J. A molecular genetic update of inherited distal motor neuropathies. Verhandelingen - Koninklijke Academie voor Geneeskunde van Belgie. 2008;70(1):25-46.
52. Selcen D, Engel AG. Myofibrillar myopathy caused by novel dominant negative alpha B-crystallin mutations. Annals of neurology. 2003;54(6):804-10.
53. Ackerley S, James PA, Kalli A, French S, Davies KE, Talbot K. A mutation in the small heat-shock protein HSPB1 leading to distal hereditary motor neuronopathy disrupts neurofilament assembly and the axonal transport of specific cellular cargoes. Human molecular genetics. 2006;15(2):347-54.
54. Lewis IA, Schommer SC, Markley JL. rNMR: open source software for identifying and quantifying metabolites in NMR spectra. Magnetic resonance in chemistry : MRC. 2009;47 Suppl 1:S123-6.
55. Goddard TD, Kneller DG. SPARKY3. University of California, San Francisco.

Chapter 3

Pharmacological Rescue of an Aggregation-Prone Small Heat Shock Protein in a Cataract Model

3.1. Abstract

Cataracts reduce vision in 50% of individuals over 70 years of age and are a common form of blindness worldwide (1). The transparency of the lens is maintained throughout an individual's lifetime by lens crystallin proteins, including the small heat shock protein αB-crystallin. Cataracts are caused when damage to crystallins, including αB-crystallin, causes their misfolding and aggregation into insoluble amyloids. In this chapter, we describe our application of high-throughput differential scanning fluorimetry to identify molecules that bind αB-crystallin and reverse its aggregation *in vitro*. The most promising compound improved lens transparency in an R120G αB-crystallin mouse model of hereditary cataract and reversed aging-associated cataracts in the human lens. These findings suggest an approach to treating cataracts by stabilizing αB-crystallin and represent the first attempt to develop a small molecule therapeutic targeting a small heat shock protein.

3.2. Introduction

αA-crystallin (HSPB4) and αB-crystallin (HSPB5) belong to a family of small heat shock proteins (sHSPs) that contain a conserved crystallin domain (2, 3). Together, αA- and αB-crystallin comprise 30% of the protein content of the eye lens, where they are responsible for maintaining lens transparency (3). In the nucleus of the lens, crystallins are only expressed during fetal development. Mature lens fiber cells exhibit no protein turnover, and so damage to lens crystallins accumulates over the lifetime of an individual (4). Accumulated damage to these proteins can lead to their misfolding, assembly into amyloid-like insoluble fibrils and age-associated cataracts (3, 5-7). Similarly, heritable mutations in αB-crystallin, such as R120G, cause hereditary forms of cataract with early onset (8). The R120G mutation abrogates two

interactions that normally help define the interface of αB-crystallin dimers (Figure 3.1). Thus, one potential way to treat cataracts would be to identify molecules that bind and stabilize crystallins, favoring the more soluble forms (9).

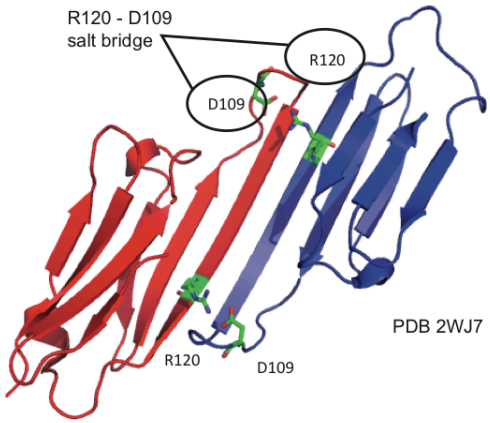

Figure 3.1. Crystal structure (PDB 2WJ7, 2.63Å) of the R120G αB-crystallin core domain, residues 67-157. An arginine at position 120 forms a salt bridge across the dimer interface with aspartic acid at position 109. Mutation of the arginine to a glycine results in disruption of two inter-dimer salt bridges.

3.3. Pharmacological chaperones for canonically undruggable proteins

Pharmacological chaperones (PCs) are small molecules that thermodynamically or kinetically stabilize the native state of a protein (10). A PC has been approved for clinical use in the treatment of transthyretin amyloidosis (11) and other PCs are being explored in late-stage clinical trials for use in treating a number of other misfolding diseases, such as Gaucher disease (12) and Anderson-Fabry disease (13). In the current work, we wanted to identify PCs that stabilize the soluble forms of αB-crystallin and inhibit its aggregation. However, unlike previous targets for PC development, αB-crystallin lacks enzymatic activity. Enzymes tend to be more straightforward targets for this type of strategy because the natural substrate can often serve as a starting point for drug design (12). Also, the enzymatic activity of the target is a convenient and relevant readout in unbiased high-throughput chemical screens (HTS), when a native ligand is not available (11). Because αB-crystallin lacks enzymatic activity and doesn't have known ligands, it falls into a family of disease-causing proteins, including tau, myocilin, a-synuclein and huntingtin, that are typically considered to be "undruggable" (14, 15).

3.4. Differential scanning fluorimetry as a discovery tool for pharmacological chaperones

We asked whether differential scanning fluorimetry (DSF) might provide a way to circumvent some of these challenges. This technique was introduced in Chapter 1 (1.9) as a strategy for screening non-enzymatic targets. In a typical DSF experiment, the apparent melting transition (T_m) of the protein target is measured in the absence and presence of potential ligands (16). Binding of a ligand usually adds free energy to the state that it binds, which shifts the apparent T_m (Figure 1.5). This method has been employed for decades in low throughput biochemical studies; however, it has only recently been developed for high throughput experiments (15, 17-19). We first purified recombinant human R120G αB-crystallin and wild type αB-crystallin and confirmed that both proteins were soluble and well behaved in solution (Figure 3.2).

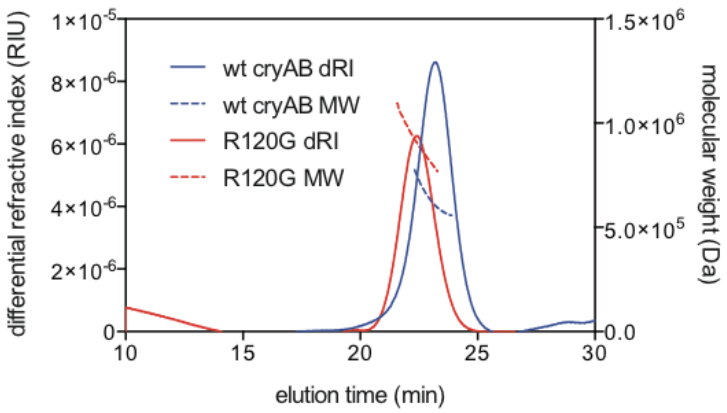

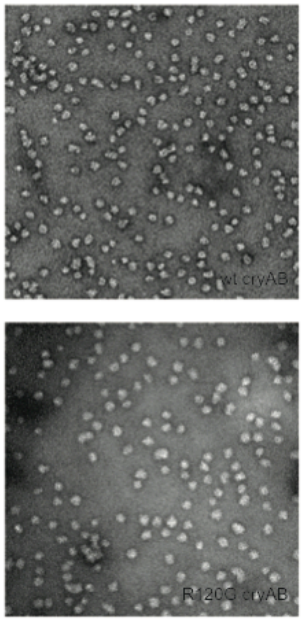

R120G cryAB calculated molecular weight = 950 ± 35 kDa
wt cryAB calculated molecular weight = 570 ± 26 kDa

	mean	SEM	n
R120G	946550	35250	2
wt cryAB	573433	25934	3

Figure 3.2. Recombinant wild type and R120G αB-crystallin (cryAB) form large, polydisperse oligomers by size-exclusion chromatography and negative stain electron microscopy, in agreement with literature characterization (20).

Upon gentle heating, R120G αB-crystallin formed amyloids more readily than wild type αB-crystallin, as measured by light scattering and electron microscopy (EM) (Figure 3.3). Because amyloids are relatively heat-resistant structures, we suspected that samples of R120G αB-crystallin might be more difficult to melt in the DSF platform. To investigate this possibility, R120G αB-crystallin and wild type αB-crystallin were heated in the ThermoFluor® DSF platform. Consistent with the model, the apparent T_m of wild type αB-crystallin was 64.1 ± 0.5 °C, whereas the T_m of the R120G αB-crystallin mutant was 68.3 ± 0.2 °C (Figure 3.3). Based on these observations, we hypothesized that molecules able to reduce the apparent T_m of R120G αB-crystallin might be good candidates for suppressing its aggregation.

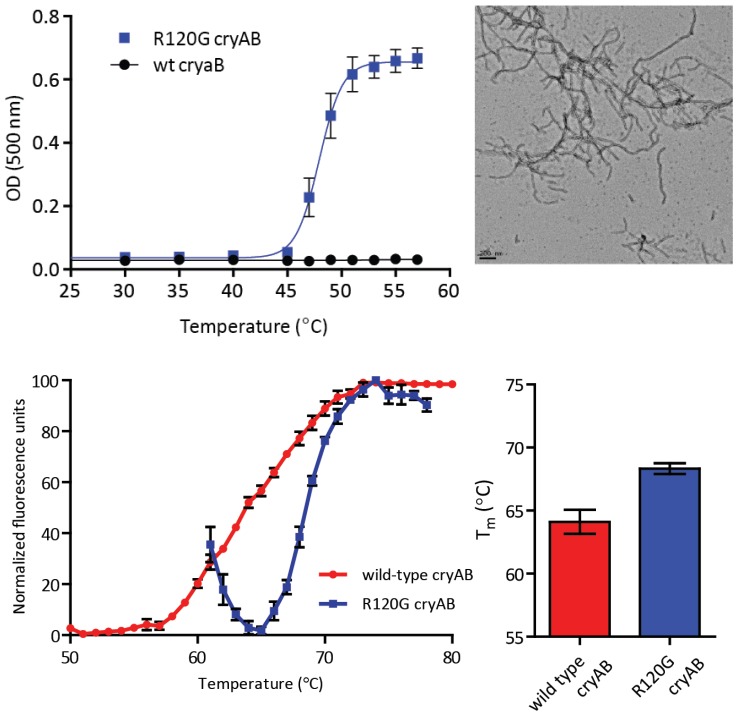

Figure 3.3. R120G αB-crystallin readily aggregates upon heating to form amyloid fibrils, while wild type protein remains soluble and transparent. In the differential scanning fluorimetry platform, R120G αB-crystallin melts at a higher temperature than the wild type protein.

For the pilot screens, we used the model human sHSP, Hsp27 (HSPB1). Hsp27 was used because it retains the highly conserved crystallin domain found in all sHSPs and because it produces a well-behaved, relatively high melting transition (T_m = 72 °C by differential scanning fluorimetry, variable temperature circular dichroism, and differential scanning calorimetry). Using Hsp27, we developed a robust and reproducible DSF protocol, with Z' factor values between 0.5 and 0.8 and an average coefficient of variation (CV) of 8% at a final volume of only 7 µL. Accordingly, we screened ~2,450 compounds from the MS2000 and NCC collections of known bioactive molecules in 384-well plates at a screening concentration between 20 and 40 µM. The primary screen identified 45 compounds (1.8%) that decreased the apparent T_m by at least three standard deviations (± 0.6 °C) (Figure 3.4). All 45 of these "actives" were explored in dose dependence experiments and we found that 32 (71%; 1.3% overall) decreased the T_m at concentrations less than 20 µM. Strikingly, twelve of the 32 confirmed actives belonged to a single class of related sterols, so we selected this scaffold for further investigation.

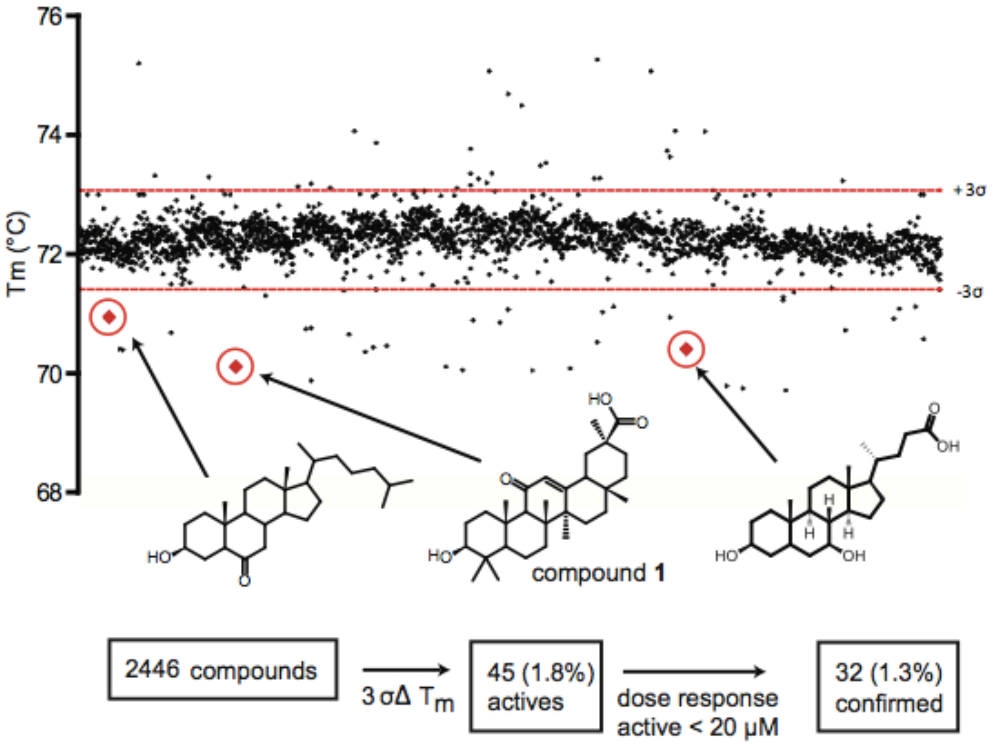

Figure 3.4. Summary of DSF screen against Hsp27. The structures of three active sterols are shown.

To test whether the sterols also had activity against R120G αB-crystallin, we collected 64 analogs with chemical structures related to sterol 1 and screened them against R120G αB-crystallin using the DSF procedure. Two compounds (28; 5a-cholestan-3b-ol-6-one and 29; 5-cholesten-3b,25-diol (Figure 3.5)) were at least 2- to 3-fold more potent than sterol 1, reducing the apparent T_m of R120G αB-crystallin by at least 2 °C. Compounds 28 and 29 also partially recovered normal melting behavior in R120G αB-crystallin samples, such that they resembled that of the more soluble, wild type αB-crystallin (Figure 3.6). Many of the other closely related sterols were inactive (e.g. compound 16 (Figure 3.5)) suggesting a specific interaction.

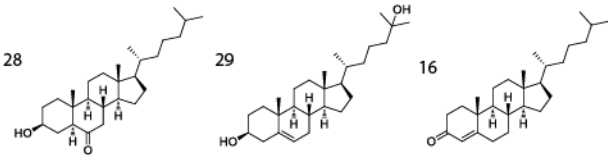

compound	Tm (% recovery vs. wild type) 100 μM	25 μM
28	83 ± 29%	32 ± 14%
29	56 ± 7.6%	31 ± 6.3%
16	-3.4 ± 2.5%	-1.1 ± 3.1%

Figure 3.5. Structures of compounds 28, 29, and negative control 16 and associated percent recoveries in T_m.

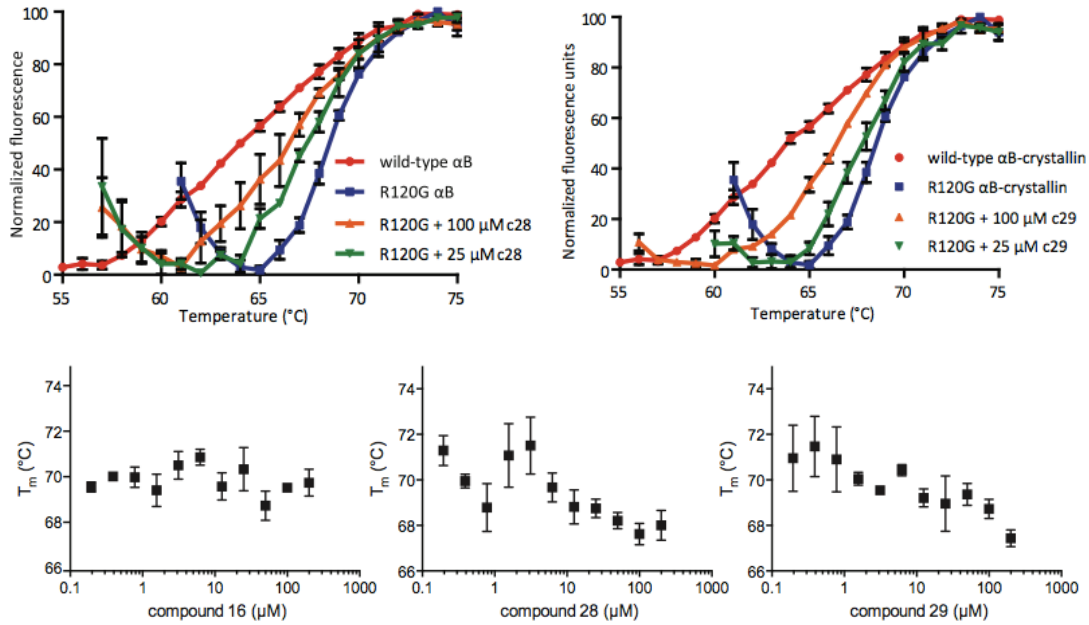

Figure 3.6. Compounds 28 and 29, but not the control compound 16, bound to the protein and recovered the T_m of R120G αB-crystallin. Results are the average of at least triplicates and error is SEM.

To confirm the direct interaction of compound 29 with R120G αB-crystallin, we used biolayer interferometry (BLI) to determine that it binds with a K_D of 10.1 ± 4.4 μM (Figure 3.7), while compound 16 did not detectably bind up to 50 μM.

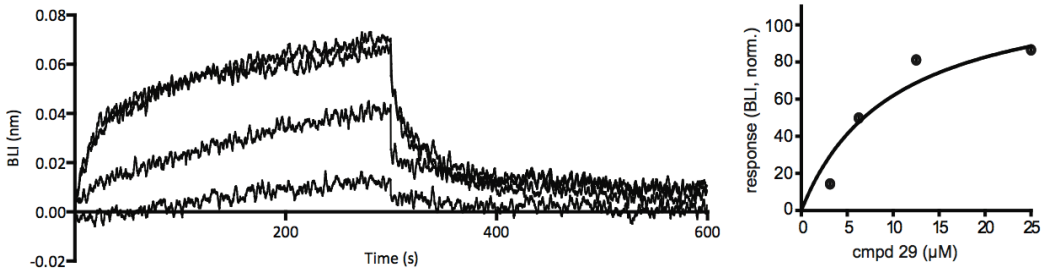

Figure 3.7. Binding of compound 29 to immobilized R120G αB-crystallin by BLI. Raw plots (left) and analysis of the binding at equilibrium (right) are shown. Results are representative of experiments performed in duplicate.

To examine where on R120G αB-crystallin this interaction takes place, we used ^{1}H, ^{15}N-HSQC NMR experiments to show that compound 29, but not compound 16, bound to the crystallin domain at the dimer interface (Figure 3.8). These results suggest that it might help stabilize the interface that is disrupted by the R120G mutation. Indeed, a docked model of compound 29 bound to the αB-crystallin core domain dimer (PDB 2WJ7) makes productive interactions with backbone amides in both protomers in the dimer (Figure 3.9); the C-3 hydroxyl hydrogen bonds with the N-terminus of one protomer and the C-25 hydroxyl hydrogen bonds with the backbone

carbonyl of an aspartic acid residue at position 80 in the other protomer. The N-terminal methionine is replaced with a serine residue in the context of the full-length protein, which may fulfill the hydrogen bond with the C-3 hydroxyl.

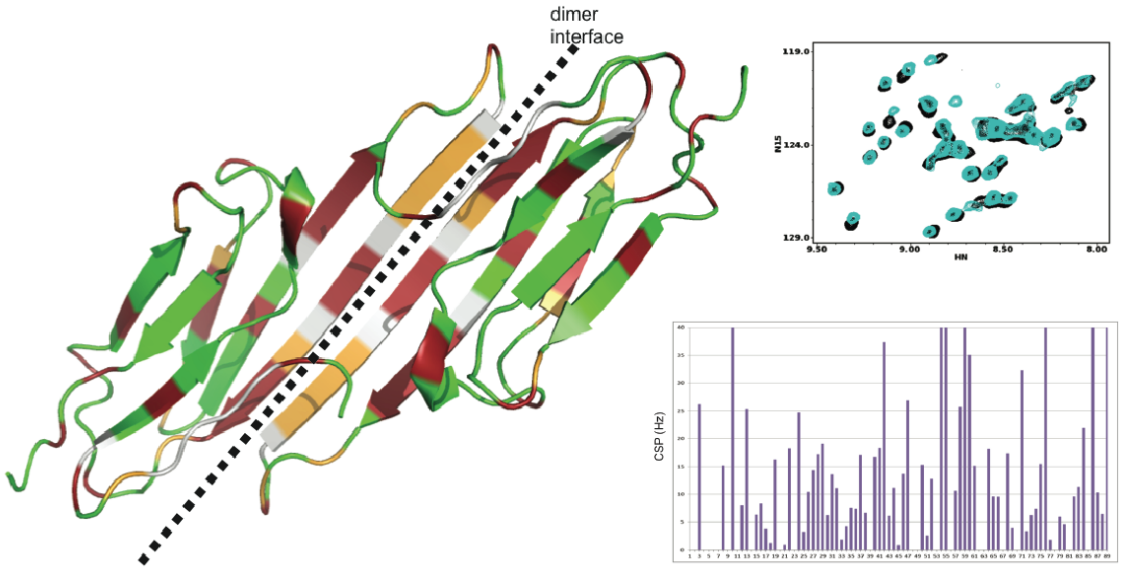

Figure 3.8. Compound 29 binds the dimer interface of R120G αB-crystallin. HSQC NMR titrations were performed on the ^{15}N-labelled crystallin domain of cryAB. Residues that underwent a significant chemical shift perturbation (>15 Hz) are shown in red. These residues clustered around the dimer interface. CSP: $(\Delta HN^2 + \Delta^{15}N^2)^{1/2}$. Compound 16 did not perturb residues with CSP >15 Hz.

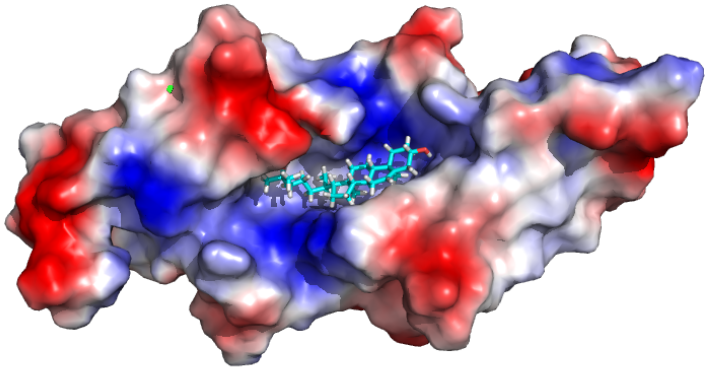

Figure 3.9. Docked model of compound 29 in the cleft bridging the αB-crystallin dimer interface. The compound makes interactions with both protomers, bridging the dimer. Surface areas of negative and positive charge are indicated in red and blue, respectively.

3.5. Compound 29 can prevent and reverse amyloid formation *in vitro*

To test whether compounds from our screening campaign might reduce amyloid formation *in vitro*, recombinant R120G αB-crystallin (15 μM) was treated with compounds 29 or 16 (100 μM)

and the extent of aggregation was examined by electron microscopy (EM). These studies confirmed that compound 29, but not 16 or the vehicle control, dramatically suppressed amyloid formation when added prior to the initiation of aggregation (Figure 3.10). To test whether 29 might also have an effect on pre-formed aggregates, we generated R120G αB-crystallin amyloids and treated them with compounds 29 or 16. Again, compound 29, but not 16, was able to reverse amyloid formation (Figure 3.10). The reversal took approximately two days, suggesting a slow equilibrium between the fibrillar amyloid and the soluble forms of αB-crystallin. To quantify these anti-aggregation activities, we again treated R120G αB-crystallin with 29 or 16, removed the insoluble material by centrifugation and measured the amount of remaining soluble protein using BCA assays. Consistent with the EM results, compound 29, but not 16 or the vehicle control, significantly improved the solubility of αB-crystallin when added either before or after aggregation (Figure 3.10). Together, these results show that compound 29 can block aggregation and reverse R120G αB-crystallin insolubility *in vitro*.

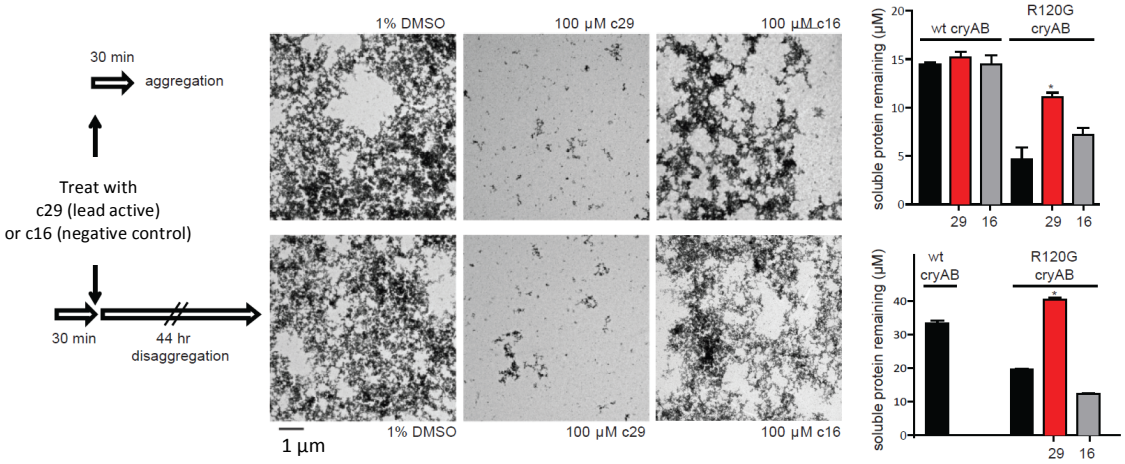

Figure 3.10. Purified R120G αB-crystallin (20 µM) was treated with compound 29 (100 µM), 16 (100 µM) or a DMSO control (1%) and then aggregated at ambient temperature with shaking for 30 minutes for the aggregation study. For the disaggregation study, amyloid fibrils were formed using the conditions above (40 µM) and then the samples were treated with 100 µM compound. Aliquots were visualized at 44 hours after treatment. Samples were visualized by electron microscopy and then centrifuged to remove insoluble material. The remaining soluble R120G αB-crystallin was assessed by absorbance at 280 nm. Results are the average of independent triplicates and the error bars represent SEM. Electron micrographs are representative of independent triplicates. Scale bar is 1 µm.

3.6. Compound 29 can reverse aggregation *in vivo* in R120G knock-in mice and *ex vivo* in human cataract tissue

The R120G αB-crystallin knock-in mouse develops severe age-associated cataracts, with 100% showing lens opacities by 20 weeks of age (21). To test whether compound 29 can reverse this process, it was delivered to the right eye of R120G αB-crystallin knock-in mice (aged 20 weeks)

from a 5 mM cyclodextrin solution via eye-dropper three times per week for two weeks. Treated eyes had a greater number of clear areas when observed by slit lamp biomicroscopy (Figure 3.11). In the heterozygous R120G αB-crystallin +/- mice, 25 of 30 mice (83%) had improved transparency in the treated lenses, while 6 of 7 (86%) of the homozygous R120G αB-crystallin -/- mice were improved. Compound 16 (5 mM) had no significant effect on lens transparency in three treated R120G αB-crystallin -/- animals, consistent with the results of the *in vitro* studies. To test whether compound 29 could restore crystallin solubility, we separated the soluble and insoluble fractions from the eye lens by centrifugation and measured the amount of crystallins (α, β and γ) by gel permeation chromatography (GPC). We found that compound 29 dramatically improved the solubility of all the α-crystallins by 63% (Figure 3.12). To verify this finding using a different method, we measured the total amount of water-soluble protein in a subset of the treated lenses by BCA assays. Although cataracts and the amount of total insoluble lens protein are only indirectly related (2), an improvement in overall protein solubility might be expected for compounds that have a particularly striking anti-aggregation activity. We found that compound 29 increased the ratio of soluble to total protein by 16 ± 5% (Figure 3.12).

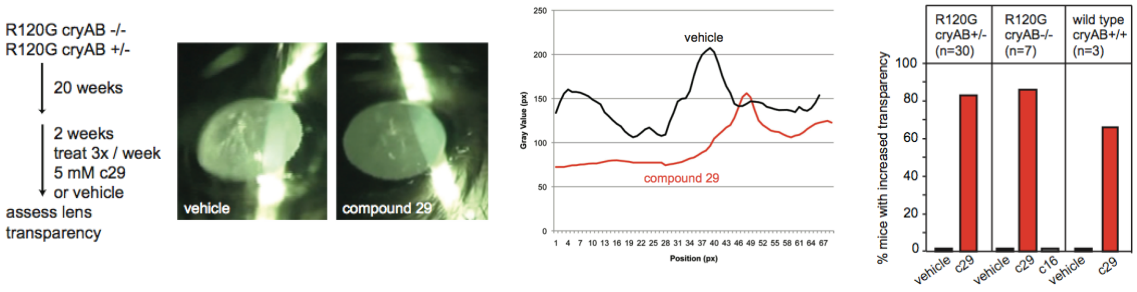

Figure 3.11. Representative image from animals treated in the right eye with compound 29 (1 drop of 5 mM cyclodextrin solution) and in the left eye with vehicle three times per week for 2 weeks. Treated animals were scored using slit lamp biomicroscopy, images were quantified using ImageJ, and the percent of animals that had improved transparency was quantified. Compound 29 improved transparency in homozygous, heterozygous and aged, wild type mice.

Hereditary cataracts are relatively rare in humans, so we next wanted to explore whether compound 29 might have an effect on the more prevalent, age-related cataracts. Three C57BL/6J wild type mice (aged 233 days) with spontaneous opacities were treated with compound 29 by eye-dropper for two weeks and then examined by slit lamp biomicroscopy. We found that compound 29, but not vehicle control, improved transparency in two of the three mice (Figure 3.10). Finally, we collected lens material from human patients (aged 70 to 80 years) and treated with either vehicle or compound 29 for six days. Compound 29, but not the vehicle,

significantly improved the ratio of soluble protein by 21 ± 13%, as assessed by BCA assays (Figure 3.11). Thus, compound 29 may be a promising lead towards the non-surgical treatment of both hereditary and age-associated cataracts.

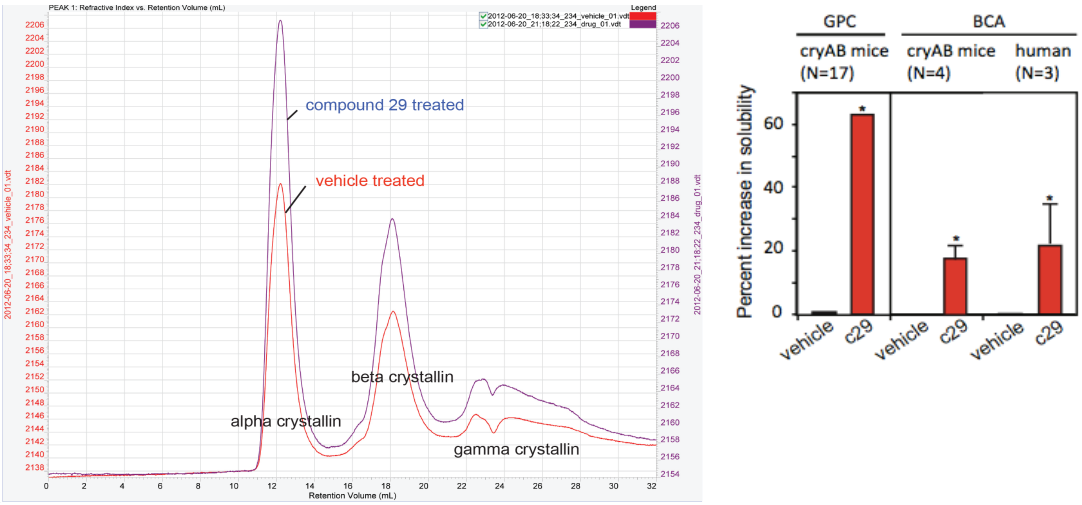

Figure 3.12. Treatment with compound 29 improves the solubility of α, β, and γ-crystallins in mouse lenses as measured by gel permeation chromatography. Compound 29 improves total protein solubility in mouse and human lenses as measured by BCA.

3.7. Conclusions and outlook

The R120G mutation abrogates two salt bridges that normally contribute to the stability of the dimer interface, resulting in a dramatically increased propensity to aggregate into amyloid fibrils. As discussed in Chapter 2, one model for the effect of this mutation is that it decreases the stability of the dimer interface, resulting in an increased proportion of free monomer, which is intrinsically unstable and rapidly forms amyloids (Figure 3.13).

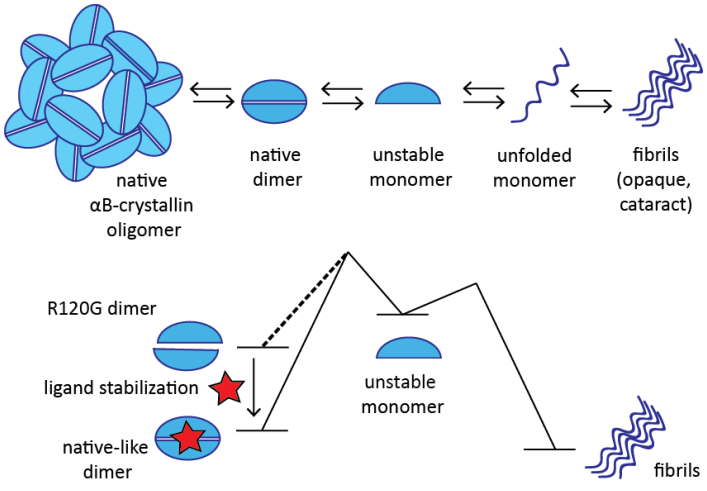

Figure 3.13. Model for the action of compound 29 as a pharmacological chaperone.

Ligand binding across this interaction surface appears to restore native-like stability to the dimer, preventing its dissociation to unstable monomer and preventing its subsequent aggregation. Likewise, compound 29 binding also appears to favor reversal of the aggregation process. This suggests that monomers can slowly dissociate from fibrils and re-form soluble dimers with the added stability of ligand binding. Together, this model suggests that compound 29 is the first pharmacological chaperone (PC) for αB-crystallin. These findings suggest that DSF-based HTS campaigns might be used to identify PCs with activity against other "undruggable" targets.

3.8. Experimental Procedures

3.8.1. Protein purification

N-terminal hexahistidine-tagged human heat shock protein 27 (His_6Hsp27) was expressed in *Escherichia coli* BL21 cells using the pET 28b vector. Human, wild-type αB-crystallin and R120G αB-crystallin were purified in *E. coli* Rosetta cells using the pMCSG7 vector. Cultures of transformed cells were grown to an optical density of 0.8 AU at 600 nm in lysogeny broth media supplemented with 50 μg/mL kanamycin (pET 28b) or ampicillin (pMCSG7) at 37 °C. Cultures were induced with 500 μM IPTG and incubated at 30 °C for 8 to 16 hours. After incubation, cells were harvested by centrifugation and suspended in 1/25 culture volume of lysis buffer (20 mM Tris pH 8.0, 100 mM NaCl, 6 M urea, 5 mM β-mercaptoethanol, 15 mM imidazole). The suspension was sonicated on ice and insoluble material removed by centrifugation. The supernatant was loaded onto Ni-NTA resin (10 mL/L culture volume) and washed with 10 column volumes of wash buffer (lysis buffer containing 30 mM imidazole). The proteins were eluted with elution buffer (lysis buffer with 150 mM imidazole) and the fractions containing protein were pooled. EDTA was added to 5 mM, and the unfolded protein was concentrated to ~20 mg/mL in 10 kDa MWCO Amicon centrifugal filter units. The proteins were refolded by injecting 1 mL samples of concentrated protein onto a Superdex 200 HR 10/30 column equilibrated with refolding buffer (20 mM sodium phosphate, pH 7.2, 100 mM NaCl) at room temperature. The refolded protein eluted as an oligomer (~24-mer) with a diameter of ~165 Å, consistent with previous literature values (22). Protein was concentrated to ~10 mg/mL before flash freezing and storing at -80 °C. The melting temperature (T_m) of Hsp27 by both circular dichroism and differential scanning calorimetry was 72°.

3.8.2. High throughput DSF screen

The screen was performed using a Thermofluor® instrument (a generous gift from Johnson & Johnson) in Abgene black 384-well PCR plates. Each well received 7 µL of 10 µM Hsp27 in 50 mM $NaPO_4$, pH 7.4, 700 mM NaCl, 50 mM LiCl, and 100 µM 1,8-ANS, with test compounds added via pin tool (200 nL) to achieve final concentrations between 20 to 40 µM (1% DMSO). The chemical library was composed of the Spectrum MS2000 and NCC collections of known bioactives. Reactions were covered with silicon oil to limit evaporation. The plates were measured in up/down mode, which was empirically determined to give better signal-to-noise than the continuous ramp mode. Plates were heated from 65 °C to 80 °C in 1 °C increments, equilibrated for 130 seconds at each high temperature, cooled to 25 °C, and held for 10 sec at 25 °C prior to imaging with a single 10 second exposure for each temperature reading. Plate uniformity tests measured the T_m of Hsp27 at 72.3 ± 0.16 °C. The Z factor was calculated to vary between ~0.59 and 0.71 and the CVs were 8%. Treatments that reduced the apparent T_m by 3 standard deviations were considered actives. For αB-crystallin and R120G αB-crystallin differential scanning fluorimetry experiments, a similar protocol was used, but the buffer contained 50 mM $NaPO_4$ pH 7.4, 350 mM NaCl, 25 mM LiCl, and 100 µM 1,8-ANS. In all cases buffers were empirically optimized to give the best melting curve shape and signal to noise.

3.8.3. HTS data analysis

The output of the differential scanning fluorimetry assay is a set of fluorescence intensities at increasing temperatures for each well. We found that a single curve-fitting algorithm will occasionally misidentify the T_m for a well. Accordingly, we minimized this problem by applying three distinct data fitting routines to the same data and using the resulting T_m values as pseudo-replicates. Two curve fitting routines were performed using the ThermoFluor® analysis software (version 1.3.7): a sigmoidal curve fit option was used with non-constant y-upper and y-lower slopes and constant dCp = 2500, and a derivative curve fit with a polynomial degree = 2 and filter points = 3. The third method used a non-linear least squares regression to fit a version of the Hill equation that allows for non-horizontal, parallel baselines. The three curve-fitting methods were used to analyze each melting curve, and wells were scored based on how closely the three fits agreed. Hit wells were then visually inspected as well, since the size of the library screened was relatively small.

3.8.4. Light scattering assay of protein aggregation

Purified recombinant wild type or R120G αB-crystallin was thawed on ice and diluted to 10 μM in 50 mM Na_2PO_4 pH 7.4, 350 mM NaCl, and 25 mM LiCl (differential scanning fluorimetry buffer). The protein was heated in a thermocycler for 130 seconds to each temperature point, then 25uL was transferred to a 384-well clear bottom plate and the absorbance at 500 nm was measured using a SpectraMax M5 microplate reader.

3.8.5. Electron microscopy

Purified recombinant R120G αB-crystallin was thawed on ice, diluted to 15 μM and treated with either solvent (1% DMSO) or 100 μM compound **29**, then incubated for 30 min at ambient temperature before applying to glow-discharged Formvar/carbon 300-mesh copper grids (Electron Microscopy Sciences) and staining with 2% uranyl formate. Grids were visualized on a Phillips CM-100 transmission electron microscope at an accelerating voltage of 80 kV with magnification settings ranging from 10500–92000×. Shown are representative images and at least 12 random fields were imaged per treatment condition. Scale bars represent 1 μm. Disaggregation experiments were performed similarly. R120G αB-crystallin was incubated at ambient temperature for 30 minutes and then a sample of this solution was visualized by EM to ensure fibril formation. The aggregated αB-crystallin was treated with either solvent (1% DMSO) or compound 29 (100 μM) and incubated an additional 44 hours at ambient temperature. No change in amyloid structure or prevalence was observed in the vehicle control between the 44 hour and 30 minute time points.

3.8.6. Binding to αB-crystallin by biolayer interference (BLI)

R120G αB-crystallin (100 μL of 2.2 mg/mL) was reacted with a twenty fold excess of NHS-PEG_4-biotin (Thermo Scientific) in DMSO for two hours at 4 °C with gentle rocking. The excess biotinylation reagent was then removed by dialysis against phosphate buffer (20 mM Na_2PO_4 pH 7.2, 100 mM NaCl) at 4 °C for 20 hours. To measure the affinity of compounds for this protein, the biotinylated R120G αB-crystallin was then immobilized on super-streptavidin pins (ForteBio) as follows: pins were first equilibrated in phosphate buffer for ~10 min before moving them to wells containing either 200 μL 150 μg/mL biotinylated His_6-R120G αB-crystallin or 200 μL 100 μg/mL biocytin for 60 min. The pins were washed in buffer for 5 min, free streptavidin sites were quenched with 100 μg/mL biocytin for 10 min, and the pins were washed again for at least 5 min

prior to beginning an experiment. All immobilization steps were carried out on-line on a ForteBio Octet Red96 instrument with 1000 rpm rotary shaking throughout. Approximately 7 nm of biolayer interference shift was consistently obtained from R120G αB-crystallin immobilization under these conditions. For each experiment, compounds were first diluted into phosphate buffer and the final DMSO concentration was held constant at 1%. Compounds were incubated with the pin surface for 5 min and tested from high to low concentration and then the experiments repeated from low to high concentration. Between experiments, pins were stored in phosphate buffer at 4 °C, and 50 µM compound **29** was used as a positive control at the beginning of each experiment to ensure the quality of the surface. Binding data was analyzed using the ForteBio software, version 7.0. Binding curves were aligned to the association phase from 0.2-0.4 s and either a matched concentration, biocytin-blocked pin response or a DMSO-only. The R120G αB-crystallin-pin response was subtracted for each compound concentration to correct for drift and bulk solvent effects. The association response from 290-300 sec was averaged for each binding curve and used to estimate the equilibrium binding affinity. Data were fit in GraphPad Prism, version 5.04, using a one-site specific binding model. The weighted mean and weighted standard deviation of the apparent K_d values across multiple experiments was calculated using

$$\bar{x} = \frac{\sum_{i=1}^{n} \frac{x_i}{\sigma_i^2}}{\sum_{i=1}^{n} \frac{1}{\sigma_i^2}} \text{ and } \sigma_{\bar{x}}^2 = \frac{1}{\sum_{i=1}^{n} \frac{1}{\sigma_i^2}}.$$

3.8.7. NMR

^{15}N-R120G αB-crystallin a-crystallin domain (ACD) was expressed and purified as described previously (23). Resonances in R120G-ACD have been assigned by standard NMR techniques. HSQC spectra were acquired on a Bruker Avance III 500 MHz spectrometer equipped with a triple resonance, z-axis gradient probe. 10 mM stock solutions of compounds **29** and **16** were made in deuterated DMSO. Spectra were acquired on a sample containing 100 µM R120G-ACD and either 1 mM compound **29** or compound **16** and compared to a reference spectrum of ^{15}N-R120G-ACD containing 20% DMSO to match the solution conditions. 256 scans were acquired per t_1 value for a total of 200 t_1s at a temperature of 32 °C. Spectral widths of 6009 Hz and 1419 Hz were used in the ^{1}H and ^{15}N dimensions, respectively. Spectra were processed with NMRPipe (24) and analyzed with NMRView (25).

3.8.8. Docking

The published crystal structure of the core domain of αB-crystallin (PDB ID 2WJ7 (26)) was minimized in solvent using OpenEye FreeForm software and c29 was docked using UCSF Dock (27) with flexible docking parameters.

3.8.9. Animals and lenses

R120G αB-crystallin knock-in mice expressing an A to G point mutation in codon 120 of mouse αB-crystallin which results in the substitution of arginine 120 with glycine (R120G) were generated as described previously (21). These mice are in the C57BL/6J background (Jackson Laboratories, Bar Harbor ME). Mice were maintained at Washington University School of Medicine in the Division of Comparative Medicine by trained veterinary staff. All protocols and procedures involving mice were approved by the Washington University Animal Studies Committee and performed by Mouse Genetics Core. Mice were euthanized by CO_2 inhalation and lenses were immediately dissected and used for analysis.

3.8.10. Treatment of mice

Wild type or R120G αB-crystallin knock-in mice were treated with vehicle (40% cyclodextrin in PBS) or compound **29** dissolved in vehicle to make 5 mM solutions. The drops were administered in six doses over two weeks, coinciding with each Monday, Wednesday, and Friday during the period of experimentation. To the left eye of each animal was administered one drop of vehicle so that the drop coated the eye. One drop of compound **29** was administered to the right eye of each animal in the same manner.

3.8.11. Slit lamp biomicroscopy

Mice were examined by slit lamp biomicroscopy on the day following final dosing. Prior to observation, pupils were dilated with 1% Topicamide Ophthalmix Solution, USP and 10% Phenylephrine Hydrochloride Solution, USP in a 9:1 ratio. The slit was positioned directly orthogonal to the mouse for best delineation of opacities and clear areas in the lens. Videos from each eye were recorded on a Sony DCR-DVD403 3MP DVD Handycam Camcorder w/10x Optical Zoom with Carl Zeiss Vario-Sonnar Super Steady Shot (Sony, Tokyo) using the camcorder attachment on the slit lamp. Night-mode was used for best identification of opacities. Still images were then extracted from each video using Topaz Moment (Topaz Labs, Dallas TX) and

selected images were analyzed for intensity of light (as gray value across a selected cross section) using the ImageJ program (http://rsb.info.gov/ij). Plot profiles were produced along horizontal and vertical cross sections of each image. Improvements in transparency were qualitatively scored by visual analysis.

3.8.12. Measurement of water-soluble lens crystallins

The control and drug eyes from each mouse were removed and the lenses excised. Lenses were either placed in a unique microcentrifuge tube with 1 mL PBS and 1:1000 protease inhibitor cocktail (Sigma, St. Louis MO), or in two instances were pooled with lenses from other mice. The lenses were homogenized using disposable grinders before centrifugation for one hour at 10,000 rpm. The samples were kept at 4 °C for the entire process. After centrifugation, the soluble fraction (supernatant) was collected filtered through a 0.22 µm filter, transferred to a vial and analyzed by gel permeation chromatography using the TDA305 detector with GPXMax injection system (Malvern, Worcestershire, UK). The system provided refractive index, ultraviolet absorbance at 280 nm, viscosity, and right and low-angle-light-scattering readings after each sample passed through a P3000 and P2500 column (Malvern). PBS was used as the mobile phase and the system was calibrated with bovine serum albumin (Sigma) as a standard. The results were displayed using OmniSec 4.7 software (Malvern). Gel permeation chromatography data were analyzed using SAS version 9.3 (SAS Institute; Cary, NC). The effect of compound **29** on the level of soluble crystallins was expressed as the percent difference in area between the treated and untreated fellow eyes. To control for differences in assay sensitivity among animals, the area under the curve in the treated eye was compared to the area in the corresponding, untreated eye and expressed as percent difference. The percent difference between treated and untreated was compared using the Wilcoxon signed rank test for the null hypothesis of no difference. The association between age and percent difference was calculated using the Spearman rank correlation coefficient. Non-parametric statistical models were used to protect from departures from normality.

3.8.13. Treatment and analysis of human lenses

Human lenses (HL) used in this study were obtained from unidentified patients (70-80 years old). A total of three lenses were obtained (HL1-3). HL1 was from an individual undergoing extracapsular cataract surgery and a preoperative clinical exam was used to classify the cataract

as mixed cortical and nuclear 3-4 l. The material had been classified as non-human discarded material. HL2 and HL3 were obtained from a deceased patient. Each lens was cut into four nearly equal parts and placed in individual tubes. To each tube was added 50 µL solution of vehicle (40% cyclodextrin in PBS containing 1:1000 protease inhibitor cocktail) or compound **29** (1 mM) in vehicle which covered the lens tissue completely. Lens tissue was incubated in these solutions for 6 days in the dark at room temperature. On the last day, the tissue was homogenized after addition of 200 µL PBS. An aliquot (40 µL) was removed and centrifuged for one hour at 10,000 rpm at 4°C, from which the supernatant was collected. Protein content in the supernatant and total homogenate was measured in triplicate using the BCA kit. The ratio of water soluble to total protein was then calculated.

3.9. Notes

A portion of this chapter is in preparation for publication as McMenimen KA*, Makley LN*, Wilson B, DeVree BT, Goldman JW, Rajagopal P, McQuade TJ, Thompson AD, Sunahara R, Klevit RE, Andley UP, and Gestwicki JE, Pharmacological Reversal of Cataracts Caused by an Amyloid-Prone Small Heat Shock Protein. The Klevit laboratory performed the NMR binding studies. The Andley laboratory carried out all mouse experiments and human lens treatments. Brian DeVree performed the original ThermoFluor screen against Hsp27 and developed the data analysis method. Andrea Thompson visualized αB-crystallin amyloid by electron microscopy. The ThermoFluor instrument was a generous gift from Johnson & Johnson, and the original 32-member sterol library was a kind gift from Roger Sunahara. Bryan Dunyak performed docking with compound 29.

3.10. References

1. Leibowitz HM, Krueger DE, Maunder LR, Milton RC, Kini MM, Kahn HA, et al. The Framingham Eye Study monograph: An ophthalmological and epidemiological study of cataract, glaucoma, diabetic retinopathy, macular degeneration, and visual acuity in a general population of 2631 adults, 1973-1975. Survey of ophthalmology. 1980;24(Suppl):335-610.
2. Bloemendal H, de Jong W, Jaenicke R, Lubsen NH, Slingsby C, Tardieu A. Ageing and vision: structure, stability and function of lens crystallins. Progress in biophysics and molecular biology. 2004;86(3):407-85.
3. Haslbeck M, Franzmann T, Weinfurtner D, Buchner J. Some like it hot: the structure and function of small heat-shock proteins. Nat Struct Mol Biol. 2005;12(10):842-6.
4. Al-Ghoul KJ, Nordgren RK, Kuszak AJ, Freel CD, Costello MJ, Kuszak JR. Structural evidence of human nuclear fiber compaction as a function of ageing and cataractogenesis. Experimental eye research. 2001;72(3):199-214.

5. Meehan S, Berry Y, Luisi B, Dobson CM, Carver JA, MacPhee CE. Amyloid fibril formation by lens crystallin proteins and its implications for cataract formation. The Journal of biological chemistry. 2004;279(5):3413-9.
6. Meehan S, Knowles TP, Baldwin AJ, Smith JF, Squires AM, Clements P, et al. Characterisation of amyloid fibril formation by small heat-shock chaperone proteins human alphaA-, alphaB- and R120G alphaB-crystallins. Journal of molecular biology. 2007;372(2):470-84.
7. Pande A, Pande J, Asherie N, Lomakin A, Ogun O, King J, et al. Crystal cataracts: human genetic cataract caused by protein crystallization. Proc Natl Acad Sci U S A. 2001;98(11):6116-20.
8. Vicart P, Caron A, Guicheney P, Li Z, Prevost MC, Faure A, et al. A missense mutation in the alphaB-crystallin chaperone gene causes a desmin-related myopathy. Nature genetics. 1998;20(1):92-5.
9. Moreau KL, King JA. Protein misfolding and aggregation in cataract disease and prospects for prevention. Trends Mol Med. 2012;18(5):273-82.
10. Cohen FE, Kelly JW. Therapeutic approaches to protein-misfolding diseases. Nature. 2003;426(6968):905-9.
11. Hammarstrom P, Wiseman RL, Powers ET, Kelly JW. Prevention of transthyretin amyloid disease by changing protein misfolding energetics. Science. 2003;299(5607):713-6.
12. Sawkar AR, D'Haeze W, Kelly JW. Therapeutic strategies to ameliorate lysosomal storage disorders--a focus on Gaucher disease. Cell Mol Life Sci. 2006;63(10):1179-92.
13. Fan JQ, Ishii S. Active-site-specific chaperone therapy for Fabry disease. Yin and Yang of enzyme inhibitors. FEBS J. 2007;274(19):4962-71.
14. Makley LN, Gestwicki JE. Expanding the number of 'druggable' targets: non-enzymes and protein-protein interactions. Chemical biology & drug design. 2013;81(1):22-32.
15. Burns JN, Orwig SD, Harris JL, Watkins JD, Vollrath D, Lieberman RL. Rescue of glaucoma-causing mutant myocilin thermal stability by chemical chaperones. ACS Chem Biol. 2010;5(5):477-87.
16. Cummings MD, Farnum MA, Nelen MI. Universal screening methods and applications of ThermoFluor. J Biomol Screen. 2006;11(7):854-63.
17. Fedorov O, Niesen FH, Knapp S. Kinase inhibitor selectivity profiling using differential scanning fluorimetry. Methods Mol Biol. 2012;795:109-18.
18. Major LL, Smith TK. Screening the MayBridge Rule of 3 Fragment Library for Compounds That Interact with the Trypanosoma brucei myo-Inositol-3-Phosphate Synthase and/or Show Trypanocidal Activity. Molecular biology international. 2011;2011:389364.
19. Lavinder JJ, Hari SB, Sullivan BJ, Magliery TJ. High-throughput thermal scanning: a general, rapid dye-binding thermal shift screen for protein engineering. Journal of the American Chemical Society. 2009;131(11):3794-5.
20. Michiel M, Skouri-Panet F, Duprat E, Simon S, Ferard C, Tardieu A, et al. Abnormal assemblies and subunit exchange of alphaB-crystallin R120 mutants could be associated with destabilization of the dimeric substructure. Biochemistry. 2009;48(2):442-53.
21. Andley UP, Hamilton PD, Ravi N, Weihl CC. A knock-in mouse model for the R120G mutation of alphaB-crystallin recapitulates human hereditary myopathy and cataracts. PloS one. 2011;6(3):e17671.
22. Dudich IV, Zav'yalov VP, Pfeil W, Gaestel M, Zav'yalova GA, Denesyuk AI, et al. Dimer structure as a minimum cooperative subunit of small heat-shock proteins. Biochim Biophys Acta. 1995;1253(2):163-8.

23. Jehle S, van Rossum B, Stout JR, Noguchi SM, Falber K, Rehbein K, et al. alphaB-crystallin: a hybrid solid-state/solution-state NMR investigation reveals structural aspects of the heterogeneous oligomer. J Mol Biol. 2009;385(5):1481-97.
24. Delaglio F, Grzesiek S, Vuister GW, Zhu G, Pfeifer J, Bax A. NMRPipe: a multidimensional spectral processing system based on UNIX pipes. J Biomol NMR. 1995;6(3):277-93.
25. Johnson BA, Blevins RA. NMR View: A computer program for the visualization and analysis of NMR data. J Biomol NMR. 1994;4(5):603-14.
26. Bagneris C, Bateman OA, Naylor CE, Cronin N, Boelens WC, Keep NH, et al. Crystal structures of alpha-crystallin domain dimers of alphaB-crystallin and Hsp20. Journal of molecular biology. 2009;392(5):1242-52.
27. Irwin JJ, Shoichet BK, Mysinger MM, Huang N, Colizzi F, Wassam P, et al. Automated docking screens: a feasibility study. Journal of medicinal chemistry. 2009;52(18):5712-20.

Chapter 4

Chemical Validation of Cryptic Binding Sites on Hsp27 using *In Silico* Solvent Mapping and Biophysical Methods

4.1. Abstract

In the post-genomic era, potential therapeutic targets accumulate genetic evidence that validates their utility in modifying the course of disease. Genetically validated targets do not necessarily possess small molecule modulators, known ligand binding sites, or even enzyme activity. Consequently, some non-enzymatic, non-receptor targets such as the small heat shock protein Hsp27 require *de novo* chemical validation. While Hsp27 is known to have disease-modifying properties, does it possess 'druggable' binding sites? Can the disease-modifying activity of Hsp27 be tuned using small molecules? Because of the complexity of this target, we designed a screening workflow in collaboration with the Carlson Laboratory that involved synergistic computational and experimental approaches to identify cryptic binding locations on Hsp27. We applied mixed solvent molecular dynamics (MixMD) to predict three possible binding sites in the core domain of Hsp27, which we confirmed and rank-ordered using an NMR-based solvent mapping scheme. Using this knowledge, we carried out an NMR-based fragment screen and a parallel peptide synthesis effort. The fragment based screen relied on ~1000 unbiased chemical fragments, while the peptide approach was based on a recently identified protein-protein interaction motif in Hsp27. Together, these approaches yielded three cryptic binding sites on Hsp27. Each of these sites was subject to medicinal chemistry efforts, and the results suggested that some of these sites are more amenable to tight binding than others. Finally, one site appears to be functionally important in maintaining the solubility of sHSPs. From these efforts, we have revealed previously uncharacterized ligand-binding sites on Hsp27 and gained insight into the allostery and function of this chaperone. These efforts also provide an informative head-to-head comparison of the emerging methods (described in Chapter 1) for finding inhibitors of 'undruggable' targets.

4.2. Structural aspects of small heat shock proteins

Hsp27 belongs to the superfamily of molecular chaperones responsible for maintaining proteostasis under stress conditions. Unlike the well known Hsp70 and Hsp90 families, Hsp27 has no intrinsic ATP hydrolyzing activity. Rather, it is known to bind its protein clients, and sequester them from self-association (aggregation) or degradation. Once the stress abates, Hsp27 can release its clients for active refolding by other chaperones. Structurally, small heat shock proteins consist of a highly conserved core immunoglobulin fold called the α-crystallin domain, flanked by less conserved and less ordered N- and C-terminal extensions (1, 2). The core α-crystallin domain forms a dimer at an antiparallel beta strand interface, and contacts in the N- and C-terminal extensions mediate higher ordered oligomerization. The ultrastructure of Hsp27 is regulated by heat shock, oxidative stress, and phosphorylation on N-terminal serine residues (3, 4). Quaternary structure dynamics control the bind-and-release properties of small heat shock proteins and allow for a high (up to equimolar) capacity for client binding (5). However, it is not clear which types of structures represent the active client-binding forms for important clients such as p53 or tau (6, 7). Moreover, Hsp27 exists as a polydisperse ensemble of large oligomers, which makes structural biology very challenging (5). Where should one place a small molecule to regulate Hsp27 structure and function? We sought to chemically validate Hsp27 as a 'druggable' protein and to make early steps towards the development of chemical probes of Hsp27 biology.

4.3. Atomic level structure of core α-crystallin domain of Hsp27

Based in part on homology with αB-crystallin, the Klevit laboratory succeeded in solving the solution structure of the core α-crystallin domain of Hsp27 by NMR spectroscopy. Thus, while no high-resolution structure of the full-length Hsp27 protein is available, we had access to atomic-level structural information for the central 98 amino acids. The monomeric unit of the protein has six β-strands that form an immunoglobulin fold or β-sandwich. The dimer interface consists of two β-strands that associate in an antiparallel fashion. Hsp27 has a single cysteine that is positioned in the dimer interface, and in the NMR structure the cysteine from one protomer is directly across from the cysteine from the other protomer in the so-called antiparallel II (APII) register of the dimer interface.

The dimeric core domain of sHsps is known to exhibit chaperone activity (1) and is also the domain that enables dimerization, which is disrupted in hereditary disease (8) and which therefore appears to be important for structure and stability. Therefore, we reasoned that this construct would be useful as a tractable starting point for small molecule discovery.

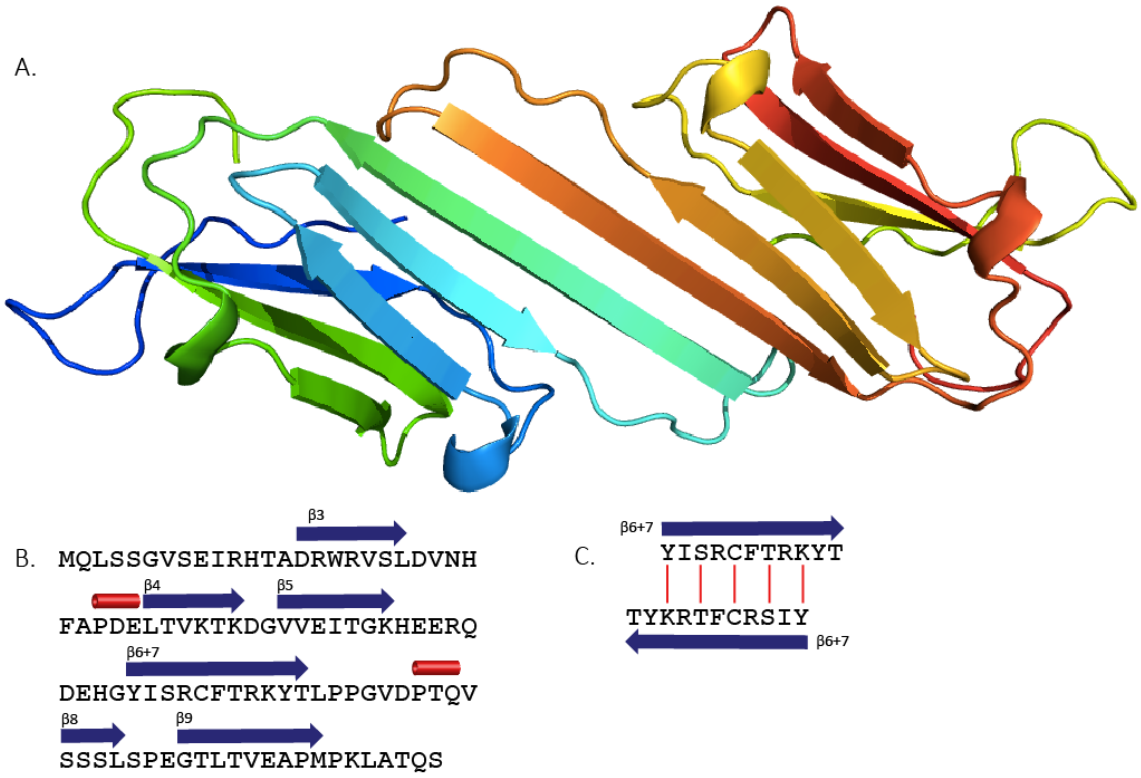

Figure 4.1. A. Solution NMR structure of Hsp27 αB-crystallin domain, residues 79-176. B. Features of the primary sequence of Hsp27 ACD. C. APII register of dimer interface showing residue pairing. Red lines indicate cross-strand hydrogen bonding pairs in the APII register.

4.4. Identification of binding sites within Hsp27's α-crystallin domain

A first step in identifying ligands is to identify potential small molecule binding sites on the target's surface. We chose to focus on the Hsp27 core domain, since we had access to a high-resolution structure of this construct, and because we hypothesized that the dimer would be a physiologically relevant target given its critical role in the substructure of Hsp27 oligomers (Chapter 2 and 4.2). Strategies for *de novo* binding site identification, including mixed-solvent molecular dynamics, were introduced in Chapter 1 (1.10). This technique uses a high-resolution structure in a virtual box of mixed aqueous and organic solvent molecules chosen to represent the typical physicochemical interactions a ligand makes with its target protein (*i.e.* hydrophobic, aromatic, and hydrogen bonding donating or accepting) (9). In a molecular dynamics simulation,

the solvent probes cluster at regions on the surface of the protein where each solvent can outcompete water, and these locations represent potential ligand binding pockets (9). We wanted to test the predictive power of the MixMD technique while using it to identify potential ligandable pockets in Hsp27's core domain. In this case, three probes were used: acetonitrile (hydrophobic), pyrimidine (aromatic), and isopropanol (hydrogen bond donating and accepting). This system was then minimized in a molecular dynamics simulation incorporating full protein flexibility. We interpreted the regions that were highly occupied by all three probes after 20 ns as sites that may be desolvated by small organic molecules. Three distinct binding sites were highly occupied by each of the three solvent probes. One of the sites, labeled Site 1 in the figure below, corresponds to a symmetry-related groove at the top of the dimer interface. The second site, labeled Site 2, appeared along the outer edge of the β-sandwich, in a pocket formed by the β4 and β8 strands. The third site occupies a concave pocket on the bottom of the dimer interface. These sites will be referred to as Site 1, Site 2, and Site 3 in the following discussion.

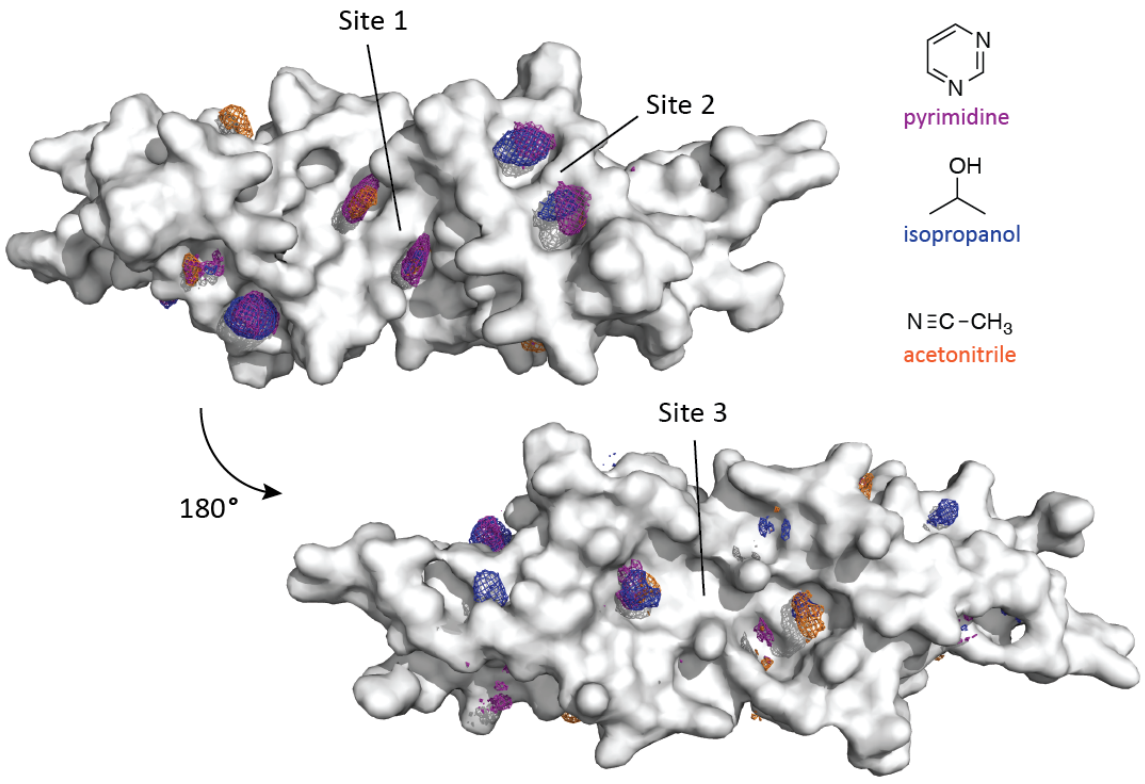

Figure 4.2. Surface rendering of NMR structure of Hsp27 αB-crystallin domain, showing three regions where each solvent probe was highly localized. The sites are labeled as indicated in the order in which they were occupied (i.e. site 1 was most highly occupied by all three solvents and site 3 was the least occupied).

4.5. Validation of MixMD result through equivalent NMR experiments and comparison with chemical shift perturbations

Using the construct of Hsp27's core domain that is well behaved in solution NMR experiments, the experimental equivalent of the MixMD simulation was carried out. Solvents (pyrimidine, isopropanol, or acetonitrile) were individually added to a solution of uniformly ^{15}N-labeled Hsp27 core domain at final concentrations ranging from 5 to 30 mM. Backbone chemical shift perturbations exceeding two standard deviations were considered to reflect a proximal solvent interaction. Significant chemical shift perturbations were seen upon titration with each solvent. Strikingly, these sites clustered around the corresponding solvent occupancy densities that were predicted from the MixMD simulations (Figure 4.3). Thus, both the computational and experimental studies suggested that there are at least three cryptic sites on Hsp27, referred to as Sites 1, 2 and 3.

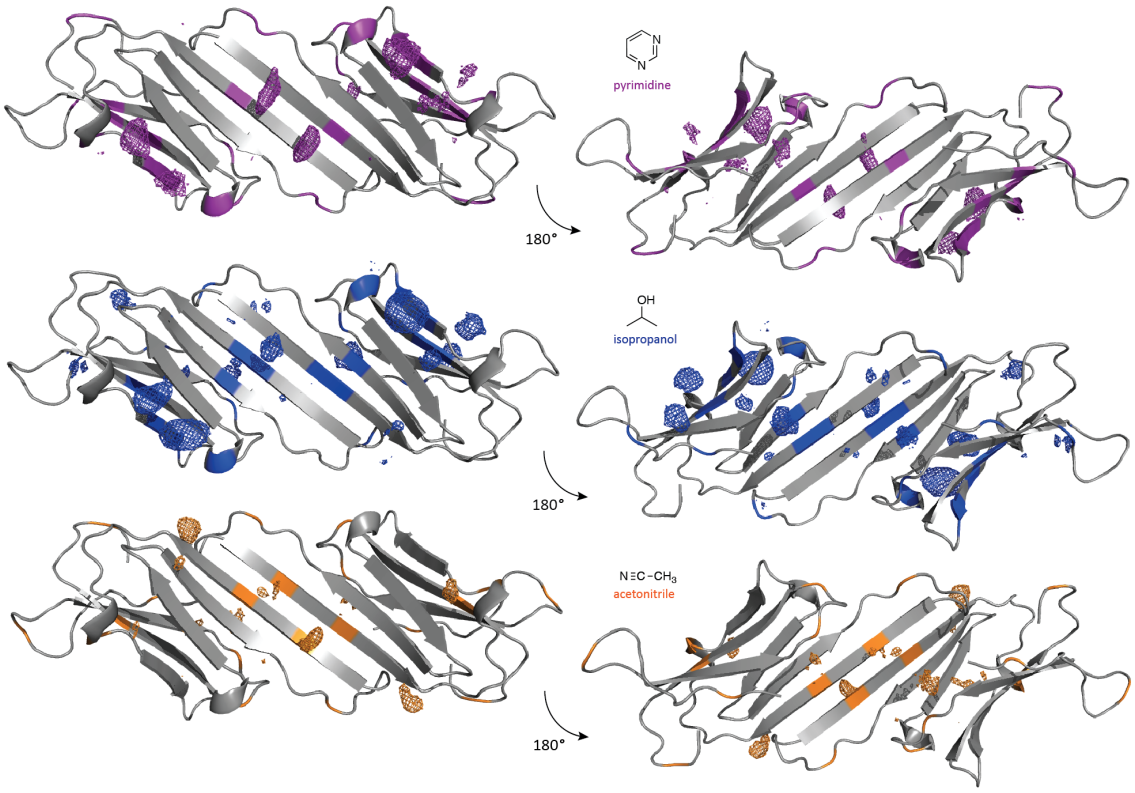

Figure 4.3. Cartoon rendering of NMR structure of Hsp27 αB-crystallin domain, showing MixMD solvent probe occupancy maps and backbone chemical shift perturbations for solvent mapping NMR experiment. Backbone shifts were considered significant if they exceeded two standard deviations of the 5 mM data set for each solvent. Significant shift perturbations are shown for the 10 mM (0.08% v/v) pyrimidine, 20 mM (0.12% v/v) isopropanol, and 10 mM (0.04% v/v) acetonitrile concentrations.

4.6. Validation of cysteine-containing Site 1

Site 1 is formed by the β6/7 strands of two protomers. This region is interesting because it comprises the monomer-monomer interactions that stabilize the core Hsp27 dimer. Thus, interactions in this region might be expected to affect chaperone function. Additional support for the presence of a ligand-binding pocket at Site 1 can be gleaned from published crystal structures of the core domains of αB-crystallin and Hsp20. In crystal structures of αB-crystallin, the crystallization additives methylpentanediol and sulfate populate this site, suggesting that it sometimes binds small molecules (10). In addition, a rat Hsp20 αB-crystallin core domain structure shows that C-terminal peptides from adjacent dimers in the crystal lattice bind in the groove of Site 1 (11). While affinity for solvent-like probes is suggestive of a ligand-binding site, we wanted to take the next step and identify drug-like small molecules engaging this site. For Site 1, we chose to take a high-throughput screening approach, beginning with differential scanning fluorimetry.

Differential scanning fluorimetry (DSF) was discussed in Chapter 1 (1.9) and applied to R120G αB-crystallin in Chapter 3. From the same pilot screen, we identified a 'hit' that altered melting temperature of the full-length Hsp27 by -1.6°C in a dose-dependent fashion (Figure 4.4). Captopril is a known angiotensin-converting enzyme inhibitor discovered in the 1970s for the treatment of hypertension. A secondary assay using the HSQC NMR platform introduced in the previous section indicated that captopril causes chemical shift perturbations in the region of the lone cysteine residue in Hsp27 (Figure 4.4). The shifts were large, distributed over the structure of the protein, and markedly similar to those observed in the presence of dithiothreitol (Figure 4.4) or β-mercaptoethanol.

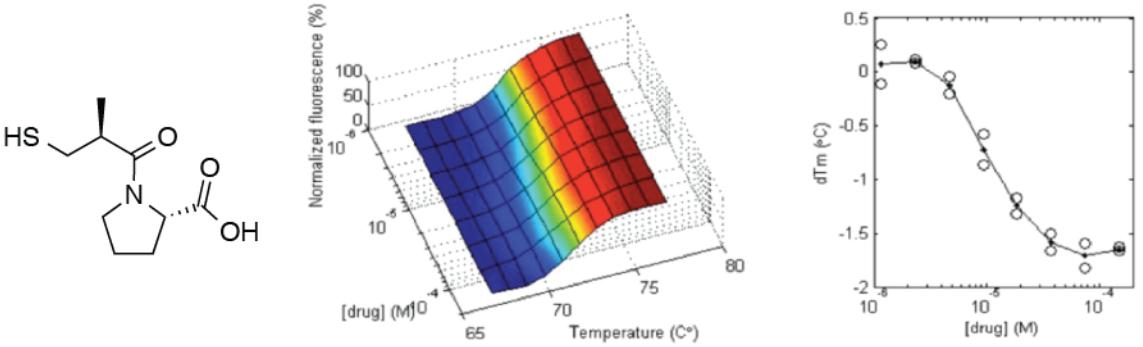

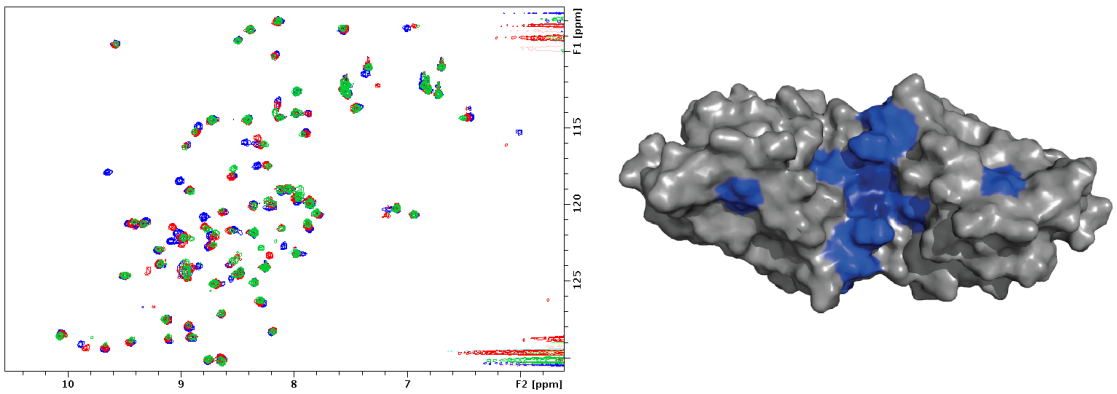

Figure 4.4. Captopril decreases the apparent melting temperature of full-length Hsp27 by 1.6°C as measured by differential scanning fluorimetry. A 3D topology of melting curves with increasing captopril concentration is shown, as is a plot of change in melting temperature versus concentration of captopril. Captopril causes backbone chemical shift perturbations similar to those seen upon treatment with dithiothreitol; control spectrum with 200 µM Hsp27c alone is shown in blue, the spectrum with the addition of 5 mM dithiothreitol in shown in red, and the spectrum including 5 mM captopril is indicated in green. F1 is the proton frequency axis and F2 is the nitrogen frequency axis. The largest chemical shift perturbations (exceeding 2 SD) are mapped in blue, and the residues that disappear entirely are mapped in navy blue.

We therefore hypothesized that the molecule was forming a mixed disulfide bond with Hsp27's cysteine, which is located at the dimer interface, in the floor of Site 1. To probe whether the affinity was purely a result of the reactive thiol, or whether the molecule also had other physicochemical interactions and noncovalent affinity with the pocket, we mutated the endogenous cysteine to alanine and repeated the HSQC binding experiment. The residues in the binding pocket still show chemical shift perturbations at high concentrations of captopril (Figure 4.5), though captopril's ability to form a mixed disulfide with the protein is eliminated by the mutation. This suggests that captopril makes weak but productive non-covalent contacts with the Site 1 pocket.

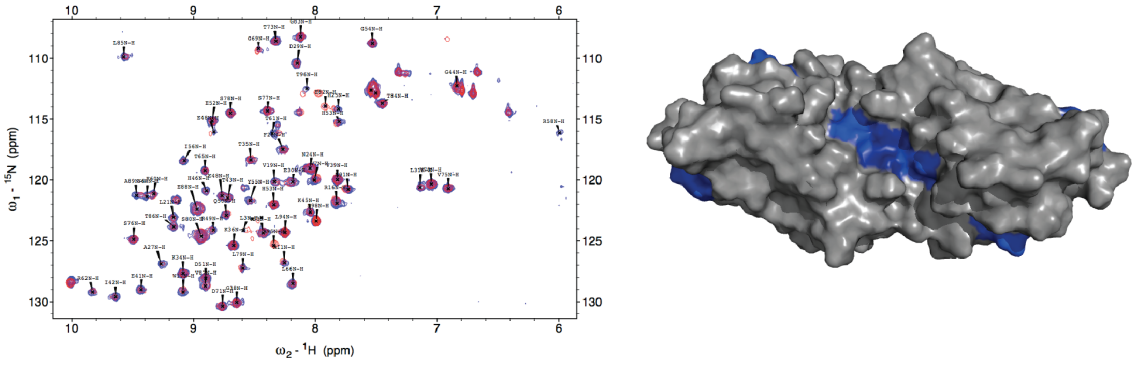

Figure 4.5. HSQC NMR chemical shift perturbations indicate that captopril interacts with C59A Hsp27c. Buffer control spectrum for 200 µM C59A Hsp27c is shown in blue, and spectrum with addition of 5 mM captopril is shown in red. Residues that shift by more than 1.5 standard deviations are colored blue on the surface representation of Hsp27c.

The role of the cysteine in Hsp27 biology is not well understood. No other human small heat shock protein has a cysteine within the dimer interface. Disulfide-bound dimers of Hsp27 are known to be present in cells, and the proportion of covalent dimer increases upon treatment of cells with oxidants including hydrogen peroxide, diamide, and arsenite (12, 13). The inter-protomer disulfide bond locks the dimer in a single registration of the β-strand interface; the cross-dimer distance between the cysteine Cα atoms is 5 Å, whereas in the other possible registers of the dimer interface it is ~8.8 Å (2) which precludes disulfide formation (14). Interestingly, disulfides formed between residues on adjacent β-strands are rare, and cross-strand disulfides formed between hydrogen-bonded residues on adjacent β-strands are even more unusual (15). A 2011 study found 2576 examples of cross-strand disulfide bonds in the PDB, only six of which are found between hydrogen-bonded pairs. Such disulfides are highly strained and usually act as redox switches (16, 17). Given the known roles of Hsp27 in protecting against oxidative stress (18, 19) and the location of the strained cross-strand disulfide at the critical dimer interface, it seems likely that the disulfide acts as a redox sensor. Several studies have examined the role of the cysteine in human Hsp27 or its murine homologue, Hsp25 (12, 13, 20-24). In cells, mutation of the cysteine residue to alanine was reported to reduce Hsp25's oligomeric size and abolish its chaperone activity towards luciferase in cells (20). Additionally, the cysteine to alanine mutation slightly reduced Hsp25's ability to protect cells from staurosporine-induced apoptosis (20). However, a second group observed no significant changes to the chaperone function, oligomeric size, or secondary structure of Hsp25 *in vitro* (13), consistent with the results of studies of the corresponding mutation in Hsp27 (23). This discrepancy may reflect the difficulty of designing *in vitro* assays that predict *in vivo* chaperone functions. Thus, small molecule probes of this binding site are expected to be useful tools that enable a better understanding of the role of Hsp27's cysteine in oxidative stress.

In ongoing work in the Gestwicki laboratory, the endogenous cysteine has been used as a handle for a tethering screen to generate chemical matter binding to Site 1. Tethering was introduced in Chapter 1 (1.8) as a site-directed screening method, in which an introduced or endogenous cysteine is used to 'tether' molecules from a screening library via mixed disulfide adducts with the protein target. An in-house library of 1280 small molecule fragments containing reactive thiols was screened for binding to Hsp27's core domain in the presence of 100 μM β-mercaptoethanol. The hit rate for the primary screen was nearly 5%, using a typical cutoff of

50% adduct formation to differentiate hits. This suggests that Site 1 is amenable to small molecule binding, as predicted by the MixMD simulation. The potential for optimal non-covalent affinity at this pocket remains to be determined, as does the functional consequence of irreversibly or reversibly engaging this site. Another graduate student has been leading the Hsp27 tethering screen and she is actively working to co-crystallize the lead molecules in complex with Hsp27's core domain.

4.7. Site 2 is involved in protein-protein interactions

Site 2 is located in a hydrophobic groove formed by the β4 and β8 strands of the core domain (Figure 4.1). Interestingly, this site is known to participate in homomeric and heteromeric protein-protein interactions. This region binds to an IXI palindromic motif, which is located in the C-terminal extension of Hsp27. The interaction of the IXI motif with Site 2 in the core domain stabilizes Hsp27 oligomers, likely mediating inter-monomer contacts (1). Several NMR and crystallography studies of αB-crystallin and Hsp27 have documented IXI peptide binding to this groove (1, 25, 26). Secondly, the β4-β8 groove is known to mediate the interaction of sHSPs with BAG3. BAG3 is a nucleotide exchange factor for heat shock protein 70 (Hsp70) and is thought to serve as a scaffolding protein that links Hsp70 with the sHSPs. The sHsps Hsp20 (HspB6), Hsp22 (HspB8), and αB-crystallin have each been reported to interact with BAG3 (27, 28). Moreover, the Landry group has carried out extensive mutagenesis and immunoprecipitation studies to identify the regions in each binding partner that are required for the interaction (27). In the case of Hsp20 and Hsp22, mutation of several conserved hydrophobic residues in the β4 and β8 abrogated the binding interaction (27). The same group used deletions and mutagenesis to identify the regions in BAG3 that are responsible for the interaction, and found that two IPV motifs within BAG3 are necessary for the binding interaction (27). These IPV motifs are very similar to the C-terminal Hsp27 IXI motifs (see alignment in Figure 4.7).

To gain more insight into Site 2, we used NMR to show that full length BAG3 and synthetic peptides containing the IPV interaction motifs bind to the Hsp27 core domain in the expected β4/β8 groove (Figure 4.6). By isothermal titration calorimetry, full length BAG3 binds to Hsp27c with an affinity of 490 ± 120 nM, and a stoichiometry of one molecule of BAG3 per Hsp27c dimer (n = 2.0 ± 0.06). The synthetic Bag3 peptides from residues 94-111 (^{H2N}IPIPVLHE^{COOH}) and

206-213 (^{H2N}ISIPVIHE^{COOH}) bind more weakly (K_Ds of 8 µM and 7 µM, respectively), as might be expected since each contains only a single interaction motif.

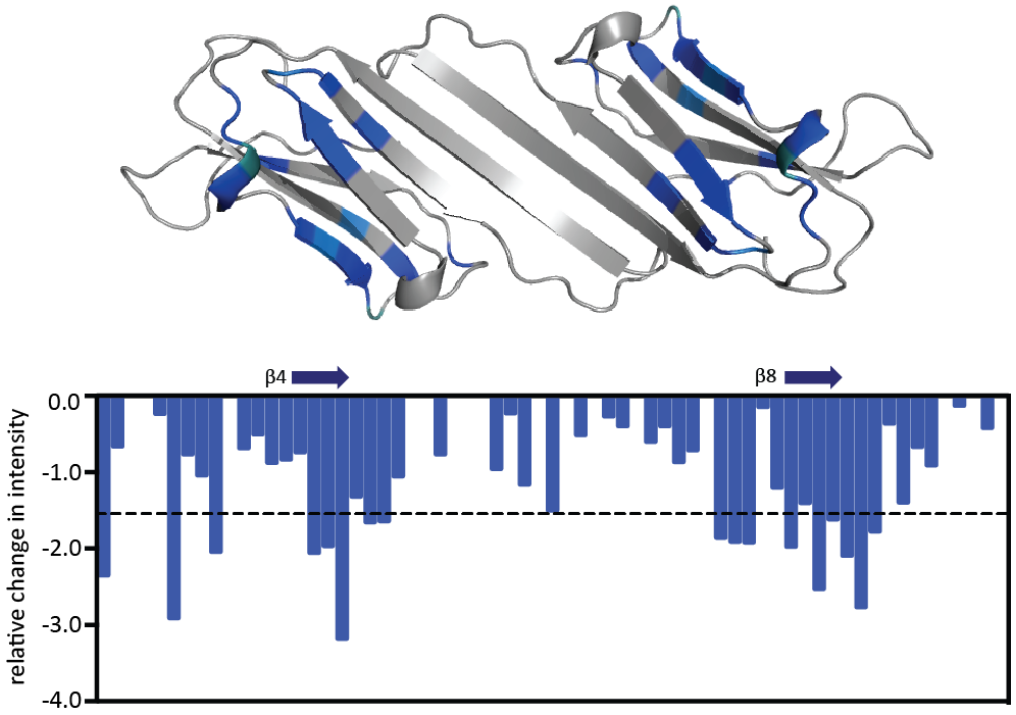

Figure 4.6. Interaction surface for full length BAG3 binding to Hsp27c. The changes in backbone amide peak intensities exceeding 2 standard deviations (dotted line in histogram) are plotted onto the cartoon representation of Hsp27c in blue. Intensity changes between 1.5 and 2 standard deviations are plotted in marine, and the locations of proline residues in the proximity of the binding site are indicated in teal, as they do not give crosspeaks in the HSQC spectra. Locations of the β4 and β8 strands are indicated above the histogram.

4.7.1. Effect of peptide binding on quaternary structure of Hsp27

Because Site 2 is involved in important protein-protein interactions, we wondered whether ligands for this region might alter the oligomerization of Hsp27. Specifically, we reasoned that peptide binding in Site 2 should compete with the ability of the Hsp27 IPV motif to bridge across dimers, weakening the oligomer structure. When 100 µM of full-length Hsp27 was incubated with 1 mM or 2 mM of the 8-mer peptide ^{H2N}IPIPVLHE^{COOH} from BAG3, a slight reduction in the size of the oligomer was observed by size exclusion chromatography coupled to multi-angle light scattering (SEC-MALS) (Figure 4.7). Though the change was relatively small, it was dose-dependent and reproducible, and each value in the table represents the average of two experiments. Because the binding of IPIPVLHE is fairly weak (K_D = 8 µM), it is difficult to reach concentrations that can compete with the self-interaction with the IPV motif. Consequently, the binding sites are not likely to be saturated in this experiment. However, ongoing work in the

Gestwicki laboratory is focused on developing more potent, synthetic analogs of the peptide. These chemical reagents will likely be useful probes of Hsp27 structure-function.

```
Hsp27 178 EITIPVTFE 186
Bag3   93 YIPIPVLHE 111
Bag3  205 YISIPVIHE 213
```

	Molecular weight (kDa)	n	Number of subunits
apo	580	2	25
1mM peptide	480	2	21
2mM peptide	440	2	19

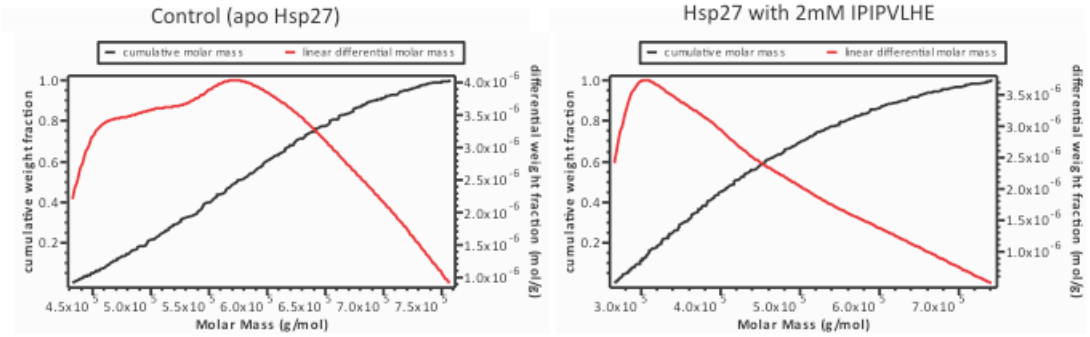

Figure 4.7. Alignment of two "IPV"-containing peptides from the sequence of BAG3 and the C-terminal extension of Hsp27. Summary table of molecular weights and corresponding oligomeric sizes of full length Hsp27 upon treatment with peptide IPIPVLHE from BAG3. Distribution analyses are shown for one control experiment and one experiment with 2 mM peptide (note the difference in horizontal axes).

4.7.2. Effect of peptide binding on stability of sHsps

The region encompassing Site 2 in αB-crystallin includes the peptides predicted to have strong propensity to form amyloids. The Eisenberg group used a steric zipper prediction algorithm to identify an 11-mer peptide encompassing the β4 strand and part of the β5 strand as the region in αB-crystallin with the highest amyloid-forming propensity (29). This 11-mer peptide formed cytotoxic amyloid oligomers with six peptide units per oligomer, and the crystal structure of the resulting oligomer was solved to reveal a hexameric β-barrel with each β-strand antiparallel to its neighbors (29). Thus, we hypothesized that engaging Site 2 with a peptide may limit re-arrangement to the amyloid conformation. Consistent with this idea, peptides from BAG3 suppressed aggregation of R140G Hsp27 as measured by light scattering (Figure 4.8) by delaying its lag time. The peptide consisting of BAG3 residues 94-111 completely suppressed aggregation over the twelve-hour experiment at a 1:2 stoichiometry of peptide to sHsp, and the peptide consisting of BAG3 residues 206-213 was effective at 1.5:1 peptide to sHsp.

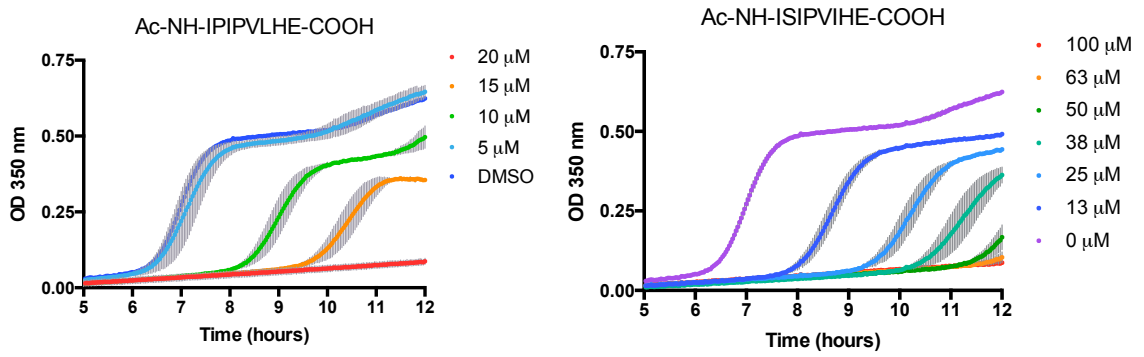

Figure 4.8. Peptides from BAG3 delay the lag time and suppress the aggregation of R140G Hsp27 as measured by light scattering. Both BAG3 94-111 and BAG3 206-213 can completely suppress aggregation. The concentration of R140G Hsp27 is 87 μM (in monomer), so the peptides are effective here at substoichiometric concentrations.

When the peptides were tested against the even more aggregation-prone R120G mutant αB-crystallin, they were effective at suppressing aggregation but exhibited different inhibition behavior in this assay (Figure 4.9). The BAG3 peptides primarily slowed the rate of aggregation of R120G αB-crystallin, had less of an effect on its lag time, and required much higher peptide concentrations. For example, the peptide containing the BAG3 residues 94-111 completely suppressed aggregation but this required more than an eleven-fold excess of peptide to sHsp.

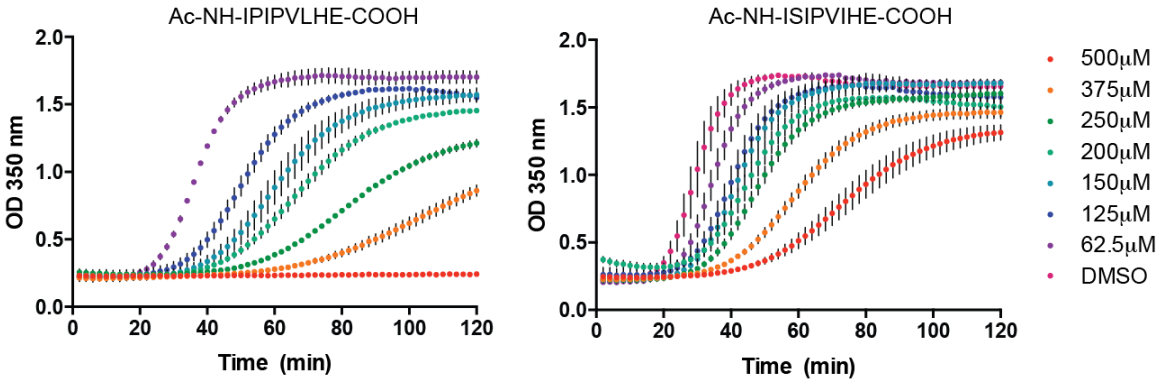

Figure 4.9. Peptides from BAG3 suppress the aggregation of R120G αB-crystallin as measured by light scattering. BAG3 94-111 can completely suppress aggregation at the highest concentration tested while BAG3 206-213 is slightly less effective. The concentration of R120G αB-crystallin is 43 μM (in monomer), so the effective peptide concentrations are in large excess.

These results suggest that the peptides bind to the native fold of the protein and prevent nucleation of aggregation (R140G Hsp27) or propagation of aggregation (R120G αB-crystallin). Thus, engaging Site 2 appears promising as a potential means of inhibition of mutant sHsp amyloid formation.

4.8. Validation of dimer-interface Site 3 through fragment-based drug design

Site 3 was unknown prior to the initiation of this work. To explore its potential druggability, we chose to apply fragment-based drug design by NMR. This method for the label-free, affinity-based selection of ligands was introduced in Chapter 1.8. In this approach, low molecular weight fragments are expected to bind weakly, but with high atom efficiency, enabling straightforward optimization by growing or combining fragments into higher-affinity ligands. The advantage of fragment-based drug design by NMR is that the binding sites of the fragments are identified as part of the routine screening process. We chose to use the Klevit laboratory's uniformly ^{15}N-labeled Hsp27 core domain as a target for a protein-observed HSQC screen of the Maybridge RO3 library of ~1,000 fragment molecules, carried out in collaboration with the Cierpicki laboratory. Because protein-observed HSQC screens are information rich but relatively low throughput, we multiplexed the fragments in groups of 20 fragments per HSQC experiment, using 125 µM Hsp27c and 250 µM of each fragment (Figure 4.10). Thirty-three mixtures exhibited large (>8 Hz) chemical shift perturbations, reflecting an unusually high hit rate for this type of screen. Hit rates from fragment-based NMR screens are sometimes used as a metric for the potential 'druggability' of a protein target, as discussed in Chapter 1.8. In Hajduk's influential analysis, targets producing experimental NMR hit rates higher than 0.2%, or exceeding two hits for a library of this size, correlated with the success of subsequent medicinal chemistry campaigns to access optimized hits with high affinity (<300 nM) (30). While we only deconvoluted six of the thirty-three mixtures of compounds that produced hits, we obtained four confirmed hit molecules (0.4%), and it is likely that the library contained many more hits than four. This analysis suggests that the core domain of Hsp27 should be considered as highly 'druggable' by this metric.

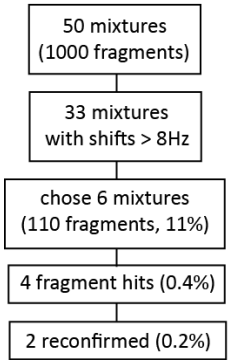

	rule of 3	Maybridge RO3 library average value
MW	≤ 300	178.3
cLogP	≤ 300	1.5
H-bond acceptors	≤ 3	2.4
H-bond donors	≤ 3	0.9
Rotatable bonds	≤ 3	0.9
PSA	≤ 60 Å²	37.0 Å²

Figure 4.10. Flowchart describing primary screening, deconvolution, and reconfirmation of NMR based screen against Hsp27c; characteristics of the Maybridge RO3 library.

4.8.1. Resynthesis of screening hits and confirmation of binding to Site 3

Of the four hit molecules from the Maybridge RO3 library, compounds 1 and 4 did not reconfirm when synthesized in-house according to the scheme in Figure 4.11, below.

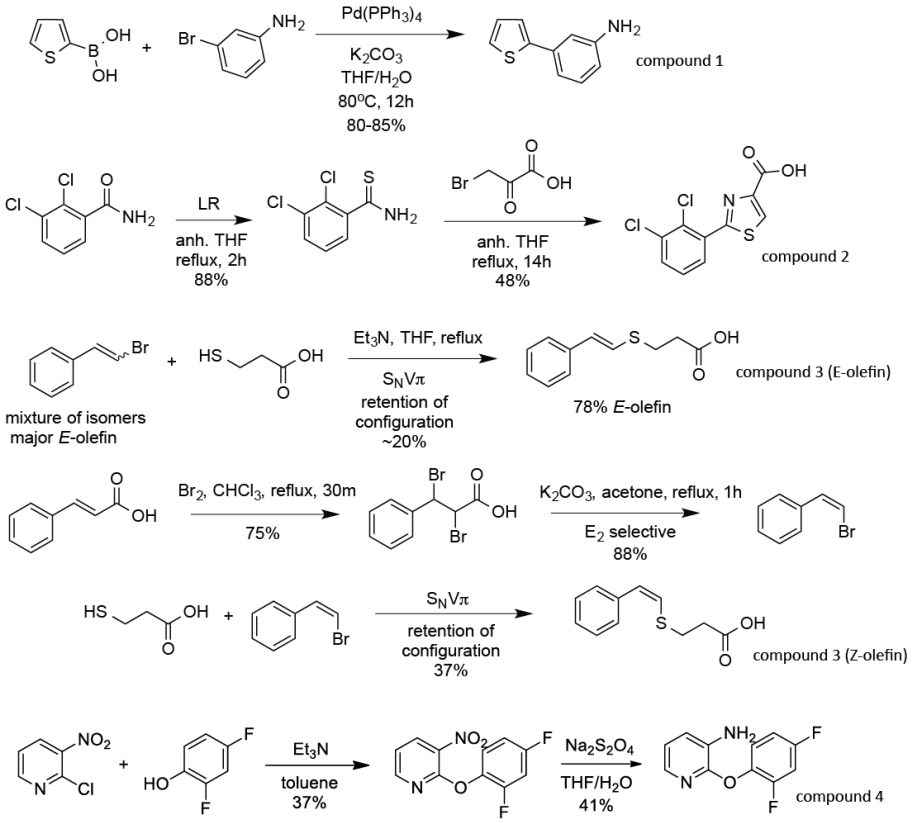

Figure 4.11. Synthetic schemes used to resynthesize fresh powders of each of the four hits from the NMR fragment-based screen.

The third molecule, the β-styrene compound 3, was resynthesized as a mixture of stereoisomers and isolated as 78% E-olefin, the molecule that was represented in the Maybridge library product information. This molecule did not bind to Hsp27c by HSQC NMR under conditions similar to the screening conditions. However, we noticed upon inspection of the proton NMR spectrum of the original screening sample that the $^{3}J_{HH}$ coupling constant for the alkenyl protons was characteristic of the Z-olefin (Figure 4.12), and not the E-olefin as drawn. The Z-olefin was obtained through a different synthetic route (Figure 4.11) and in fact did bind to Hsp27c in a reconfirmation experiment.

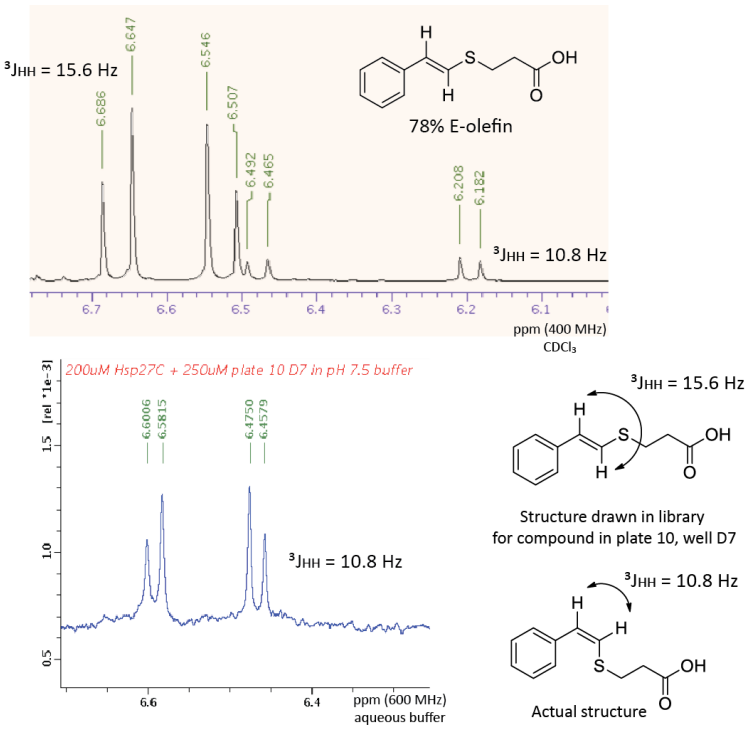

Figure 4.12. Identification of correct isomeric structure of compound 3 from $^3J_{HH}$ coupling analysis.

The remaining primary screening hit, the diaryl ether compound 4, clearly reconfirmed when it was resynthesized as fresh powder. Both the Z-olefin and the diaryl ether molecules resulted in large chemical shift perturbations in the proximity of the dimer interface, and because the diaryl ether compound was more easily accessible in two synthetic steps and had the advantage of a diverse range of commercially available starting materials, we focused our optimization effort here.

A library of 48 analogues was assembled to probe the druggability of Site 3. Each molecule was dissolved in DMSO and tested at a single concentration in the HSQC binding assay. If significant (>8 Hz) chemical shift perturbations were observed relative to the vehicle control, a full titration series was performed. When possible, a plot of chemical shift versus concentration was fit with a hyperbolic one-site binding model and an apparent affinity was extracted (Table 4.1). Asterisks denote compounds that were purchased from commercial libraries. The synthetic procedures and analytical characterization for each compound synthesized in-house may be found in the Experimental Procedures section of this chapter (4.11).

Table 4.1. Structure-activity relationships obtained for analogues of diaryl ether compound 4.

Name	Structure	HSQC affinity (ligand efficiency)
original hit **4**	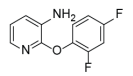	> 1 mM
5	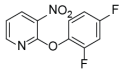	177 ± 16 µM (0.29)
6	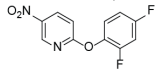	63 ± 3 µM (0.32)
7	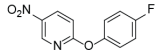	64 ± 7 µM (0.34)
8	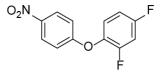	68 ± 9 µM (0.32)
9	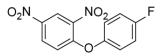	47 ± 10 µM (0.30)
10	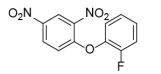	80 µM (0.28)
11	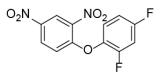	16 ± 2 µM (0.32)
12	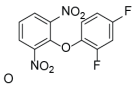	70 µM (0.27)
13*	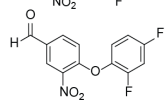	160 µM (0.26)
14*	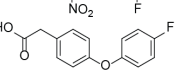	250 µM (0.28)
15*	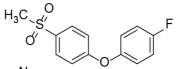	240 µM (0.28)
16*	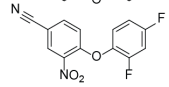	40 µM (0.30)
17*	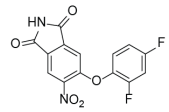	80 µM (0.25)

Name	Structure	HSQC affinity (ligand efficiency)
18	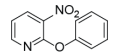	subtle CSPs, KD ND
19	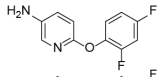	subtle CSPs, KD ND
20*	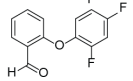	subtle CSPs, KD ND
21	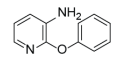	no binding
22	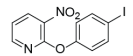	no binding
23	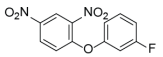	no binding
24	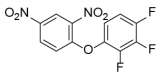	no binding
25	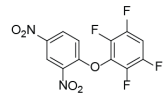	no binding
26	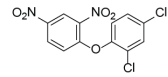	no binding
27	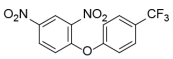	no binding
28	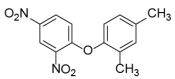	no binding
29	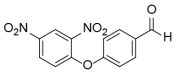	no binding
30	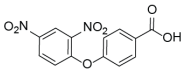	no binding

Name	Structure	HSQC affinity (ligand efficiency)
31*	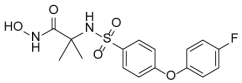	no binding
32	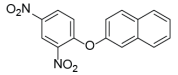	no binding
33	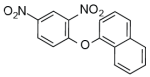	no binding
34	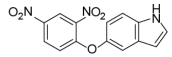	no binding
35*	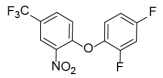	no binding
36*	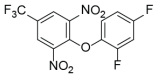	no binding
37	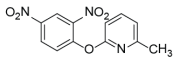	no binding
38	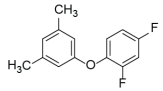	no binding
39	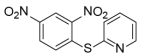	no binding
40	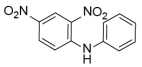	no binding
41	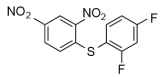	9.6 ± 2 µM (0.33)
42	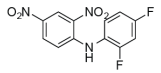	no binding
43	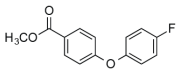	no binding

Name	Structure	HSQC affinity (ligand efficiency)
44	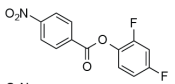	no binding
45	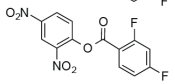	no binding
46	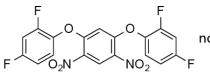	no binding
47	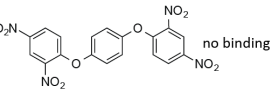	no binding

The original diarylether hit **4** bound weakly and a titration analysis of chemical shift perturbation versus concentration of compound was linear up to 1 mM. The unreduced nitropyridine starting material **5** bound more tightly, giving saturable binding curves in the HSQC titration and an apparent affinity of 177 ± 16 μM. Nitro substitution at the 5-position instead of the 3-position resulted in a further improvement in affinity to 63 ± 3 μM (**6**). Removal of either the pyridine nitrogen or 2-fluoro substituent individually had little effect on affinity (compounds **7** and **8**, respectively). Ligand efficiency is a metric often used in fragment optimization efforts that is intended to control for the effect of molecular weight or number of heavy atoms in affinity (31). Ligand efficiency was calculated using the formula –ΔG (kcal/mol)/#heavy atoms, where ΔG was calculated at 303 K (the temperature at which all NMR experiments were carried out) and all non-hydrogen atoms were counted as heavy atoms (31). Interestingly, 2,4-difluoro substitution on the right-hand ring was found to be optimal when the left-hand ring bore nitro substituents at the 2 and 4 positions (compare **11** to **9** and **10**). The position of the nitro groups was important, as seen from a comparison of compounds **11** and **12**. This precludes a purely electronic effect of the nitro substituents on the left-hand ring. Similarly, the effect of the fluorines on the right-hand ring does not appear to be a purely electronic effect, as can be seen from compounds **23**-**25**, which do not bind. Interestingly, a nitrile can be accommodated in the 4-position (compound **16**), but a trifluoromethyl group cannot (compound **35**). Replacement of the fluorines with other halogens, a trifluoromethyl group, methyl groups, an aldehyde, or a carboxylic acid is poorly tolerated (compounds **22**, **26-30**). Interestingly, the ether oxygen can be replaced by sulfur with a slight improvement in affinity (**41**), but not with a nitrogen atom (compounds **40** and **42**). The nitrogen substitution would be expected to restrict the possible orientations of the two planar rings relative to one another, which may preclude binding. Similarly, insertion of a carbonyl as in **44** or **45** abolishes binding. We hypothesized that introducing a third ring system in a symmetrical fashion might allow for binding to both sides of the dimer interface, and so compounds **46** and **47** were synthesized. However, no chemical shift perturbations were observed from these larger molecules. Future work aims to co-crystallize the most ligand-efficient fragments (**7, 11,** and **41)** with Hsp27c to enable further, rational optimization.

4.8.2. Confirmation of fragment binding site with mutagenesis

Since Site 1 and Site 2 are related by their locations on either side of the β-sheet dimer interface, and since the HSQC experiment reports on the electronic environment of the backbone amides, the observed chemical shift perturbations are ambiguous as to which binding site is engaged (Figure 4.13). To distinguish Site 1 and Site 3 and identify which residues are engaged with ligand binding, we systematically mutated each of the side chains involved in Site 1 and Site 3 and tested the optimized compound **11** (1-(2,4-difluorophenoxy)-2,4-dinitrobenzene) for binding to each mutant in the same HSQC platform (Figure 4.14). Several mutations in Site 3 severely reduced (*e.g.* H46A) or completely abolished binding (*e.g.* R58A, F60A, and R62A). Conversely, mutations in Site 1 had only minor effects on the apparent binding affinity. These studies confirmed that the diaryl ether scaffold engages Site 3, likely via critical contacts with residues H46, R58, F60, and R62. These results validate Site 3 as a *bona fide* ligand-binding pocket.

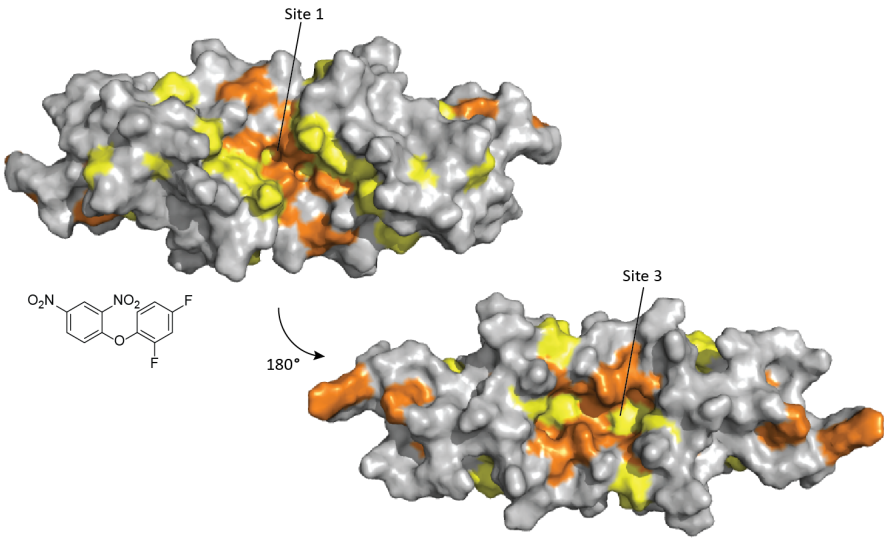

Figure 4.13. Backbone chemical shift perturbations from **11** (1-(2,4-difluorophenoxy)-2,4-dinitrobenzene) binding to Hsp27c do not permit differentiation between Site 1 and Site 3. 250 μM compound was added to 125 μM protein; residues that exhibit chemical shift perturbations greater than 2 standard deviations are colored orange, and residues that are perturbed between 1 and 2 standard deviations are colored yellow.

Mutation	Side Chain in Site 1 or 3	Apparent Affinity (μM)	Fold Change in Affinity vs Wild Type
C59A	1	67 ± 12	4
T61L	1	32 ± 5	2
L21A	3	42 ± 4	3
V23A	3	69 ± 12	4
I56A	3	63 ± 10	4
H46A	3	240 ± 20	15
R58A	3	no binding	NA
F60A	3	no binding	NA
R62A	3	no binding	NA

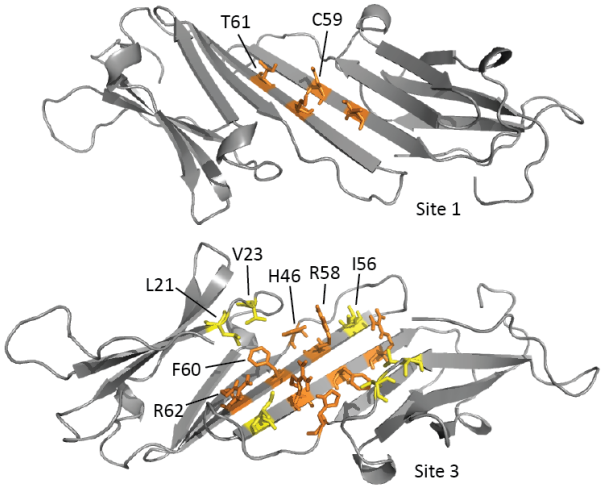

Figure 4.14. Summary of mutagenesis studies for binding of compound **11** 1-(2,4-difluorophenoxy)-2,4-dinitrobenzene to Hsp27 with residues in Site 1 or Site 3 mutated. The numbering system used for the mutation is for the core domain of Hsp27 (not the full-length protein). Locations of mutated residues are shown in the cartoon diagrams.

4.9. Conclusions

In the post-genomic era, genetically validated targets do not necessarily possess ligand binding sites or convenient starting points for ligand design. Therefore, non-enzyme, non-receptor targets, such as Hsp27, require chemical validation to understand their therapeutic potential. In this Chapter, we identified three 'druggable' binding sites on the surface of Hsp27's αB-crystallin domain and described ongoing efforts to identify and optimize small molecules or peptides that engage each. We demonstrated that one of the sites is functionally important in preventing the aggregation of R120G αB-crystallin. In doing so, we validated the predictive power of MixMD as a *de novo* binding site identification technique in a blinded fashion. Future work will continue to expand upon this suite of chemical ligands, which represent valuable starting points for the development of useful probes for chemical biology and perhaps also for the development of Hsp27-targeted therapeutics.

4.10. Experimental procedures

4.10.1. Protein purification

Proteins were purified as described in Chapter 2; see 2.13.2 for details. Hsp27 core domain mutants were purified using the protocol for the wild type protein, except that for mutations that changed the charge of the protein, the NaCl gradient used in the MonoQ purification step was altered accordingly.

4.10.2. NMR studies

HSQC spectra were acquired at 30 °C on a 600 MHz Bruker Avance III spectrometer equipped with cryoprobe, running Topspin version 2.1, or a Bruker DRX500 with a QCI Z-axis gradient cryoprobe, running Topspin version 1.3. Spectra were acquired on samples containing 150-200 µM Hsp27 core domain in 50 mM NaPi, pH 7.5, 100 mM NaCl at 30°C and always compared to solvent-controlled reference spectra. 256 scans were acquired per t_1 value and spectral widths of 1500 Hz and 9615 Hz were used in the ^{1}H and ^{15}N dimensions, respectively. Processing and spectral visualization was performed using rNMR (32) and Sparky (33).

4.10.3. Differential scanning fluorimetry screen

The differential scanning fluorimetry screen was carried out as described in Chapter 3; see Chapter 3.8.2 and 3.8.3 for experimental details.

4.10.4. SEC-MALS

Oligomeric samples were resolved by analytical size exclusion chromatography with a Shodex 803 column on an Ettan LC (GE Healthcare). Molecular weights were determined by multiangle laser light scattering using an in-line DAWN HELEOS detector and an Optilab rEX differential refractive index detector (Wyatt Technology Corporation). The system was equilibrated in analysis buffer containing 20 mM NaPi, pH 7.2, 100 mM NaCl containing 0.001% Tween-20 and 2% DMSO prior to analysis. Samples contained 50 µL of 0.5 mg/mL protein and 0, 1, or 2 mM peptide.

4.10.5. Light scattering assay

The light scattering assay was carried out essentially as described in Chapter 2; see Chapter 2.13.6 for experimental details.

4.11. Synthetic procedures and analytical characterization

^{1}H NMR spectra were obtained on Varian 300 MHz and 400 MHz spectrometers with $CDCl_3$ or d_6-DMSO as solvent, and chemical shifts are recorded in δ (ppm). Mass spectrometry analysis was performed using a Micromass LCT electrospray ionization instrument.

4.11.1 Peptides from BAG3 sequence (Ac-NH-IPIPVLHE-COOH and Ac-NH-ISIPVIHE-COOH)

Peptides were synthesized using standard solid-phase microwave-assisted coupling techniques using Wang resin as a solid support. Before cleaving from the resin, N-termini were acetylated using 10% acetic anhydride in DMF. Peptides were cleaved from the solid support using a cocktail of 88% trifluoroacetic acid, 5% phenol, 5% CH_2Cl_2 and 2% triisopropylsilane for 30 min at room temperature under nitrogen gas. After filtering, the cleaved peptides were isolated evaporating most of the trifluoroacetic acid by rotary vacuum as an azeotrope with CH_2Cl_2. The peptides were precipitated by adding the resulting oils dropwise to diethyl ether at -78 °C to result in a fluffy white solid, which was isolated by filtering and washing with ice-cold ether. The crude peptides were dissolved in DMSO and purified by semi-preparative reverse-phase HPLC using a gradient of 0 to 100% acetonitrile containing 0.1% trifluoroacetic acid. Fractions containing peptides were identified by MS, pooled, evaporated under rotary vacuum, and lyophilized to yield the pure peptides **Ac-NH-IPIPVLHE-COOH** (1.7 mg, 2% based on resin hydroxyl groups): MS *m/z* 960.1 (M+H); and **Ac-NH-ISIPVIHE-COOH** (11.4 mg, 12.9% based on resin hydroxyl groups): MS *m/z* 950.0 (M+H). The purity of each peptide was confirmed by analytical reverse-phase HPLC and exceeded 90%.

4.11.2. Synthesis of fragment screening hits 1-4

3-(thiophen-2-yl)aniline (**1**) was synthesized according to (34). Briefly, 3-bromoaniline (0.172 g, 1.0 mmol, 1.0 eq) was dissolved in 10 mL THF to give a clear solution. Potassium carbonate (0.415 g, 3.0 mmol, 3.0 eq) dissolved in 2 mL H_2O was added, followed by 2-thienylboronic acid (0.166 g, 1.3 mmol, 1.3 eq). Tetrakis(triphenylphosphine)palladium(0) (0.034 g, 0.03 mmol, 0.03 eq) was then added, and the reaction solution was heated to reflux at 80°C for 12 hours until TLC in 50:50 hexanes:EtOAc indicated completion (R_f = 0.5); staining with ρ-anisaldehyde gave a purple spot for product. EtOAc (100 mL) was added to the reaction and it was extracted with H_2O (3 x 35 mL), then brine (1 x 35 mL), dried with Na_2SO_4, filtered, and evaporated under rotary vacuum to give a reddish brown oil. The crude product was purified by silica gel chromatography in 75:25 hexanes:EtOAc; pure fractions were combined and evaporated under reduced pressure to yield **1** as a bright yellow crystalline solid (144 mg, 83%): MS *m/z* 176.1 (M+H); ^{1}H NMR (400 MHz, d_6-DMSO): δ 7.67-7.61 (m, 5H), 7.28 (d, 1H), 7.17 (t, J = 4 Hz, 1H).

2,3-dichlorobenzothioamide was synthesized according to (35). 2,3-dichlorobenzamide (192 mg, 1.0 mmol, 1 eq) was dissolved in 20 mL anhydrous THF and Lawesson's reagent (445 mg, 1.1 mmol, 1.1 eq) was added. The reaction was heated to reflux for 5 hours, then evaporated under rotary vacuum, washed with 3N HCl (10 mL), and neutralized with saturated $NaHCO_3$ (30 mL) before extracting with CH_2Cl_2 (3 x 40 mL). The crude product was purified by silica gel chromatography in 80:20 hexanes: EtOAc to give **2,3-dichlorobenzothioamide** as a yellow oil (183 mg, 88%; a repeat reaction gave 146 mg, 72%): MS *m/z* 206.0 (M+H); ^{1}H NMR (400 MHz, d_6-DMSO): δ 8.08 (bs, 1H), 7.46 (d, J = 7.6, 2H), 7.24-7.19 (m, 2H).

2-(2,3-dichlorophenyl)thiazole-4-carboxylic acid (2) was synthesized according to (36). 2,3-dichlorobenzothioamide (210 mg, 1.02 mmol, 1 eq) was dissolved in 6 mL anhydrous THF, and bromopyruvic acid (170 mg, 1.02 mmol, 1 eq) was added. The solution was heated to reflux at 70 °C for 14 hours, then cooled to room temperature and evaporated under reduced pressure. The resulting solid **2** was recrystallized from EtOAc (40 mL) to yield pale peach crystals (72 mg, 48%): ^{1}H NMR (400 MHz, d_6-DMSO): δ 13.22 (s, 1H), 8.70 (s, 1H), 8.11 (dd, J = 7.9, 1.4 Hz, 1H), 7.4 (dd, J = 8.0, 1.4 Hz, 1H), 7.58-7.56 (m, 1H).

(E)-3-(styrylthio)propanoic acid (3, E-olefin). 3-mercaptoproprionic acid (174 µL, 2 mmol, 2 eq) was brought up in 12 mL THF and triethylamine (0.55 mL, 4 mmol, 4 eq) was added, followed by β-bromostyrene (128 µL, 1 mmol, 1 eq). The mixture was heated to reflux while stirring for 1 hr until TLC in 2.5% MeOH/CH_2Cl_2 + 0.05% AcOH indicated completion and the formation of a white precipitate was observed, which was thought to be the triethylamine HBr salt. This precipitate was filtered and rinsed with CH_2Cl_2 and the supernatant was stripped to give a clear oil. The crude material was purified by silica gel chromatography in 1.7% MeOH/CH_2Cl_2 to yield 3 as 86% E-olefin (61.6 mg, 30%): ^{1}H NMR (400 MHz, $CDCl_3$): δ 11.2 (bs, 1H), 7.29-7.17 (m, 5H), 6.68 (d, J = 15.5 Hz, 1H), 6.52 (d, J = 15.5 Hz, 1H), 3.02 (t, J = 7.23, 2H), 1.66 (t, J = 7.80, 2H).

2,3-dibromo-3-phenylpropanoic acid. Trans-cinnamic acid (1.0 g, 6.8 mmol, 1 eq) was dissolved in $CHCl_3$ (25 mL), and bromine (0.35 mL, 6.8 mmol, 1 eq) was added. The solution was heated to reflux for 30 minutes, with immediate formation of a precipitate upon heating, then cooled to 0 °C. The white precipitate was filtered and washed with cold $CHCl_3$ (25 mL) and dried to give pure **2,3-dibromo-3-phenylpropanoic acid** (2.075g, 83%; a repeat reaction gave 1.88 g, 78%): MS *m/z*

308.2 (M+H). ^{1}H NMR (400 MHz, d_6-DMSO): δ 13.7 (bs, 1H), 7.62 (d, J = 7.2 Hz, 2H), 7.37 (dd, J = 8, 1.6 Hz, 3H), 5.53 (d, J = 11.7 Hz, 1H), 5.31 (d, J = 11.7 Hz, 1H).

(Z)-(2-bromovinyl)benzene. 2,3-dibromo-3-phenylpropanoic acid (300 mg, 0.97 mmol, 1 eq) was dissolved in 10 mL of acetone dried over molecular sieves and Na_2SO_4. Potassium carbonate (300 mg, 2.2 mmol, 2.2 eq) was added, and the resulting suspension was heated to reflux at 80°C for one hour until TLC (5% MeOH/CH_2Cl_2) indicated the absence of the starting material acid. The reaction mixture was evaporated under rotary vacuum to give an oily white solid, which was dissolved in CH_2Cl_2 (20 mL) and washed with aqueous 1 N HCl (3 x 30 mL). The combined aqueous layers were back-extracted with CH_2Cl_2 (3 x 20 mL) and the combined organic layers were washed with brine (30 mL) and dried with Na_2SO_4. Evaporation gave **(Z)-(2-bromovinyl)benzene** as a clear oil requiring no further purification (646 mg, 88%; a repeat reaction gave 470 mg, 64%): ^{1}H NMR (400 MHz, d_6-DMSO): δ 7.71 (d, J = 7.6 Hz, 2H), 7.419-7.344 (m, 3H), 7.087 (d, J = 7.8 Hz, 1H), 6.449 (d, J = 8.0 Hz, 1H).

(Z)-3-styrylthio)propanoic acid (3, Z-olefin). 3-mercaptoproprionic acid (349 µL, 4 mmol, 2 eq) was brought up in toluene (10 mL) and triethylamine (0.87 mL, 6.3 mmol, 3 eq) and added slowly via addition funnel to a mixture of (Z)-(2-bromovinyl)benzene (0.384 g, 2.1 mmol, 1 eq) and tetrakis(triphenylphosphine)palladium(0) (0.116 g, 0.1 mmol, 0.05 eq) in toluene (10 mL). The mixture was heated to 90 °C under a reflux condenser while stirring for 12 h until TLC in 2.5% MeOH/CH_2Cl_2 with AcOH indicated completion. The toluene was evaporated under rotary vacuum as an azeotrope with CH_2Cl_2 and the dried material was extracted from H_2O with CH_2Cl_2 (3 x 30 mL), dried with brine (30 mL) and Na_2SO_4. The crude product was a crude yellow oil which was purified by column chromatography on silica gel using a gradient of 0 to 2.5% MeOH in CH_2Cl_2. The product **(Z)-3-styrylthio)propanoic acid** was isolated as a white solid (161 mg, 37%; a repeat reaction on a larger scale gave 414 mg, 41%). ^{1}H NMR (400 MHz, d_6-DMSO): δ 12.34 (bs, 1H), 7.62-7.53 (m, 1H), 7.41-7.18 (m, 3H), 6.48 (d, J = 11.0 Hz, 1H), 6.44 (d, J = 10.9 Hz, 1H), 3.00 (t, J = 6.99, 2H), 2.60 (t, J = 6.95, 2H).

2-(2,4-difluorophenoxy)-3-nitropyridine (5) was synthesized according to (37). 2-chloro-3-nitropyridine (0.476 g, 3 mmol, 1 eq) and 2,4-difluorophenol (0.28 mL, 3 mmol, 1 eq) were combined in acetone (20 mL) with potassium carbonate (0.48 g, 3.45 mmol, 1.15 eq) and heated

to reflux for 6 hours. The mixture was acidified with 1N HCl and extracted with ether (3 x 30 mL). The combined organic layers were dried with brine (20 mL) and Na_2SO_4, filtered, and the solvents were evaporated under reduced pressure to give a yellow oil. Addition of ~2 drops H_2O induced crystallization of the crude material, which was recrystallized from isopropanol to give **2-(2,4-difluorophenoxy)-3-nitropyridine** as yellow crystalline solid (307 mg, 41%; a repeat reaction on a smaller scale gave 71 mg, 47%). MS *m/z* 253.1 (M+H); ^{1}H NMR (400 MHz, d_6-DMSO): δ 8.60 (d, J = 9.6, 1H), 8.41 (d, J = 4.8, 1H), 7.51-7.40 (m, 3H), 7.17 (t, J = 9.6, 1H).

2-(2,4-difluorophenoxy)pyridin-3-amine (4) was synthesized according to (37). 2-(2,4-difluorophenoxy)-3-nitropyridine (150 mg, 0.60 mmol, 1 eq) was dissolved in 4 mL THF. A solution of sodium dithionite ($Na_2S_2O_4$, 1.5 g, 8.6 mmol, 14.4 eq) in 14.6 mL H_2O was added, and the mixture was allowed to stir at room temperature for 2.5 h at which point TLC in 80:20 hexanes:EtOAc indicated completion. The reaction mixture was quenched with saturated $NaHCO_3$ (10 mL) and extracted with CH_2Cl_2 (3 x 15 mL), dried with brine (30 mL) and Na_2SO_4. Evaporation of solvent under reduced pressure gave pure product **4** as a white solid which was used without further purification (50 mg, 37%; a repeat reaction on a larger scale gave 156 mg, 30%): ^{1}H NMR (400 MHz, d_6-DMSO): δ 7.40-7.29 (m, 2H), 7.12 (dd, J = 4.70, 1.17, 1H), 7.11-6.82 (m, 2H), 8.20 (dd, J = 7.82, 4.70, 1H), 5.29 (s, 1H).

4.11.3. Synthesis of analogues of fragment screening hit 4

General procedure for nucleophilic aromatic substitutions.

The substituted chlorobenzene (1.1 mmol, 1 eq) was dissolved in anhydrous DMF (2.5 mL) and the phenol component (1.1 mmol, 1 eq) was added. Cesium carbonate (1.3 mmol, 1.15 eq) was then added, and the reaction was allowed to proceed at room temperature until TLC indicated completion. Upon completion, the reaction mixture was filtered to remove the cesium carbonate, acidified with the addition of 1 N HCl and extracted with CH_2Cl_2. The organic layers were washed with brine and dried with Na_2SO_4. Typically, the crude products were recrystallized from iPrOH or EtOAc, and the yield and characterization is reported for only the first crop of crystals. Where recrystallizations failed, products were purified by silica gel chromatography as indicated.

2-(2,4-difluorophenoxy)-5-nitropyridine (6) was synthesized according to an adapted protocol. To a solution of 2-chloro-5-nitropyridine (0.951 g, 6 mmol, 1 eq) in acetone (40 mL) was added 2,4-difluorophenol (0.56 mL, 6 mmol, 1 eq) and potassium carbonate (0.954 g, 6.9 mmol, 1.15 eq). The reaction mixture was heated to reflux overnight and then worked up according to the general protocol. The product was recrystallized from iPrOH to give pale yellow needles (1.10 g, 73%). ^{1}H NMR (400 MHz, d_6-DMSO): δ 9.02 (d, J = 2.8 Hz, 1H), 8.66 (dd, J = 9.0, 2.7 Hz, 1H), 7.54-7.40 (m, 2H), 7.2 (t, J = 8 Hz, 1H).

2-(4-fluorophenoxy)-5-nitropyridine (7) was recrystallized from iPrOH to give a yellow solid (96 mg, 46%): ^{1}H NMR (400 MHz, d_6-DMSO): δ 9.03 (d, J = 2.8 Hz, 1H), 8.62 (dd, J = 9.4, 2.8 Hz, 1H), 7.31-7.27 (m, 5H).

2,4-difluoro-1-(4-nitrophenoxy)benzene (8) was purified by silica gel column chromatography using 2% EtOAc in hexanes as eluent to give a clear oil (65 mg, 33%): ^{1}H NMR (400 MHz, d_6-DMSO): 8.24 (d, J = 8.8 Hz, 2H), 7.58-7.46 (m, 2H), 7.25-7.19 (m, 1H), 7.15 (d, J = 9.2 Hz, 2H).

1-(4-fluorophenoxy)-2,4-dinitrobenzene (9) was recrystallized from iPrOH (107 mg, 50%): ^{1}H NMR (400 MHz, d_6-DMSO): δ 8.9 (s, 1H), 8.46-8.42 (m, 1H), 7.41-7.34 (m,4H), 7.18-7.15 (m, 1H).

1-(2-fluorophenoxy)-2,4-dinitrobenzene (10) was recrystallized from iPrOH to give a yellow crystalline solid (165 mg, 53%): ^{1}H NMR (400 MHz, d_6-DMSO): 8.90 (d, J = 2.4 Hz, 1H), 8.44 (dd, J = 9.2, 2.4 Hz, 1H), 7.54-7.33 (m, 4H), 7.17 (d, J = 9.2 Hz, 1H).

1-(2,4-difluorophenoxy)-2,4-dinitrobenzene (11) was recrystallized from iPrOH at -30°C overnight to give yellow needles (170 mg, 75%; a repeat reaction on a larger scale yielded 2.70 g, 62%): ^{1}H NMR (400 MHz, d_6-DMSO): δ 8.9 (d, J = 2.4 Hz, 1H), 8.43 (dd, J = 8, 2 Hz, 2H), 7.68-7.57 (m, 2H), 7.30-7.22 (m, 2H).

2-(2,4-difluorophenoxy)-1,3-dinitrobenzene (12) was recrystallized from iPrOH to give a yellow powder (94 mg, 42%): ^{1}H NMR (400 MHz, d_6-DMSO): δ 7.69 (d, J = 5.6 Hz, 2H), 6.98 (t, J = 5.6, 1H), 6.69-6.65 (m, 1H), 6.23-6.18 (m, 2H).

3-nitro-phenoxypyridine (18) was synthesized according to an adapted protocol. To a solution of 2-chloro-5-nitropyridine (0.476 g, 3 mmol, 1 eq) in acetone (20 mL) was added phenol (0.28 mL, 3 mmol, 1 eq) and potassium carbonate (0.350 g, 3.45 mmol, 1.15 eq). The reaction mixture was heated to reflux overnight and then worked up according to the general protocol. The product was recrystallized from EtOAc (313 mg, 48%): ^{1}H NMR (400 MHz, d_6-DMSO): δ 8.56 (dd, J = 8, 1.6 Hz, 1H), 8.39 (dd, J = 4.8, 1.6 Hz, 1H), 7.42 (t, J = 7.6, 2H), 7.36 (dd, J = 8, 4.8 Hz, 1H), 7.26 (t, J = 7.6 Hz, 1H), 7.20 (d, J = 7.6 Hz, 2H).

6-(2,4-difluorophenoxy)pyridine-3-amine (19) was synthesized from 2-(2,4-difluorophenoxy)-5-nitropyridine using the same procedure used to prepare **4** and recrystallized from iPrOH to give 21 (90.6 mg, 23%): ^{1}H NMR (400 MHz, d_6-DMSO): δ 7.41-7.34 (m, 2H), 7.24 (dd, J = 14.8, 9.2 Hz, 1H), 7.10-7.06 (m, 2H), 6.82 (d, J = 8.8, 1H), 5.04 (s, 2H).

2-phenoxypyridin-3-amine (21) was synthesized from 3-nitro-phenoxypyridine using the same procedure used to prepare **4** and was used without further purification (24.7 mg, 22%): ^{1}H NMR (400 MHz, d_6-DMSO): δ 7.37 (t, J = 7.6 Hz, 2H), 7.31 (dd, J = 4.8, 1.2 Hz, 1H), 7.14 (t, J = 7.2 Hz, 1H), 7.07 (m, 3H), 6.86 (dd, J = 7.6, 4.8 Hz, 1H), 5.23 (s, 2H).

2-(4-iodophenoxy)-3-nitropyridine (22) was synthesized according to an adapted protocol. To a solution of 2-chloro-5-nitropyridine (0.476 g, 3 mmol, 1 eq) in acetone (20 mL) was added 4-iodophenol (0.66 g, 3 mmol, 1 eq) and potassium carbonate (0.350 g, 3.45 mmol, 1.15 eq). The reaction mixture was heated to reflux overnight and then worked up according to the general protocol. The product was recrystallized from iPrOH (412 mg, 40%). ^{1}H NMR (400 MHz, d_6-DMSO): δ 8.59 (d, J = 8 Hz, 1H), 8.42 (d, J = 4.8 Hz, 1H), 7.79 (d, J = 8.8 Hz, 2H), 7.4 (dd, J = 8, 4.8 Hz, 1H), 7.07 (d, J = 8.4, 2H).

1-(3-fluorophenoxy)-2,4-dinitrobenzene (23) was recrystallized from iPrOH to give pale peach crystals (126 mg, 41%): ^{1}H NMR (400 MHz, d_6-DMSO): δ 8.90 (d, J = 2.8 Hz, 1H), 8.47 (dd, J = 9.2, 2.8 Hz, 1H), 7.57 (dd, J = 15.2, 8 Hz, 1H), 7.31-7.19 (m, 3H), 7.13 (d, J = 7.6 Hz, 1H).

1-(2,4-dinitrophenoxy)-2,3,4-trifluorobenzene (24) was slowly recrystallized from iPrOH overnight at -30°C to give pale yellow crystals (165 mg, 47%): ^{1}H NMR (400 MHz, d_6-DMSO): δ 8.92 (d, J = 2.8 Hz, 1H), 8.44 (dd, J = 9.2, 2.8 Hz, 1H), 7.55-7.39 (m, 3H).

3-(2,4-dinitrophenoxy)-1,2,4,5-tetrafluorobenzene (25) was recrystallized from iPrOH to give cream colored crystals (88 mg, 43%): ^{1}H NMR (400 MHz, d_6-DMSO): δ 8.95 (d, J = 2.8 Hz, 1H), 8.46 (dd, J = 9.6, 2.8 Hz, 1H), 8.11-8.02 (m, 1H), 7.65 (d, J = 9.6 Hz, 1H).

2,4-dichloro-1-(2,4-dinitrophenoxy)benzene (26) was recrystallized from iPrOH to give a pale yellow solid (230 mg, 100%): ^{1}H NMR (400 MHz, d_6-DMSO): δ 8.93 (d, J = 2.4 Hz, 1H), 8.43 (dd, J = 9.2, 2.4 Hz, 1H), 7.94 (d, J = 2 Hz, 1H), 7.63-7.53 (m, 2H), 7.18 (d, J = 9.2 Hz, 1H).

2,4-dinitro 1-(4-(trifluoromethyl)phenoxy)-benzene (27) was recrystallized from iPrOH to give iridescent yellow crystals (132 mg, 52%): ^{1}H NMR (400 MHz, d_6-DMSO): δ 8.11 (s, 1H), 7.67 (d, J = 6 Hz, 1H), 7.07 (d, J = 5.2 Hz, 2H), 6.64 (d, J = 5.6 Hz, 2H), 6.58 (d, J = 6.4, 1H).

1-(2,4-dimethylphenoxy)-2,4-dinitrobenzene (28) was recrystallized from iPrOH to give fine yellow crystals (60 mg, 19%): ^{1}H NMR (400 MHz, d_6-DMSO): δ 8.89 (d, J = 2 Hz, 1H), 8.41 (dd, J = 9.2, 2 Hz, 1H). 7.25 (s, 1H), 7.16 (d, J = 8 Hz, 1H), 7.09 (d, J = 8.4 Hz, 1H), 6.93 (d, J = 9.6 Hz, 1H).

4-(2,4-dinitrophenoxy)benzaldehyde (29) was recrystallized from iPrOH to give a pale yellow solid (154 mg, 69%): ^{1}H NMR (400 MHz, d_6-DMSO): δ 10.01 (s, 1H), 8.94 (d, J = 2.8, 1H), 8.52 (dd, J = 9.6, 2.8 Hz, 1H), 8.05 (dd, J = 6.4, 2.0 Hz, 2H), 7.43 (m, 3H).

4-(2,4-dinitrophenoxy)benzoic acid (30) was purified by silica gel column chromatography using 50:50 hexanes:EtOAc, then recrystallized from iPrOH to give a yellow solid (62 mg, 21%): ^{1}H NMR (400 MHz, d_6-DMSO): 13.08 (s, 1H), 8.95-8.90 (m, 1H), 8.53-8.46 (m, 1H), 8.26 (t, J = 8.8 Hz, 2H), 8.05 (m, 3H).

2-(2,4-dinitrophenoxy)naphthalene (32) was recrystallized from iPrOH to give yellow crystals (137 mg, 40%): ^{1}H NMR (400 MHz, d_6-DMSO): δ 8.93 (d, J = 2.4 Hz, 1H), 8.43 (dd, J = 8.8 Hz, 2.4,

1H), 8.10 (d, J = 8.8 Hz, 1H), 8.0 (d, J = 7.6 Hz, 1H), 7.9 (d, J = 7.6 Hz, 1H), 7.81 (s, 1H), 7.61-7.54 (m, 2H), 7.45 (dd, J = 8.8, 2 Hz, 1H), 7.25 (d, J = 9.2 Hz, 1H).

1-(2,4-dinitrophenoxy)naphthalene (33) was synthesized on a smaller scale from 1-napthol (38 mg, 0.26 mmol, 1 eq) and 1-chloro-2,4-dinitrobenzene (53 mg, 0.26 mmol, 1 eq) with cesium carbonate (98 mg, 0.3 mmol, 1.15 eq) and worked up as described in the general procedure. The product was recrystallized from iPrOH to give a yellow-orange solid (39 mg, 48%): ^{1}H NMR (400 MHz, d_6-DMSO): δ 8.97 (d, J = 2.4 Hz, 1H), 8.37 (dd, J = 9.2, 2.8 Hz, 1H), 8.10 (d, J = 8 Hz, 1H), 7.98 (d, J = 8 Hz, 1H), 7.92 (d, J = 8 Hz, 1H), 7.65-7.61 (m, 3H), 7.45 (d, J = 7.2 Hz, 1H), 7.01 (d, J = 9.6 Hz, 1H).

5-(2,4-dinitrophenoxy)-1*H*-indole (34) was purified by column chromatography in 100% CH_2Cl_2 which gave incomplete separation. Only fractions that appeared to contain pure product (by TLC) were pooled, from which the product was isolated (42 mg, 18% purified yield): ^{1}H NMR (400 MHz, d_6-DMSO): 9.12 (s, 1H), 8.94 (s, 1H), 8.66-8.63 (m, 1H), 8.05 (dd, J = 8.8, 1.6 Hz, 1H), 7.45 (t, J = 2.8, 1H), 7.05 (d, J = 8.4, 1H), 6.98 (s, 1H), 6.7 (d, J = 8.8, 1H), 6.66 (s, 1H).

2-(2,4-dinitrophenoxy)-6-methylpyridine (37) was recrystallized from iPrOH to give pale yellow needles (159 mg, 75%): ^{1}H NMR (400 MHz, d_6-DMSO): δ 8.86 (d, J = 2.8 Hz, 1H), 8.70 (dd, J = 9.2 Hz, 2.4 Hz, 1H), 7.86 (t, J = 7.6 Hz, 1H), 7.70 (d, J = 9.2 Hz, 1H), 7.11 (d, J = 7.6 Hz, 1H), 7.07 (d, J = 8.4 Hz, 1H), 2.26 (s, 3H).

1-(3,5-dimethylphenoxy)-2,4-difluorobenzene (38) was synthesized via a Chan-Lam coupling. To a stirring suspension of copper (II) acetate monohydrate (300 mg, 1.5 mmol, 1.5 eq) in CH_2Cl_2 (10 mL) containing 4Å molecular sieves was added 2,4-difluorophenol (95 µL, 1 mmol, 1 eq), pyridine (161 µL, 2 mmol, 2 eq), and 3,5-dimethylphenylboronic acid (330 mg, 2.2 mmol, 2.2 eq). The reaction was allowed to proceed at room temperature open to the air overnight (12 hours), then filtered through Celite, acidified with 1 N HCl (20 mL) and extracted with in CH_2Cl_2 (3 x 20 mL). The organic layers were washed with brine and dried with Na_2SO_4, then evaporated under rotary vacuum to leave the crude product as a brown oil. The product was purified by silica gel chromatography using 5% EtOAc in hexanes as eluent to yield **40** as a pale yellow-orange oil (18

mg, 8%): ^{1}H NMR (400 MHz, d_6-DMSO): δ 7.46-7.43 (m, 1H), 7.25-7.19 (m, 1H), 7.12-7.07 (m, 1H), 6.73 (s, 1H), 6.55 (s, 2H), 2.22 (s, 6H).

2-((2,4-dinitrophenyl)thio)pyridine (39) was synthesized according to the general procedure for nucleophilic aromatic substitutions using 2-mercaptopyridine in place of a substituted phenol. The product was recrystallized from iPrOH to give yellow needles (184 mg, 86%): MS *m/z* 278.4 (M+H); ^{1}H NMR (400 MHz, d_6-DMSO): δ8.9 (d, J = 3.65, 1H), 8.68-8.66 (m, 1H), 8.37 (dd, J = 8.8, 2.5 Hz, 1H), 7.98-7.96 (m, 1H), 7.79 (d, J = 7.82 Hz, 1H), 7.53 (dd, J = 7.6, 4.9 Hz, 1H), 7.44 (d, J = 9.0, 1H).

2,4-dinitro-*N*-phenylaniline (40) was recrystallized from iPrOH to give fuzzy, deep orange crystals (48 mg, 24%): ^{1}H NMR (400 MHz, d_6-DMSO): δ 10.16 (s, 1H), 8.89 (d, J = 2.4 Hz, 1H), 8.22 (dd, J = 9.60, 2.44, 1H), 7.52 (t, J = 7.6 Hz, 2H) 7.40-7.35 (m, 3H), 7.10 (d, J = 9.6 Hz, 1H).

(2,4-difluorophenyl)(2,4-dinitrophenyl)sulfane (41) was synthesized according to the general procedure but with 2,4-difluorothiophenol instead of a phenol. The reaction proceeded more quickly than the analogous reactions with phenols, requiring only 2 hours at room temperature to proceed to completion by TLC (50:50 EtOAc:hexanes). The product was worked up according to the general procedure and the recrystallized with iPrOH to yield pure **43** (1.56, 76%): ^{1}H NMR (400 MHz, d_6-DMSO): δ 8.89 (s, 1H), 8.31 (d, 1H), 7.91-7.80 (m, 1H), 7.63-7.59 (m, 1H), 7.37-7.33 (m, 1H), 7.05 (d, J = 9.2H, 1H).

***N*-(2,4-difluorophenyl)-2,4-dinitroaniline (42)** was synthesized according to the general procedure but with 2,4-difluoroaniline instead of a phenol and triethylamine as the base. The product was worked up extractively according to the general protocol but was used without further purification: **44** (1.56, 76%): ^{1}H NMR (400 MHz, d_6-DMSO): δ 8.92 (d, 1H), 8.48-8.43 (m, 2H), 7.68-7.62 (m, 2H), 7.45 (d, 1H), 7.37 (d, 1H), 7.29 (d, 1H).

Methyl 4-(4-fluorophenoxy)benzoate (43) was synthesized via a Chan-Lam coupling. To a stirring suspension of 4-methoxycarbonylphenylboronic acid (32 mg, 0.18 mmol, 1 eq) in anhydrous CH_2Cl_2 (3.5 mL) containing 4 Å molecular sieves was added 4-fluorophenol (40 mg, 0.39 mmol, 2.2 eq), pyridine (31 µL, 0.36 mmol, 2 eq), and copper (II) acetate (48 mg, 0.267

mmol). The reaction was allowed to proceed at room temperature open to the air for 6 h, then was filtered through Celite, acidified with 1 N HCl (20 mL) and extracted with in CH_2Cl_2 (3 x 20 mL). The organic layers were washed with brine and dried with Na_2SO_4, then evaporated under rotary vacuum to leave the crude product as a brownish oil. The product was purified by silica gel chromatography using 5% EtOAc in hexanes as eluent to yield **40** as a colorless oil, which crystallized upon standing (68 mg, 82%): ^{1}H NMR (400 MHz, d_6-DMSO): δ 7.94 (d, J = 8.8 Hz, 2H), 7.30-7.26 (m, 2H), 7.19-7.16 (m, 2H), 7.01 (d, J = 8.8 Hz, 2H).

2,5-difluorophenyl 4-nitrobenzoate (44). 4-nitrobenzoyl chloride (2 g, 10.8 mmol, 1 eq) was dissolved in CH_2Cl_2 (40 mL). 2,4-difluorophenol (1.5 g, 11.9 mmol, 1.1 eq) was then added, followed by triethylamine (1.82 mL, 14.0 mmol, 1.3 eq). The reaction was allowed to stir at RT for 8 hours, then worked up by addition of saturated aqueous $NaHCO_3$ (50 mL) and extracted with CH_2Cl_2 (3 x 30 mL). The combined organic layers were washed with brine and dried with Na_2SO_4, then evaporated under rotary vacuum to leave the crude product as a yellow powdery solid, which was recrystallized from iPrOH to yield pure **46** (1.93 g, 64%; a repeat reaction on a larger scale yielded 4.91 g, 81%): ^{1}H NMR (400 MHz, d_6-DMSO): δ 8.4 (d, J = 10 Hz, 4H), 7.61-7.53 (m 2H), 7.23 (s, 1 H).

2,4-dinitrophenyl 2,4-difluorobenzoate (45). 2,4-dinitrophenol stabilized with water (2.4 g, ~12.4 mmol, ~1.1 eq) was added to a 100 mL round-bottomed flask and dissolved in CH_2Cl_2 (40 mL). Activated powdered molecular sieves (4Å) were added to absorb the water from the reagent. 2,4-difluorobenzoyl chloride (1.4 mL, 11.3 mmol, 1 eq) was added via syringe, followed by triethylamine (1.82 mL, 14.0 mmol, 1.3 eq). The color of the solution immediately lightened from a vivid yellow to a pale yellow. The reaction was allowed to stir at RT for 8 hours, then was worked up by addition of saturated aqueous $NaHCO_3$ (50 mL) and extracted with CH_2Cl_2 (3 x 30 mL). The combined organic layers were washed with brine and dried with Na_2SO_4, then evaporated under rotary vacuum to leave the crude product as a bright yellow solid, which was recrystallized from iPrOH to yield pure **46** as yellow needles (2.44 g, 66%): ^{1}H NMR (400 MHz, d_6-DMSO): δ 8.93 (d, J = 2.4 Hz, 1H), 8.71 (dd, J = 9.2, 3.2 Hz, 1H), 8.28-8.22 (m, 1H), 8.00 (d, J = 8.8 Hz, 1H), 7.60-7.55 (m, 1H), 7.40-7.35 (m, 1H).

4,4'-((4,6-dinitro-1,3-phenylene)bis(oxy))bis(1,3-difluorobenzene) (46) was synthesized according to the general procedure for nucleophilic aromatic substitutions, except that 2.5 eq of 2,4-difluorophenol (1.0 mL, 10.5 mmol) and 4 eq of cesium carbonate (5.5 g, 16.9 mmol) were reacted with 1,5-dichloro-2,4-dinitrobenzene (1.0 g, 4.2 mmol, 1 eq) in DMF (40 mL). TLC in 90:10 hexanes:EtOAc indicated that the reaction was complete after stirring for about 15 min at RT, at which point the reaction mixture was filtered to remove the cesium carbonate, acidified with the addition of 1 N HCl (100 mL) and extracted with EtOAc (3 x 40 mL). The organic layers were washed with brine and dried with Na_2SO_4. The crude product was recrystallized from isopropanol to yield **48** as pale yellow crystals (1.13 g, 63%): ^{1}H NMR (400 MHz, d_6-DMSO): δ 8.98 (s, 1H), 7.55-7.49 (m, 2H), 7.46-7.40 (m, 2H), 7.17-7.15 (m, 2H), 6.43 (s, 1H).

1,4-bis(2,4-dinitrophenoxy)benzene (47). 1-chloro-2,4-dinitrobenzene (3.7 g, 18.2 mmol, 2 eq) was dissolved in DMF (50 mL) and hydroquinone (1 g, 9.1 mmol, 1 eq) was added. Triethylamine (0.78 mL, 20 mmol, 2.2 eq) was added, which caused a color change from bright yellow-orange through red, then brown, then green. After 3 h of stirring at RT TLC in 50:50 EtOAc:hexanes still showed starting material 1-chloro-2,4-dinitrobenzene, but also showed several other spots, so the reaction was stopped. The pH of the reaction mixture was determined to be 5.5, so it was neutralized with the addition of saturated aqueous $NaHCO_3$ (50 mL) and extracted with EtOAc (3 x 40 mL). The organic layers were washed with brine and dried with Na_2SO_4. The crude product was recrystallized from isopropanol to yield **49** (720 mg, 18%): ^{1}H NMR (400 MHz, d_6-DMSO): δ 8.92 (d, J = 2.8 Hz, 1H), 8.46 (dd, J = 9.6, 2.8 Hz, 2H), 7.45 (s, 4 H), 7.31 (dd, J= 9.6, 2.8 Hz, 2H).

4.12. Notes

The fragment-based screen by NMR was carried out with Tomek Cierpicki and help from members of the Cierpicki laboratory, especially George Lund. The Klevit laboratory provided a vector containing the Hsp27 core domain as well as purified, isotopically labelled protein that was used in the original primary screen. Xiaokai Li is gratefully acknowledged for synthetic chemistry advice. Phani Ghanakota ran the MixMD simulation with Heather Carlson, and made suggestions on additional compounds to synthesize for Site 3. Brian DeVrees carried out the pilot differential scanning fluorimetry screen that resulted in the identification of captopril for Site 1. The affinities of full length BAG3 and IXI peptides binding to Site 2 were determined by isothermal calorimetry experiments carried out by Jennifer Rauch and Rebecca Freilich in the

Gestwicki laboratory. Rebecca Freilich is leading the tethering screening effort for Site 1 and co-crystallization efforts for each of the ligand binding sites.

4.13. References

1. Hochberg GK, Ecroyd H, Liu C, Cox D, Cascio D, Sawaya MR, et al. The structured core domain of alphaB-crystallin can prevent amyloid fibrillation and associated toxicity. Proceedings of the National Academy of Sciences of the United States of America. 2014;111(16):E1562-70.
2. Baranova EV, Weeks SD, Beelen S, Bukach OV, Gusev NB, Strelkov SV. Three-dimensional structure of alpha-crystallin domain dimers of human small heat shock proteins HSPB1 and HSPB6. Journal of molecular biology. 2011;411(1):110-22.
3. Lelj-Garolla B, Mauk AG. Self-association and chaperone activity of Hsp27 are thermally activated. The Journal of biological chemistry. 2006;281(12):8169-74.
4. Lambert H, Charette SJ, Bernier AF, Guimond A, Landry J. HSP27 multimerization mediated by phosphorylation-sensitive intermolecular interactions at the amino terminus. The Journal of biological chemistry. 1999;274(14):9378-85.
5. Stengel F, Baldwin AJ, Painter AJ, Jaya N, Basha E, Kay LE, et al. Quaternary dynamics and plasticity underlie small heat shock protein chaperone function. Proceedings of the National Academy of Sciences of the United States of America. 2010;107(5):2007-12.
6. Arrigo AP. Human small heat shock proteins: protein interactomes of homo- and hetero-oligomeric complexes: an update. FEBS letters. 2013;587(13):1959-69.
7. Arrigo AP, Simon S, Gibert B, Kretz-Remy C, Nivon M, Czekalla A, et al. Hsp27 (HspB1) and alphaB-crystallin (HspB5) as therapeutic targets. FEBS letters. 2007;581(19):3665-74.
8. Almeida-Souza L, Goethals S, de Winter V, Dierick I, Gallardo R, Van Durme J, et al. Increased monomerization of mutant HSPB1 leads to protein hyperactivity in Charcot-Marie-Tooth neuropathy. The Journal of biological chemistry. 2010;285(17):12778-86.
9. Lexa KW, Carlson HA. Full Protein Flexibility Is Essential for Proper Hot-Spot Mapping. J Am Chem Soc. 2010;133(2):200-2.
10. Clark AR, Naylor CE, Bagneris C, Keep NH, Slingsby C. Crystal structure of R120G disease mutant of human alphaB-crystallin domain dimer shows closure of a groove. Journal of molecular biology. 2011;408(1):118-34.
11. Bagneris C, Bateman OA, Naylor CE, Cronin N, Boelens WC, Keep NH, et al. Crystal structures of alpha-crystallin domain dimers of alphaB-crystallin and Hsp20. Journal of molecular biology. 2009;392(5):1242-52.
12. Eaton P, Fuller W, Shattock MJ. S-thiolation of HSP27 regulates its multimeric aggregate size independently of phosphorylation. The Journal of biological chemistry. 2002;277(24):21189-96.
13. Zavialov A, Benndorf R, Ehrnsperger M, Zav'yalov V, Dudich I, Buchner J, et al. The effect of the intersubunit disulfide bond on the structural and functional properties of the small heat shock protein Hsp25. International journal of biological macromolecules. 1998;22(3-4):163-73.
14. Sowdhamini R, Srinivasan N, Shoichet B, Santi DV, Ramakrishnan C, Balaram P. Stereochemical modeling of disulfide bridges. Criteria for introduction into proteins by site-directed mutagenesis. Protein engineering. 1989;3(2):95-103.
15. Indu S, Kochat V, Thakurela S, Ramakrishnan C, Varadarajan R. Conformational analysis and design of cross-strand disulfides in antiparallel beta-sheets. Proteins. 2011;79(1):244-60.

16. Haworth NL, Feng LL, Wouters MA. High torsional energy disulfides: relationship between cross-strand disulfides and right-handed staples. Journal of bioinformatics and computational biology. 2006;4(1):155-68.
17. Wouters MA, George RA, Haworth NL. "Forbidden" disulfides: their role as redox switches. Current protein & peptide science. 2007;8(5):484-95.
18. Arrigo AP. Hsp27: novel regulator of intracellular redox state. IUBMB life. 2001;52(6):303-7.
19. Christians ES, Ishiwata T, Benjamin IJ. Small heat shock proteins in redox metabolism: implications for cardiovascular diseases. The international journal of biochemistry & cell biology. 2012;44(10):1632-45.
20. Diaz-Latoud C, Buache E, Javouhey E, Arrigo AP. Substitution of the unique cysteine residue of murine Hsp25 interferes with the protective activity of this stress protein through inhibition of dimer formation. Antioxidants & redox signaling. 2005;7(3-4):436-45.
21. Arrigo AP, Virot S, Chaufour S, Firdaus W, Kretz-Remy C, Diaz-Latoud C. Hsp27 consolidates intracellular redox homeostasis by upholding glutathione in its reduced form and by decreasing iron intracellular levels. Antioxidants & redox signaling. 2005;7(3-4):414-22.
22. Zavialov AV, Gaestel M, Korpela T, Zav'yalov VP. Thiol/disulfide exchange between small heat shock protein 25 and glutathione. Biochimica et biophysica acta. 1998;1388(1):123-32.
23. Pasupuleti N, Gangadhariah M, Padmanabha S, Santhoshkumar P, Nagaraj RH. The role of the cysteine residue in the chaperone and anti-apoptotic functions of human Hsp27. Journal of cellular biochemistry. 2010;110(2):408-19.
24. Mymrikov EV, Seit-Nebi AS, Gusev NB. Large potentials of small heat shock proteins. Physiological reviews. 2011;91(4):1123-59.
25. Jehle S, Rajagopal P, Bardiaux B, Markovic S, Kuhne R, Stout JR, et al. Solid-state NMR and SAXS studies provide a structural basis for the activation of alphaB-crystallin oligomers. Nature structural & molecular biology. 2010;17(9):1037-42.
26. Delbecq SP, Jehle S, Klevit R. Binding determinants of the small heat shock protein, alphaB-crystallin: recognition of the 'IxI' motif. The EMBO journal. 2012;31(24):4587-94.
27. Fuchs M, Poirier DJ, Seguin SJ, Lambert H, Carra S, Charette SJ, et al. Identification of the key structural motifs involved in HspB8/HspB6-Bag3 interaction. The Biochemical journal. 2010;425(1):245-55.
28. Hishiya A, Salman MN, Carra S, Kampinga HH, Takayama S. BAG3 directly interacts with mutated alphaB-crystallin to suppress its aggregation and toxicity. PloS one. 2011;6(3):e16828.
29. Laganowsky A, Liu C, Sawaya MR, Whitelegge JP, Park J, Zhao M, et al. Atomic view of a toxic amyloid small oligomer. Science. 2012;335(6073):1228-31.
30. Hajduk PJ, Huth JR, Fesik SW. Druggability indices for protein targets derived from NMR-based screening data. J Med Chem. 2005;48(7):2518-25.
31. Abad-Zapatero C. Ligand efficiency indices for effective drug discovery. Expert opinion on drug discovery. 2007;2(4):469-88.
32. Lewis IA, Schommer SC, Markley JL. rNMR: open source software for identifying and quantifying metabolites in NMR spectra. Magnetic resonance in chemistry : MRC. 2009;47 Suppl 1:S123-6.
33. Goddard TD, Kneller DG. SPARKY3. University of California, San Francisco.
34. Moradei O, inventorPreparation of amide derivatives as inhibitors of histone deacetylase2005.
35. Colabufo NA, Berardi F, Perrone MG, Cantore M, Contino M, Inglese C, et al. Multi-drug-resistance-reverting agents: 2-aryloxazole and 2-arylthiazole derivatives as potent BCRP or MRP1 inhibitors. ChemMedChem. 2009;4(2):188-95.

36. Gillespie P, Goodnow R, Kowalczyk A, Le K, Zhang Q, inventors; Hoffman-La Roche Inc, assignee. Preparation of thiazoles as inhibitors of 11beta-hydroxysteroid dehydrogenase2007.
37. Nakayama H, Ishihara K, Akiba S, Uenishi J. Synthesis of N-[2-(2,4-Difluorophenoxy)trifluoromethyl-3-pyridyl]sulfonamides and their inhibitory activities against secretory phospholipase A(2). Chemical & pharmaceutical bulletin. 2011;59(8):1069-72.

Chapter 5

Conclusions and Future Directions

5.1. Conclusions

Small heat shock proteins are important molecular chaperones that are poorly understood despite widespread interest in their disease-modifying capacity. We were interested in sHsps not only because of their demonstrated therapeutic value, but also because they are emblematic of a large number of potential drug targets identified through recent genome-wide association studies. sHsps have many features of so-called 'undruggable' targets, as discussed in Chapter 1, and they therefore represented an interesting test case for the application of computational and biophysical ligand discovery strategies. We reasoned that discovery strategies that proved useful for sHsps might also be valuable for many other non-enzymatic and chemically unvalidated potential targets. The goal of this thesis was to identify small molecule modulators of sHsps, and in doing so to understand the utility of a number of different ligand discovery techniques for non-canonical targets. I intended to develop chemical tools that would enable the study of these enigmatic proteins by perturbing the structure and function in predictable ways, potentially informing the development of future therapeutic agents.

As discussed in Chapter 2, it quickly became clear that sHsps were prone to aggregation, which led to the hypothesis that sHsp ligands might be useful as pharmacological chaperones (PCs). PCs act by stabilizing native conformations of proteins to discourage unfolding and aggregation. Together with others inside and outside of the laboratory, I applied a number of orthogonal ligand identification strategies that were introduced in Chapter 1 to target sHsps. Collectively, these efforts resulted in four small molecule or peptidic scaffolds that engage three distinct sites within the conserved α-crystallin domain of at least two sHsps (Figure 5.1). In Chapter 3, we described the development of a class of oxysterol ligands for αB-crystallin that prevent and reverse the protein aggregation associated with cataracts; this scaffold is being further developed as a potential therapeutic for the treatment of cataracts. In Chapter 4, we described

the application of computational approaches, differential scanning fluorimetry, fragment-based NMR screening and rational design to identify ligands for Hsp27. We identified chemical matter that engaged three binding sites within Hsp27, and found that short peptides engaging one site can also act as PCs. Thus, despite the absence of sHsp enzymatic activity, known small molecule binding sites, or previously known small molecule ligands, we identified PCs that bind to two distinct sites.

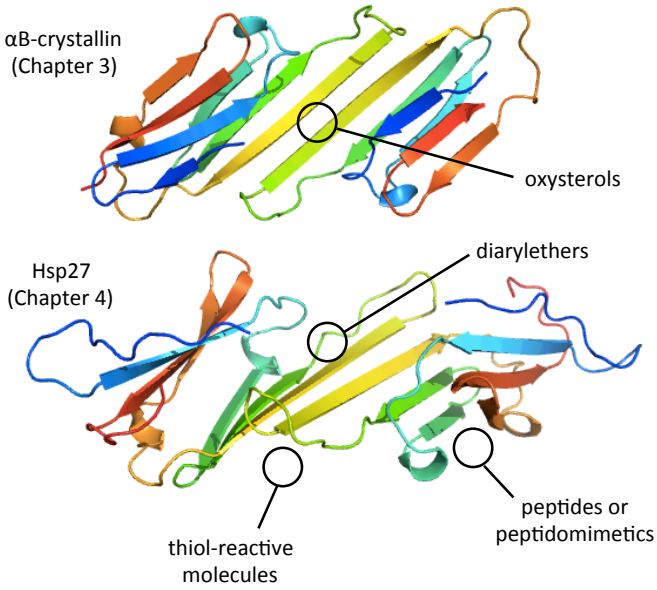

Figure 5.1: Biophysical methods for ligand discovery for the 'undruggable' sHsps resulted in four scaffolds with affinity for three distinct sites in the conserved core α-crystallin domains of αB-crystallin and Hsp27, representing important first steps towards the development of chemical probes and potential therapeutics targeting sHsps.

In post-genomic target identification, the identification of first-in-class ligands is an important step towards the development of therapeutics targeting new proteins. Newly discovered disease-modifying targets can be genetically validated through genome-wide association studies, the study of point mutations, and animal models. However, such targets must also be 'chemically validated,' demonstrating the presence of function-modifying binding sites that can accommodate ligands with good affinity. This work may be a useful precedent for PC or other ligand discovery for new non-canonical or challenging targets; the strengths and weaknesses of the approaches applied in this thesis should inform the future design of screening campaigns against other 'undruggable' targets.

In the next sections, I will discuss some ideas for how this thesis might provide a framework for the further development of ligands and potential therapeutics for sHsps, as well as the application of these principles to other non-canonical targets.

5.2. Future directions

5.2.1. Immediate next steps in ligand development for sHsps

The immediate goals for further development of ligand development for αB-crystallin are translational in nature, while the immediate next steps for Hsp27 ligands are oriented more towards chemical biology. The pharmacological chaperones for R120G αB-crystallin that were discussed in Chapter 3 will be developed as potential therapeutics for the treatment of cataracts; first, their safety and efficacy will be evaluated in animal models of disease, and the pharmacokinetics of the lead molecules in the lens will be systematically studied. Important outstanding questions will be addressed. First, the duration of therapeutic effect will be studied: once cataract is reversed, does protein aggregation recur? How long after the molecule is excreted from the lens tissue does this happen? Second, the mechanism of oxysterol action will be further investigated: what quaternary forms of αB-crystallin are favored by small molecule treatment *in vivo*? Does oxysterol binding cause the protein to revert back to native-like oligomers? Can we observe and measure the recovery of αB-crystallin chaperone function towards other lens structural proteins *in vitro*? Additionally, second-generation molecules based on this scaffold and on potential hits identified from a second, larger high-throughput screen will be developed.

On the other hand, each Hsp27-binding scaffold will be evolved into high-affinity, specific, cell-permeable probes for Hsp27 biology targeting each binding site described in Chapter 4. Co-crystal structures of each molecule with the Hsp27 α-crystallin domain are expected to significantly facilitate these efforts. Another graduate student in the Gestwicki laboratory, Rebecca Freilich, is already working towards these goals. Tight-binding scaffolds that engage each site should inform our understanding of allostery within the Hsp27 structure. Site 2, the site of the endogenous protein-protein interaction, appears to be promising as a pharmacological chaperone binding site and may also accommodate inhibitors of the homomeric (Hsp27-Hsp27) and heteromeric (Hsp27-BAG3) protein-protein interactions.

There is still a long way to go to develop αB-crystallin PCs for the treatment of cataracts and the remaining scaffolds into useful tools for sHsp chemical biology; this work represents a very early effort to identify small molecule modulators of small heat shock proteins. However, by analogy with the Hsp70 chemical biology work carried out in the Gestwicki lab over the past nine years, further elaboration of these scaffolds and binding sites is expected to accelerate the comprehensive study of these interesting and unusual chaperones.

5.2.2. The use of chemical probes to address outstanding questions in sHsp biology

As discussed in Chapter 2, aggregation of these proteins appears to be an important contributing factor to the pathology associated with many of the disease-causing mutations. But what regulates the function of the native conformations of the proteins? Do discrete structures have exposed client-binding regions with various properties, and can chemical probes be identified which stabilize those discrete structures? Pharmacological chaperones are molecules that preferentially stabilize native forms of a protein to prevent unfolding and aggregation, but can this principle be extended to the identification of molecules that stabilize a particular native conformation of a protein? While the ligands identified in this body of work appear to differentiate between native and non-native conformations, can tools be identified which stabilize one native conformation over another native conformation? Analogues for this type of PC exist in other areas of biology. For example, recent work identified a peptidic inhibitor of caspase-6 that stabilizes an inactive, tetrameric conformation of the protein (1). Even some ligands from classic pharmacology might, in fact, act via a PC mechanism; for example, recent studies suggest that nicotine exerts its effects by thermodynamically stabilizing a single conformation of the acetylcholine receptor (2, 3). However, our emerging understanding of sHsp structure is one of a dynamic, fluid system made up of a number of low-affinity interactions, and there is a dearth of structural knowledge of the full-length proteins. It remains to be seen if small molecules can be identified which differentiate between native tertiary or quaternary structures.

An extension of the screening strategies used in this work might explicitly address this question, using a technique that directly reports on the native, quaternary structure of an sHsp. For example, a high-throughput size based separation technique like capillary electrophoresis or thermophoresis could be leveraged to directly screen for molecules that perturb the quaternary

structure of Hsp27. Techniques such as SEC-MALS, analytical ultracentrifugation, small angle x-ray scattering, and electron microscopy would be useful for the lower-throughput characterization of conformations favored by hits identified in such platforms and their subsequent optimization. If a set of small molecules favoring distinct native-like quaternary conformations could be identified, such a toolkit would be fascinating to study in a cellular context. The ultimate goal of this discovery effort would be to identify a molecule that could activate the protein in a disease model to phenocopy genetic modulation of protein expression level. As discussed in Chapter 1, a small molecule that could increase the concentration of an 'active' chaperone conformation of an sHsp and phenocopy overexpression would be expected to be powerfully protective in neurodegeneration and in many other diseases of protein misfolding as well.

5.2.3. Development of first-in-class ligands for nontraditional or 'undruggable' targets

A generalized flowchart for target validation and discovery in the post-genomic era might look like the one presented in Figure 5.2. Many targets are identified through genome-wide association studies, in which proteins are overexpressed in response to disease conditions and thereby implicated in pathology. However, a subset of those also have disease-associated point mutations that cause congenital manifestations of similar illnesses in a small patient population. An even smaller subset may have proof-of-concept in modifying the progression of disease in animal models. Non-canonical targets that possess two or three of these characteristics may be most promising for discovery efforts. In addition to providing support for the disease-modifying capacity of the target, point mutations that modify the target's activity provide a starting framework for differentiating healthy and pathological characteristics of the protein of interest, and suggest an avenue towards the identification of activity-modifying ligands. Small heat shock proteins, especially Hsp27 and αB-crystallin, have all three of these types of genetic evidence supporting their promise as therapeutic targets.

In an ideal situation, parallel development paths would be taken. One workflow would be focused on understanding the effects of the mutations on relevant protein-protein interactions, substrate or ligand interactions, enzyme activity if the target has such, subcellular trafficking or localization, protein folding and stability, tertiary and quaternary structure, and post-translational modifications. One of the unanticipated difficulties surrounding this project and

discovery against non-enzymes in general is the lack of appropriate secondary follow-up assays. Thus, concurrent with discovery efforts, the development of bioassays that report on relevant biological activity is essential. A parallel workflow might resemble the work undertaken against Hsp27 in Chapter 4: first, structurally characterize the target, in whole or in part, and then use a validated computational technique (like MixMD) or experimental techniques (like solvent mapping by NMR or fragment-based screening) to identify ligandable binding sites in the target. Then, suitable screening techniques can be applied to generate first-in-class ligands for any identified pockets. Once ligands are identified, they may then be characterized for activity in each category in the left-hand column of Figure 5.2. The iterative process of optimization of subsequent screening hits, the continuing assessment and improvement of useful bioassays for probing the target's biological function, and the understanding of the target's biological function can all subsequently improve in parallel.

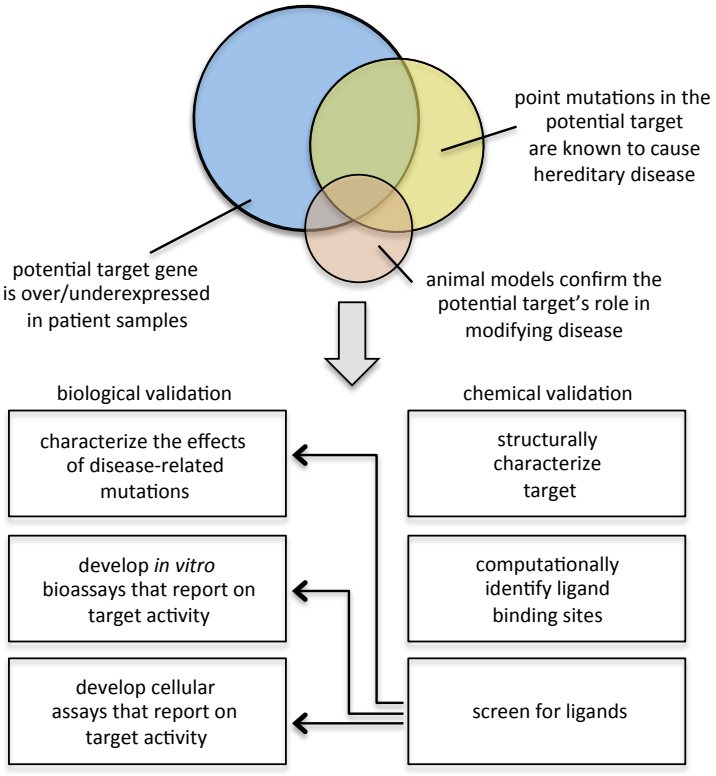

Figure 5.2. General workflow for the identification of ligands for non-canonical targets.

A 2011 analysis suggested that only 435 unique biomolecules in the human genome are the targets of therapeutic drugs (4). The same study found that in an average year, only four new drugs are approved that hit novel targets in the human genome, and the majority of those

targets are enzymes, receptors, or transporters (4). To truly leverage the wealth of knowledge that genomics provides supporting the identification of new drug targets, it is important to work towards expanding the definition of 'druggable,' and develop approaches that are tailored for targets other than enzymes and receptors. As discussed in Chapter 1, this means expanding our armamentarium of chemical libraries and screening techniques. Lastly, the broader utility of the pharmacological chaperone concept should be explored, especially in diseases of protein misfolding.

5.3. Closing thoughts: the concept of 'druggability' is evolving

Are sHsps 'druggable' targets? When I began this project, I envisioned the discovery of allosteric small molecules that perturbed structure in a targeted way, *i.e.* by shifting the oligomerization of an sHsp towards dimers or tetramers, or by altering the tertiary structure in such a way that a high-affinity substrate binding site was exposed. Our screening efforts were in theory open-ended enough to enable the discovery of such molecules, though they were not biased towards that end. However, as it turned out, the major contribution of this work was the discovery and development of molecules that stabilize the native fold over non-native species as opposed to molecules that distinguish between native quaternary or tertiary structures. We learned that many of the pathological mutations in sHsps cause gain of toxic function aggregation, and we identified molecules that bind to native conformations to disfavor (and even to reverse) the aggregation of these proteins. Our hypotheses have evolved and become better suited to the study of sHsps, given an understanding of their complexities and a practical knowledge of the assays that are amenable for their study. Pharmacological chaperones that discriminate between native tertiary and quaternary conformations of sHsps are conceptually intriguing as tools for chemical biology, but their discovery may require a more focused approach and would certainly be facilitated by a better structural understanding of sHsps.

In a broader sense, I want to highlight a fundamental dilemma associated with categorizing 'druggable' targets and 'drug-like' molecules on the basis of past success stories (5). If we categorize 'druggable' targets as only those that resemble successfully drugged targets, and 'drug-like' small molecules as only those that resemble current FDA-approved compounds, then we limit innovation and exclude the possibility that either target space or drug space might be expanded by new technology. In other words, until we try – and fail – it is not clear that any

target is ‘undruggable’ and, even then, it is only ‘undruggable’ under the current paradigm. Accordingly, we have focused this thesis on exploring high-throughput methods for selecting ligands with affinity for non-canonical targets. These methods have been used against small heat shock proteins, targets that lack enzymatic activity, structural information, existing ligands, or known ligand binding sites. Because of these characteristics, small heat shock proteins are challenging examples of non-canonical targets. However, using multiple methods, I show that they are amenable to drug discovery. Combined with efforts to expand chemical space and enrich for modulators of non-canonical targets, these advances are helping to expand the definition of ‘druggable’. However, it is unlikely that these examples represent the final word on drug discovery for post-genomic targets. The real lesson is that no target is ‘undruggable’.

5.4. References

1. Stanger K, Steffek M, Zhou L, Pozniak CD, Quan C, Franke Y, et al. Allosteric peptides bind a caspase zymogen and mediate caspase tetramerization. Nat Chem Biol. 2012;8(7):655-60.
2. Kuryatov A, Luo J, Cooper J, Lindstrom J. Nicotine acts as a pharmacological chaperone to up-regulate human alpha4beta2 acetylcholine receptors. Mol Pharmacol. 2005;68(6):1839-51.
3. Lester HA, Xiao C, Srinivasan R, Son CD, Miwa J, Pantoja R, et al. Nicotine is a selective pharmacological chaperone of acetylcholine receptor number and stoichiometry. Implications for drug discovery. AAPS J. 2009;11(1):167-77.
4. Rask-Andersen M, Almen MS, Schioth HB. Trends in the exploitation of novel drug targets. Nature reviews Drug discovery. 2011;10(8):579-90.
5. Drewry DH, Macarron R. Enhancements of screening collections to address areas of unmet medical need: an industry perspective. Curr Opin Chem Biol. 2010;14(3):289-98.

Appendix

Evaluation of a differential scanning fluorimetry platform to identify ligands of the transcription factor HSF1

A.1. Abstract

HSF1 is a compelling therapeutic target for diseases in which proteostasis is dysregulated, including neurodegenerative diseases (1). Like sHsps, HSF1 is a noncanonical target for drug discovery: it lacks enzymatic activity, known small molecule ligands and known ligand binding sites. We evaluated differential scanning fluorimetry as a potential screening platform for the identification of ligands for HSF1. This appendix describes a series of experiments undertaken in order to optimize the performance of the DSF platform for the analysis of HSF1 and describes a DSF pilot screen targeting this important transcription factor. The results of the pilot screen and a partial reconfirmation effort are presented, and alternative screening strategies are discussed. Initial efforts to characterize domain constructs of HSF1 by electron microscopy are also presented, along with future directions for this project.

A.2. HSF1 is the master regulator of the heat shock response

Chaperone proteins are upregulated in response to a number of cellular stresses, including elevated temperature, oxidative stress, exposure to heavy metals, inflammation, and infection. Molecular chaperones operate as an interconnected network to maintain proteostasis under such stresses. Heat shock transcription factor 1 (HSF1) coordinates and controls the cellular heat shock response by mediating the expression of each stress-inducible chaperone (2). Its transcriptional activity is tightly regulated by a number of factors, including complexation with chaperone proteins, quaternary structure, subcellular localization, and post-translational modifications (1). Targeting HSF1 may enable the coordinated upregulation of generally protective stress-responsive chaperones at the level of transcription (1).

A.2.1. Activation of HSF1

Activation of HSF1 is a highly regulated process. Under unstressed conditions, HSF1 is localized in the cytoplasm in a metastable state, bound to Hsp90, Hsp70, and other chaperones (3). Under proteotoxic stress conditions, increased levels of unfolded proteins compete with HSF1 for binding to the chaperone components of the multiprotein complex, freeing HSF1 from Hsp90 (1, 4). HSF1 can then homotrimerize and translocate to the nucleus. Trimerization is mediated by three leucine zipper domains near the N-terminus of the protein and enforced by oxidation of disulfide bonds and phosphorylation of serine residues (5, 6). Inside the nucleus, the HSF1 trimer can bind to *cis*-acting heat shock elements in the promoter regions of heat shock genes, consisting of repeating nGAAn sequences. After binding to DNA, HSF1 releases Hsp70 and its co-chaperones (7). HSF1 is then sumoylated and recruits the transcriptional elongation factor p-TEFb and RNA polymerase II, thus initiating increased expression of heat shock proteins. The residence of HSF1 on its promoter regions is regulated by a negative feedback loop; increased expression of chaperone proteins eventually favors sequestration of HSF1 in the cytoplasm (2, 8, 9).

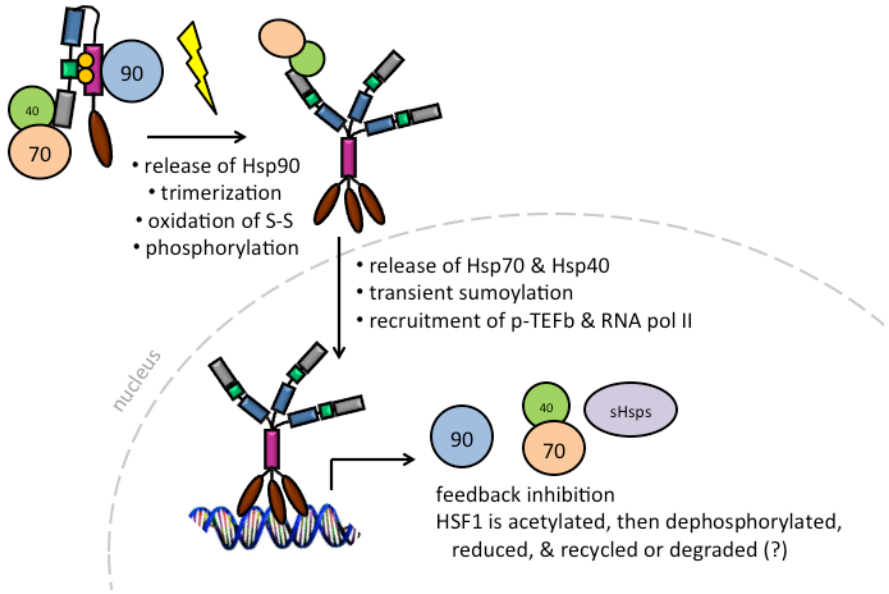

Figure A.1. HSF1 trimerizes, translocates to the nucleus, and initiates expression of heat shock proteins in response to stress conditions. Adapted from (2).

A.2.2. Domain structure of HSF1

HSF1 is a 529-residue, 57-kDa multidomain protein (Figure A.2). The N-terminus contains a wing-turn-helix DNA binding domain and three leucine zippers that mediate trimerization of the transcription factor. Deletion of the leucine zipper repeats impairs trimerization, accompanied by a reduced heat shock response in cells (2). The leucine zipper repeat domain is followed by a

20 kDa middle regulatory domain that is proposed to interact with Hsp90. This region is extensively modified by phosphorylation, sumoylation, and acetylation (4, 7, 8, 10). A fourth leucine zipper (LZ4) appears to repress trimerization by interacting with the first three leucine zippers in the monomeric conformation (2, 11). Finally, the extreme C-terminus contains an acidic, intrinsically disordered transactivation domain, which is thought to contain the binding site for Hsp70 (2).

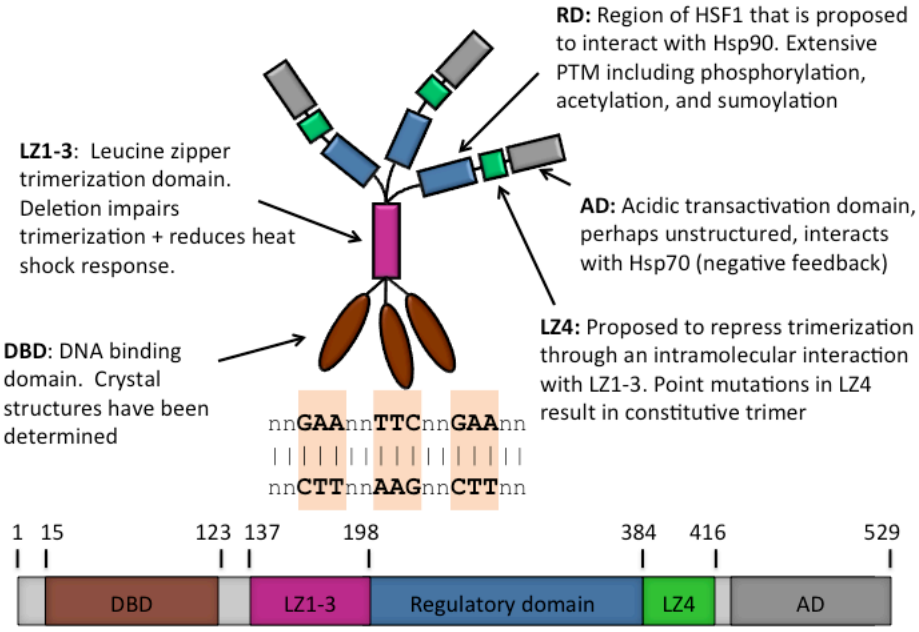

Figure A.2. Domain architecture of HSF1 and idealized heat shock element sequence.

A.2.3. HSF1 is a non-canonical therapeutic target

HSF1 activation deploys higher levels of expression of chaperones, including sHsps. For this reason, activation of HSF1 may be a promising therapeutic strategy in diseases of protein misfolding (2). A small molecule modulator could activate HSF1 in a number of different ways. A ligand could directly bind HSF1 and inhibit its interaction with chaperones in the cytoplasm, favoring diffusion into the nucleus; it could induce or stabilize trimerization, which would be expected to favor DNA binding; or it could otherwise stabilize the HSF1-nucleic acid complex. Similar to sHsps, HSF1 activation confers a selective advantage to cancer cells, which have to survive under stress conditions. Thus, a pharmacological means to activate or upregulate HSF1 would be expected to be protective in protein–misfolding associated neurotoxicities, but inhibition of HSF1 would be preferable in cancers (1, 2). There is a lack of detailed mechanistic understanding of the mechanism of action of HSF1 and especially its protein-protein

interactions. Chemical probes that tune its structure and DNA-binding capacity in predictable ways *in vitro* would be invaluable tools for HSF1 biology in cell culture and *in vivo* (1).

However, HSF1 does not have known small molecule binding sites, and its protein-protein interactions are poorly characterized. It lacks structural characterization with the exception of its conserved DNA binding domain. DNA binding domains are notoriously difficult targets due to the electrostatic character of nucleic acid binding interactions (12). Moreover, HSF1's DNA binding activity is the only robust *in vitro* metric associated with its structure and function; like sHsps, it lacks intrinsic enzymatic activity. Its homo-oligomerization is linked to regulation of its transcriptional activities, further complicating ligand discovery efforts. Chemical validation of HSF1 as a potential therapeutic target necessitates asking the same types of questions that apply to sHsps: Are there ligand binding pockets? Can molecules be found which modulate its structure and function? What is the 'active' conformation of the protein? What does it mean to activate or inhibit HSF1? How can one design a screen for allosteric small molecule modulators? Because HSF1 represents an interesting target and because its study could benefit from identified ligands, we considered strategies for screening against HSF1. We chose to examine differential scanning fluorimetry as a method for the identification of small molecule ligands.

A.3. Characterization of HSF1 by differential scanning fluorimetry

Differential scanning fluorimetry is a stability-based, label-free biophysical screening technique, introduced in Chapter 1 and applied to sHsps in Chapters 3 and 4. DSF is well suited to the identification of ligands that interact with a target protein in the absence of knowledge of ligand binding sites, and is not impeded by conformational heterogeneity. The technique is high-throughput, uses small amounts of protein, and is amenable to discovery in the absence of target enzymatic activity. Ligands contribute free energy of binding to native or nonnative forms of the protein or otherwise favor alternative conformations that exhibit differential stabilities. We wanted to assess the utility of DSF for the identification of HSF1 ligands.

Recombinantly expressed and purified HSF1 was found to be well behaved in the DSF platform, giving consistent sigmoidal melting curves with midpoints ranging from 33.0°C and 47.0°C, depending on the composition of the buffer used in the assay. We first wanted to examine the effect of DNA binding on the melting temperature of HSF1. An idealized 22-base double-

stranded heat shock element oligonucleotide was used as a model of a heat shock promoter. The sequence of this oligonucleotide is 5'-CC**TGGAATATTCCCGAACT**GGC-3', where the HSF1 recognition sequences are indicated in bold and underlined. This sequence can accommodate the binding of a trimer of HSF1. A 22-base double-stranded oligonucleotide with each binding site mutated to nonbinding sequences, 5'-CCTG**GCG**TA**GTC**CC**CGC**CTGGC-3', was used as a negative control. The heat shock element-containing oligonucleotide (HSE) was found to bind to purified monomeric HSF1 with an apparent affinity of 122.9 ± 25.1 nM by a fluorescence polarization binding assay, while the negative control (HSE mutant) did not exhibit detectable binding up to 300 nM. In the differential scanning fluorimetry platform, the HSE oligonucleotide induced a large and dose-dependent increase in melting temperature of monomeric HSF1, while the HSE mutant oligonucleotide had no effect (Figure A.3).

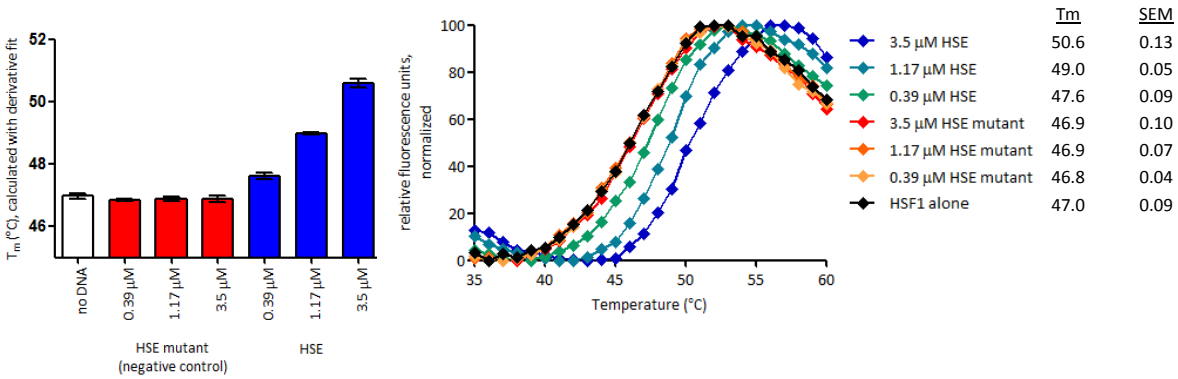

Figure A.3. Binding of HSE but not the HSE mutant induces a large and dose dependent increase in the apparent thermal stability of HSF1.

This suggested that DSF might be a sensitive platform for reporting on the interaction of ligands with HSF1. Next, we wanted to optimize the conditions of this assay with the goal of carrying out a pilot high-throughput screen to identify small molecule ligands for HSF1.

A.4. Optimization of screening conditions

Prior to carrying out a pilot screen to evaluate the utility of the differential scanning fluorimetry platform for the identification of ligands for HSF1, each component of the assay was systematically optimized. First, the effect of DMSO was determined by systematically varying DMSO concentration from 0 to 5%. The environmentally sensitive chromophore used in this assay, 1-anilinonaphthalene-8-sulfonic acid, was prepared in a stock solution of DMSO and contributed an additional 0.15% DMSO to each sample. DMSO was found to have no effect on

melting temperature of wild type HSF1 alone or on the change in T_m observed upon binding a stoichiometric ratio of HSE DNA.

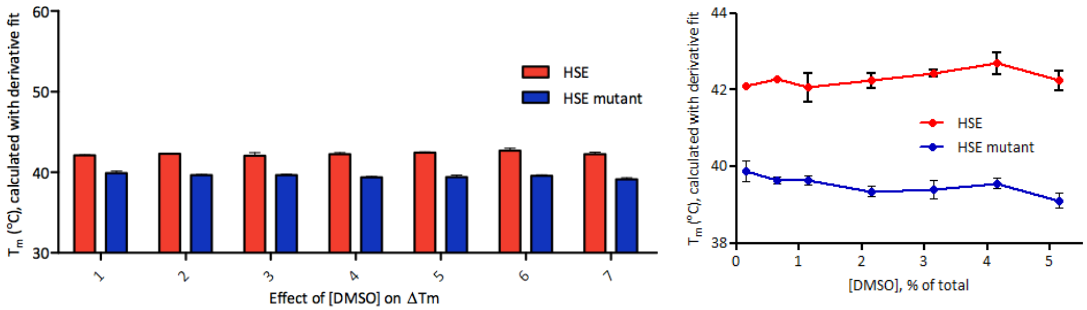

Figure A.4. DMSO concentration does not affect the change in Tm from HSE binding. DMSO was systematically varied from 0.15% (sample 1) to 5.15% (sample 7). In the bar graph, each value is the average of four replicates, and the error bars represent standard error. T_ms were calculated using the derivative fit. Red bars represent samples containing a 1:1 ratio of HSE DNA to HSF1 (calculated relative to trimeric HSF1), while the blue bars represent samples containing a 1:1 ratio of HSE mutant DNA to HSF1.

Next, the concentration of sodium chloride in the assay buffer was systematically varied, as DNA-protein interactions are known to be sensitive to salt concentration. Indeed, lower concentrations of salt (75 mM as shown in Figure A.5) appeared to potentiate the increase in thermal stability associated with HSE DNA binding. This may be due to sodium ions competing for ionic interactions with the DNA backbone. We chose to include 75 mM NaCl in the assay buffer. Inclusion of lower salt also led to a 'flattening' in the HSE-bound HSF1 melting curve (see Figure A.5) and an associated reduction in signal to noise for the HSE-bound form, but the curves were still cleanly interpretable and the signal to noise was acceptable.

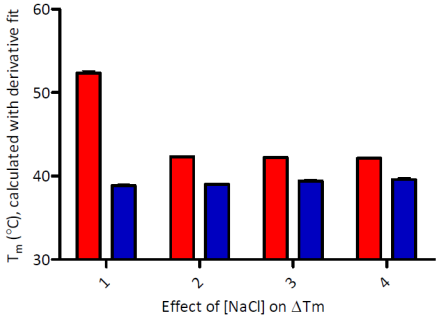

	+ HSE			+HSE mutant			
	Tm	SEM	N	Tm	SEM	N	ΔTm (°C)
75 mM NaCl	52.3	0.3	3	38.9	0.2	4	13.4
100 mM NaCl	42.3	0.1	4	39.0	0.1	4	3.3
125 mM NaCl	42.3	0.05	4	39.4	0.2	4	2.9
150 mM NaCl	42.1	0.1	4	39.6	0.2	4	2.5

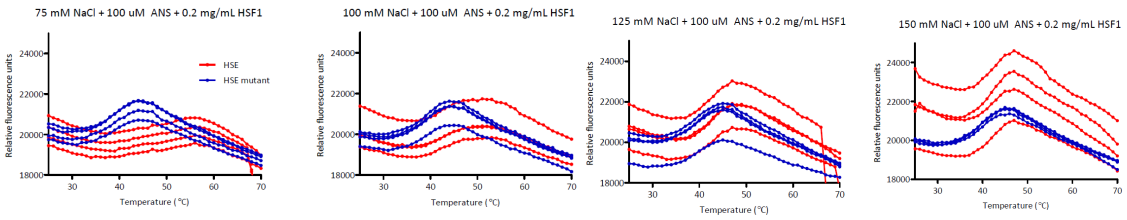

Figure A.5. Optimization of NaCl concentration for detection of HSF1-HSE complex formation by differential scanning fluorimetry. Sample 1 is 75 mM NaCl; 2: 100 mM, 3: 125 mM, 4: 150 mM. In the bar graph, each value is the average of four replicates (raw curves are shown), and the error bars represent standard error. Tms were calculated using the derivative fit. Red bars represent samples containing a 1:1 ratio of HSE DNA to HSF1 (calculated relative to trimeric HSF1), while the blue bars represent samples containing a 1:1 ratio of HSE mutant DNA to HSF1.

As discussed in section A.2.1, HSF1 contains several cysteines that form intramolecular and perhaps also intermolecular disulfide bonds. Consequently, we next examined the effect of reducing agent on the behavior of HSF1 and HSE-bound HSF1 in the differential scanning fluorimetry assay. Interestingly, inclusion of the reducing agent dithiothreitol (DTT) had a profound effect on the observed ΔT_m of HSE DNA binding (Figure A.6). Moreover, the effect of DTT was dependent on the amount of salt that was included. At 100 mM NaCl, inclusion of 5 mM DTT decreased the unbound HSF1 T_m and increased the bound HSF1 T_m such that the resulting ΔT_m of HSE binding was 15.6°C (as compared to 3.3°C in the absence of reducing agent). Conversely, in the presence of 150 mM NaCl, inclusion of 5 mM DTT decreased the unbound HSF1 T_m as in the lower salt condition but only increased the bound HSF1 T_m slightly. The resulting ΔT_m of HSE binding was therefore only 8.8°C (as compared to 2.5°C in the absence of reducing agent). A model that may explain this observation is drawn in Figure A.6. It may be that the recombinant purified HSF1 is trapped in a disulfide-bound conformation that is not competent to fully bind HSE DNA. Inclusion of reducing agent frees those disulfide bonds, leading to an apparently less stable HSF1 conformation that melts at a lower temperature in the absence of DNA binding. However, in the presence of HSE DNA, this conformation is more competent to bind DNA, which dramatically increases its apparent stability. Inclusion of higher concentrations of salt inhibits this DNA binding interaction.

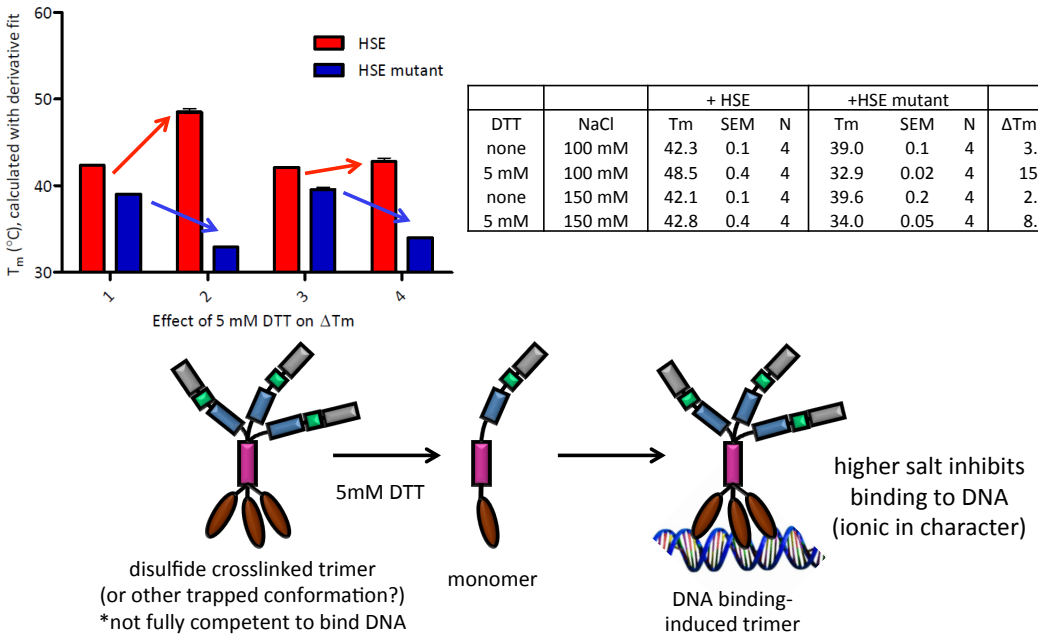

		+ HSE			+HSE mutant			
DTT	NaCl	Tm	SEM	N	Tm	SEM	N	ΔTm (°C)
none	100 mM	42.3	0.1	4	39.0	0.1	4	3.3
5 mM	100 mM	48.5	0.4	4	32.9	0.02	4	15.6
none	150 mM	42.1	0.1	4	39.6	0.2	4	2.5
5 mM	150 mM	42.8	0.4	4	34.0	0.05	4	8.8

Figure A.6. Effect of the reducing agent DTT on HSF1-HSE complex monitoring by differential scanning fluorimetry. In the bar graph, each value is the average of four replicates, and the error bars represent standard error. Tms were calculated using the derivative fit. Red bars represent samples containing a 1:1 ratio of HSE DNA to HSF1 (calculated relative to trimeric HSF1), while the blue bars represent samples containing a 1:1 ratio of HSE mutant DNA to HSF1.

Next, we asked whether the reducing agent tris(2-carboxyethyl)phosphine hydrochloride (TCEP-HCl) would have the same effect as DTT in this platform. Either TCEP-HCl or the equivalent concentration of HCl was included in order to control for any changes in pH from the acidic reagent. Figure A.7 demonstrates that TCEP does have a very similar effect to DTT, though the observed ΔT_m of HSE binding was smaller for TCEP than for DTT (15.3°C instead of 20.7°C). The curveshapes were also slightly different for the two reducing agents, as is shown in Figure A.7. TCEP is often used in high-throughput screening because it is more inert to reaction with electrophilic small molecules in screening libraries than DTT, so we chose to include it in the assay buffer. The amount of TCEP was optimized by systematically varying its concentration and holding other variables constant. The inclusion of 1 mM TCEP decreased the unbound melting temperature of HSF1 and increased the apparent melting temperature of the DNA-bound form (Figure A.8). Higher concentrations of TCEP (2 mM or 2.5 mM) decreased the upper, post-denaturation fluorescence baseline of the DNA-bound form of HSF1 such that the signal-to-noise of the transition was also lower. Therefore, 1 mM TCEP was included in the buffer for the pilot screen.

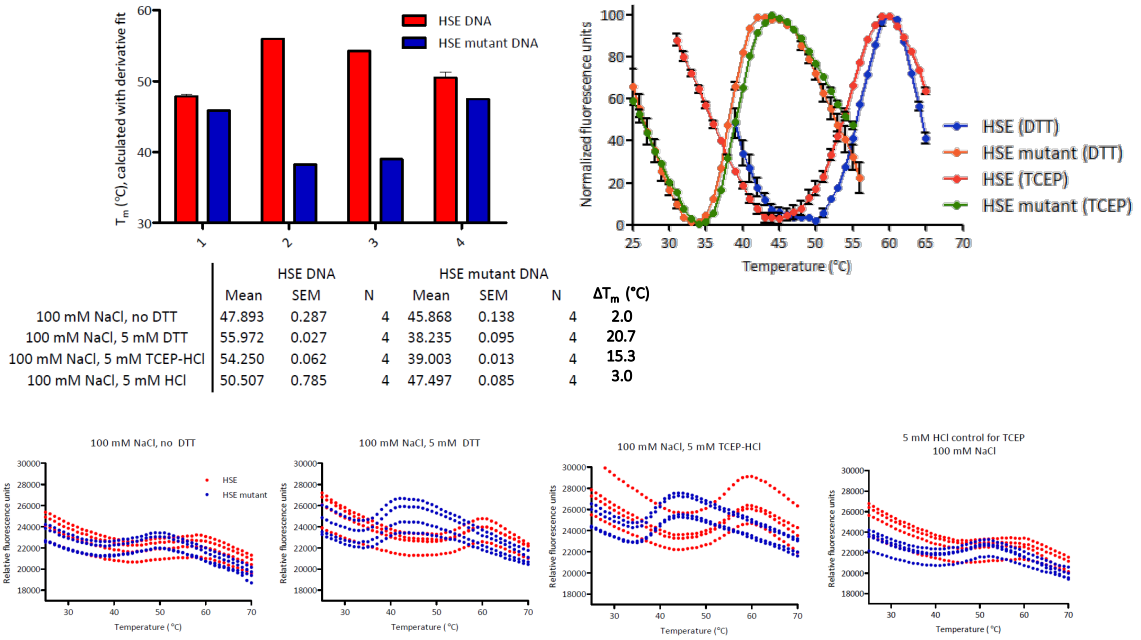

	HSE DNA			HSE mutant DNA			
	Mean	SEM	N	Mean	SEM	N	ΔT_m (°C)
100 mM NaCl, no DTT	47.893	0.287	4	45.868	0.138	4	2.0
100 mM NaCl, 5 mM DTT	55.972	0.027	4	38.235	0.095	4	20.7
100 mM NaCl, 5 mM TCEP-HCl	54.250	0.062	4	39.003	0.013	4	15.3
100 mM NaCl, 5 mM HCl	50.507	0.785	4	47.497	0.085	4	3.0

Figure A.7. Effect of reducing agent TCEP on HSF1-HSE complex monitoring by differential scanning fluorimetry. In the bar graph, each value is the average of four replicates, and the error bars represent standard error. Tms were calculated using the derivative fit. Red bars represent samples containing a 1:1 ratio of HSE DNA to HSF1 (calculated relative to trimeric HSF1), while the blue bars represent samples containing a 1:1 ratio of HSE mutant DNA to HSF1.

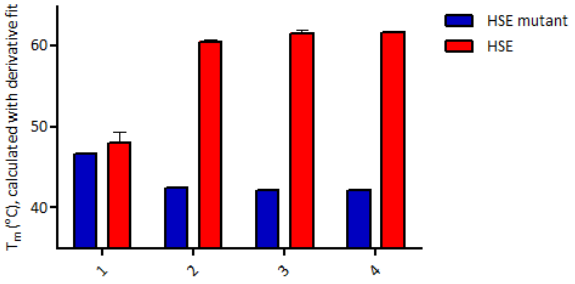

Figure A.8. Effect of varying TCEP concentration on HSF1-HSE complex detection by differential scanning fluorimetry. 1: no TCEP; 2: 1 mM TCEP, 3: 2 mM TCEP, 4: 2.5 mM TCEP. Each value is the average of four replicates, and the error bars represent standard error. T_ms were calculated using the derivative fit. Red bars represent samples containing a 1:1 ratio of HSE DNA to HSF1 (calculated relative to trimeric HSF1), while the blue bars represent samples containing a 1:1 ratio of HSE mutant DNA to HSF1.

Because of the pronounced effect of NaCl on the ΔT_m of HSE binding, we wanted to control for the effect of $MgCl_2$ as well. Magnesium chloride decreases the ΔTm of HSE binding in both the presence and absence of TCEP (shown in the presence of TCEP in Figure A.9.) While the reason for this effect is unknown, we speculate that magnesium competes for ionic interactions involved in the interaction of HSE DNA with the DNA binding domain. To reduce the probability of identifying false positives, we included 1 mM $MgCl_2$ in the assay buffer.

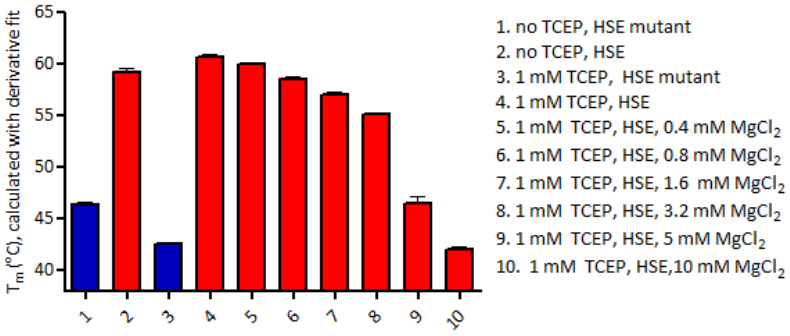

Figure A.9. Effect of varying $MgCl_2$ concentration on HSF1-HSE complex detection by differential scanning fluorimetry. Each value is the average of four replicates, and the error bars represent standard error. Tms were calculated using the derivative fit. Red bars represent samples containing a 1:1 ratio of HSE DNA to HSF1 (calculated relative to trimeric HSF1), while the blue bars represent samples containing a 1:1 ratio of HSE mutant DNA to HSF1.

Because differential scanning fluorimetry (and other HTS techniques) are prone to the identification of false positives from aggregation-prone compounds, we wanted to include 0.005% Tween-20 in the assay conditions to reduce the probability of discovering aggregators. Inclusion of this concentration of Tween-20 had no significant effect on T_m or ΔT_m (Figure A.10.) The shape of the curve was also unaffected by inclusion of the detergent.

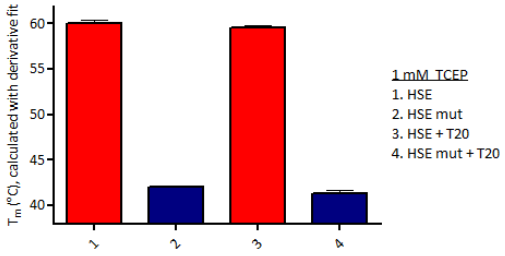

Figure A.10. Inclusion of detergent Tween-20 does not appear to affect Tm observed for HSE binding. Each value is the average of four replicates, and the error bars represent standard error. Tms were calculated using the derivative fit. Red bars represent samples containing a 1:1 ratio of HSE DNA to HSF1 (calculated relative to trimeric HSF1), while the blue bars represent samples containing a 1:1 ratio of HSE mutant DNA to HSF1.

Interestingly, addition of nucleotide slightly affected the T_m of free and bound HSF1 and the ΔT_m of HSE binding. Under these conditions (100 mM NaCl and no reducing agent), the presence of 1 mM ATP or ADP increased the ΔT_m from 2°C to 2.8°C or 2.6°C, respectively (Figure A.11.). It is not clear what the physical explanation for this effect may be, as HSF1 is not thought to contain a nucleotide-binding site.

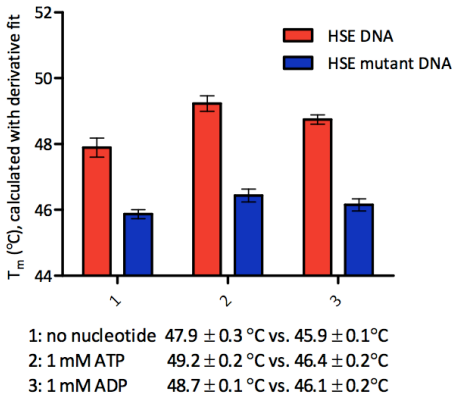

Figure A.11. The presence of nucleotide affects T_m of free and bound HSF1 and the ΔT_m of HSE binding but the reason for this effect is unknown. Each value is the average of four replicates, and the error bars represent standard error. Tms were calculated using the derivative fit. Red bars represent samples containing a 1:1 ratio of HSE DNA to HSF1 (calculated relative to trimeric HSF1), while the blue bars represent samples containing a 1:1 ratio of HSE mutant DNA to HSF1.

A.5. Pilot high throughput screen for small molecule ligands of HSF1

The final conditions for the pilot screen included 0.1 mg/mL (~1.7 µM) wild type monomeric HSF1 and 50 µM 1,8-ANS in 25 mM HEPES pH 7.5 containing 75 mM NaCl, 1 mM $MgCl_2$, 1 mM TCEP, 0.005% Tween-20, and 0.5% DMSO. Compounds were tested at 10 µM and singleplexed. Each well contained a final well volume of 10 µL overlaid with 2 µL silicon oil. Plates were centrifuged for 2 min at 1000 rpm before running, and the signal was measured to be stable over 10 hours when stored at 4°C in the dark (to ensure that a day's plates could all be made up in the morning and run over the course of the day, without compromising data quality). Negative controls contained 0.5% DMSO only, and positive controls contained 0.5% DMSO + 560 nM HSE DNA. Plates were run on the Johnson & Johnson ThermoFluor instrument from 25-70°C in continuous ramp mode, at a rate of 30 sec per degree. A shutter-closed image was taken before heating and background subtracted throughout. A 16x16 pixel integration box was used.

Library	Description	Compounds
MicroSource Spectrum 2000	Known bioactive compounds	2000
BioFocus NCC clinical collection	FDA-approved drugs	446
CCG focused collections	Molecules targeted towards protein kinases, proteases, and cannabinoid receptors; targets involved in autophagy, the Wnt signaling pathway, and epigenetics; redox active molecules and natural products	1037
Total		3154

Table A.1. Characteristics of the screening libraries included in pilot screen.

A total of 3154 compounds were screened, which required thirteen plates and two days to complete. Characteristics of the three libraries that were screened are described in Table A.1. The hit rates for the primary screen are described in the flowchart in Figure A.12, below. Using a three standard deviation cutoff (calculated for the negative controls across the entire campaign) a total of 85 hits were identified from the automated analysis protocol described briefly in Chapter 3 (3.8.3.). This corresponds to a hit rate of 2.6%. Of these, 68 hits caused negative deflection in T_m while 17 hits increased T_m. The melting curves for each hit were visually inspected and excluded if the curve shape was poor, noisy, or suggested a fluorescent compound, aggregation of the protein, or a quenching interaction with the solvatochromic dye. This excluded 9 wells, leaving 61 negative hits and 15 positive hits. A wide range of T_ms was seen for the 61 negative hits (spanning -1.3°C to -7.8°C relative to the average of the negative controls), and relatively small positive changes were observed from the 15 positive hits (spanning +1.3°C to +2.7°C). From these, 16 hits were obtained for reconfirmation, equally representing negative and positive hits and chosen based on physicochemical properties, chemical structures, and practical availability.

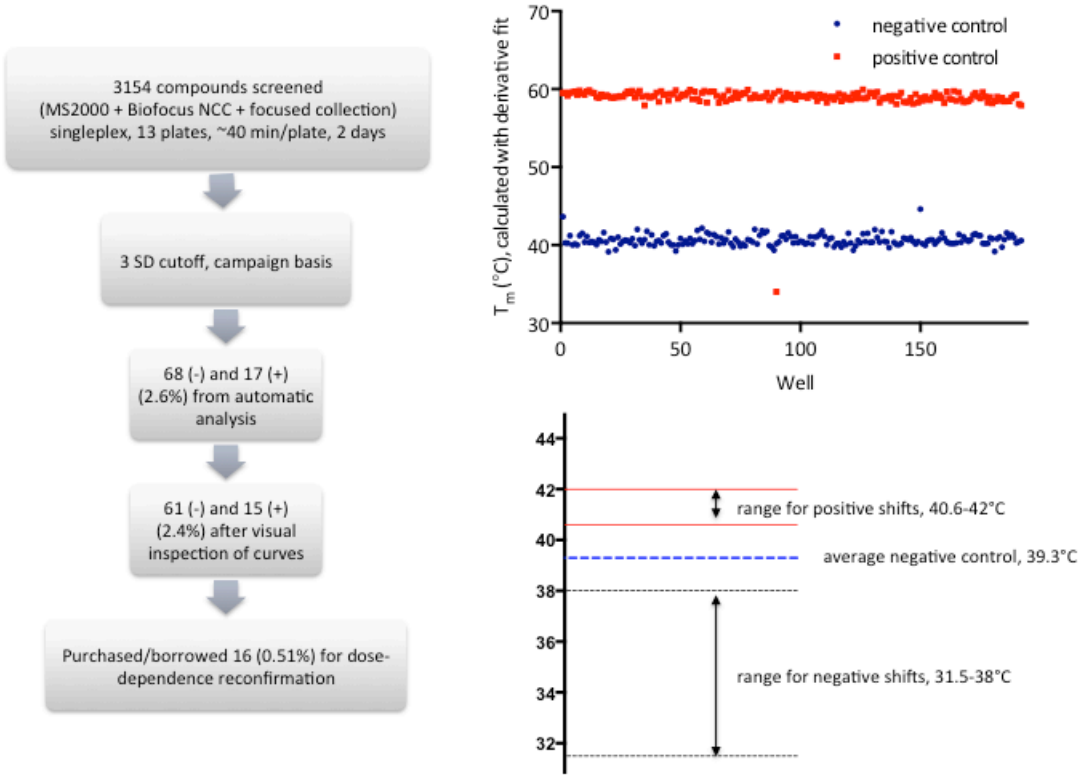

Figure A.12. Flowchart of high-throughput screening process. Distribution of positive and negative controls are shown for a 50/50 plate of positive and negative controls, from which the Z' factor was determined to be 0.92. The average Z' across the whole screen was 0.85. A larger range of negative shifts was seen for the 61 negative hits (spanning -

1.3°C to -7.8°C) than the relatively small positive changes observed from the 15 positive hits (spanning +1.3°C to +2.7°C).

The results of the reconfirmation effort are shown in Figure A.13 in a bar graph and summary table. The chemical structures for the sixteen reconfirmation compounds are shown in Figure A.14. Compounds were again screened at 10 µM under the same conditions as in the screen. While the controls wells performed as expected, only epigallocatechin gallate (EGCG, **15**) and cedryl acetate (**16**) appeared to reconfirm in this experiment. The original change in T_m for EGCG was -2.2°C, and in the reconfirmation experiment it was only about -1°C. Upon closer inspection, it appeared that EGCG competed with or quenched 1,8-ANS fluorescence and the resulting altered curve shape accounted for the decrease in T_m. Additionally, polyphenols are known to be very promiscuous binders and so EGCG was not considered as a viable scaffold for further development. The changes observed in the reconfirmation experiments with cedryl acetate were not significant (Figure A.15).

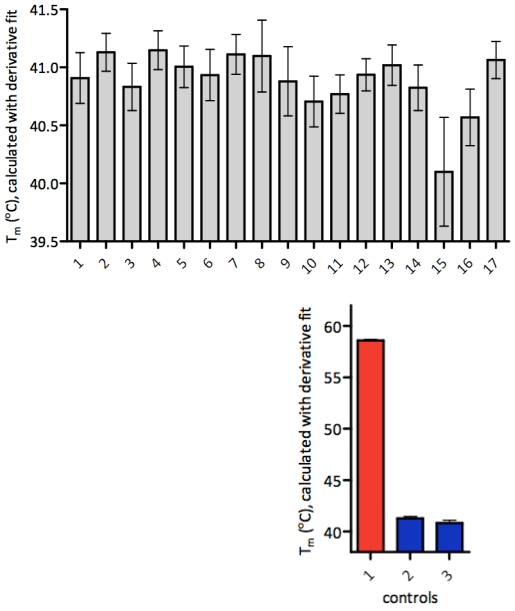

	compound	mean	SEM	n
1	ancitabine	40.91	0.22	8
2	atropine	41.13	0.16	8
3	boldine	40.83	0.20	8
4	bromhexine	41.15	0.17	8
5	buflomedil	41.01	0.18	8
6	bupivacaine	40.93	0.22	8
7	carbofuran	41.11	0.17	8
8	D. lactone	41.10	0.31	8
9	propanil	40.88	0.30	8
10	tolterodine tartrate	40.71	0.22	8
11	tranilast	40.77	0.16	8
12	α-tocopherol	40.94	0.14	8
13	cephalosporin C, K+	41.02	0.17	8
14	catechin	40.82	0.20	8
15	EGCG	40.10	0.47	8
16	cedryl acetate	40.57	0.24	8
17	DMSO only	41.06	0.16	16

Figure A.13. Result of single-concentration reconfirmation (at 10 µM) from 16 repurchased or borrowed hits. Each value is the average of eight replicates, and the error bars represent standard error. T_ms were calculated using the derivative fit. Positive controls (red) and two sets of negative controls (blue) are shown in the bar graph, showing that the assay performance was similar to the primary assay.

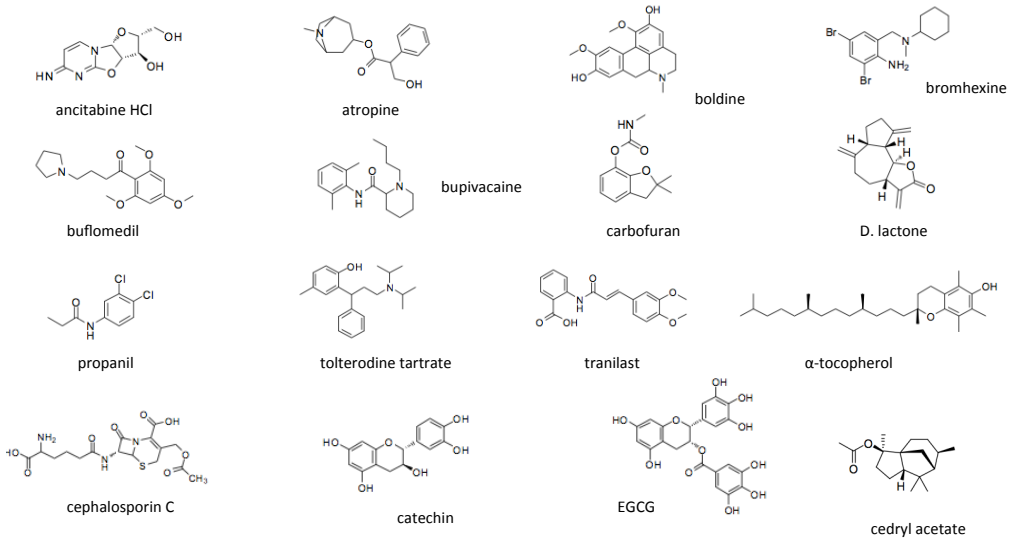

Figure A.14. Chemical structures of 16 hits assembled for retesting. EGCG and cedryl acetate are shown.

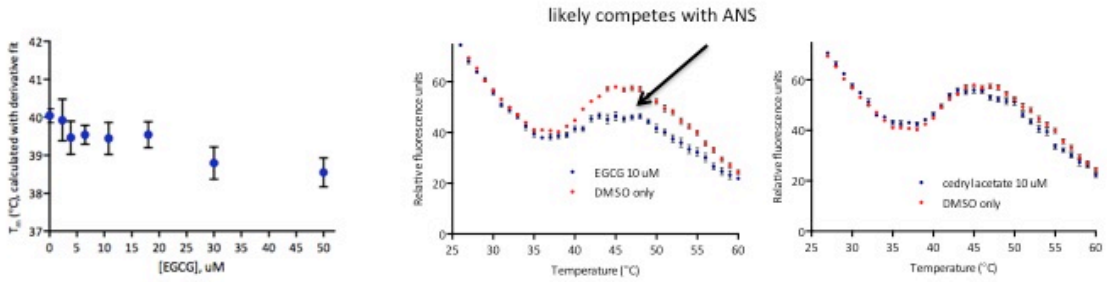

Figure A.15. No hit compounds reconfirmed of the 16 that were re-tested in the primary screening assay. Each value is the average of four replicates, and the error bars represent standard error. T_ms were calculated using the derivative fit.

It is not clear why the sixteen original hits from the primary assay did not reconfirm. A different preparation of protein was used for the reconfirmation versus the primary screen, which may contribute to variability. It is possible that degradation products or contaminants in the screening library accounted for the original activity of the hit molecules. It is also possible that more robust hits are present in the 60 scaffolds that were not repurchased for reconfirmation experiments.

A.6. Alternative screening strategies

The pilot screen described in the previous section used monomeric, wild type HSF1 in the presence of reducing agent and in the absence of any of HSF1's binding partners, including HSE DNA or molecular chaperones. The differential scanning fluorimetry platform can easily be applied to screening different conformations or complexes of HSF1. For a conformationally

heterogeneous target protein, ligand-induced changes in thermal stability can reflect a number of distinct physicochemical phenomena. These include straightforward increases in thermal stability due to the energy of ligand binding to a given conformation or conformations, complex formation with nucleic acid, and conformational changes of HSF1 that reflect differential thermal stabilities of the predominant protein conformations or oligomeric states. In the presence of reducing agent and low salt concentrations, the change in T_m upon DNA binding is very large (~20°C), and may be useful as a sensitive reporter of ligand-induced changes in nucleic acid binding. That is, screening in the presence of a concentration of HSE DNA in the middle of the dynamic range of the HSE-induced ΔT_m may result in the identification of ligands that inhibit or potentiate DNA binding (Figure A.16).

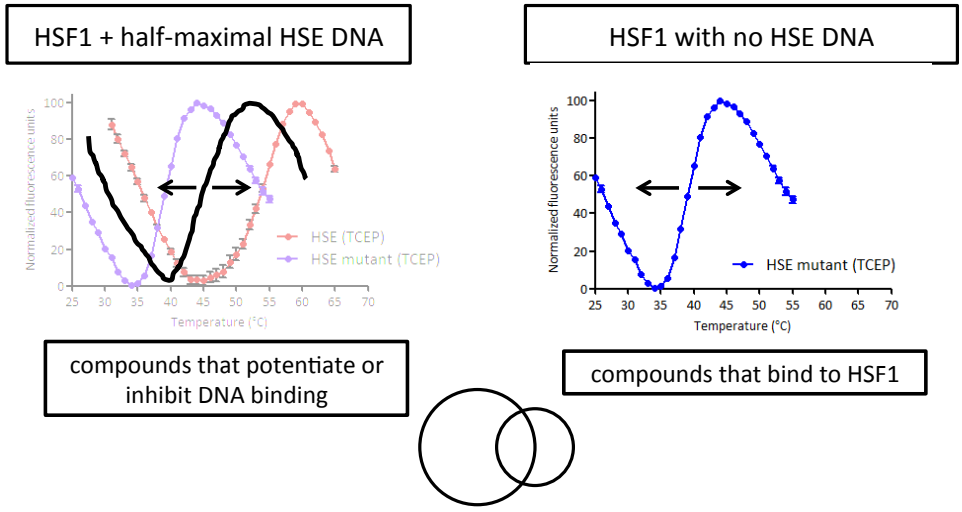

Figure A.16. An alternative setup for a DSF-based HTS may rely on DNA binding as a reporter of quaternary structure (left) and may be expected to result in some common but some different chemical hits, as diagrammed above.

Similarly, characterization of constructs with different conformations or quaternary structures may help to identify the biophysical signatures of different conformations. This in turn would enable a DSF screen for identifying ligands that favor specific protein conformations or oligomeric states of HSF1. In addition to the monomeric form, the recombinant wild type protein elutes as an oligomer (possibly a trimer) when purified by size-exclusion chromatography by members of the Thiele laboratory. Additionally, the Thiele laboratory has developed constructs of HSF1 that lack critical oligomerization domains or are constitutively oligomerized. We began to study these proteins by differential scanning fluorimetry in order to gain insight into the observed behaviors of monomeric HSF1 binding its recognition element. The monomeric and oligomeric forms of HSF1 behave distinctly in DNA binding platforms, with

apparent affinities for the HSE oligonucleotide of 122.9 ± 25.1 nM and 12.1 ± 2.1 nM respectively.

The LZ1-3 construct lacks the leucine zipper trimerization domain, and so it is constitutively monomerized (Figure A.17). As expected, the constitutive monomer binds rather weakly to the HSE oligonucleotide with an apparent affinity of 609.3 ± 160.5 nM as measured by FP. By DSF, this construct does not appear to bind to HSE DNA at a stoichiometric concentration (Figure A.18). The LZ4 construct has L391M, L395P, and L398P point mutations in the LZ4 domain that result in a constitutively trimerized HSF1 (11) (Figure A.17). Its affinity for HSE oligonucleotide is 35 ± 7.1 nM by FP. Interestingly, the thermal stability of this construct in the absence of DNA resembles that of wild type, trimeric HSF1 (as well as wild type, monomeric, reduced HSF1). The ΔT_m of HSE binding resembles that of the wild type, monomeric protein (Figure A.18).

Lastly, the Agard laboratory has cloned a slightly shortened construct lacking the N- and C-terminal intrinsically disordered regions, which might be more amenable to structural characterization than the full-length protein. The truncations do not impair the normal trimerization contacts, and so it was included in the DSF experiments as a control. As expected, the T_m and ΔT_m of HSE binding are identical to those of the wild type protein.

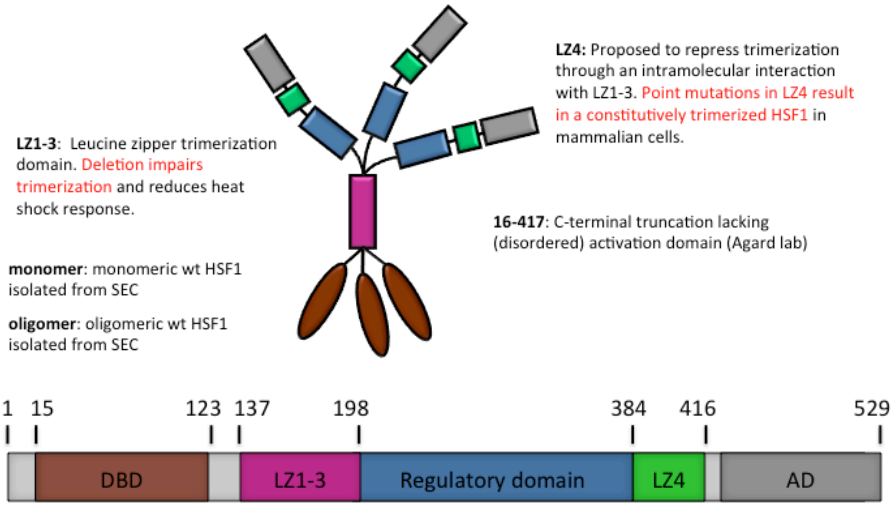

Figure A.17. Alternative constructs of HSF1 that may prove useful in HTS efforts.

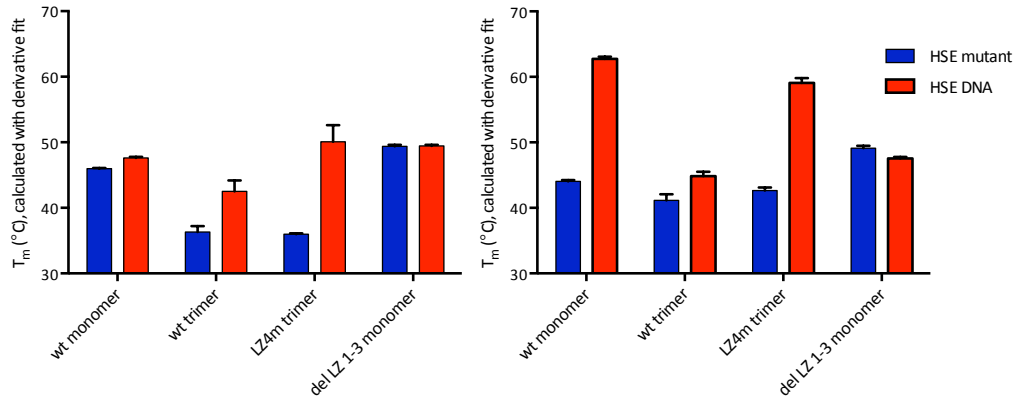

	HSE mutant		HSE			HSE mutant		HSE		
	Tm (°C)	SEM	Tm (°C)	SEM	ΔTm (°C)	Tm (°C)	SEM	Tm (°C)	SEM	ΔTm (°C)
wt monomer	45.99	0.07	47.61	0.19	1.62	44.02	0.21	62.74	0.33	18.72
wt trimer	36.32	0.91	42.52	1.67	6.20	41.10	0.94	44.86	0.66	3.76
LZ4m trimer	35.97	0.14	50.09	2.54	14.13	42.63	0.46	59.08	0.73	16.45
ΔLZ 1-3 monomer	49.38	0.24	49.46	0.15	0.08	49.09	0.36	47.56	0.22	-1.53

Figure A.18. DSF characterization of alternative constructs of HSF1 that may prove useful in conducting or interpreting future HTS efforts. DSF experiments were carried out as described above in the absence or presence of reducing agent and HSE or HSE mutant oligonucleotide at a concentration stoichiometric to the theoretical concentration of trimeric HSF1 (560 nM oligonucleotide to 1.7 µM HSF1). Each value is the average of four replicates, and error is SEM.

As an alternative to DSF, a technique that reports directly on the oligomeric state of HSF1 (e.g. monomer versus trimer) may be useful as a screening platform. High-throughput capillary electrophoresis may be well-suited to the identification of modulators of the homomeric HSF1 protein-protein interactions (13). Lastly, the fluorescence polarization platform developed in the Thiele laboratory may be a useful alternative technique for the identification of allosteric ligands that perturb quaternary structure. Since the affinities of monomer and oligomer binding to the idealized HSE differ by an order of magnitude, DNA binding may be useful as an indirect reporter of quaternary structure.

A.7. Preliminary electron microscopy and DNA scaffolding strategy to visualize complex

There are no published structures of full-length HSF1 at any resolution, though crystal structures of its highly conserved DNA binding domain have been solved. Monomeric HSF1 is 57 kDa, which is near the lower limit of detection by negative stain transmission electron microscopy. Trimeric HSF1, however, is approximately 172 kDa in size and thus is expected to be readily visible. We took early steps towards characterizing HSF1 by electron microscopy and optimizing conditions to obtain a homogenous dispersion of particles for class averages. Despite separation by size-exclusion chromatography immediately prior to the preparation of grids, HSF1 was observed as a heterogeneous mixture of conformations (Figure A.19).

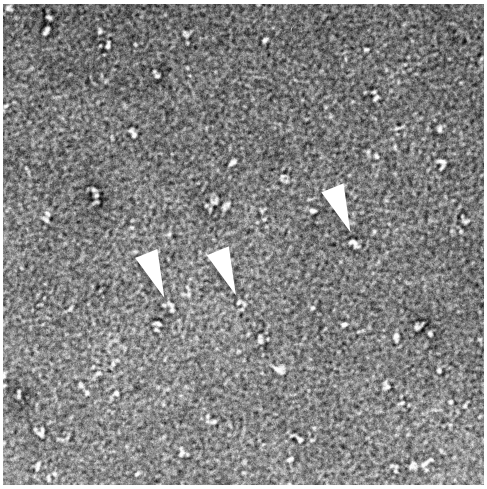

Figure A.19. Preliminary negative stain electron microscopy images of HSF1 in the absence of DNA. The heterogeneity of the shapes and sizes of particles in the sample is apparent. White arrows indicate probable trimers of HSF1.

To facilitate the preparation of homogenous grids and assure the identification of trimeric HSF1 uncomplicated by the presence of other quaternary structures, we considered a DNA-templating strategy. A double stranded DNA oligonucleotide was designed containing five idealized HSEs in sequence (Figure A.20). Using DSF and an electrophoretic mobility shift assay, HSF1 was confirmed to bind to the oligonucleotide. However, the stoichiometry of the binding interaction is not clear from these measurements, and an optimized electrophoretic mobility shift assay with greater resolution would be helpful in elucidating the stoichiometry. The scaffolding may require optimization in number, spacing, and orientation of HSEs.

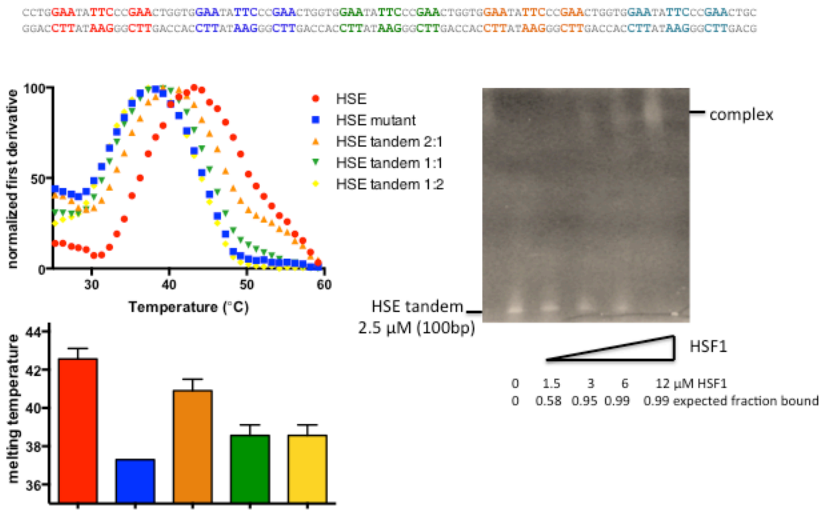

Figure A.20. Organization of five tandem repeats of heat shock elements in oligonucleotide, and binding of HSF1 to tandem repeats by DSF and by EMSA. See Experimental Procedures (A.9) for details.

However, since HSF1 is known to bind to DNA as trimers, this templating strategy may prove useful to facilitate its structural characterization. Electron microscopy of HSF1 is expected to provide a useful tool for the study of small molecules that alter oligomerization state. Additionally, this platform may enable the future characterization of chaperone-HSF1 interactions, and warrants further development.

A.8. Conclusions and future directions

The long-term goals of this work are to understand how we can activate HSF1 using small molecules with the end goal of developing therapeutics for neurodegenerative diseases. Where are the small molecule binding sites within HSF1? Is it possible to inhibit the interactions of Hsp70 and Hsp90 with HSF1 by binding to HSF1? Can one develop an HSF1 ligand that potentiates DNA binding, possibly through stabilization of the trimeric form? Future work should extend the DSF screening effort described herein towards the goal of identifying such modulators, and complete the reconfirmation effort of the other scaffolds identified in the initial pilot screen. A parallel comparison of a second small pilot screen carried out against the complex of HSF1 with HSE DNA (Figure A.16) should be informative as to the best path forward. If neither format of the DSF screen is fruitful in producing robust, reproducible hits, then the fluorescence polarization assay or capillary electrophoresis should next be explored as alternative screening platforms.

A.9. Experimental Procedures

A.9.1. Differential scanning fluorimetry optimization

Optimization assays utilized 0.1 mg/mL (~1.7 µM) or 0.2 mg/mL (~3.4 µM) wild type monomeric HSF1 and 50 or 100 µM 1,8-ANS in 25 mM HEPES pH 7.5 containing varying amounts of NaCl, $MgCl_2$, DTT or TCEP, Tween-20, and DMSO as indicated. Typically, samples were made up using manual or Matrix automatic pipettes in a 96-well PCR plate, then transferred to a 384-well black skirted low volume PCR plate (Thermo Fisher) in sets of four replicates using a Matrix automatic pipette. Each well contained a final well volume of 10 µL and was overlaid with 2 µL silicon oil. Plates were centrifuged for 2 min at 1000 rpm before running on a Johnson & Johnson ThermoFluor instrument from 25-70°C in continuous ramp mode, at a rate of 30 sec per degree. A shutter-closed image was taken before heating and background subtracted throughout. A 16x16 pixel integration box was consistently used.

A.9.2. Differential scanning fluorimetry pilot screen

As described in the text, the conditions used for the pilot screen included 0.1 mg/mL (~1.7 μM) wild type monomeric HSF1 and 50 μM 1,8-ANS in 25 mM HEPES pH 7.5 containing 75 mM NaCl, 1 mM $MgCl_2$, 1 mM TCEP, 0.005% Tween-20, and 0.5% DMSO. Compounds were tested at 10 μM and added directly to 384-well black-skirted low volume PCR plates (Thermo Fisher). Compound stocks were added in 200 nL drops by a pin tool in the Center for Chemical Genomics and followed by a protein, 1,8-ANS, and buffer solution. Negative controls contained 0.5% DMSO only, and positive controls contained 0.5% DMSO + 560 nM HSE DNA. Plates were run as described above.

A.9.3. Electrophoretic mobility shift assay

The electrophoretic mobility shift assay protocol was adapted from (14). Briefly, a vertical, native 4% polyacrylamide gel was equilibrated by pre-running in tris-glycine running buffer containing 40 mM Tris base, 400 mM glycine, and 2 mM EDTA at pH 8.0. The pI of HSF1 is 5.0, so the transcription factor-DNA complex is negatively charged at this pH. Then, 10 μL samples were loaded which contained a final concentration of 2.5 μM tandem HSE DNA, final concentrations of 0, 1.5, 3, 6, or 12 μM HSF1 monomer, and 2 μL of glycerol-only loading dye (bromophenol blue was found to interfere with detection of the DNA). The gel was electrophoresed for one hour at 200V and stained with ethidium bromide.

A.9.4. Electron microscopy

HSF1 was separated by size exclusion chromatography using an analytical SuperDex200 column equilibrated in 25 mM HEPES pH 7.5, 150 mM NaCl. A sample of 675 μL of 0.25 mg/mL HSF1 was injected and separated at 0.5 mL/min, eluting as a single peak centered at 14 mL elution volume. A fraction in the center of this peak was collected, diluted 1:10 into freshly filtered buffer, and applied to glow-discharged Formvar/carbon 300-mesh copper grids (Electron Microscopy Sciences). The total time from elution from the chromatography column to gridding samples was less than ten minutes. Grids were washed with water, stained with 2% uranyl formate, and micrographs were taken at 22,000x magnification on a 100 kV Morgagni microscope using a Gatan Orius CCD.

A.10. Notes

Alex Jaeger in Dennis Thiele's laboratory at Duke University expressed and purified the wild type, ΔLZ1-3, and LZ4m HSF1 proteins, designed the HSE and HSE mutant DNA oligonucleotides, and measured the binding constants using fluorescence polarization. A construct containing residues 16-417, lacking the disordered C-terminal activation domain, was cloned, expressed, and purified by Joe Tao of the Agard laboratory. Thomas McQuade in the University of Michigan Center for Chemical Genomics (CCG) kindly set up the plates for the pilot screen and provided useful help and feedback in the design of the screen.

A.11. References

1. Neef DW, Turski ML, Thiele DJ. Modulation of heat shock transcription factor 1 as a therapeutic target for small molecule intervention in neurodegenerative disease. PLoS biology. 2010;8(1):e1000291.
2. Neef DW, Jaeger AM, Thiele DJ. Heat shock transcription factor 1 as a therapeutic target in neurodegenerative diseases. Nature reviews Drug discovery. 2011;10(12):930-44.
3. Bharadwaj S, Ali A, Ovsenek N. Multiple components of the HSP90 chaperone complex function in regulation of heat shock factor 1 In vivo. Molecular and cellular biology. 1999;19(12):8033-41.
4. Akerfelt M, Morimoto RI, Sistonen L. Heat shock factors: integrators of cell stress, development and lifespan. Nature reviews Molecular cell biology. 2010;11(8):545-55.
5. Sorger PK, Nelson HC. Trimerization of a yeast transcriptional activator via a coiled-coil motif. Cell. 1989;59(5):807-13.
6. Ahn SG, Thiele DJ. Redox regulation of mammalian heat shock factor 1 is essential for Hsp gene activation and protection from stress. Genes & development. 2003;17(4):516-28.
7. Abravaya K, Myers MP, Murphy SP, Morimoto RI. The human heat shock protein hsp70 interacts with HSF, the transcription factor that regulates heat shock gene expression. Genes & development. 1992;6(7):1153-64.
8. Guo Y, Guettouche T, Fenna M, Boellmann F, Pratt WB, Toft DO, et al. Evidence for a mechanism of repression of heat shock factor 1 transcriptional activity by a multichaperone complex. The Journal of biological chemistry. 2001;276(49):45791-9.
9. Shi Y, Mosser DD, Morimoto RI. Molecular chaperones as HSF1-specific transcriptional repressors. Genes & development. 1998;12(5):654-66.
10. Ahn SG, Liu PC, Klyachko K, Morimoto RI, Thiele DJ. The loop domain of heat shock transcription factor 1 dictates DNA-binding specificity and responses to heat stress. Genes & development. 2001;15(16):2134-45.
11. Neef DW, Jaeger AM, Thiele DJ. Genetic selection for constitutively trimerized human HSF1 mutants identifies a role for coiled-coil motifs in DNA binding. G3. 2013;3(8):1315-24.
12. Bauer RA, Wurst JM, Tan DS. Expanding the range of 'druggable' targets with natural product-based libraries: an academic perspective. Current opinion in chemical biology. 2010;14(3):308-14.
13. Rauch JN, Nie J, Buchholz TJ, Gestwicki JE, Kennedy RT. Development of a capillary electrophoresis platform for identifying inhibitors of protein-protein interactions. Analytical chemistry. 2013;85(20):9824-31.

14. Zuo J, Baler R, Dahl G, Voellmy R. Activation of the DNA-binding ability of human heat shock transcription factor 1 may involve the transition from an intramolecular to an intermolecular triple-stranded coiled-coil structure. Molecular and cellular biology. 1994;14(11):7557-68.